

applied sciences

Special Issue Reprint

Superhydrophobic and Icephobic Coatings as Passive Ice Protection Systems for Aeronautical Applications

Edited by
Filomena Piscitelli

[mdpi.com/journal/applsci](https://www.mdpi.com/journal/applsci)



Superhydrophobic and Icephobic Coatings as Passive Ice Protection Systems for Aeronautical Applications

Superhydrophobic and Icephobic Coatings as Passive Ice Protection Systems for Aeronautical Applications

Editor

Filomena Piscitelli



Basel • Beijing • Wuhan • Barcelona • Belgrade • Novi Sad • Cluj • Manchester

Editor

Filomena Piscitelli

Department of Materials
and Structures

CIRA - Italian Aerospace

Research Centre

Capua

Italy

Editorial Office

MDPI

St. Alban-Anlage 66

4052 Basel, Switzerland

This is a reprint of articles from the Special Issue published online in the open access journal *Applied Sciences* (ISSN 2076-3417) (available at: www.mdpi.com/journal/applsci/special-issues/Superhydrophobic_and_Icephobic_Coatings_as_Passive_Ice_Protection_Systems_for_Aeronautical_Applications).

For citation purposes, cite each article independently as indicated on the article page online and as indicated below:

Lastname, A.A.; Lastname, B.B. Article Title. <i>Journal Name</i> Year , <i>Volume Number</i> , Page Range.
--

ISBN 978-3-7258-0764-2 (Hbk)

ISBN 978-3-7258-0763-5 (PDF)

doi.org/10.3390/books978-3-7258-0763-5

Cover image courtesy of Filomena Piscitelli

© 2024 by the authors. Articles in this book are Open Access and distributed under the Creative Commons Attribution (CC BY) license. The book as a whole is distributed by MDPI under the terms and conditions of the Creative Commons Attribution-NonCommercial-NoDerivs (CC BY-NC-ND) license.

Contents

About the Editor	vii
Preface	ix
Filomena Piscitelli	
Special Issue “Superhydrophobic and Icephobic Coatings as Passive Ice Protection Systems for Aeronautical Applications”	
Reprinted from: <i>Appl. Sci.</i> 2024 , <i>14</i> , 1288, doi:10.3390/app14031288	1
Filomena Piscitelli	
Characterization in Relevant Icing Conditions of Two Superhydrophobic Coatings	
Reprinted from: <i>Appl. Sci.</i> 2022 , <i>12</i> , 3705, doi:10.3390/app12083705	4
Filomena Piscitelli, Salvatore Palazzo and Felice De Nicola	
Icing Wind Tunnel Test Campaign on a Nacelle Lip-Skin to Assess the Effect of a Superhydrophobic Coating on Ice Accretion	
Reprinted from: <i>Appl. Sci.</i> 2023 , <i>13</i> , 5183, doi:10.3390/app13085183	23
Michele Ferrari and Francesca Cirisano	
Superhydrophobic Coating Solutions for Deicing Control in Aircraft	
Reprinted from: <i>Appl. Sci.</i> 2023 , <i>13</i> , 11684, doi:10.3390/app132111684	43
Katarzyna Zietkowska, Bartłomiej Przybyszewski, Dominik Grzeda, Rafał Kozera, Anna Boczkowska and Malwina Liszewska et al.	
Transparent Silicone–Epoxy Coatings with Enhanced Icephobic Properties for Photovoltaic Applications	
Reprinted from: <i>Appl. Sci.</i> 2023 , <i>13</i> , 7730, doi:10.3390/app13137730	59
Lei Yu, Yuan Wu, Huanyu Zhao and Dongyu Zhu	
A Study on the Sensitivities of an Ice Protection System Combining Thermoelectric and Superhydrophobic Coating to Icing Environment Parameters	
Reprinted from: <i>Appl. Sci.</i> 2023 , <i>13</i> , 6607, doi:10.3390/app13116607	74
Lizhong Wang, Huanyu Zhao, Dongyu Zhu, Li Yuan, Hongjun Zhang and Peixun Fan et al.	
A Review on Ultrafast Laser Enabled Excellent Superhydrophobic Anti-Icing Performances	
Reprinted from: <i>Appl. Sci.</i> 2023 , <i>13</i> , 5478, doi:10.3390/app13095478	89
Naiheng Song and Ali Benmeddour	
Erosion Resistant Hydrophobic Coatings for Passive Ice Protection of Aircraft	
Reprinted from: <i>Appl. Sci.</i> 2022 , <i>12</i> , 9589, doi:10.3390/app12199589	122
Giulio Croce, Nicola Suzzi, Marco Pretto and Pietro Giannattasio	
Numerical Modelling of Droplets and Beads Behavior over Super-Hydrophobic and Hydrophilic Coatings under in-Flight Icing Conditions	
Reprinted from: <i>Appl. Sci.</i> 2022 , <i>12</i> , 7654, doi:10.3390/app12157654	135
Nadine Rehfeld, Björn Speckmann and Volkmar Stenzel	
Parameter Study for the Ice Adhesion Centrifuge Test	
Reprinted from: <i>Appl. Sci.</i> 2022 , <i>12</i> , 1583, doi:10.3390/app12031583	148
Jean-Denis Brassard, Dany Posteraro, Sarah Sobhani, Marco Ruggi and Gelareh Momen	
A Multi-Tool Analysis to Assess the Effectiveness of Passive Ice Protection Materials to Assist Rotorcraft Manual De-Icing	
Reprinted from: <i>Appl. Sci.</i> 2021 , <i>11</i> , 11847, doi:10.3390/app112411847	165

About the Editor

Filomena Piscitelli

Filomena Piscitelli, senior researcher at the Italian Aerospace Research Centre - CIRA, works on the design, development, and characterization of nanostructured materials for aeronautical and space applications. She also carries out the surface modification, development and characterization of superhydrophobic/icephobic coatings as passive Ice Protection Systems (IPS) to combine them with active IPSs. She obtained her Master's degree in Industrial Chemistry in 2004 at the University of Naples, Federico II. From 2005 to 2006, she attended a second-level degree university master course in Material Science in Micro- and Nanotechnology at the IUSS of Pavia, as winner of a university grant. In 2010, she attended the Laboratoire Des Matériaux Macromoléculaires de l'Insa-Lyon (France) and gained her PhD Degree in Materials and Structures Engineering at the University of Naples, Federico II. From 2005 to 2006, she worked at Pirelli Labs; from 2006 to 2011, she worked for the National Council of Research; since 2011 she has been working as a researcher at the Italian Aerospace Research Centre in the Materials and Structures Department. She is author and co-author of more than 60 scientific papers and 2 patent families.

Preface

The aim of this Special Issue is to give a short overview of how passive Ice Protection Systems (IPSs) can help in reducing ice accretion. This Special Issue is just a droplet in the enormous world of the scientific literature focused on the development of solutions that are helpful in reducing ice formation during flight, but we hope it may be of inspiration for many readers. The wide field of active IPSs involves designing, manufacturing, and optimization with the aim of reducing the amount of fuel needed and, subsequently, the amount of CO₂ emissions produced. The possibility of combining active IPSs with passive IPSs through the design of surfaces with superhydrophobic or icephobic properties opens the door to the design of new hybrid IPSs wherein active and passive IPSs work in a synergistic way with the aim of reducing the amount of power consumption needed. Looking to a green world, passive IPSs developed in the aviation field have direct applications in other areas, such as energetic or transportation fields, paving a way to a more sustainable future.

*“No cloud above, no earth below,
A universe of sky and snow.”
John Greenleaf Whittier*

Filomena Piscitelli
Editor

Editorial

Special Issue “Superhydrophobic and Icephobic Coatings as Passive Ice Protection Systems for Aeronautical Applications”

Filomena Piscitelli 

Italian Aerospace Research Centre—CIRA, Via Maiorise, 81043 Capua, Italy; f.piscitelli@cira.it

The formation of ice can be very dangerous to flight safety, especially in cold climates, since ice accumulated on the surfaces of the aircraft can alter the aerodynamics, increase the weight, and reduce lift, leading to catastrophic stall situations in some cases. Currently, risks caused by ice accretion are mitigated by using energy-demanding active ice protection systems (IPs), which work by either preventing ice (anti-icing) or removing ice (de-icing). However, for future sustainable aviation, low-energy-demanding IPS must be designed. Hybrid IPs, which combine active IPs with passive superhydrophobic/icephobic coatings, able to prevent, delay, and/or reduce the ice accretion, might represent a valuable solution, reducing the energy consumption and the CO₂ emissions [1–5]. Recently, Morita et al. [6] found that the combination of icephobic coatings with electrothermal heating IPS reduces the energy requirements by more than 70% at LWC of 0.6 g/m³ and a median volume diameter (MVD) of 15 μm at 75 m/s. However, in wet icing conditions, more than a 30% reduction in power is achieved. A reduced power consumption by more than 50% compared with IPS without coatings was also observed by Yu et al. [7], which demonstrated the ability of superhydrophobic coatings to prevent run-back ice.

In this scenario, this Special Issue collects research achievements, ideas, chemical formulations, applications of superhydrophobic and icephobic coatings as passive IPS working alone or in combination with active IPs, IPS parameter design, and icing wind tunnel (IWT) test campaigns, covering diverse technologies and application domains, such as aeronautical and energetic.

Some studies have focused on the design of the hybrid IPs, providing numerical tools able to simulate the effects of superhydrophobic and icephobic coatings under icing conditions [8], including the sensitivities of IPs to icing environmental parameters [7]. These first results demonstrated that it is actually possible to predict the beneficial effect of properly designed coatings for ice mitigation purposes in real-world applications [8]. Physical parameters, coating compositions, structure, roughness, morphology, and durability are properties not to be neglected in the design and development of reliable IPs in aircraft maintenance [9].

In addition to high superhydrophobicity or icephobicity, a protective coating to be used on aircraft must meet comprehensive property requirements, such as workability, heat and low temperature resistance, weatherability, erosion durability, and reparability. Among these, erosion resistance is one of the most important; for instance, coatings applied to the leading edge of a wing or helicopter rotor blades, where icing tends to occur and cause the most negative impact on aircraft operation, may experience excessive wear due to the high-speed (e.g., 100–300 m/s) impact of sand, airborne dust, rain droplets, and hail [10]. Elastomeric coatings with water contact angles ranging from 100 to 115°, high mechanical strength (19–27 MPa), high elongation at break (640–730%), and low tensile set (20–35%) have been demonstrated to reduce the ice adhesion from 622 kPa to 480–220 kPa, while combining excellent erosion resistance against both high-speed solid particles and water droplets [10].

The question remains as to whether such coatings could provide durability and performance in relevant flight icing conditions. Superhydrophobic coatings were demonstrated to



Citation: Piscitelli, F. Special Issue “Superhydrophobic and Icephobic Coatings as Passive Ice Protection Systems for Aeronautical Applications”. *Appl. Sci.* **2024**, *14*, 1288. <https://doi.org/10.3390/app14031288>

Received: 8 January 2024

Accepted: 29 January 2024

Published: 4 February 2024



Copyright: © 2024 by the author. Licensee MDPI, Basel, Switzerland. This article is an open access article distributed under the terms and conditions of the Creative Commons Attribution (CC BY) license (<https://creativecommons.org/licenses/by/4.0/>).

be helpful in reducing the ice accretion by 12% to 100% at temperatures higher than $-12\text{ }^{\circ}\text{C}$ and velocities of 50 and 95 m/s during an IWT test campaign carried out on coatings applied on two NACA0015 wing profiles, with no active IPS switched on [11].

The use of passive IPSs becomes essential during takeoff operations since, according to the Federal Aviation Administration regulation, active IPSs cannot be switched on until the aircraft reaches 400 feet above the takeoff surface to avoid engine thrust reduction [12]. IWT tests performed at the takeoff and first climb conditions [13] on a nacelle lip-skin at $T = -5\text{ }^{\circ}\text{C}$ and $-12\text{ }^{\circ}\text{C}$, $v = 70$ and 95 m/s , at an altitude of 3000 m, with a median volumetric diameter (MVD) equal to $20\text{ }\mu\text{m}$ and liquid water content (LWC) equal to 0.3 and 1 g/m^3 , demonstrated that the application of a superhydrophobic coating with active IPS switched off reduces the ice thickness, up to -49% , and the ice accreted impingement length up to -10% . At a higher LWC, i.e., 1 g/m^3 , a reduced length and number of ice rivulets have also been observed for coated configurations [14].

A fundamental parameter to know about a coatings' performance in icing flight conditions is the ice adhesion strength on the aircraft surfaces. The lack of a standard for the ice adhesion measurements offers many opportunities and opens new routes in this area. The effects of ice types, test parameters, and surface properties on the measurement data of ice adhesion centrifuge tests have been studied elsewhere [15]. Surfaces with low ice adhesion strength, achieved through the application of coatings [16] or through laser texturing [17], might also be highly useful in facilitating or assisting the manual de-icing process performed by the crew members [18].

Technological solutions found for the aeronautical applications can be transferred in diverse domains, since ice accretion poses serious problems not only in the aviation industry, but also for dams and locks, express trains, air conditioners, refrigerators, wind turbines, solar panels, power lines, suspension bridges, heat pumps, and offshore oil platforms [19]. For instance, one of the problems involving the use of photovoltaic technology to produce renewable energy is that photovoltaic panels are subject to a significant loss of efficiency due to the accumulation of dust and dirt and, during the winter season, of snow and ice, which reduce or stop the energy production. The application of transparent coatings with superhydrophobic self-cleaning and icephobic properties might be proposed as valuable solution [20]. The results demonstrated that the ice adhesion of photovoltaic panels decreased by 69%, and the freezing delay time increased 17-fold compared with those of the unmodified surface. Jointly, the contact angle hysteresis and roll-off angle of coated surfaces were significantly reduced, and transparency, which is a key requirement for photovoltaic applications, was preserved.

Although their application on vehicles' surfaces is still challenging, the development of hybrid IPSs offers new perspectives in the field of aviation, paving the way for more sustainable and efficient solutions for flight safety.

Acknowledgments: Thanks to all the authors and peer reviewers for their valuable contributions to the Special Issue "Superhydrophobic and Icephobic Coatings as Passive Ice Protection Systems for Aeronautical Applications".

Conflicts of Interest: The author declares no conflicts of interest.

References

1. Antonini, C.; Innocenti, M.; Horn, T.; Marengo, M.; Amirfazli, A. Understanding the Effect of Superhydrophobic Coatings on Energy Reduction in Anti-icing System. *Cold Reg. Sci. Technol.* **2011**, *67*, 58–67. [CrossRef]
2. Fortin, G.; Adomou, M.; Perron, J. *Experimental Study of Hybrid Anti-Icing Systems Combining Thermoelectric and Hydrophobic Coatings*; SAE Technical Paper 2011-38-0003; SAE: Warrendale, PA, USA, 2011. [CrossRef]
3. Mangini, D.; Antonini, C.; Marengo, M.; Amirfazli, A. Runback Ice Formation Mechanism on Hydrophilic and Superhydrophobic Surfaces. *Cold Reg. Sci. Technol.* **2015**, *109*, 53–60. [CrossRef]
4. Strobl, T.; Storm, S.; Kolb, M.; Haag, J.; Hornung, M. Development of a Hybrid Ice Protection System Based on Nanostructured Hydrophobic Surfaces. In Proceedings of the 29th Congress on International Council of Aeronautical Sciences, St. Petersburg, Russia, 7–12 September 2014.

5. Piscitelli, F.; Ameduri, S.; Volponi, R.; Pellone, L.; De Nicola, F.; Concilio, A.; Albano, F.; Elia, G.; Notarnicola, L. *Effect of Surface Modification on the Hybrid Ice Protection Systems Performances*; SAE Technical Paper 2023-01-1452; SAE: Warrendale, PA, USA, 2023. [CrossRef]
6. Morita, K.; Kimura, S.; Sakaue, H. Hybrid System Combining Ice-Phobic Coating and Electrothermal Heating for Wing Ice Protection. *Aerospace* **2020**, *7*, 102. [CrossRef]
7. Yu, L.; Wu, Y.; Zhao, H.; Zhu, D. A Study on the Sensitivities of an Ice Protection System Combining Thermoelectric and Superhydrophobic Coating to Icing Environment Parameters. *Appl. Sci.* **2023**, *13*, 6607. [CrossRef]
8. Croce, G.; Suzzi, N.; Pretto, M.; Giannattasio, P. Numerical Modelling of Droplets and Beads Behavior over Super-Hydrophobic and Hydrophilic Coatings under in-Flight Icing Conditions. *Appl. Sci.* **2022**, *12*, 7654. [CrossRef]
9. Ferrari, M.; Cirisano, F. Superhydrophobic Coating Solutions for Deicing Control in Aircraft. *Appl. Sci.* **2023**, *13*, 11684. [CrossRef]
10. Song, N.; Benmeddour, A. Erosion Resistant Hydrophobic Coatings for Passive Ice Protection of Aircraft. *Appl. Sci.* **2022**, *12*, 9589. [CrossRef]
11. Piscitelli, F. Characterization in Relevant Icing Conditions of Two Superhydrophobic Coatings. *Appl. Sci.* **2022**, *12*, 3705. [CrossRef]
12. FA Regulation. Airworthiness Standard: Transport Category Airplanes Part 25 Appendix C. Federal Aviation Administration: Atlantic City, NJ, USA, 1982.
13. Yang, Q.; Guo, X.; Dong, W.; Wang, A. Ice accretion and aerodynamic effects on a turbofan engine nacelle under takeoff conditions. *Aerosp. Sci. Technol.* **2022**, *126*, 107571–107584. [CrossRef]
14. Piscitelli, F.; Palazzo, S.; De Nicola, F. Icing Wind Tunnel Test Campaign on a Nacelle Lip-Skin to Assess the Effect of a Superhydrophobic Coating on Ice Accretion. *Appl. Sci.* **2023**, *13*, 5183. [CrossRef]
15. Rehfeld, N.; Speckmann, B.; Stenzel, V. Parameter Study for the Ice Adhesion Centrifuge Test. *Appl. Sci.* **2022**, *12*, 1583. [CrossRef]
16. Shamshiri, M.; Jafari, R.; Momen, G. Potential use of smart coatings for icephobic applications: A review. *Surf. Coat. Technol.* **2021**, *424*, 127656. [CrossRef]
17. Wang, L.; Zhao, H.; Zhu, D.; Yuan, L.; Zhang, H.; Fan, P.; Zhong, M. A Review on Ultrafast Laser Enabled Excellent Superhydrophobic Anti-Icing Performances. *Appl. Sci.* **2023**, *13*, 5478. [CrossRef]
18. Brassard, J.-D.; Posteraro, D.; Sobhani, S.; Ruggi, M.; Momen, G. A Multi-Tool Analysis to Assess the Effectiveness of Passive Ice Protection Materials to Assist Rotorcraft Manual De-Icing. *Appl. Sci.* **2021**, *11*, 11847. [CrossRef]
19. Kreder, M.J.; Alvarenga, J.; Kim, P.; Aizenberg, J. Design of anti-icing surfaces: Smooth, textured or slippery? *Nat. Rev. Mater.* **2016**, *1*, 15003. [CrossRef]
20. Ziętkowska, K.; Przybyszewski, B.; Grzęda, D.; Kozera, R.; Boczkowska, A.; Liszewska, M.; Pakuła, D.; Przekop, R.E.; Sztorch, B. Transparent Silicone–Epoxy Coatings with Enhanced Icephobic Properties for Photovoltaic Applications. *Appl. Sci.* **2023**, *13*, 7730. [CrossRef]

Disclaimer/Publisher’s Note: The statements, opinions and data contained in all publications are solely those of the individual author(s) and contributor(s) and not of MDPI and/or the editor(s). MDPI and/or the editor(s) disclaim responsibility for any injury to people or property resulting from any ideas, methods, instructions or products referred to in the content.

Article

Characterization in Relevant Icing Conditions of Two Superhydrophobic Coatings

Filomena Piscitelli 

Department of Materials and Structures, CIRA–Italian Aerospace Research Centre, Via Maiorise, 1, 81043 Capua, Italy; f.piscitelli@cira.it

Abstract: The formation of ice can be very detrimental to flight safety, since the ice accumulated on the surfaces of the aircraft can alter both the aerodynamics and the weight, leading in some cases to catastrophic stall situations. To date, only active Ice Protection Systems (IPS), which require energy to work, are being employed. The use of passive coatings able to prevent, delay, or reduce ice accretion in real flight icing conditions can be viewed as a valuable instrument to reduce the environmental footprint of aircraft. The majority of work in the literature focuses on testing superhydrophobic coatings at a speed equal to or lower than 50 m/s or rather in combination with an active system. The present study was aimed at understanding the effectiveness of two superhydrophobic coatings applied on two NACA0015 wing profiles in reducing the ice formation in relevant flight icing conditions, through tests carried out in an Icing Wind Tunnel at 50 and 95 m/s and at temperatures ranging between -3 and -23 °C. Results demonstrated that at temperatures higher than -12 °C, at both 50 and 95 m/s, with exposure time ranging between 72 and 137 s, the developed coatings can be helpful in reducing the ice accretion by 12 to 100%.

Keywords: coatings; superhydrophobic coating; icephobic coating; passive Ice Protection System; Icing Wind Tunnel Tests



Citation: Piscitelli, F.

Characterization in Relevant Icing Conditions of Two Superhydrophobic Coatings. *Appl. Sci.* **2022**, *12*, 3705. <https://doi.org/10.3390/app12083705>

Academic Editor: Jacek Tomków

Received: 9 March 2022

Accepted: 1 April 2022

Published: 7 April 2022

Publisher's Note: MDPI stays neutral with regard to jurisdictional claims in published maps and institutional affiliations.



Copyright: © 2022 by the author. Licensee MDPI, Basel, Switzerland. This article is an open access article distributed under the terms and conditions of the Creative Commons Attribution (CC BY) license (<https://creativecommons.org/licenses/by/4.0/>).

1. Introduction

Aircraft icing has been widely recognized as a severe weather hazard to flight safety in cold climates [1], since the ice accretion on aircraft surfaces alters the flight aerodynamics, reducing lift and increasing weight and drag, thus leading to dangerous stall conditions with a temporary or permanent loss of control of the aircraft.

Currently, to hinder the ice accretion dangers, active Ice Protection Systems (IPS) requiring energy are being employed, either to prevent icing (anti-icing) or to remove ice once it has been formed (de-icing). The use of active IPS, which can be thermal, electro-mechanic [2], electro-thermal [3], pneumatic, or a glycol-based fluid type [4], implicates an increase in construction complexity, weight, manufacturing, and management costs, an increase of onboard power consumption, and then an increase of CO₂ emissions [5].

It would be highly desirable and advantageous if surfaces could passively reduce or delay the ice formation and facilitate ice removal. While active methods rely on energy input from an external system for the anti-/de-icing operation, passive methods take advantage of the physical properties of the airframe surfaces (e.g., surface wettability) to prevent, delay, or reduce ice formation and accretion [1], and avoid/reduce the run-back of ice [6].

In this contest, superhydrophobic coatings owing to their extraordinary water repellency and no requirement for additional energy consumption can be viewed as excellent candidates for icephobicity in this area [7,8].

However, whether or not superhydrophobicity implies icephobicity, is a debated topic [9,10], and, generally, it is a misunderstanding to believe that to design a surface with high contact angles should consequently lead to an icephobic surface [9].

Cao et al. [11] found that the anti-icing capability of surfaces depends not only on their superhydrophobicity but also on the surface morphology; Varanasi et al. [12] found that icephobic properties of superhydrophobic surfaces can be compromised in the case of frost formation, so under high humidity, the surface turns into a hydrophilic surface; Chen et al. [13] found that the superhydrophobic surfaces cannot reduce the ice adhesion, and the ice adhesion strength on superhydrophobic surfaces is comparable to that observed for superhydrophilic surfaces, because of the mechanical interlocking between the ice and the surface texture.

During a flight, ice accretion is usually due to supercooled water droplets impinging on aircraft surfaces, and the icephobicity of a surface not only depends on intrinsic surface properties but also on the ice formation conditions [5].

Therefore, it would be highly recommended and helpful to assess the icephobicity of these coatings through a test conducted at aircraft cruise velocities and in relevant icing conditions. However, most studies use droplets' impact velocities below 10 m/s [14,15] or freezing conditions not in line with typical aircraft icing conditions [13,16].

To the best of our knowledge, only in a few studies of superhydrophobic surfaces were tested in an Icing Wind Tunnel (IWT) at relevant speed, i.e., 50 m/s or higher, and by generating both rime and glaze ice [17–19]. Other studies were focused on the effect of hydrophobic/superhydrophobic coatings on the reduction of power supply needed to keep the aircraft surfaces ice-free when combined with active Ice Protection Systems (IPS) [6,9,20–22]. Table 1 represents a short review of these studies, performed to the best of our knowledge.

Table 1 highlights that IWT tests at a speed higher than 50 m/s were carried out only by combining coatings with active IPS [20].

In this scenario, the present work aims to test at 50 and 95 m/s and at temperatures ranging between -3 and -23 °C, two superhydrophobic coatings applied on two NACA0015 wing profiles, without any active IPS. Selected IWT test conditions take into account common performances of General Aviation, CS-23, and CS-25 categories [23]. Ice accretion was assessed by measuring the ice thickness at the stagnation region and the extension length of the compact ice accreted along the airfoils.

The wetting properties of surfaces were studied by static contact angles, surface free energy, and work of adhesion measurements. The surface morphology of the coating's surfaces was observed by optical and scanning electron microscopy, and the roughness was opportunely measured. Cutting and a tape test and adhesion test at 23 and -30 °C were performed in order to assess the durability of these coatings, especially at low temperatures.

Table 1. Review of Icing Wind Tunnel (IWT) test conditions performed on hydrophobic and superhydrophobic coatings and the main results.

Surface Properties		IWT Test Conditions					Results	
Reference	Contact Angle [deg]	Ra [μm]	v [m/S]	T [$^{\circ}\text{C}$]	Liquid Water Content [g/m^3]	Median Volumetric Diameter [μm]		Active IPS
[19]	88–119	0.2–2.8	50	–8	0.36	20	NO	–29–33% ice reduction with respect to Al6061-T6; the lower the contact angle, the lower the accreted ice.
[18]	158	8	50	–10; –20	0.5	20	NO	–25% ice reduction with respect to Al6061-T6.
[21]	110–153	2–5	30 Blade rotation	–7.5; –15	0.8	20–30	YES	At -15°C the coating with a contact angle of 110° reduces the power consumption in anti-icing up to 44%; no relevant improvement for the other coatings.
[20]	150		75	–5; –8; –10	0.5; 0.6; 1.3	15; 16; 21	YES	Reduced power consumption by 30 to 70%.
[9]	Advancing angle 159; 169	1.1; 2.4	400 rpm	–8––16	0.5; 2	30	YES	About –60% in adhesion load of a sample with angle 159° at -8°C and $2\text{ g}/\text{m}^3$ and –70% in adhesion load of a sample with angle 169° at -16°C and $0.5\text{ g}/\text{m}^3$, with respect to Inconel 625.
[6]	Advancing angle 161	2.7	28	–17	1.5; 12.3	50; 750	YES	Up to 80% heating power saving.
[22]	101–152		21	–5; –20	0.3	20	YES	Energy savings of 33% for glaze ice and about 13% for rime for superhydrophobic surface; of 5–10% for both hydrophobic surfaces, in both rime and glaze.

2. Materials and Methods

Two nanostructured coatings (hereafter labeled as 1 and 2) [24] were applied with an aerograph with a layer-by-layer process, as a usual paint, on three different substrates: (1) $5 \times 5 \text{ cm} \times \text{cm}$ flat composite samples made of carbon fiber and epoxy resin painted with a commercial aeronautical paint purchased from Akzo-Nobel (labeled as C); (2) $5 \times 5 \text{ cm} \times \text{cm}$ flat samples in stainless steel (hereafter labeled as S) pretreated with a sandpaper P40 to increase the roughness surface and improve the coating's adhesion, and; (3) two wing profiles NACA0015 manufactured with a 3D printing machine, having a length of 135 mm and a chord of 100 mm made of acrylonitrile butadiene styrene (hereafter labeled as A). Samples were named as: X-i with X = Substrate, which is C, S, or A, and I = Surface, namely, R for Reference, and 1 or 2 for coatings. Hence AR, CR, and SR are the references, whereas A1, A2, C1, C2, S1, and S2 are the coated samples.

Unlike samples C and S, sample A had one-half painted with coatings, leaving the other half uncoated as a reference to better compare the coating and reference.

The roughness of substrates before and after the application of the coating was measured by employing a SAMA SA6260 surface roughness meter. Roughness measurements, performed according to the ISO 4288 [25], were reported as Ra, which represents the arithmetic average of the absolute values of the profile height deviations from the mean line.

The optical images were acquired with a microscope USB Dino-Lite AM4815ZTL at $140\times$.

The contact angle (CA) measurements were performed at 23°C in compliance with the ASTM D7490–13 [26] standard, with $3 \mu\text{L}$ of water (H_2O) and diiodomethane (CH_2I_2), by acquiring at least six measurements. Contact angles were rapidly acquired, within 30 s of depositing the drop, to avoid changes in angles. The mean values and standard deviations of CA were the input data of a Matlab tool (a CIRA home-made tool) which solves the two equations (1), derived by the application of the Owens-Wendt-Kaelble method [27,28] for the assessment of the solid surface free energy (SFE). Due to the stochastic nature of the CA experimental measurements, a third liquid was introduced, i.e., formamide (HCONH_2) [29,30]. The software uses the third liquid to minimize the error on the third Equations (2) and (3), giving as output the optimized values of the CA, along with an assessment of polar and dispersive components of SFE, which is useful to calculate the SFE through Equation (4), the work of adhesion (W_A) through Equation (5), and the surface polarity (SP) through Equation (6).

$$\begin{cases} \frac{\gamma_{I_1}(1+\cos\theta_1)}{2} = (\gamma_{I_1}^d \gamma_s^d)^{1/2} + (\gamma_{I_1}^p \gamma_s^p)^{1/2} \\ \frac{\gamma_{I_2}(1+\cos\theta_2)}{2} = (\gamma_{I_2}^d \gamma_s^d)^{1/2} + (\gamma_{I_2}^p \gamma_s^p)^{1/2} \end{cases} \quad (1)$$

$$\min_{\gamma_s^d, \gamma_s^p} \left((\gamma_{I_3}^d \gamma_s^d)^{1/2} + (\gamma_{I_3}^p \gamma_s^p)^{1/2} - \frac{\gamma_{I_3}(1+\cos\theta_3)}{2} \right) \quad (2)$$

$$\text{s.t.} \begin{cases} (\gamma_{I_1}^d \gamma_s^d)^{1/2} + (\gamma_{I_1}^p \gamma_s^p)^{1/2} - \frac{\gamma_{I_1}(1+\cos\theta_1)}{2} = 0 \\ (\gamma_{I_2}^d \gamma_s^d)^{1/2} + (\gamma_{I_2}^p \gamma_s^p)^{1/2} - \frac{\gamma_{I_2}(1+\cos\theta_2)}{2} = 0 \\ E[\theta_1] - \sigma_{\theta_1} \leq \theta_1 \leq E[\theta_1] + \sigma_{\theta_1} \\ E[\theta_2] - \sigma_{\theta_2} \leq \theta_2 \leq E[\theta_2] + \sigma_{\theta_2} \\ E[\theta_3] - \sigma_{\theta_3} \leq \theta_3 \leq E[\theta_3] + \sigma_{\theta_3} \end{cases} \quad (3)$$

$$\gamma_s = \gamma_s^p + \gamma_s^d \quad (4)$$

$$W_A = 2(\gamma_s^p \gamma_{I_1}^p)^{1/2} + 2(\gamma_s^d \gamma_{I_1}^d)^{1/2} \quad (5)$$

$$SP = \frac{\gamma^p}{\gamma^p + \gamma^d} \quad (6)$$

Here γ_{li}^P and γ_{li}^D are the polar and dispersive components of the liquid i , γ_s^P and γ_s^D are the polar and dispersive components of the solid, respectively, and θ_i is the CAs measured with the liquid i .

Sample morphology and coatings' thickness were acquired using a field emission scanning electron microscope (SEM) Tescan Mira3 (Tescan Orsay Holding, Brno-Kohoutovice, Czech). Samples were observed in the top section after metallization.

Cutting and tape tests were carried out according to the ASTM D 3359-09 standard [31] by making a grid incision with a specific cutter on the coated samples and then applying adhesive tape to cover the cut area. The test adhesive was vigorously removed and the involved area was inspected. According to the standard, the test passed if the area involved had detached flakes of coating at intersections less than 15%.

The adhesion tests were carried out according to the ASTM C633 [32]. The test consisted of coating one face of a substrate fixture, bonding this coating to the face of a loading fixture, and subjecting this assembly of coating and fixtures to a tensile load normal to the plane of the coating. The tensile load to the assembly of the coating and fixtures should not permit eccentric load or bending moment to the specimen. A cyanoacrylate was employed as adhesive. Adhesion or cohesion strength was calculated as *Maximum load/cross-sectional area*. The adhesion strength of the coating was given a failure if rupture was entirely over the coating-substrate interface. The cohesion strength of the coating was validated if rupture was only within the coating. This test was performed at room temperature and at $-30\text{ }^\circ\text{C}$.

Icing wind tunnel (IWT) tests were performed in the CIRA IWT facility, which is a closed-loop circuit, refrigerated wind tunnel with three interchangeable test sections and one open jet configuration, whose main mission is to perform icing tests. The cloud generation for icing conditions simulation is carried out by the spray bar system, which is able to generate water droplets with diameters (median volumetric diameter—MVD) and concentrations (liquid water content—LWC) covering nearly all the envelope as prescribed by the CS-25 Appendix C for both continuous and intermittent cloud conditions. Two samples A and two coatings, i.e., 1 and 2, were contemporary tested by dividing each sample into two parts, one of which was coated with a coating of A1 and A2, and the other left uncoated as a reference (AR) (see Figure 1). The two samples were mounted with the two reference sides in opposite positions, as shown in Figure 1b, in order to minimize the effect of a possible cloud inhomogeneity.

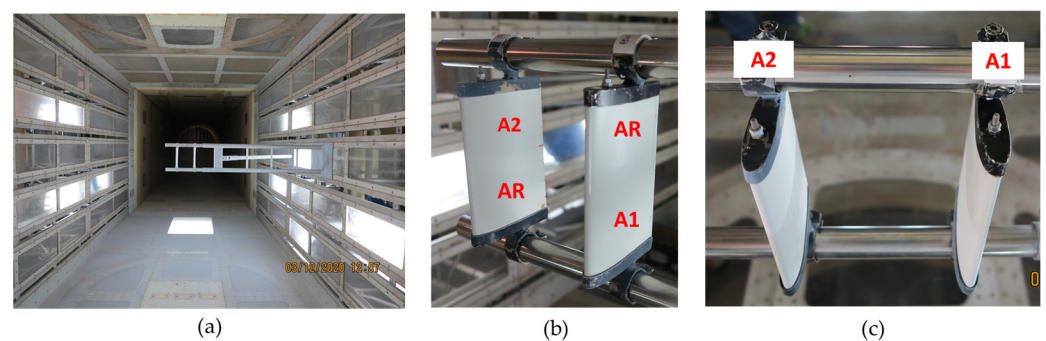


Figure 1. Different views of samples A mounted in the IWT facility; (a) front view, (b) lateral view, and (c) top view.

To have a three-dimensional shape of the accumulated ice overlapped with the neat airfoil, 3D laser scan reconstructions were performed (Figure 2). Three-dimensional ice measurements and reconstruction were performed using an all-purpose portable measuring arm system integrated with a laser scanner for fast 3D surface data capture (ROMER 8525-7). Innovmetric PolyWorks was employed to get data points, align the ice point clouds to the 3D model of the corresponding “clean” sample, and, finally, generate a polygon mesh.



Figure 2. 3D laser scan reconstructions performed before and after IWT test 6.

3. Results

3.1. Coatings' Characterization

3.1.1. Roughness

Figure 3 shows the mean values of roughness measured on C and S samples before and after the application of the coatings. The roughness of the SR sample before the sandpaper treatment was $0.39 \mu\text{m}$ which increased to $1.3 \mu\text{m}$ after the P40 treatment, as reported in Figure 3. After the application of coating 1 (S1), the roughness did not change significantly, but it did after the application of coating 2 (S2) and achieved a $R_a = 3.1 \mu\text{m}$. Whereas sample CR had a roughness of $3.7 \mu\text{m}$, which did not appreciably change after the application of both coatings since only a slight increase of the roughness could be measured, and only for C1 (from 3.7 to $4.1 \mu\text{m}$).

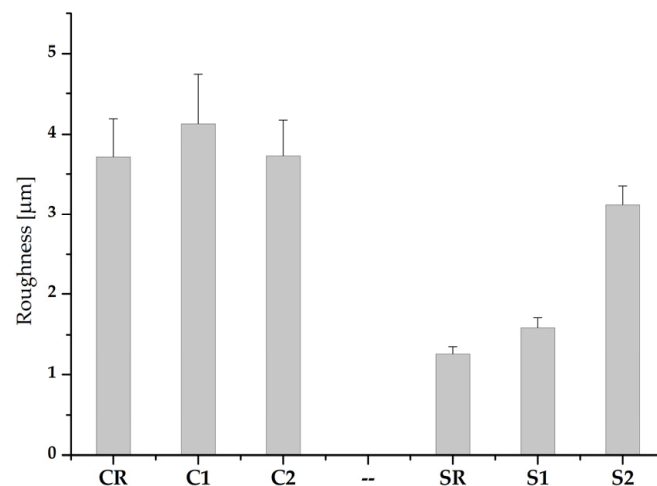


Figure 3. Roughness mean values R_a for C and S samples, before and after the application of the coatings.

3.1.2. Optical Microscopy

Figure 4 displays the optical images acquired at $140\times$ of magnification of all flat samples' surfaces, along with the corresponding roughness profiles. It highlights that the surface morphology of the CR sample was homogeneous and it became slightly denser and more compact after the application of the coatings (C1 and C2 in Figure 4b,c). The shape of the roughness profiles confirmed the homogenous succession of peaks and valleys in all C samples. Contrary, the treatment of SR with the sandpaper P40 gave the coarse morphology shown in Figure 4g. As a consequence, in the SR roughness profile (Figure 4l), the valleys appeared larger than the peaks as a footprint of the scratches. Although at this magnification the scratches were still visible and after the application of the coatings (Figure 4h,i), the roughness profiles of coated samples displayed that both coatings partially filled the valleys and created their own roughness with a homogeneous distribution of peaks and valleys (Figure 4m,n).

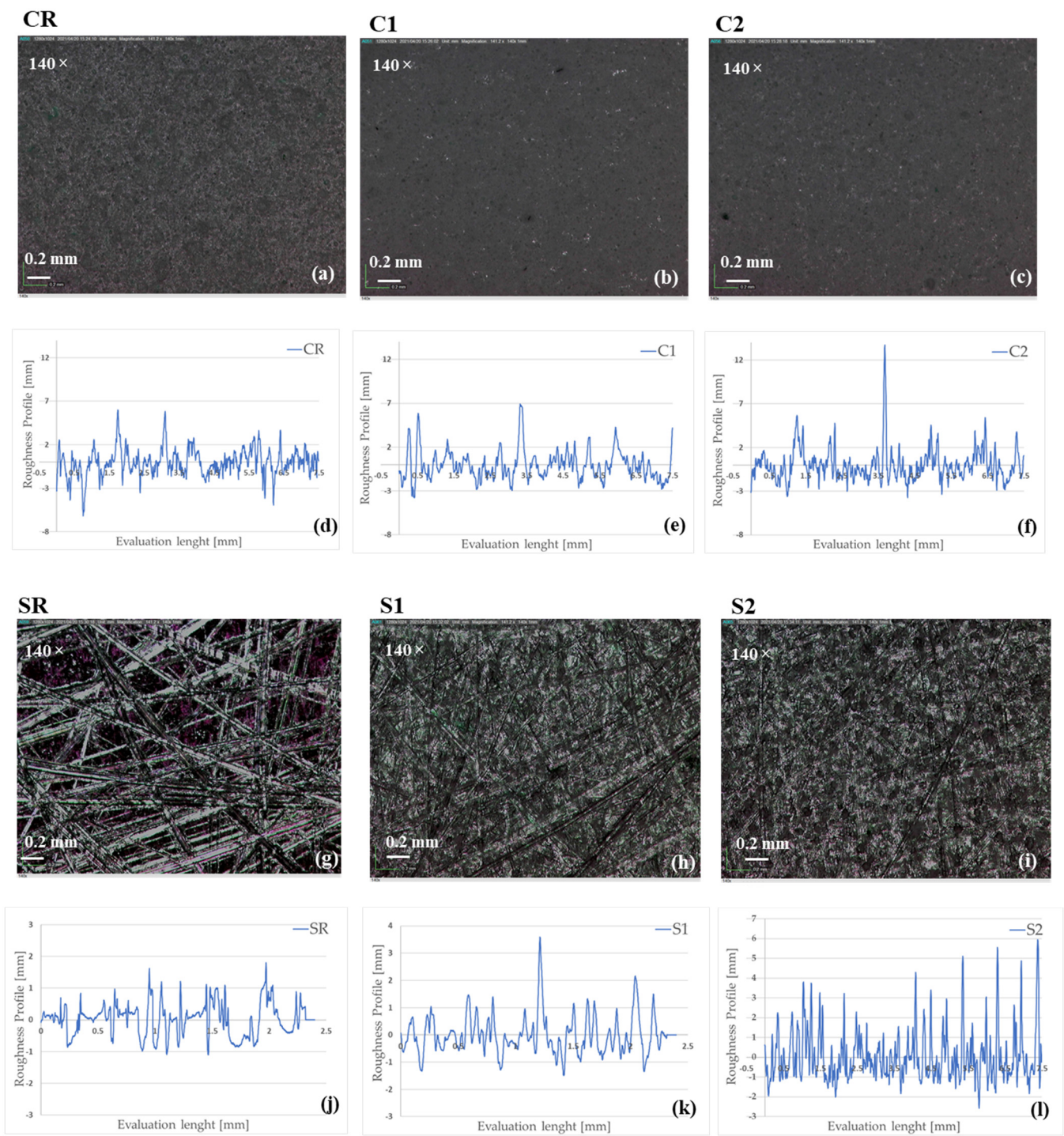


Figure 4. Optical microscopy images acquired at 140× of CR (a), C1 (b), C2 (c), SR (g), S1 (h), and S2 (i) samples’ surfaces, and the corresponding roughness profiles for CR (d), C1 (e), C2 (f), SR (j), S1 (k), and S2 (l).

3.1.3. Scanning Electron Microscopy

In order to further investigate the morphology at the micro- and nano-scale, SEM images in the top view were acquired at different magnifications (see Figure 5).

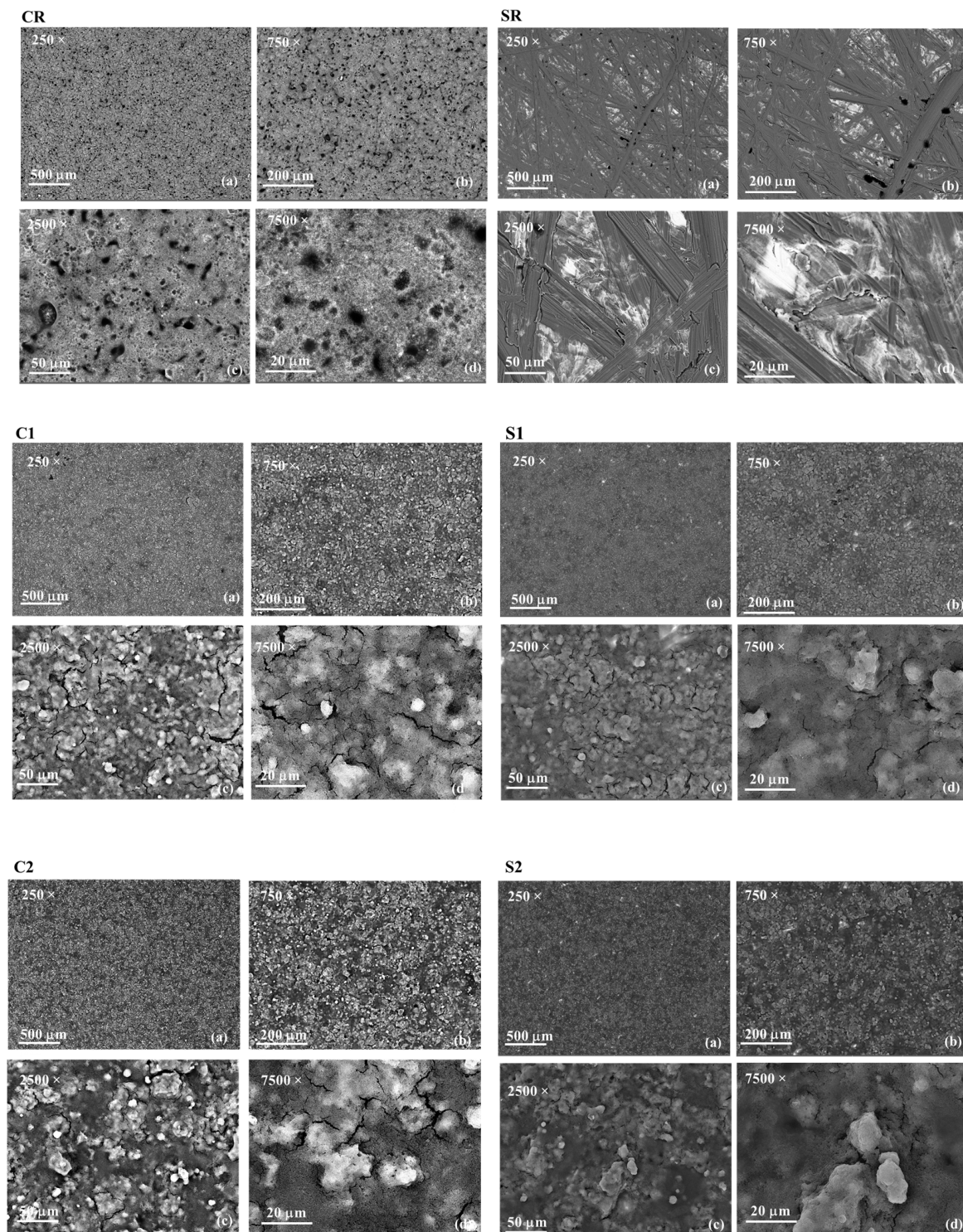


Figure 5. Top View of SEM images at 250× (a), 750× (b), 2500× (c), and 7500× (d) of CR, SR, C1, S1, C2, and S2 samples.

By comparing the SEM images of C1 and C2 and S1 and S2 samples with CR and SR, respectively, it highlighted that in both cases, the coatings were able to completely cover the substrate morphology, since neither the sponge-like morphology of the commercial paint, characterized by the presence of micropores, nor the scratches of the SR surface were visible once the coatings were applied. Generally speaking, it seemed that the same coating, applied on different substrates generated the same morphology, with the presence

of micro-sized aggregates which emerged from the matrix. However, some little differences could be detected. In fact, by comparing C1 and S1, and C2 and S2 samples, it seemed that for both coatings, the aggregation of nanoparticles emerged in the C samples more than it occurred for the S samples. This result could be ascribed to the different surface nature and/or morphology of the substrates. The same results were observed by Yilgor et al. [33] by applying the same layers number of the same coating to different polymeric substrates. In fact, they found different nanoparticles aggregation at the surface depending on the substrate nature (i.e., TPSU, PMMA, PC, and TPU), which could probably be responsible for the slight differences in CA. In Figure 5, it should also be noticed that at the highest magnification, small microcracks and fractures appear, most of all on C1 and C2 surfaces. As reported in [19], during the IWT tests, these fractures on the samples' surfaces could become ice nucleation sites.

3.1.4. Wettability

Due to the superhydrophobicity of coatings, the CA measurements on 3D samples (A1 and A2) have been impossible to be performed; the water droplets, in fact, do not retain on the surfaces but quickly glide away. Therefore, for A1 and A2 samples, the success of the coatings' application and then the superhydrophobicity of surfaces was assessed by observing that the water droplets slipped rapidly away from the A1 surface (right side of Figure 6), whereas they adhered to the AR surface (left side of Figure 6). The same behavior was observed for the A2 sample (data not shown for brevity). Instead, Figure 7 shows a representative picture of 3 μL of water droplets on all flat surfaces, i.e., CR, C1, C2, SR, S1, and S2 samples. The CA measurements and the corresponding optimized values are listed in Table 2, whereas the SFE, W_A , and SP of coated and reference surfaces are displayed in Figure 8.

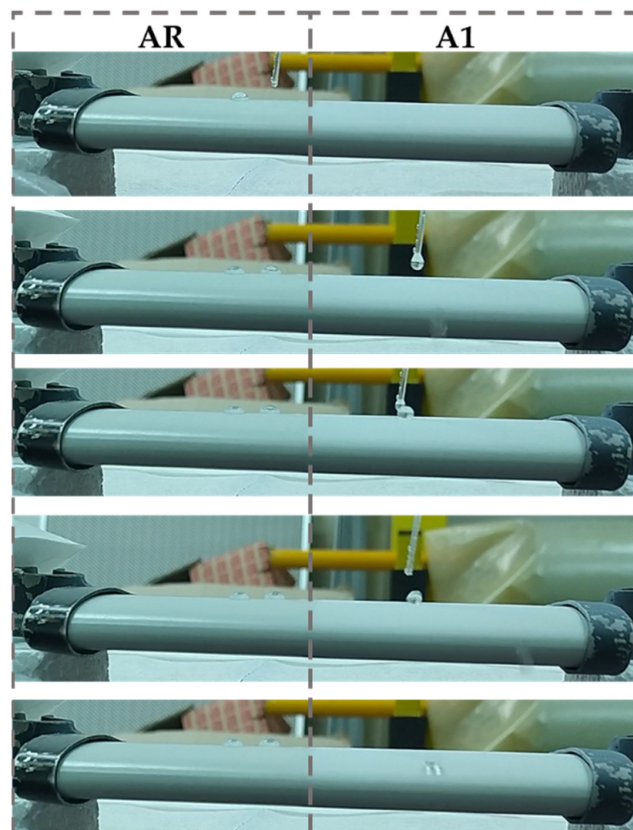


Figure 6. Images sequences of water droplets dropping on AR (left) and A1 (right) surfaces.

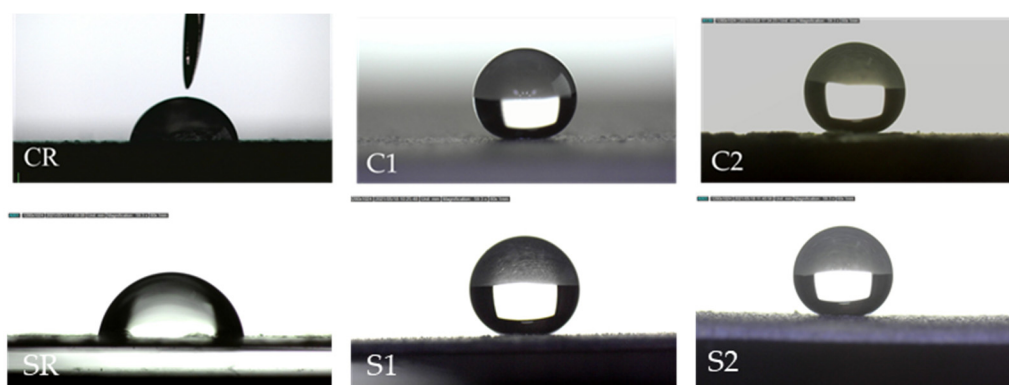


Figure 7. Water CA measurements on CR, C1, and C2 (top) and SR, S1, and S2 samples (bottom).

Table 2. Experimentally measured CA; the optimized values are also reported.

Contact Angle [DEG]	H ₂ O		CH ₂ I ₂		HCONH ₂	
	Measured	Optimized	Measured	Optimized	Measured	Optimized
CR	70 ± 4	74	48 ± 6	46	62 ± 3	62
SR	82 ± 3	85	55 ± 5	52	69 ± 6	75
C1	161 ± 7	155	146 ± 8	148	152 ± 8	153
S1	157 ± 9	148	140 ± 10	130	136 ± 6	142
C2	164 ± 6	157.5	141 ± 8	148.5	137 ± 10	141.5
S2	161 ± 5	156	136 ± 7	139	139 ± 11	150

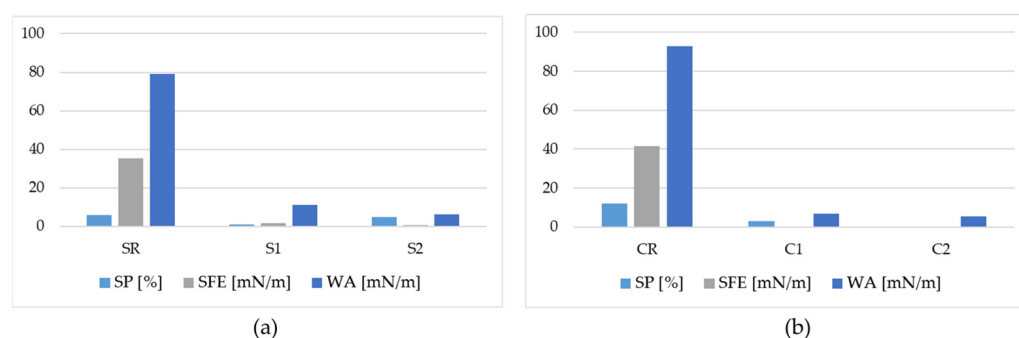


Figure 8. SFE, WA, and SP of SR, S1, and S2 (a), and of CR, C1, and C2 (b) samples.

As reported in Table 2, all coated surfaces were superhydrophobic. However, some little difference in the wettability of the samples prepared by applying the same coating on different substrates could be noticed. In fact, the CA of S1 and S2 were slightly lower than those measured for C1 and C2, respectively. This could be ascribed to slightly different morphologies observed for C and S samples, also responsible for the different measured roughness (Figure 3). In fact, as reported in Section 3.1.3 and in Figure 5, in the C samples, the micro-aggregates emerge more than occurred for the S samples, thereby improving the roughness (Figure 3) and the Cassie-Baxter state, and reducing the wettability as a consequence. This is in line with that observed by other authors who found such increased contact angles with the increased surface roughness [34].

The SFE of reference samples SR and CR were 35 mN/m ($\gamma_s^P = 2$ mN/m and $\gamma_s^D = 33$ mN/m) and 42 mN/m ($\gamma_s^P = 5$ mN/m and $\gamma_s^D = 36.5$ mN/m), respectively, whereas the values of 79 and 93 mN/m were found for the corresponding W_A . After the application of the coating, we observed a reduction of 99% in SFE in the C samples (0.3 mN/m for both C1 and C2), and 95–98% for the S samples (1.6 mN/m for S1 and 0.8 mN/m for S2). Accordingly, the W_A was reduced by 93–94% for the C samples (6.8 mN/m for C1 and 5.5 mN/m for C2) and by 86–92% for the S samples (11.1 M/m for S1 and 6.3 mN/m for

S2). With respect to CR, SP decreased by 75% and 100% in C1 and C2, from 12 to 3 and 0, respectively, whereas it was reduced by 83% and 17% for S1 and S2, from 6 to 1 and 5, respectively, with respect to SR.

3.2. Durability Tests

3.2.1. Cutting and Tape Test

An inspection of surfaces after the cutting and tape test revealed that both coatings passed the test since the area involved in detached flakes of coating at intersections was less than 15% (Figure 9-top). Moreover, after the test, the surfaces remained superhydrophobic as highlighted by the residual low wettability of the surfaces after the test (see pictures of water droplets at the bottom of Figure 9).

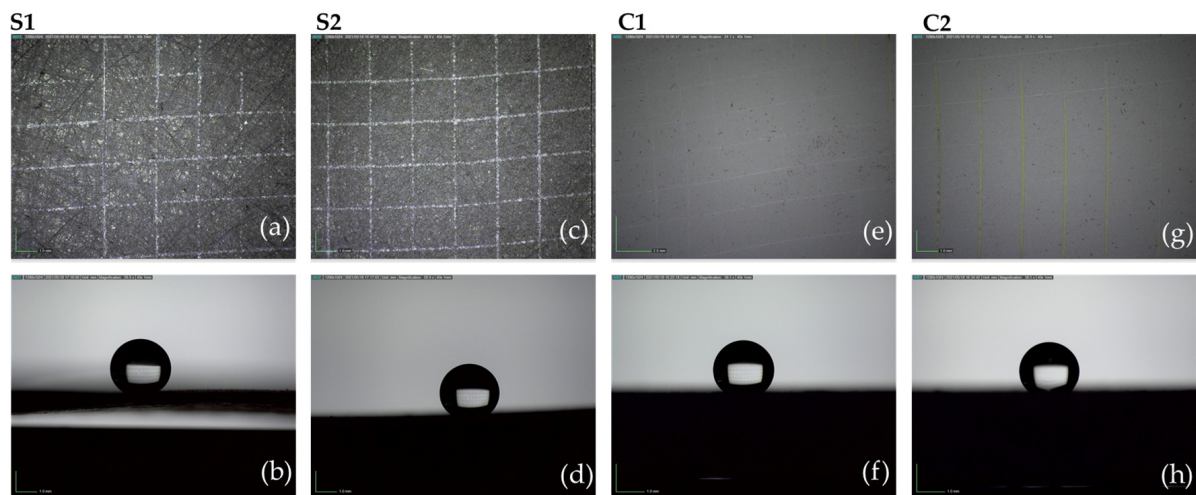


Figure 9. Cutting and tape test carried out on S1 (a,b), S2 (c,d), C1 (e,f), and C2 (g,h) samples. On the top are the images of surfaces after the test; on the bottom, water droplets on tested surfaces to measure the residual wettability.

3.2.2. Adhesion Tests

Figure 10a shows the Zwick Roll Z010 machine employed to perform the adhesion test. Some pictures of samples before and after the test are also displayed (Figure 10b,c, respectively). Tests performed at room temperature revealed that failure at adhesive-coating interfaces occurred for SR and S1 samples, at an adhesion strength of 8.1 and 9.9 MPa, respectively; whereas, failures at adhesive-substrate interfaces (see the schematic drawing in Figure 11b) occurred for S2 (10.7 MPa), CR (19.9 MPa), C1 (7.2 MPa), and C2 (10.2 MPa), meaning that the adhesion strength of the interface adhesive-coating was higher than the reported strength. At $-30\text{ }^{\circ}\text{C}$, only C samples were tested. It was found that also at low temperatures for CR, C1, and C2 sample failures occurred at the adhesive-substrate interface at adhesion strengths of 2.9 MPa per CR, 2.2 MPa for C1, and 1.8 for C2. So, the adhesion strength of the adhesive-coating interfaces was higher than the measured values. The measured adhesion strength decreased as the temperature decreased, as shown in Figure 11a, which may be due to the more brittleness of adhesive at low temperatures [35]. In Figure 11b, a schematic drawing of the failure at the adhesive-substrate interface is shown for clarity.

3.3. IWT Tests

Table 3 details the IWT test conditions selected by taking into account common performances of General Aviation, CS-25 (Test 1,2), and CS-23 (Test 4–6) categories [23]. The temperatures investigated ranged from -3 to $-23\text{ }^{\circ}\text{C}$, at an altitude of 3000 m and an LWC of 0.3 g/m^3 . Two different speeds were considered, i.e., 50 and 95 m/s, so the covered flight path (in clouds) ranged between about 7 and 13 km. Tests 1 referred to the CS-25

vehicles category and investigated the lowest temperatures ($-23\text{ }^{\circ}\text{C}$), the highest speed (95 m/s), and the highest LWC ($0.5\text{--}0.6\text{ g/m}^3$). Test 2 replicated the test 1 conditions, but at sea level (altitude 83 m). Test 3–6 referred to the CS-23 vehicles category, investigating the temperature ranging between -3 and $-12\text{ }^{\circ}\text{C}$, LWC was fixed to 0.3 g/m^3 and MVD at $20\text{ }\mu\text{m}$, and altitude at 3000 m, corresponding to severe icing cloud conditions which can occur at altitudes above 600 m [36]. In tests 3–6, along with the temperature, also the effect of speed was investigated (50 and 95 m/s).

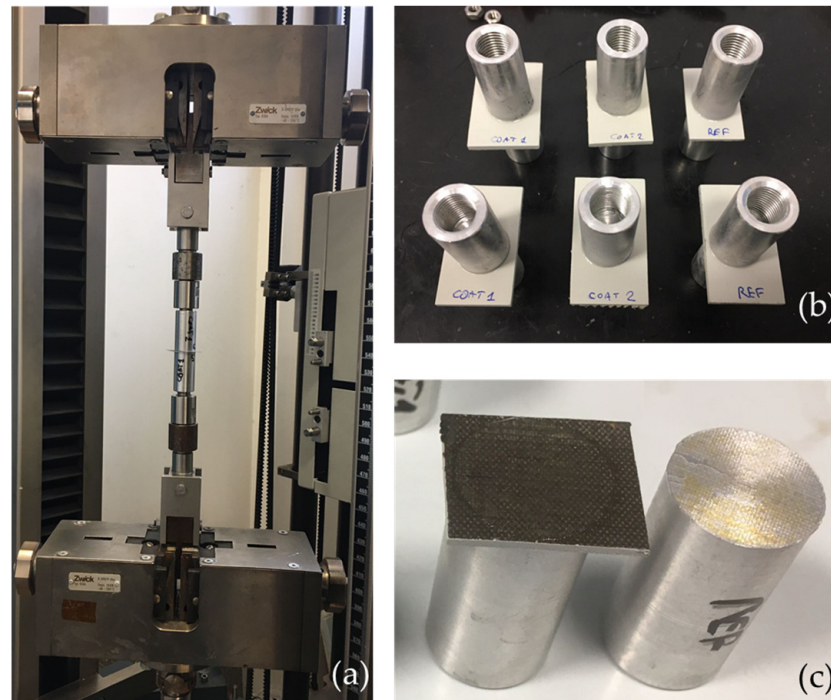


Figure 10. The Zwick Roll Z010 machine employed to perform the adhesion test (a), C samples before (b) and after the test (c).

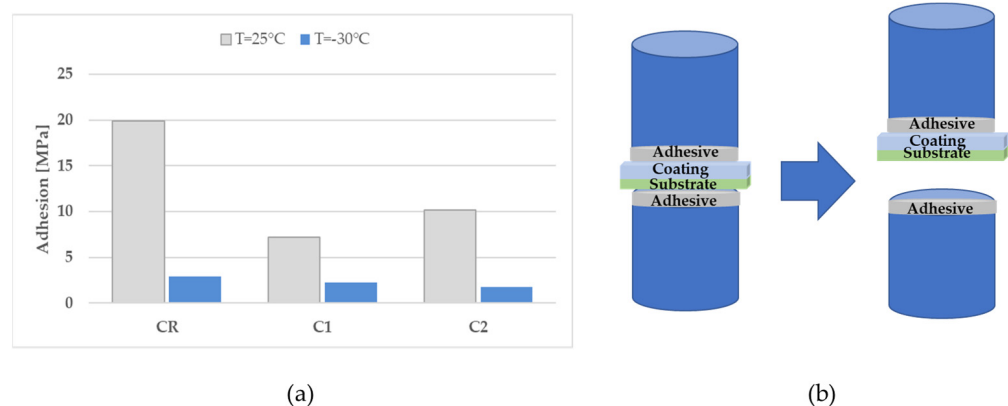


Figure 11. Adhesion test results performed on C samples at $25\text{ }^{\circ}\text{C}$ and $-30\text{ }^{\circ}\text{C}$ (a); schematic draw of most adhesion failures occurred during the testing of C samples (b).

Figure 12 shows the pictures of both samples after each test. The surface of each sample was one-half superhydrophobic (A1 and A2 sites), whereas the other half was left as a reference (AR). First of all, it must be noted that the rime ice generated in tests 1, 2, and 5 (Figure 12a,b,e) covered quite uniformly the two samples, without taking into account the different wettability of the two half-sites of the samples. A deeper analysis of images revealed the presence of isolated frozen droplets along the airfoil, especially for coated surfaces which were evident in test 2 and test 5 (Figure 12b,e).

Table 3. IWT test matrix.

TEST ID	Static T [°C]	V [m/s]	Total T [°C]	Altitude [m]	LWC [g/m ³]	MVD [μm]	Mach	Test Duration [s]	Flight Path [km]
1	−22.98	94.9	−18.55	3001	0.602	22.08	0.299	79	7.50
2	−22.95	94.5	−18.57	83	0.553	19.92	0.298	77	7.27
3	−5.97	95.0	−1.53	3002	0.307	22.27	0.290	137	13.01
4	−3.10	50.0	−1.91	3001	0.297	20.04	0.152	227	11.35
5	−12.18	50.0	−10.98	3000	0.298	20.05	0.154	228	11.39
6	−7.96	95.0	−3.52	3007	0.293	21.90	0.291	72	6.84

On the other hand, in glaze ice conditions, the low wettability of coated surfaces caused a reduction of the accreted ice, as highlighted in tests 3, 4, and 6 (Figure 12c,d,f), with a larger amount of isolated frozen droplets. This result seemed to provide evidence that, especially in glaze ice conditions, the high degree of surfaces' hydrophobicity caused the droplets to easily roll on the surface, reducing contact duration and thus ice accumulation. Additionally, in both rime and glaze ice, the isolated frozen droplets had a spherical shape, meaning that they preserved the low wettability at low temperatures and in dynamic conditions. The same behavior was observed at -5 °C by Fortin et al. [22] on hydrophobic and superhydrophobic surfaces (CA of 118–152°).

Most of the droplets frozen as isolated ice had dimensions larger than the frozen droplets near the denser ice (L_{ci} in Figure 13a), probably because the droplets slipped on the superhydrophobic surface until they met an isolated iced droplet on which they could grow.

Measurements of the accreted ice thickness, t_{ice} , and the extension length of the compact ice, L_{ci} , accreted along the airfoils (continuous blue zone in the schematic drawing in Figure 13a), were performed. In detail, for the measurements of t_{ice} , seven marks were drawn on each airfoil at a 2 cm distance, and t_{ice} was measured as the difference in the chord length before and after the IWT tests (see pictures in Figure 13b,c).

Results, displayed in Figure 14a,b, show that in rime ice conditions, the t_{ice} measured on A1 and A2 was similar to or higher than those measured on AR; whereas in glaze ice conditions, in test 3 and test 6, the t_{ice} measured on A1 was reduced by -12 and -34% , respectively, with respect to the AR site; lower differences were observed in all other cases. This was because, at the stagnation point ("A" in Figure 13a for an attack angle equal to zero), the ice accretes in spite of the surface properties since the local velocity of the airflow there is zero. For the A1 surface in test 4, in fact, the ice accreted only at the stagnation point.

The extension length of the compact ice L_{ci} was measured after each test and compared to the corresponding reference. Values were subtracted of the corresponding t_{ice} and reported in Figure 15.

Results show that in rime ice conditions (test 1 and test 2), the ice accreted along the coated airfoil generally increased with respect to the reference. In detail, L_{ci} measured on the A1 site in test 1 and test 2 was $+5\%$ and -5% , respectively, compared to those measured on the AR. In both tests, L_{ci} on the A2 site was higher than the AR ($+39$ and $+22\%$, respectively).

A different scenario could be observed in glaze ice conditions (tests 3, 4, and 6) and in test 5, for which L_{ci} measured on A1 and A2 was considerably lower than those measured on the AR (from -12 to -100%). By supposing that in all cases the high hydrophobicity of the surface caused the droplets to easily roll on the surface, these results seemed to give evidence that the lower the temperature, the faster the freezing of droplets. As a consequence, in test 1 and test 2, the droplets froze before rolling away, increasing L_{ci} . Whereas in tests 3–6, the droplets slipped away, froze as isolated droplets, or did not freeze at all.

Hence, as the temperature increased, the effect of the superhydrophobicity increased and the difference of L_{ci} (ΔL_{ci}) measured on coated and reference surfaces became larger (Figure 16).

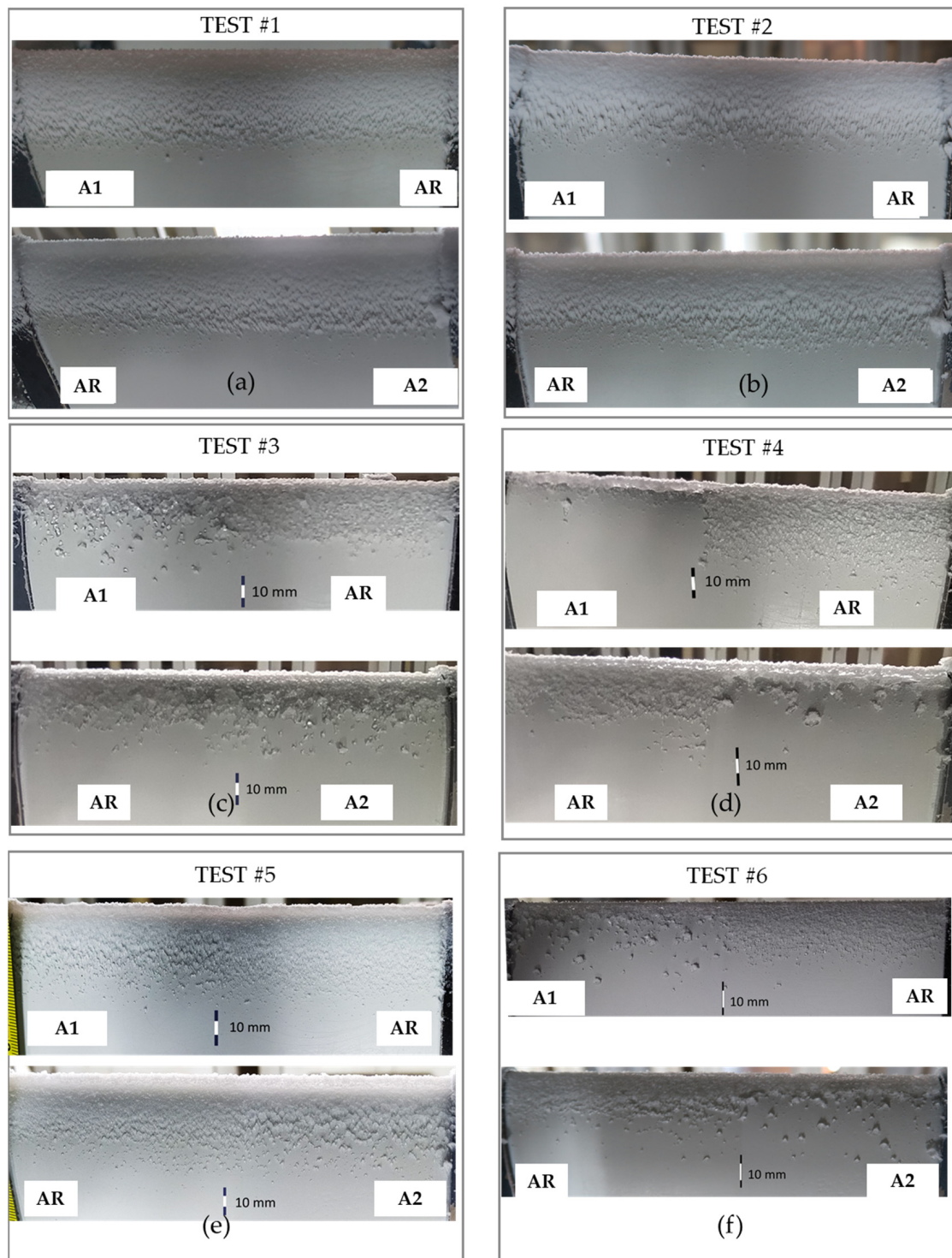


Figure 12. Pictures of ice accreted on A1, A2, and AR samples during the IWT test 1 (a), test 2 (b), test 3 (c), test 4 (d), test 5 (e), test 6 (f).

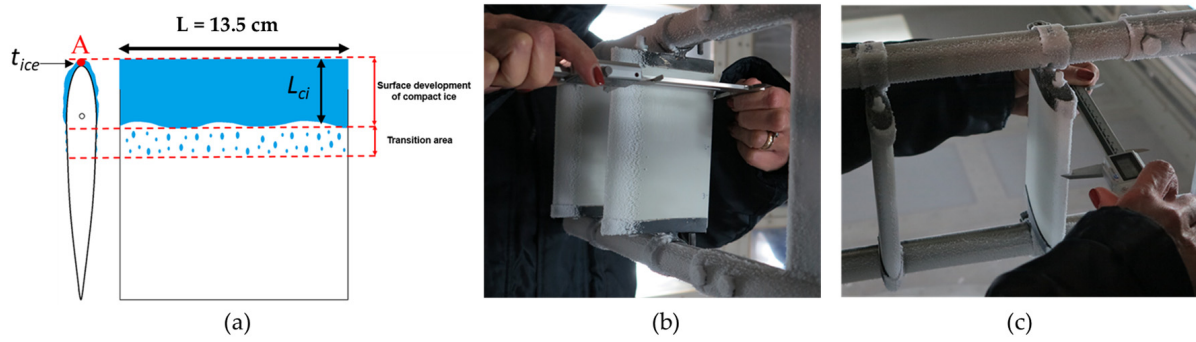


Figure 13. Schematic drawing of the accreted ice shape. With an angle of attack equal to zero, A represents the stagnation point (a). Measurement of the samples' chord length after each test (b,c).

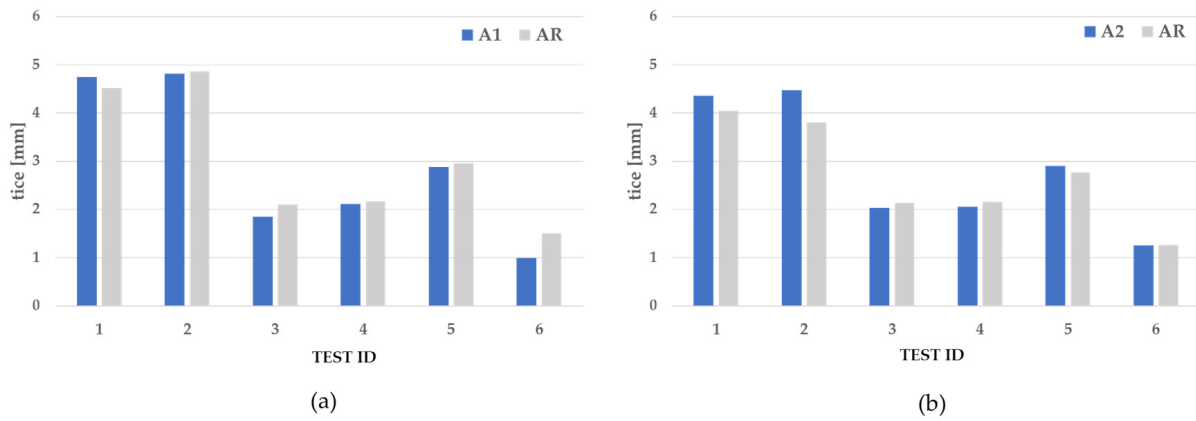


Figure 14. Accreted ice thickness t_{ice} on A1 and AR (a), and on A2, and AR (b), during the IWT tests.

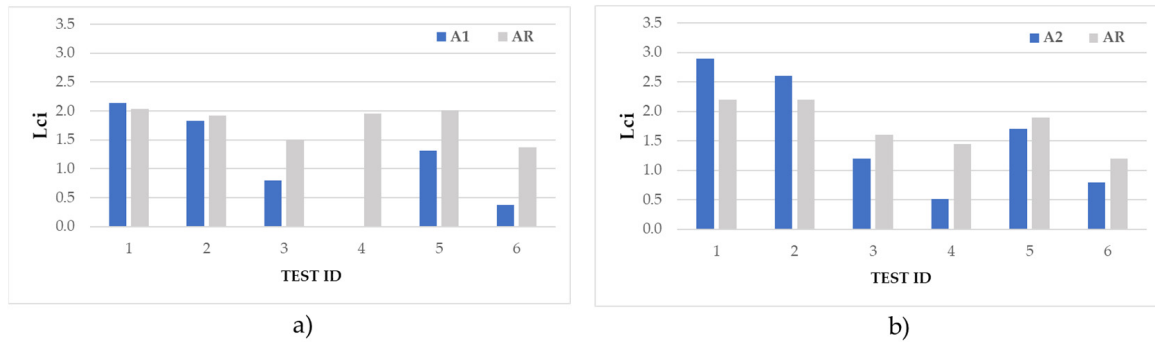


Figure 15. Length of the compact ice L_{ci} accreted from the leading edge alongside the airfoils A1 and AR (a), and A2 and AR (b) during the IWT tests.

The superhydrophobicity of A1 and A2 was preserved after the IWT test campaign.

The 3D scan acquired after test 6 was overlapped with the neat airfoil 3D reconstruction (Figure 17). In the inset (Figure 17d,e), a magnification of the airfoils with an assessment of the lengths of the compact ice L_{ci} accumulated starting from the leading edge was also reported. These values were in good agreement with those measured and reported in Figure 15, and listed in Table 4. The comparison was made by adding the thickness of the ice accumulated at the stagnation point.

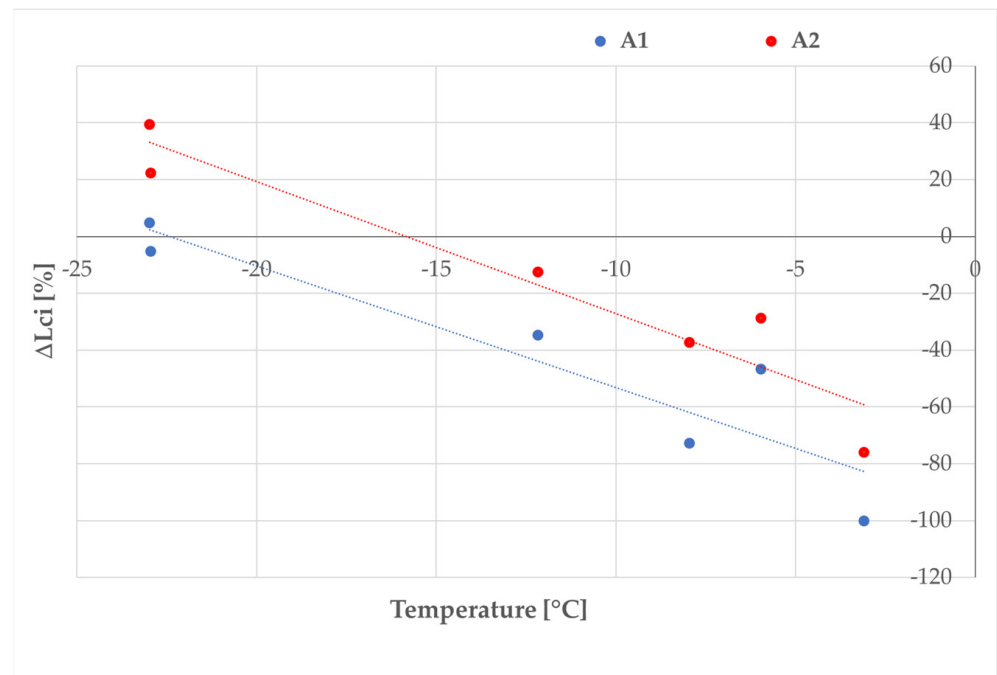


Figure 16. Percentage variation in *Lci* of coated surfaces with respect to the references as a function of the tests' temperature.

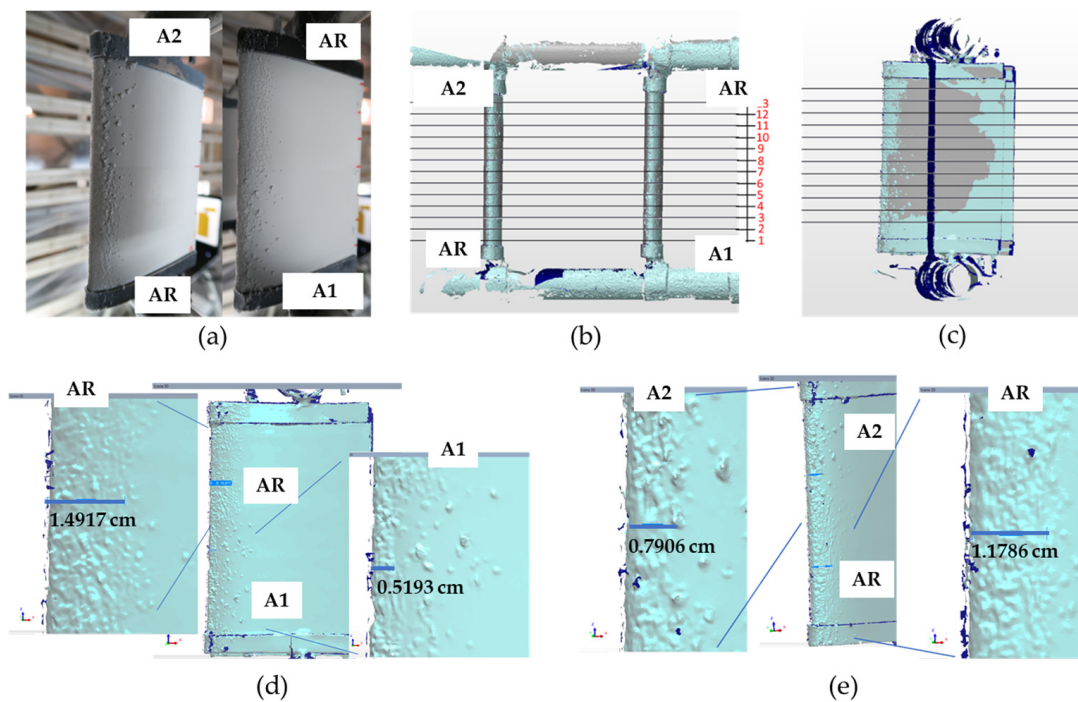


Figure 17. (a) Pictures of samples after test 6; (b,c) front and side view of slices where the ice contour was extracted; (d,e) 3D scan of A1 and A2 samples after test 6.

Table 4. Comparison between *Lci* values measured experimentally and through 3D scan (test 6).

		Experimental [cm]	3D Scan [cm]
SAMPLE 1	A1	0.5	0.52
	AR	1.5	1.49
SAMPLE 2	A2	0.8	0.79
	AR	1.2	1.18

4. Discussion and Conclusions

To be an anti-icing material, the hydrophobic/superhydrophobic coatings must significantly prevent, delay, or reduce the ice accretion in real flight icing conditions. The majority of work in the literature (see Table 1) focuses on testing superhydrophobic coatings at a speed equal to or lower than 50 m/s or rather in combination with an active system.

The present study was aimed at understanding the effectiveness of superhydrophobic coatings to reduce ice formation in relevant flight icing conditions, at 50 and 95 m/s and at temperatures ranging between -3 and -23 °C. Two superhydrophobic coatings generated as a combination of roughness and low SFE were applied on two NACA0015 wing profiles and tested in an IWT without any active IPS.

First, we observed the morphology of surfaces and measured their roughness and wettability; then, we evaluated the durability of these surfaces; finally, we tested them in an IWT. We found that at -23 °C and 95 m/s, with an exposure time of 77–79 s, the application of superhydrophobic coatings seems even detrimental, causing an increase of accreted ice on both the stagnation region (-1 – $+17\%$) and along the airfoils (-5 – $+39\%$). Whereas, at 95 m/s, but in glaze conditions, i.e., -6 and -8 °C, both superhydrophobic coatings achieved lower ice accretion at both the stagnation region (-2 – -34%) and along the airfoils (-29 – -73%) for an exposure time of 72–137 s. At 50 m/s for a longer exposure time (227–228 s) and at temperatures of -3 and -12 °C, the accreted ice was reduced mainly along the airfoils (by -12 – -100%), whereas no differences can be observed at the stagnation region (-5 – $+5\%$), probably due to the higher exposure time.

These findings suggest that the effectiveness of these coatings in reducing the ice accretion largely depends on the tested conditions, so they can be highly helpful for a short exposure time, also at 95 m/s, and mainly in glaze ice conditions. Instead, for use in a wide range of flight icing conditions, both rime and glaze, and long exposure time, they must be considered as a support to an active system.

5. Patents

Data reported in this manuscript refer to coatings of a formulation that is protected by the patent submission: Piscitelli, F. Italian Patent Application N. IT102021000032444, “Rivestimento superidrofobico e ghiacciofobico di un substrato, metodo per il suo ottenimento e substrato così rivestito”, 23 December 2021.

Funding: This research was funded by The Italian Ministry for Education, University and Research (MIUR) through the National Aerospace Research Program (PRORA) D.M. 305/98 art. 4 comma 1 as SMOS (SMart On-board Systems) project.

Institutional Review Board Statement: Not Applicable.

Informed Consent Statement: Not Applicable.

Data Availability Statement: Not Applicable.

Acknowledgments: The author would like to thank Lorenzo Notarnicola for his support, and Floriana Albano, Antonio Auletta, Antonio Ragni, Marco Schettino and all other CIRA IWT colleagues for the IWT test execution and the interesting discussions about IWT results. The author would like to thank especially Gianpaolo Elia for the 3D reconstruction of accreted ice and Francesco Marra for the execution of the adhesion test and for SEM acquisitions.

Conflicts of Interest: The author declares no conflict of interest.


References

1. Ma, L.; Zhang, Z.; Gao, L.; Liu, Y.; Hui, H. Bio-Inspired Icephobic Coatings for Aircraft Icing Mitigation: A Critical Review. *Rev. Adhes. Adhes.* **2020**, *8*, 168–198. [CrossRef]
2. Schulz, M.; Sinapius, M. *Evaluation of Different Ice Adhesion Tests for Mechanical Deicing Systems*; SAE Technical Paper; SAE: Warrendale, PA, USA, 2015.
3. Zhao, Z.; Chen, H.; Liu, X.; Liu, H.; Zhang, D. Development of high-efficient synthetic electric heating coating for anti-icing/de-icing. *Surf. Coat. Technol.* **2018**, *349*, 340–346. [CrossRef]
4. Yao, X.; Chen, B.; Morelle, X.P.; Suo, Z. Anti-icing propylene-glycol materials. *Extrem. Mech. Lett.* **2021**, *44*, 101225. [CrossRef]
5. Huang, X.; Tepylo, N.; Pommier-Budinger, V.; Budinger, M.; Bonaccorso, E.; Villedieu, P.; Bennani, L. A survey of icephobic coatings and their potential use in a hybrid coating/active ice protection system for aerospace applications. *Prog. Aerosp. Sci.* **2019**, *105*, 74–97. [CrossRef]
6. Antonini, C.; Innocenti, M.; Horn, T.; Marengo, M.; Amirfazli, A. Understanding the effect of superhydrophobic coatings on energy reduction in anti-icing systems. *Cold Reg. Sci. Technol.* **2011**, *67*, 58–67. [CrossRef]
7. Kreder, M.J.; Alvarenga, J.; Kim, P.; Aizenberg, J. Design of anti-icing surfaces: Smooth, textured or slippery? *Nat. Rev. Mater.* **2016**, *1*, 15003. [CrossRef]
8. Lv, J.; Song, Y.; Jiang, L.; Wang, J. Bio-Inspired Strategies for Anti-Icing. *ACS Nano* **2014**, *8*, 3152–3169. [CrossRef]
9. Tarquini, S.; Antonini, C.; Amirfazli, A.; Marengo, M.; Palacios, J. Investigation of ice shedding properties of superhydrophobic coatings on helicopter blades. *Cold Reg. Sci. Technol.* **2014**, *100*, 50–58. [CrossRef]
10. Hejazi, V.; Sobolev, K.; Nosonovsky, M. From superhydrophobicity to icephobicity: Forces and interaction analysis. *Sci. Rep.* **2013**, *3*, 2194. [CrossRef]
11. Cao, L.; Jones, A.K.; Sikka, V.K.; Wu, J.; Gao, D. Anti-Icing Superhydrophobic Coatings. *Langmuir* **2009**, *25*, 12444–12448. [CrossRef]
12. Varanasi, K.K.; Deng, T.; Smith, J.D.; Hsu, M.; Bhate, N. Frost formation and ice adhesion on superhydrophobic surfaces. *Appl. Phys. Lett.* **2010**, *97*, 234102. [CrossRef]
13. Chen, J.; Liu, J.; He, M.; Li, K.; Cui, D.; Zhang, Q.; Zeng, X.; Zhang, Y.; Wang, J.; Song, Y. Superhydrophobic surfaces cannot reduce ice adhesion. *Appl. Phys. Lett.* **2012**, *101*, 111603. [CrossRef]
14. Kulinich, S.; Farzaneh, M. On ice-releasing properties of rough hydrophobic coatings. *Cold Reg. Sci. Technol.* **2011**, *65*, 60–64. [CrossRef]
15. Kulinich, S.A.; Farhadi, S.; Nose, K.; Du, X.W. Superhydrophobic Surfaces: Are They Really Ice-Repellent? *Langmuir* **2011**, *27*, 25–29. [CrossRef] [PubMed]
16. Susoff, M.; Siegmann, K.; Pfaffenroth, C.; Hirayama, M. Evaluation of icephobic coatings—Screening of different coatings and influence of roughness. *Appl. Surf. Sci.* **2013**, *282*, 870–879. [CrossRef]
17. Yeong, Y.H.; Sokhey, J.; Loth, E. Ice Adhesion on Superhydrophobic Coatings in an Icing Wind Tunnel. In *Contamination Mitigating Polymeric Coatings for Extreme Environments*; Springer: Cham, Switzerland, 2018.
18. Mora, J.; García, P.; Muelas, R.; Agüero, A. Hard Quasicrystalline Coatings Deposited by HVOF Thermal Spray to Reduce Ice Accretion in Aero-Structures Components. *Coatings* **2020**, *10*, 290. [CrossRef]
19. Rivero, P.J.; Rodríguez, R.J.; Larumbe, S.; Monteserín, M.; Martín, F.; García, A.; Acosta, C.; Clemente, M.J.; García, P.; Mora, J.; et al. Evaluation of Functionalized Coatings for the Prevention of Ice Accretion by Using Icing Wind Tunnel Tests. *Coatings* **2020**, *10*, 636. [CrossRef]
20. Morita, K.; Kimura, S.; Sakaue, H. Hybrid System Combining Ice-Phobic Coating and Electrothermal Heating for Wing Ice Protection. *Aerospace* **2020**, *7*, 102. [CrossRef]
21. Villeneuve, E.; Blackburn, C.; Volat, C. Design and Development of an Experimental Setup of Electrically Powered Spinning Rotor Blades in Icing Wind Tunnel and Preliminary Testing with Surface Coatings as Hybrid Protection Solution. *Aerospace* **2021**, *8*, 98. [CrossRef]
22. Fortin, G.; Adomou, M.; Perron, J. *Experimental Study of Hybrid Anti-Icing Systems Combining Thermoelectric and Hydro-Phobic Coatings*; SAE International: Montreal, QC, Canada, 2011.
23. EASA. Available online: <https://www.easa.europa.eu/document-library/certification-specifications/cs-25-amendment-26-0> (accessed on 22 December 2020).
24. Piscitelli, F. Rivestimento Superidrofobico e Ghiacciofobico di un Substrato, Metodo per il Suo Ottenimento e Substrato Così Rivestito. Italian Patent Application N. IT102021000032444, 23 December 2021.
25. ISO 4288:1996; Geometrical Product Specifications (GPS)—Surface Texture: Profile Method—Rules and Procedures for the Assessment of Surface Texture. International Organization for Standardization: Geneva, Switzerland, 1996.
26. D7490-13; Standard Test Method for Measurement of the Surface Tension of Solid Coatings, Substrates and Pigments using Contact Angle Measurements. American Society for Testing and Materials: West Conshohocken, PA, USA, 2013.
27. Owens, D.K.; Wendt, R.C. Estimation of the surface free energy of polymers. *J. Appl. Polym. Sci.* **1969**, *13*, 1741–1747. [CrossRef]
28. Żenkiewicz, M. Methods for the calculation of surface free energy of solids. *J. Achiev. Mater. Manuf. Eng.* **2007**, *24*, 137–145.

29. Piscitelli, F.; Chiariello, A.; Dabkowski, D.; Corrado, G.; Marra, F.; Di Palma, L. Superhydrophobic Coatings as Anti-Icing Systems for Small Aircraft. *Aerospace* **2020**, *7*, 2. [CrossRef]
30. Piscitelli, F.; Tescione, F.; Mazzola, L.; Bruno, G.; Lavorgna, M. On a simplified method to produce hydrophobic coatings for aeronautical applications. *Appl. Surf. Sci.* **2019**, *472*, 71–81. [CrossRef]
31. *ASTM D3359-09*; Standard Test Methods for Measuring Adhesion by Tape Test. ASTM: West Conshohocken, PA, USA, 2009.
32. *ASTM C633-13*; Standard Test Method for Adhesion or Cohesion Strength of Thermal Spray Coatings. ASTM: West Conshohocken, PA, USA, 2017.
33. Yilgor, I.; Bilgin, S.; Isik, M.; Yilgor, E. Facile preparation of superhydrophobic polymer surfaces. *Polymer* **2012**, *53*, 1180–1188. [CrossRef]
34. Shang, H.M.; Wang, Y.; Takahashi, K.; Cao, G.Z.; Li, D.; Xia, Y.N. Nanostructured superhydrophobic surfaces. *J. Mater. Sci.* **2005**, *40*, 3587–3591. [CrossRef]
35. Adams, R.D.; Mallick, V. The Effect of Temperature on the Strength of Adhesively-Bonded Composite-Aluminium Joints. *J. Adhes.* **1993**, *43*, 17–33. [CrossRef]
36. Fortin, G.; Ilinca, A.; Perron, J. A study of Icing Events at Murdochville: Conclusions for the Wind Power Industry. In Proceedings of the Quebec Premier Wind Energy Event, International Conference, Wind Energy Remote Regions, Magdalene Islands, QC, Canada, October 2005.

Article

Icing Wind Tunnel Test Campaign on a Nacelle Lip-Skin to Assess the Effect of a Superhydrophobic Coating on Ice Accretion

Filomena Piscitelli * , Salvatore Palazzo and Felice De Nicola

Italian Aerospace Research Centre, CIRA, Via Maiorise, 1, 81043 Capua, Italy; s.palazzo@cira.it (S.P.); f.denicola@cira.it (F.D.N.)

* Correspondence: f.piscitelli@cira.it

Abstract: The formation of ice on nacelle causes the reduction or loss of aerodynamic performance, fuel consumption increases, reduced thrust, and the ingestion of ice, which can damage the engine. The piccolo tube anti-icing employed as an active ice protection system has limitations in terms of performance losses and energy costs. Furthermore, according to the FAA regulation, it cannot be activated during takeoff and initial flight phases in order to avoid engine thrust reduction. This work reports on an icing wind tunnel test campaign performed at initial flight phases conditions on the M28 PZL nacelle before and after the application of a superhydrophobic coating in order to study the effect of wettability on ice accretion. Results highlighted that an ice thickness reduction of -49% has been recorded at $-12\text{ }^{\circ}\text{C}$, matched to an increase in the impingement length of 0.5% . At 95 m/s and at 420 s of exposure time, the ice thickness was reduced by -27% and -14% , respectively, whereas the impingement length reductions were -9.6% and -7.6% . Finally, an ice thickness reduction of -8% was observed at a liquid water content of 1 g/m^3 , matched to an increase in the impingement length of 3.7% and to a reduction in length and number of the frozen rivulets.

Keywords: superhydrophobic coatings (SHC); nacelle lip-skin; passive ice protection system; icing wind tunnel tests



Citation: Piscitelli, F.; Palazzo, S.; De Nicola, F. Icing Wind Tunnel Test Campaign on a Nacelle Lip-Skin to Assess the Effect of a Superhydrophobic Coating on Ice Accretion. *Appl. Sci.* **2023**, *13*, 5183. <https://doi.org/10.3390/app13085183>

Academic Editor: Theodore E. Matikas

Received: 23 March 2023

Revised: 15 April 2023

Accepted: 19 April 2023

Published: 21 April 2023



Copyright: © 2023 by the authors. Licensee MDPI, Basel, Switzerland. This article is an open access article distributed under the terms and conditions of the Creative Commons Attribution (CC BY) license (<https://creativecommons.org/licenses/by/4.0/>).

1. Introduction

Ice accretion on the nacelle lip-skin surface which occur upon flying through clouds containing super cooled water droplets (SWD) can result in a reduction or a loss of aerodynamic performance due to the formation of non-aerodynamic profile [1,2]. When this occurs, the fuel consumption increases due to the higher drag force, and the thrust reduces as a consequence of the restriction of airflow through the fan due to ice accumulated on the inner surface portion of the nacelle lip-skin [3]. The worst scenario occurs when broken ice particles are absorbed, the ingestion of which can critically damage the engine. For these reasons, protection against icing is required as it is a potential cause of aircraft crashes. A typical anti-icing system used for the nacelle is the piccolo tube anti-icing (PTAI), which is one of the most popular hot-bleed-air anti-icing devices utilized for wings, among others [4–6]. The parameters affecting the thermal performance of the PTAI include the hot air mass flow rate, jet spacing, the distance from the holes to the surface, the impingement angle, etc. [7]. This high-performance system is better than other ice protection systems with respect to efficiency and reliability; nevertheless, it has limitations in terms of performance losses, energy costs, complexity, weight, and hotspot issues [8].

Furthermore, the engine nacelle is mainly exposed to the icing environment with SWD during the takeoff and the initial climb phases of flight [1,9]. According to the Federal Aviation Administration regulation, the anti-icing systems cannot be activated until the aircraft reaches 400 feet above the takeoff surface to avoid engine thrust reduction [10]. Therefore, the PTAI cannot protect the nacelle against ice accretion during these two flight

phases. Therefore, it could be highly desirable, mainly in these two flight phases, to use a passive ice protection system (IPS) such as a superhydrophobic coating (SHC) which is able to reduce the droplets permanence on the surface nacelle lip-skin, thereby reducing de facto the accreted ice [11]. Additionally, during the whole flight, the passive SHC could be used in combination with the active PTAI to reduce the needed hot air mass flow, and consequently mitigate some limitations of the active PTAI system, such as the increased fuel consumption, the reduced overall thermal efficiency, and the performance losses.

Several previous studies focused on the simulation study of the effect of PTAI on the lip-skin of the nacelle [3,8,9,12–14], but very little can be found in the literature with regard to the experimental tests in icing wind tunnel (IWT). For example, Papadakis [15] conducted icing tests in the NASA Glenn wind tunnel for a full-sized engine inlet and documented ice shapes on the leading edge under different icing conditions. Tian et al. [16] conducted an experimental campaign to study the dynamic ice accretion on rotating aeroengine spinner and fan blades, with the aim to evaluate the icing-induced performance degradation to the fan rotor. With the perspective to reduce the energy cost of the PTAI system, in [17], the authors carried out an experimental study to quantify the dynamic ice accretion process on aeroengine inlet guide vanes in order to optimize the design paradigms to reduce the requirements of the bleed air. Finally, they also suggested as a novel anti-/de-icing strategy to leverage hydrophobic/icephobic coatings to further reduce the requirements of the bleed air for the inlet guide vanes' anti-/de-icing operation, thereby minimizing the performance penalties to the aeroengines. Studies on the effect of a superhydrophobic surface (SHS) and anti-icing coatings on rotating aeroengine fan blades were reported in [18], where the authors highlighted that both SHS and icephobic coatings have advantages in anti-icing. SHS facilitated the blades' surface with much less ice under both glazed and rimed icing conditions, while icephobic coating prevents large ice-chunk formation in the leading edge as ice chunks easily shed from the leading edge, compared with the SHS blade and blades with a hydrophilic coating.

In this context, the present work reports an experimental test campaign performed in the Italian Aerospace Research Centre (CIRA) IWT with the aim to evaluate the effect of a SHC on the ice accretion occurring on the nacelle lip-skin belonging to the M28 PZL vehicle, possessing dimensions of 50 cm × 50 cm × 20 cm and is made of stainless-steel (the PTAI) and composite (the back side). To the best of our knowledge, no previous work focused on this topic. IWT tests were performed at the takeoff and first climb conditions [9], which represent the worst case for ice accretion due to the switched off PTAI system in these two flight phases, at $T = -5\text{ }^{\circ}\text{C}$ and $-12\text{ }^{\circ}\text{C}$, $v = 70$ and 95 m/s , at an altitude of 3000 m, with a median volumetric diameter (MVD) equal to $20\text{ }\mu\text{m}$ and liquid water content (LWC) equal to 0.3 and 1 g/m^3 . Tests were performed before and after the application of a SHC, in order to study the effect of the SHC application on ice accretion. Accreted ice was measured after each test in terms of thickness and impingement length. In a previous work [11], the authors studied the effect of the SHC on the ice accretion occurring on two wing profiles of NACA0015 made of acrylonitrile butadiene styrene and manufactured with a 3D printing machine, having a length of 135 mm and a chord of 100 mm. Broader ranges of IWT parameters were considered in the previous work, i.e., temperatures ranging between $-3\text{ }^{\circ}\text{C}$ and $-23\text{ }^{\circ}\text{C}$, speed 50 and 95 m/s, and LWC 0.3 and 0.6 g/m^3 .

The present work was developed in the framework of the Clean Sky 2 SAT-AM (More Affordable Small Aircraft Manufacturing) project, whose main goal was to investigate new technologies for a future small aircraft able to fly with low fuel consumption. The reference vehicle for this project was the M28 designed and manufactured by Consortium Partner Polskie Zakłady Lotnicze (PZL), Mielec (PL). It is a commuter category 19 passenger, twin-engine high-wing cantilever monoplane, suited for passenger and/or cargo transportation and certified under EU CS-23 and USA FAR 23 requirements.

2. Materials and Methods

A nanostructured coating developed at CIRA [19,20] was applied with an aerograph using de-humidified air at 3 bars, with a layer-by-layer technique. The coating was cured in an autoclave at 80 °C.

Roughness of surfaces before and after the application of the coating was measured by employing a SAMA SA6260 surface roughness meter. Roughness measurements, performed according to the ISO 4288 [21], were reported as Ra, which represents the arithmetic average of the absolute values of the profile height deviations from the mean line.

The optical images were acquired with a microscope USB Dino-Lite AM4815ZTL at 140×.

The contact angle (CA) measurements were performed at 23 °C in compliance with the ASTM D7490-13 [22] standard, with 3 µL of water (H₂O). Contact angles were rapidly acquired within 30 s of depositing the drop to avoid changes in angles.

The thickness of the dry coating was measured according to ISO 2360 [23] using the Defelsko PosiTector 6000 FSN2, manufactured by DeFelsko Corporation, Ogdensburg, NY, USA.

IWT tests were performed in CIRA IWT facility, which is a closed loop circuit, refrigerated wind tunnel with three interchangeable test sections and one open jet configuration, whose main purpose is to perform icing tests. The cloud generation for icing conditions simulation is carried out by the spray bar system (Figure 1), able to generate water droplets with diameters (MVD) and concentrations (LWC) covering nearly the overall envelope prescribed by the Appendix C CS-25 for both continuous and intermittent cloud conditions.



Figure 1. Pattern configurations of spray bar nozzles: 1:2 grid, one half of the spray bar nozzles working (a); 1:4 grid, one quarter of spray bar nozzles working (b).

Ice accretion measurements were performed after each test. A cold stop at −20 °C guaranteed to freeze the accreted ice on the test article, in order to allow the CIRA team to enter the tunnel, take pictures and measurements of thickness and impingement lengths performed in correspondence to 13 sections drawn before tests on the metallic leading edge (red and blue lines in Figure 2). Measurements of the ice thickness as the difference of measured length section before and after each test taken using a Mitutoyo CD-20DAX digital centesimal caliber, with an accuracy better than 0.02 mm (Figure 3a). For each test condition, the ratios between the mean values of the difference between the ice thicknesses recorded at the measuring stations in coated and uncoated configurations and the mean values of the ice thicknesses measured during the corresponding uncoated tests were evaluated in order to have a quantitative global estimation of the SHC performance on the ice accretion performance in terms of the percentage change of ice accretion thickness. The impingement length of the accreted ice was calculated as the difference between the total length of metallic part and length free from ice (see picture in Figure 3b), measured using the Mitutoyo CD-20DAX digital centesimal caliber. During the measurements, the caliper was aligned with the reference lines drawn before tests on the test article. In Figure 3c, a schematic draw of the accreted compact ice and isolated droplets observed during the IWT test campaign is displayed. Similar to the ice thickness data, for each test condition, the ratios between the mean values of the difference between the impingement length recorded at the measuring stations in coated and uncoated configurations and the mean

values of the impingement length measured during the corresponding uncoated tests were evaluated in order to have a quantitative global estimation of the SHC performance on the impingement length as percentage change of the impingement length. During the measurements (Figure 3a,b) the IWT test section was kept at subzero temperature in order to avoid ice melting.

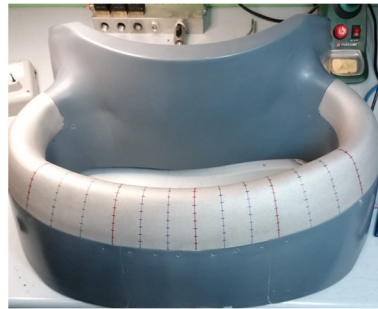


Figure 2. Sections drawn on the test article before tests.

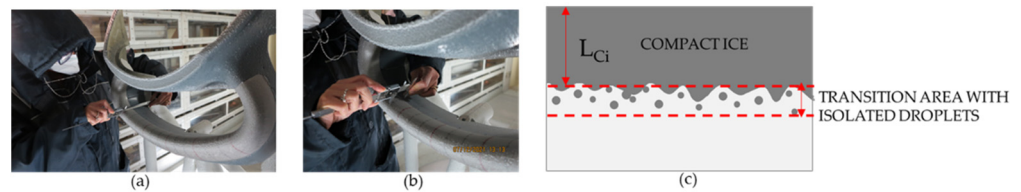


Figure 3. Measurements of thickness measurement (a) and of the impingement length (b); schematic draw of the accreted compact ice L_{Ci} and isolated droplets (c).

3. Results

3.1. Superhydrophobic Coating Application

Since paint adheres to rougher surfaces more strongly than to smooth surfaces because of the increased contact area and an interlocking effect, a specific roughness of the test article substrate was required. A previous work [24] established the best roughness at about 3–4 μm achieved through sand blasting. Figure 4a shows the M28 PZL vehicle highlighted in the red circle of the nacelle test article, whereas Figure 4b,c display the nacelle lip-skin before and after the sand blasting useful for achieving the required $Ra = 3.2 \mu\text{m} \pm 0.2$. Figure 4d shows the nacelle lip-skin after the application of the CIRA SHC [19,20], having a thickness of $32 \mu\text{m} \pm 6$ and a roughness $Ra = 1.6 \mu\text{m} \pm 0.3$.

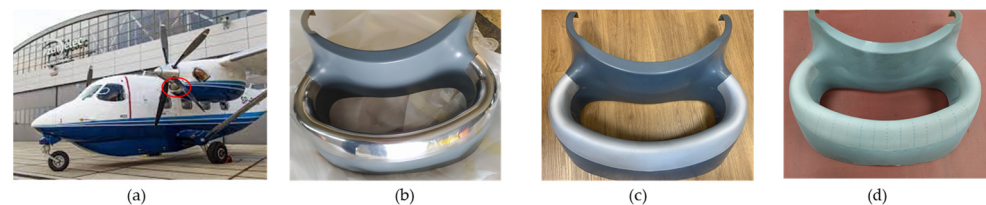


Figure 4. M28 PZL vehicle (a) and nacelle test article before (b) and after (c) the sand blasting treatment, and after the application of the superhydrophobic coating (d).

The test article surface after the sand blasting treatment has a uniform sponge-like morphology (Figure 5a,b) which was preserved after the application of the coating (Figure 5c). This morphology is helpful to guarantee a good adhesion of the coating due to the mechanical interlocking occurring around the interphase substrate-coating. Moreover, the sponge-like morphology preserved after the application of the coating is useful to trap air and contribute to superhydrophobicity [25].

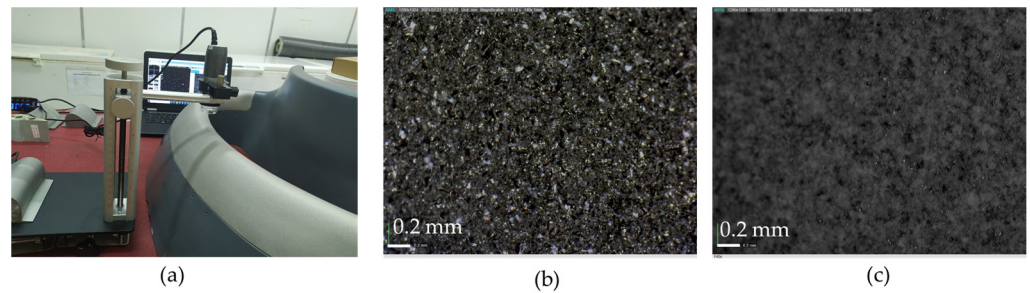


Figure 5. Set-up for the optical microscopy acquisitions (a); microscope images at 140× of the lip-skin nacelle surface before (b) and after (c) the coating’s application.

Figure 6 shows pictures of water droplets on flat samples, representative of the nacelle test article having the same roughness, at 25 °C and −27 °C [24]. Measurements of water contact angles performed at 25 °C give values of 44° and 164° on the uncoated and coated surfaces, respectively (Figure 6a,c). These values seem to be preserved at −27 °C (Figure 6b,d). Wettability measurements have also been performed on the test article before and after the coating application using the set-up in Figure 7a. The test confirmed the measured CA on the uncoated surface; however, due to the low wettability of the applied SHC, it has been impossible to perform the measurements of the wettability on the coated surface since water droplets bounce or roll away from the 3D-coated surface, thereby making the acquisition of the static water contact angle impossible. Therefore, on coated surfaces, the quality of the coating application and its corresponding low wettability were assessed through the slipping and/or the bouncing off of water droplets impacting the coated surface, as shown in Figure 7b,c, where the movement of the water droplet is highlighted by a red arrow.

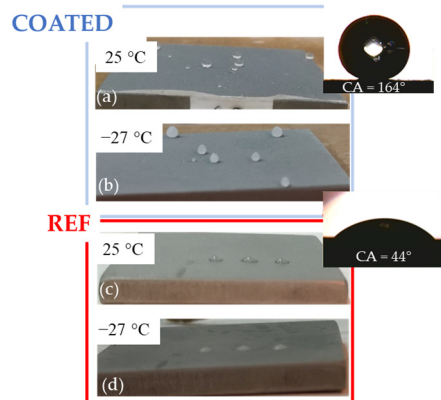


Figure 6. Wettability tests of the coated flat sample representative of the test article performed at 25 °C (a) and −27 °C (b); wettability of reference performed at 25 °C (c) and at −27 °C (d) [24].

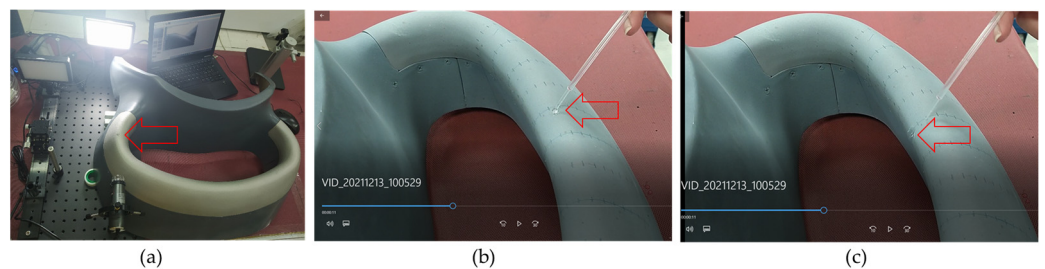


Figure 7. Wettability test carried out on the test article before (a) and after (b,c) the application of the SHC. The red arrow points at the movement of the water droplet.

3.2. IWT Tests

3.2.1. Installation of Nacelle in the Icing Wind Tunnel

The test article has been installed in the IWT main test section (Figure 8), whose dimensions are: width 2.3 m, height 2.35 m, length 7 m. The test section is equipped with two turntables for model attitude setting; the maximum attainable Mach number is about 0.4 and the minimum static temperature is $-32\text{ }^{\circ}\text{C}$. In this configuration, the model is generally vertically mounted between the wind tunnel floor and ceiling, using as fixing points two interface plates fastened on the two turntables. The interface plates are customized for each test campaign. In this case, only the lower turntable has been used for model installation. The test article was fixed on the interface plate by means of four fixing points, each one made of four M10 bolts.

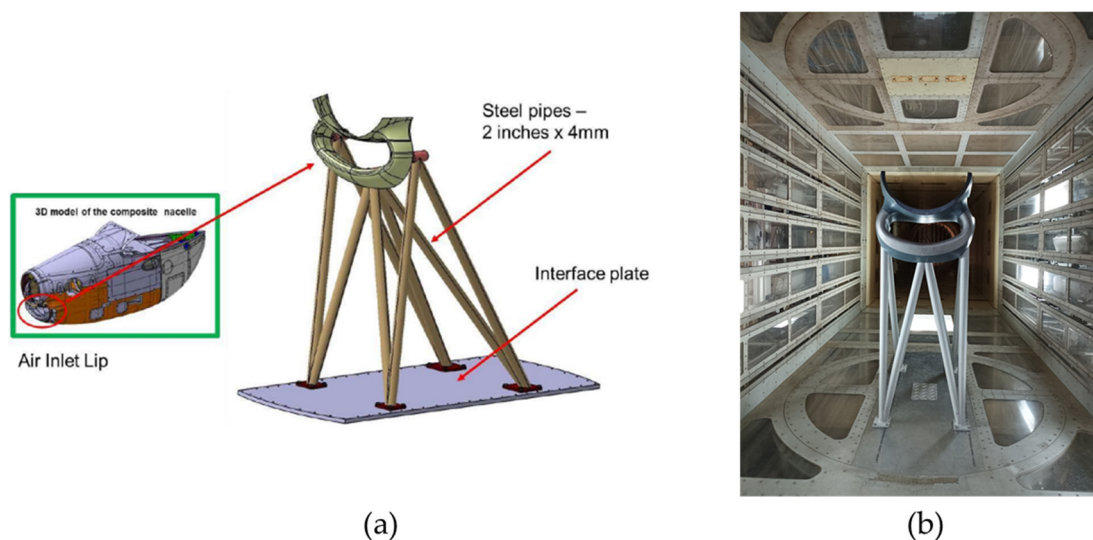


Figure 8. Design of the test article support for the IWT tests (a); test article mounted in the IWT facility (b).

3.2.2. IWT Test Definition

The M28 PZL is a commuter turboprop airplane, belonging to the CS-23 Normal, Utility, Aerobatic and Commuter Airplanes, that is the 14 CFR, Part 23. According to the 14 CFR Appendix C of Part 25 (Electronic Code of Federal Regulations (eCFR)), the CS-23 class aviation is regulated by the FAR 25 Appendix C, to be used as reference once the aircraft performances are known. The test matrix for the IWT test was defined by taking into account the maximum and the cruise speed of the M28 PZL, which are 355 km/h (98.6 m/s) and 244 km/h (67.8 m/s), respectively, as well as the flight altitude of 3000 m for the cruise altitude, to which corresponds a $T = -4.5\text{ }^{\circ}\text{C}$, according to the standard atmosphere of 1976. For all tests, an MVD of $20\text{ }\mu\text{m}$ and a flight altitude of 3000 m were considered. All other IWT test conditions are detailed in Table 1, which also correspond to the take-off and the first climb conditions of an aircraft CS-25 class aviation [9]. Tests have been performed before on the neat test article (UNCOATED in Table 1), and then, after the application of the SHC, on the coated one (COATED in Table 1). With respect to the baseline, corresponding to the standard temperature of $-5\text{ }^{\circ}\text{C}$, the cruise speed of 70 m/s, an LWC equal to 0.3 g/m^3 , and an exposure time of 140 s (test 1–2), the following effects have been analyzed: (a) LWC (equal to 1 g/m^3 in tests 3 and 4), (b) temperature (reduced to $-12\text{ }^{\circ}\text{C}$ in tests 5 and 6), (c) exposure time (increased to 420 s in tests 7 and 8), and (d) velocity (increased to the maximum speed equal to 95 m/s in tests 9, 10, and 11). During tests, a humidity ranging from 89% to 93% has been measured. The formation of glaze, rime, and mixed ices was observed [26,27].

Table 1. IWT test conditions.

Test ID	Coating	T [°C]	v [m/s]	Liquid Water Content [g/m ³]	Exposure Time [s]	Flight Path [km]
1	UNCOATED	−5	70	0.3	140	9.8
3		−5	70	1	140	9.8
5		−12	70	0.3	140	9.8
7		−12	70	0.3	420	29.4
9		−5	95	0.3	140	13.3
2	COATED	−5	70	0.3	140	9.8
4		−5	70	1	140	9.8
6		−12	70	0.3	140	9.8
8		−12	70	0.3	420	29.4
10		−5	95	0.3	140	13.3
11		−5	95	0.3	140	13.3

3.2.3. IWT Test Results

In the following, the results related to the IWT tests performed on the coated and uncoated test article are reported.

Test 1–2 T = −5 °C; v = 70 m/s; H = 3000 m; MVD = 20 μm; LWC = 0.3 g/m³; t = 140 s—Baseline

Tests 1 and 2, performed at −5 °C with a velocity of 70 m/s near the cruise velocity of the M28 PZL vehicle and an LWC of 0.3 g/m³, represent the base-line tests for the uncoated and coated test article, respectively. Test 1 has been performed on the uncoated surface (Figure 9a–d) and test 2 on the coated one (see results in Figure 9e–h). The pictures taken after the two tests highlighted that in these conditions and for the selected exposure time, i.e., 140 s, the amount of the ice accreted on both uncoated and coated surfaces is poor and concentrated at the impingement area, whereas both inner and outer sides of the nacelle lip-skin were free from ice. Average thickness values of 1.78 mm and 1.16 mm were measured at the uncoated and coated leading edge, respectively. The accreted ice seems similar to dry rime ice [27–29]. Nevertheless, beyond the dense and compact ice, an area with isolated ice droplets appears, as schematically illustrated in Figure 3c, especially for the coated surface. Here, the isolated ice droplets are greater in quantity and size (Figure 9g) than those observed on the uncoated surface. Moreover, they have the same spherical shape as that observed for isolated droplets of ice frozen in static conditions (Figure 6).

Test 3–4: T = −5 °C; v = 70 m/s; H = 3000 m; MVD = 20 μm; LWC = 1 g/m³; t = 140 s—LWC Effect

In order to study the effect of the LWC, tests 3 and 4 have been performed at an LWC equal to 1 g/m³. Pictures taken after test 3 of the uncoated test article are shown in Figure 10a–c, whereas pictures of test 4 carried out on the coated test article are displayed in Figure 10d–f. By comparing the pictures in Figure 10 with those in Figure 9 (baseline test), it is highlighted that the effect of increasing the LWC corresponds to an increased amount of accreted ice, which was observed mainly in correspondence to the impingement area and alongside the internal part of the nacelle lip. Here, the ice has accreted as frozen rivulets instead of isolated ice droplets, as observed at the lower LWC. This is due to the larger amount of liquid water as the impacted water mass would only freeze partially, while the remaining water would coalesce into rivulets and run back over the downstream surface. Instead, the ice accreted in a spherical-like shape can be observed only at the impingement line, before the rivulets, on both the uncoated and coated surfaces. They seem to make a separation between the dense ice below them and the rivulets beyond the stagnation line. The formation of this spherical-like ice accumulated at the stagnation line along with the isolated rivulets downstream are typical of glazed ice accretion [27]. The average thickness of ice measured on uncoated and coated surfaces were, respectively, 1.75 mm and 1.74 mm. Measurements of the impingement length of the accreted ice, L_{ci} , reported in Figure 11 reveal that no differences can be observed between the uncoated

and coated surfaces. Rather, the L_{ci} for the uncoated surface seems to be slightly shorter than that measured on the coated surface. Here, the values of L_{ci} measured for the coated surface in Section 8 and uncoated surface in Section 11 are reported as isolated dots and are not included in the trend due to a substantial deviating rate. This deviation could be due to some imperfections in the nacelle surface, highlighted in these tests more than in the others. Finally, by comparing the rivulets' lengths in Figure 10c,f, it is notable that these are much longer and that the rivulets' distribution is denser on the uncoated surface than on the coated one.

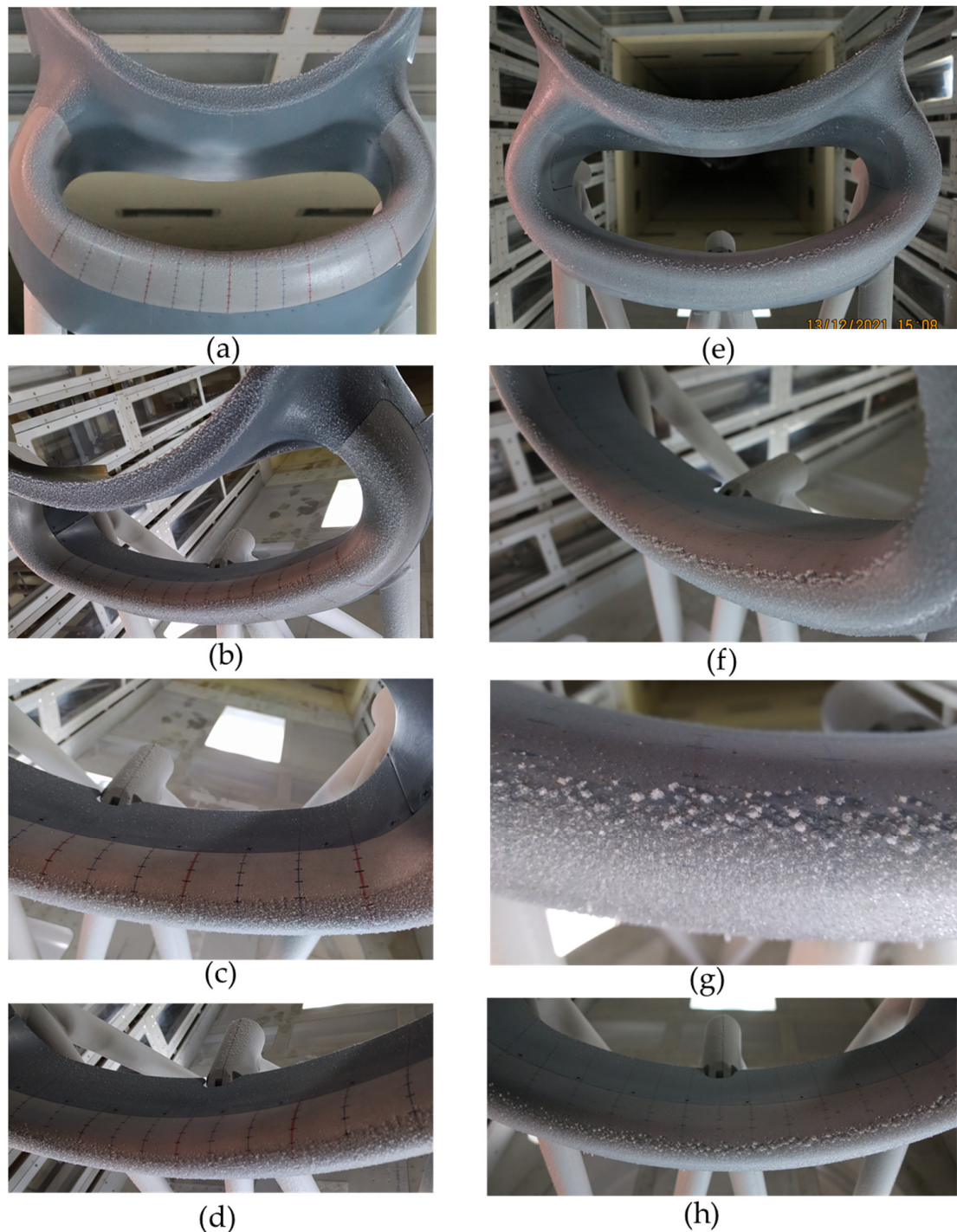


Figure 9. Results of test 1 performed on the uncoated test article (a–d) and of test 2 carried out on the coated test article (e–h).

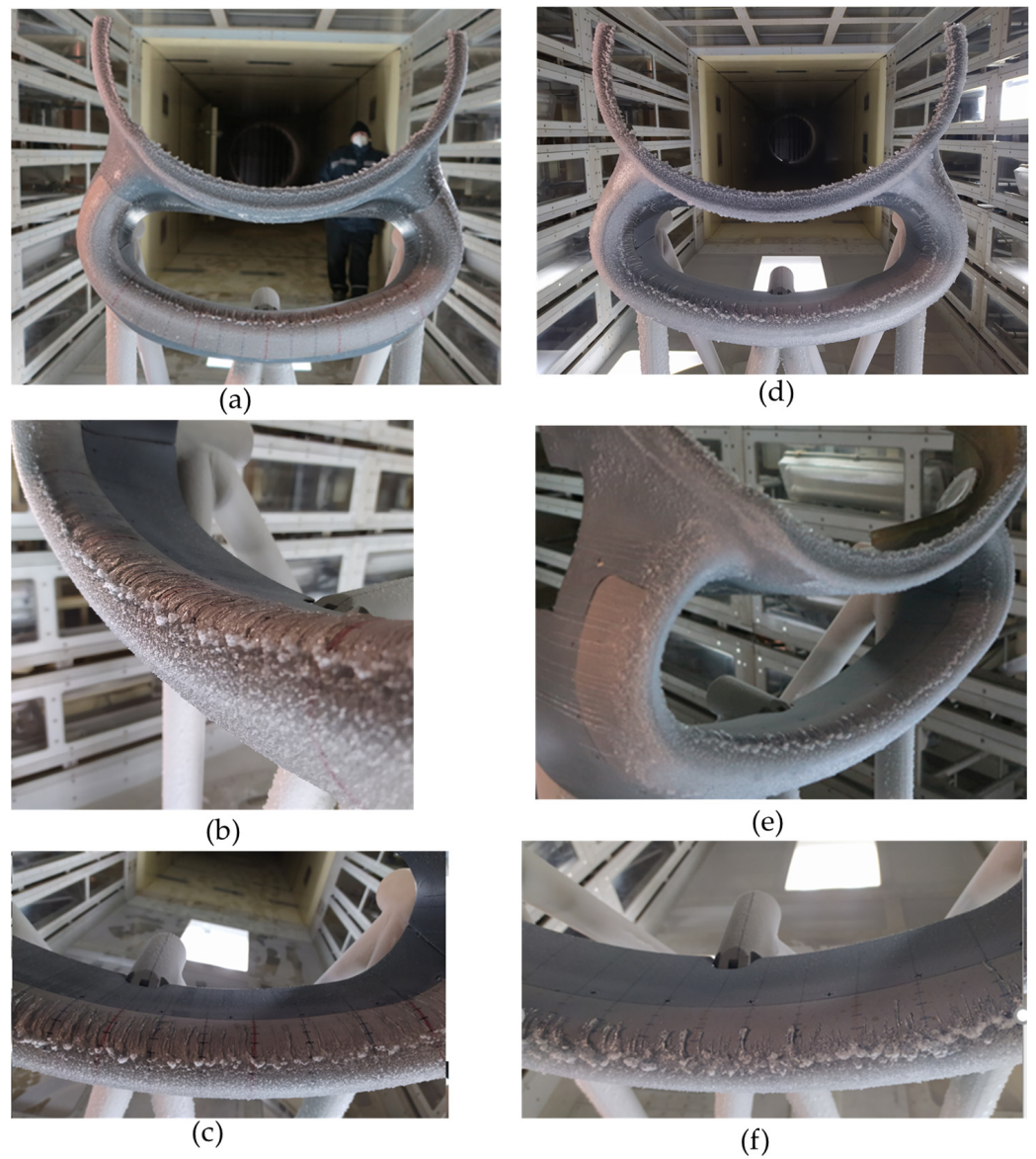


Figure 10. Results of test 3 (a–c) on uncoated surface of test article and test 4 (d–f) on coated surface of test article.

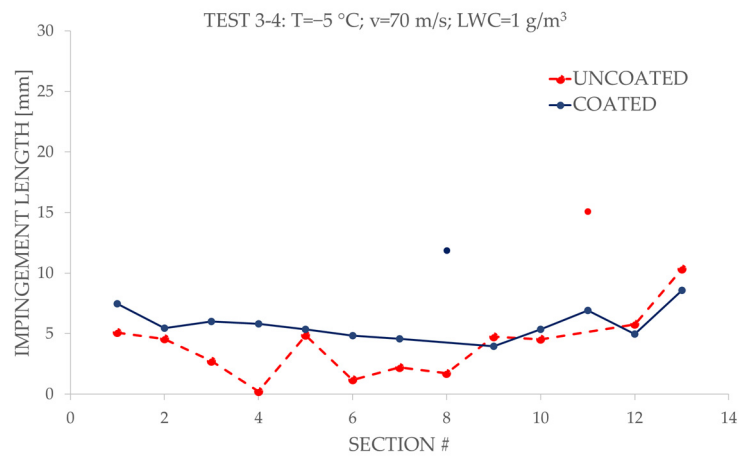


Figure 11. Impingement length measured after tests 3 and 4.

Test 5–6: $T = -12\text{ }^{\circ}\text{C}$; $v = 70\text{ m/s}$; $H = 3000\text{ m}$; $MVD = 20\text{ }\mu\text{m}$; $LWC = 0.3\text{ g/m}^3$; $t = 140\text{ s}$ —T Effect (Baseline for Tests 7 and 8)

The effect of the decreased temperature was assessed with tests performed at $-12\text{ }^{\circ}\text{C}$. Pictures of tests performed on uncoated and coated surfaces are displayed in Figure 12a–j, respectively. As for baseline tests 1 and 2, sparse ice droplets having spherical shapes appear on both coated and uncoated surfaces, displaying a typical dry rime ice accretion [27]. However, the coated surface has more isolated ice droplets, which result in a less dense transition area, and the ice droplets have larger dimensions than those accreted on the uncoated surface. Average thicknesses of accreted ice on uncoated and coated surfaces were 1.51 mm and 0.77 mm, respectively. No significant difference can be observed in the impingement lengths (see Figure 13).

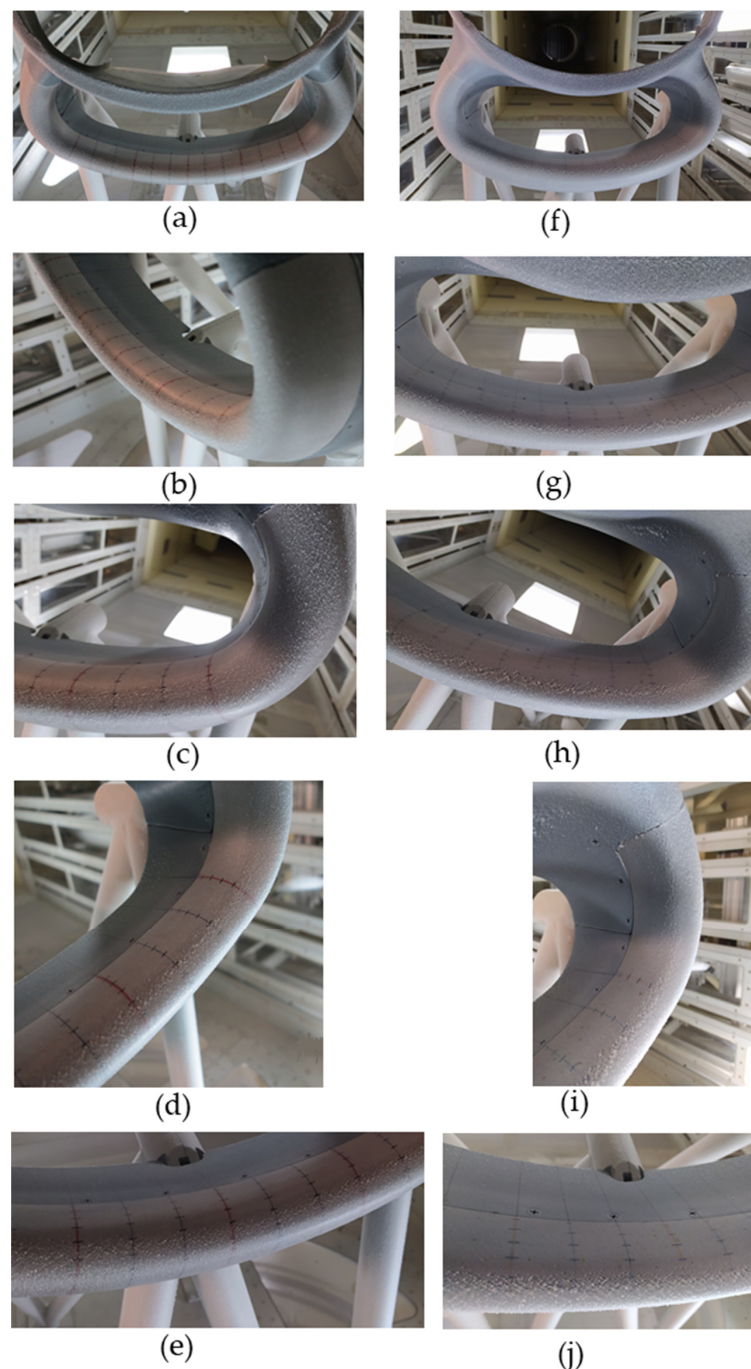


Figure 12. Results of test 5 (a–e), on uncoated test article and test 6 (f–j) on coated test article.

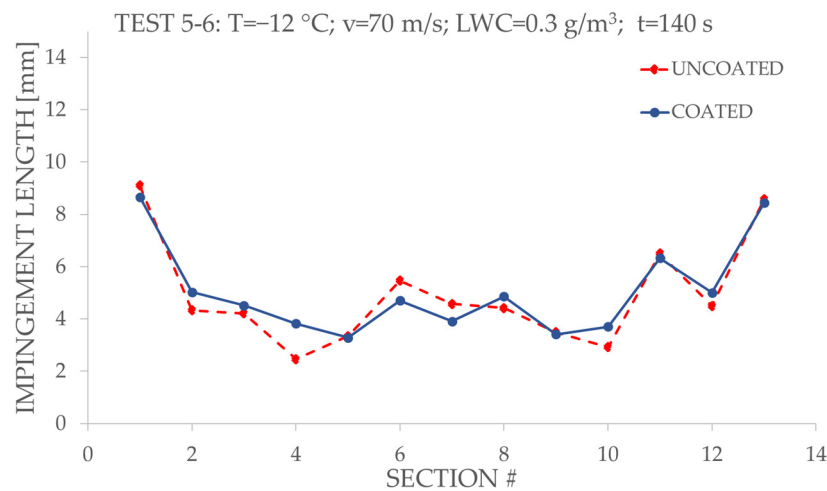


Figure 13. Impingement length measured after test 5 and test 6.

Test 7–8: $T = -12\text{ }^{\circ}\text{C}$; $v = 70\text{ m/s}$; $H = 3000\text{ m}$; $MVD = 20\text{ }\mu\text{m}$; $LWC = 0.3\text{ g/m}^3$; $t = 420\text{ s}$ —Exposure Time and Temperature Effect

Starting from tests 5 and 6 performed at $-12\text{ }^{\circ}\text{C}$, the exposure time was increased to 420 s. Pictures of tests 7 and 8, performed on uncoated and coated surfaces, were shown in Figure 14a–j, respectively. By comparing pictures in Figure 12 at a shorter exposure time with those of Figure 14, it can be observed that the ice accumulated on both uncoated and coated surfaces increases as the exposure time increases, as expected. The accreted ice assumes two different shapes: it is milky with crystalline structures on the upstream area, typical of rime ice, whereas it appears to be less dense with columnar structures at the stagnation line, typical of glaze ice [27,29]. Quite no differences can be observed in the shape and appearance of the ice grown on coated and uncoated surfaces. However, it was found that the impingement length of ice accreted on the coated surface is on average 3 mm shorter than that measured on the uncoated surface (Figure 15). Finally, measured thickness was 3.46 mm and 2.97 mm for uncoated and coated surfaces, respectively.

Test 12–13–14: $T = -5\text{ }^{\circ}\text{C}$; $v = 95\text{ m/s}$; $H = 3000\text{ m}$; $MVD = 20\text{ }\mu\text{m}$; $LWC = 0.3\text{ g/m}^3$; $t = 140\text{ s}$ —V Effect

Velocity was increased to 95 m/s in tests 9 and 10; pictures of results are displayed in Figure 16a–d for uncoated and Figure 16e–h for coated test article. A test of repeatability was performed on the coated surface (test 11), and results are shown in Figure 17. Compared with the baseline tests (Figure 9), it was found that as the incoming flow velocity increased, the water droplets on the uncoated surface would move more rapidly downstream and then freeze as thin and narrow runback rivulets due to the increased aerodynamic stress acting on the rivulet flows, as observed also by Gao et al. [27]. A striking contrast is the dynamic of icing on the coated surface. Here, the formation of rivulets stopped at the beginning phase (see Figure 16f,g and Figure 17g,h), and the area downstream was free of ice. As a consequence, the impingement length of compact ice L_{ci} was reduced on an average of 4 mm with respect to the uncoated surface, as shown in Figure 18. Far from the impingement line, on the right and left sides of the test article and in the area below the impingement line, the formation of isolated, spherical, and large frozen water droplets were observed only on the coated surface (Figures 16h and 17b,f). A repeatability test performed on the coated test article confirms both the accreted ice shape (Figure 17) and the measured length of the compact ice (Figure 18). Measurements of thickness provided average values of 1.10 mm for the uncoated test, and 0.90 mm and 0.81 mm for the two coated tests.

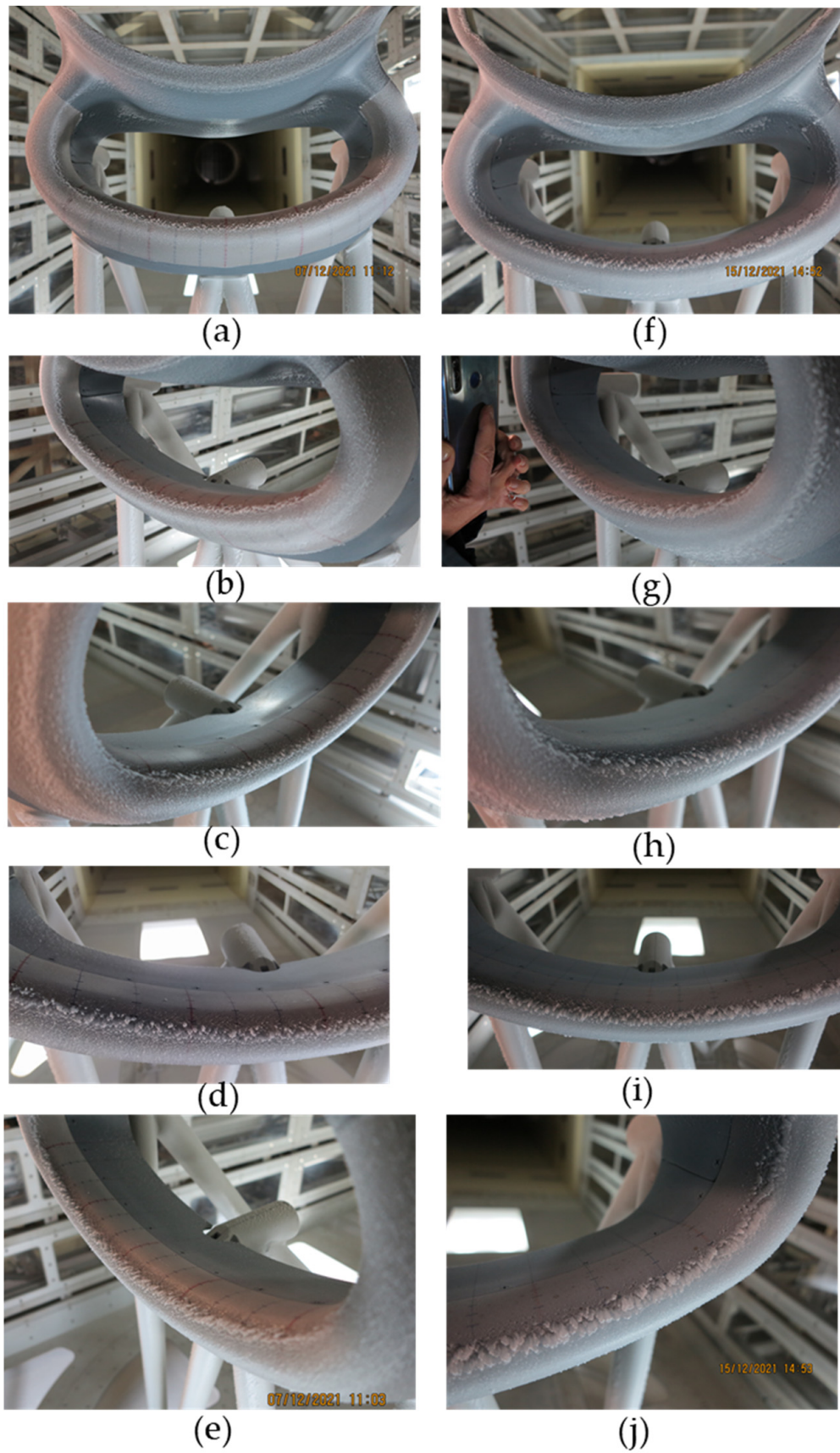


Figure 14. Results of test 7 (a–e) on uncoated test article and test 8 (f–j) on coated test article.

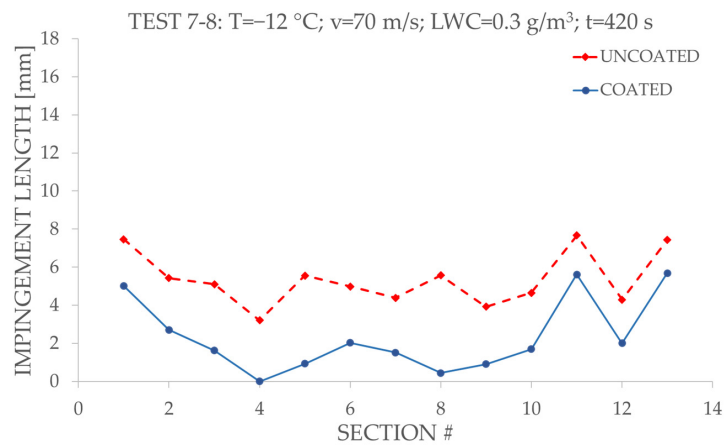


Figure 15. Impingement length measured after tests 7 and 8.

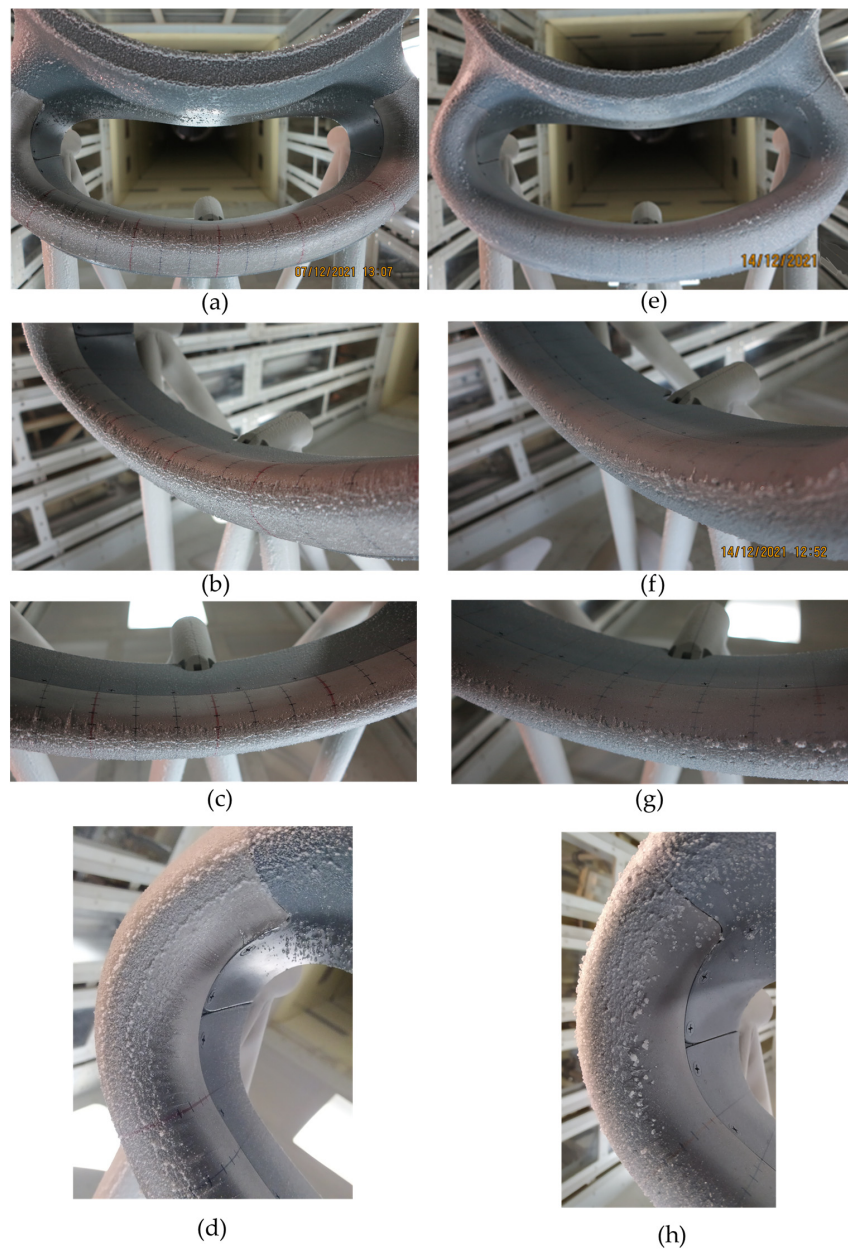


Figure 16. Results of test 9 (a–d) on uncoated test article and test 10 (e–h) on coated test article.

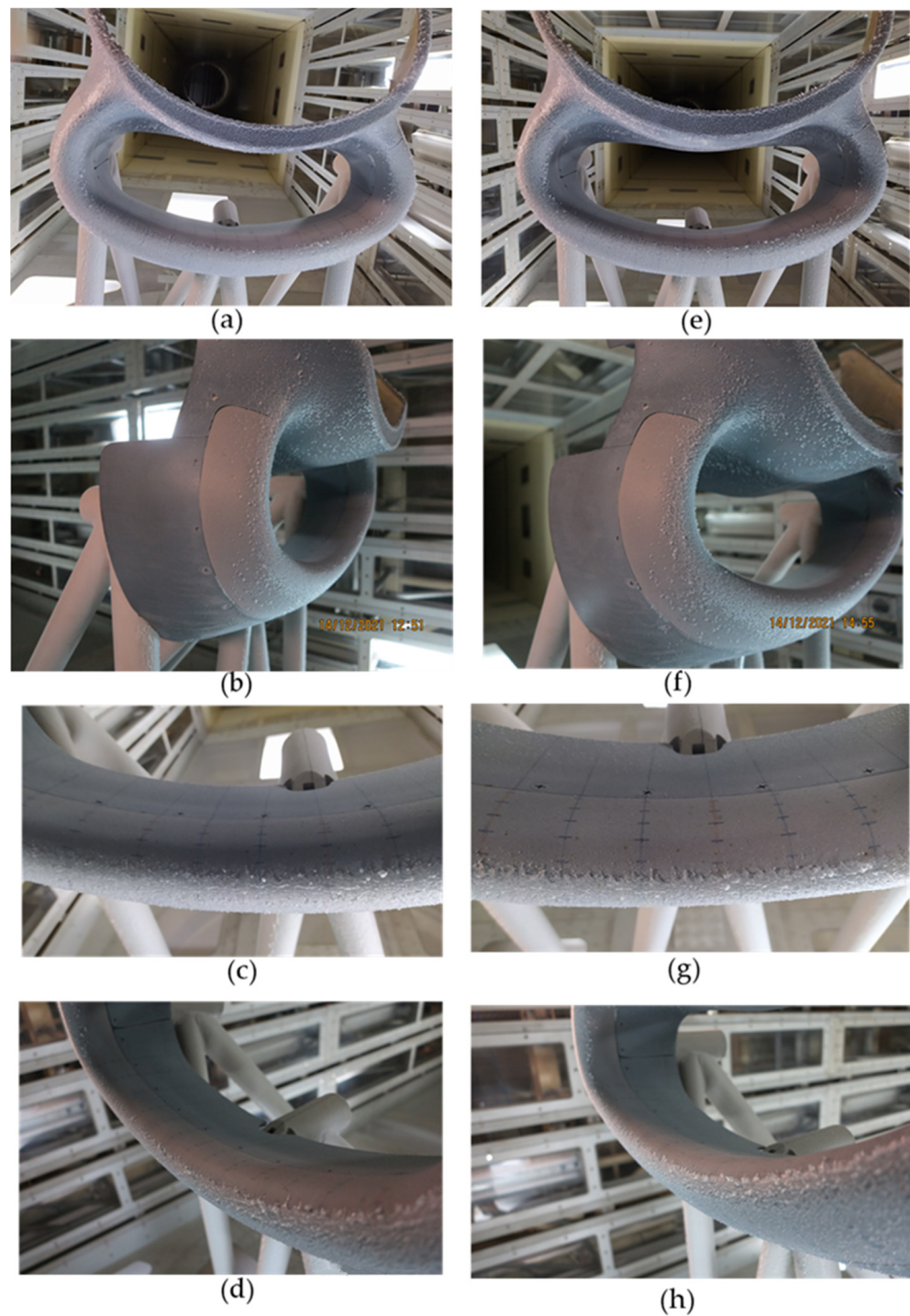


Figure 17. Repeatability test results on coated test article: test 10 (a–d) and test 11 (e–h).

3.3. Wettability after Icing/De-icing Cycles

Pictures of the test article after the IWT tests shown in Figure 19 highlight that the distribution of the SHC seems to be ununiform as after recent application, but the milky color of the coating resembles a leopard-spot distribution. However, the low wettability of all the test article surfaces was preserved since water droplets impacting it rapidly bounce and slide off (Figure 20).

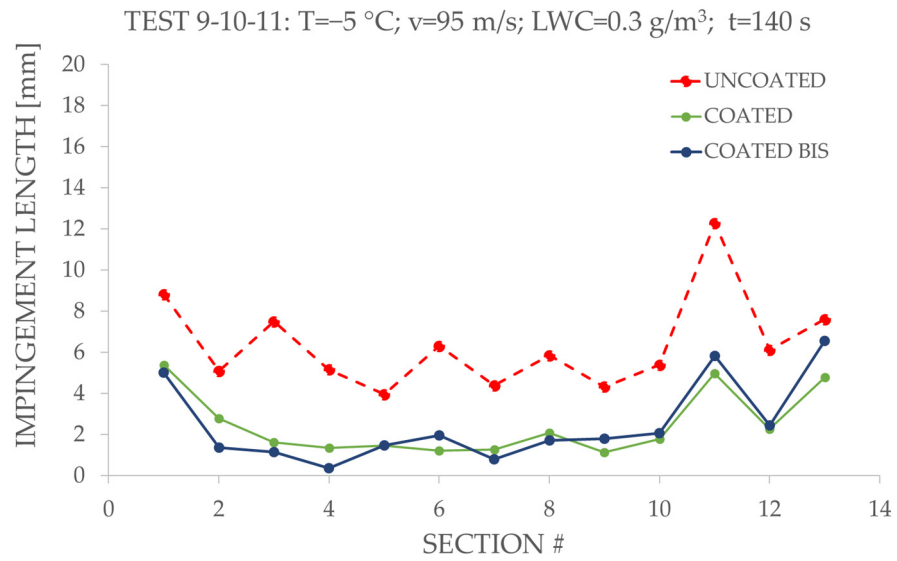


Figure 18. Impingement length measured after tests 9, 10, and 11.

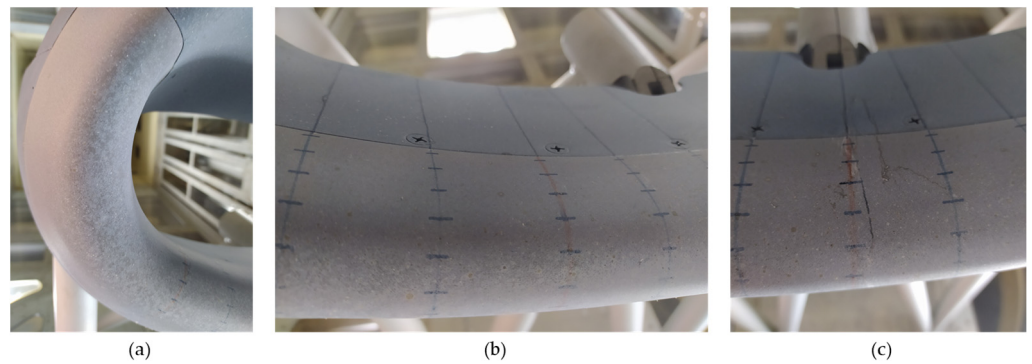


Figure 19. Images of the coated surface of the test article after IWT test campaign; left side of the test article (a); middle side of test article (b,c).

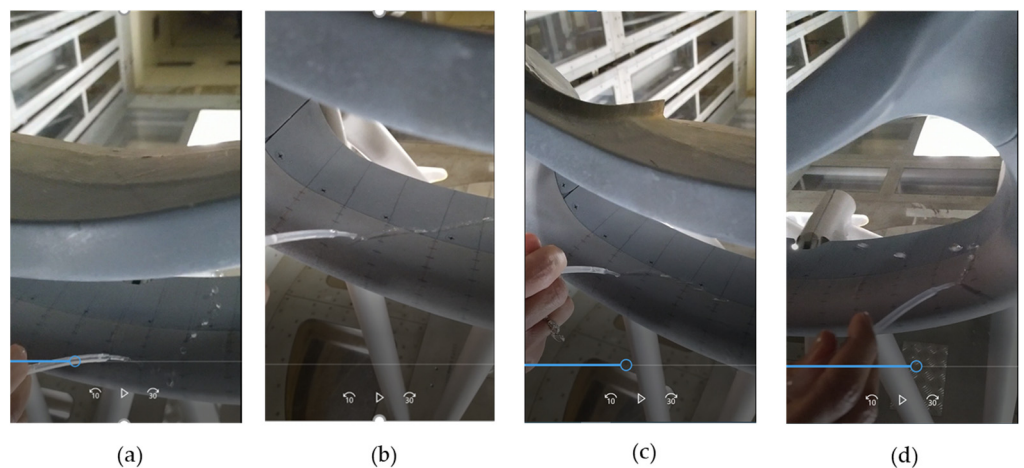


Figure 20. Wettability test performed on the test article after the IWT test campaign (a–d).

4. Discussion

Pictures of ice accreted on the uncoated and coated surfaces acquired after tests can be meaningful and useful to understand the different icing dynamics. A summary of the IWT test campaign results is shown in Figure 21.

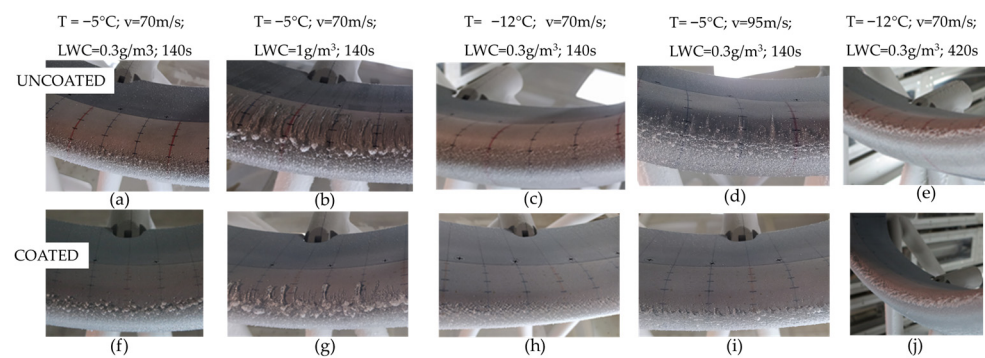


Figure 21. Summary of the IWT test campaign results found on uncoated (a–e) and coated (f–j) surfaces of the test article.

It appears that one difference raised during the IWT tests between coated and uncoated surfaces is the presence of isolated ice droplets observed especially on coated surfaces and in tests 1–2 (Figures 9, 12 and 21a,f,c,h). The presence of isolated frozen water droplets can be ascribed to the low wettability and consequently the low rolling angles [30] of coated surfaces, so the water droplets impacting the coated surface quickly bounce on it and/or slide off. Thus, depending on the test conditions, they take a longer path before freezing or not freeze at all. From a microscopic perspective, this evidence could be explained with the classical nucleation theory [31,32], according to which the larger the contact angle is, the larger the free energy barrier ΔG for the formation of ice nucleus and the smaller the nucleation rate J , so the nucleation becomes more difficult and slower. The small contact area of the applied SHC and the dynamic behavior of water droplets reduce the probability of nucleation, thus reducing the probability of ice on the surface. As a matter of fact, the isolated ice droplets observed on the coated surface are located at a bigger distance from the impingement area with respect to the uncoated one, thereby increasing de facto the transition area (see for instance Figure 9 and scheme in Figure 3c). Another remarkable finding is that the isolated ice droplets accreted on the coated surface have a spherical shape and larger dimensions than those frozen on the uncoated surface. The shape of the isolated ice droplets on the coated surface can be ascribed to the low wettability of SHC at low temperature (Figure 6), so the surface also retains the Cassie–Baxter state at low temperature, whereas the larger dimensions could be explained by imagining that the fewer water droplets frozen on the coated surface become ice nucleation points, causing the other incoming droplets to freeze on them, thus increasing their dimensions. The high-humidity environment of test conditions [33] and some surface imperfections could be the reason why there is a transition from the Cassie–Baxter to the Wenzel state with penetration and condensation into the surface cavities [33]. Therefore, these microdroplets nucleate and grow, becoming anchoring points for further incoming water droplets. The authors observed the same behavior in other previous IWT tests [11] performed on two-wing profiles NACA0015 tested at temperatures ranging between $-3\text{ }^{\circ}\text{C}$ and $-23\text{ }^{\circ}\text{C}$, speed 50 and 95 m/s, and LWC 0.3 and 0.6 g/m^3 . Here, the isolated and spherical water droplets were observed in all tests performed at temperatures higher than $-12\text{ }^{\circ}\text{C}$.

At low temperature, sparse ice droplets appear on both coated and uncoated surfaces, displaying a typical dry rime ice accretion [27]. Once again, the presence of isolated ice droplets which reduce the density of the transition area can be observed especially on the coated surface, but compared to the baseline tests at $-5\text{ }^{\circ}\text{C}$, at $-12\text{ }^{\circ}\text{C}$, this phenomenon is largely reduced and the larger isolated ice droplets are relatively absent (Figure 21a,f,c,h). This is most likely because the lower temperature allows the water droplets to freeze immediately upon impact with the surface, so their sliding off is hugely reduced. This evidence agrees with studies from Xu et al. [34], according to which the frosting time reduces as the temperature reduces.

Increase in exposure time at low temperature has the effect to increase the accumulated ice, as expected, and no differences can be observed in the shape and appearance of ice accreted on coated and uncoated surfaces (Figure 21e,j).

The major advantage in applying a SHC can be highlighted at a higher LWC and higher velocity, where the nucleation is more difficult and slower for SHC with respect to the uncoated surface [31,32]. At a higher LWC, the isolated ice droplets disappear and, in their place, several ice rivulets appear alongside the internal part of the nacelle lip (Figure 21b,g). The presence of rivulets on both uncoated and coated surfaces is due to the increased amount of impacted liquid water, which would only freeze partially, while the remaining water would coalesce into rivulets and run back over the downstream surface [27]. Figure 21b,g highlight a prominent difference in the length of rivulets frozen on coated and uncoated surfaces ascribed once again to the low wettability of the applied SHC, which allows the liquid water to slide off before freezing, thereby reducing the length of the frozen rivulets. At the impingement line, the impacting water quickly freezes, accreting as spherical-like ice regardless of the wettability of the surface. This is because at the impingement line, no helpful forces are present to take advantage from the low wettability of the SHC and allow water to slide off.

On the other hand, at a higher velocity, the high-speed water droplets colliding with the test article surface do not get enough time to freeze. Incoming airflow pushes these droplets further away from the stagnation line which leads, on the uncoated surface, to the accumulation of these droplets along upper and lower sides of the stagnation line as thin and narrow runback rivulets. In contrast to the uncoated surface, the high-speed water droplets for the coated surface slip away rapidly without freezing at all downstream the stagnation line (Figure 21d,i), and so reducing de facto the length of the accreted compact ice L_{ci} , leaving the area upper the stagnation line free of ice.

A direct comparison between the present and the previous [11] IWT test campaign can be made only between the test performed at higher velocity, namely at $-5\text{ }^{\circ}\text{C}$, $v = 95\text{ m/s}$, $\text{LWC} = 0.3\text{ g/m}^3$, and exposure time = 140 s, and the previous one carried out at $-6\text{ }^{\circ}\text{C}$, $v = 95\text{ m/s}$, $\text{LWC} = 0.3\text{ g/m}^3$, and exposure time = 137 s (test 3 in [11]). Ascribed to the different geometrical configuration of the two test articles, many differences can be observed for the ice accumulated on both the uncoated and coated surfaces of the test article. In fact, instead of thin and narrow runback rivulets, in the previous work, a typical dry rime ice accretion can be observed on the uncoated surface, with ice droplets which become less dense and isolated on the coated one. On the contrary, in the present work, the isolated frozen water droplets can be seen only at the inner left and right sides of the test article (Figure 16h).

Figure 22 displays the percentage change of the ice thickness and the impingement length calculated for each test conditions as ratios between the mean values of the differences between measurements taken on coated and uncoated configurations and the mean values of those acquired on the uncoated configuration, showing the effect of the main investigated parameters (LWC, T, exposure time and airspeed).

Results highlight a reduction in the ice thickness accreted on the coated surfaces with respect to the uncoated one across the entire spectrum of test conditions investigated. The maximum ice thickness reduction, i.e., -49% , which was recorded during the tests at $-12\text{ }^{\circ}\text{C}$, matched to an increase in the impingement length of 0.5% . Significant ice thickness and ice impingement length reductions have been recorded in the tests aimed to evaluate the airspeed and the exposure time. In particular, the application of the SHC allows the ice thickness to be reduced to values of -27% and -14% , at 95 m/s and at 420 s of exposure time, respectively. The impingement length reductions were -9.6% and -7.6% , respectively. The repeatability tests performed at higher airspeed show a good agreement between them, corroborating the overall quality of the carried-out measurements. Finally, the test aimed to assess the LWC effect presents a moderate reduction in the ice thickness, i.e., -8% , matched to an increase in the impingement length, i.e., 3.7% . Nevertheless, the

relevant finding at a higher LWC is the reduced length and number of the ice rivulets observed for the coated configuration.

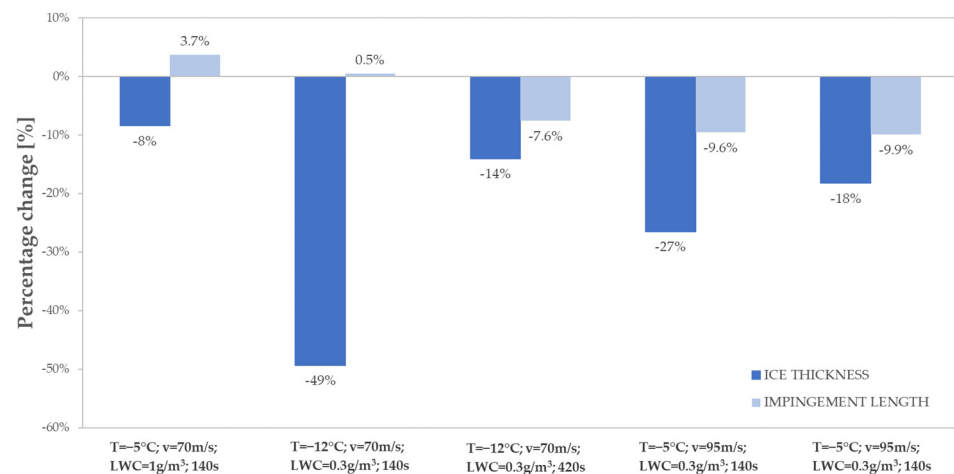


Figure 22. Percentage change of ice thickness and impingement length measured at investigated test conditions.

Ultimately, the lesson learned from the two IWT test campaigns is that the low wettability of the SHC reduces the permanence time of water droplets on surfaces and the probability of icing on the coated surfaces with respect to the uncoated ones, but the thickness and the impingement length of the accreted ice largely depend on the geometrical configuration of the test article. As a consequence, it was found that the ice thickness variations observed in the previous work [11] for tests carried out at temperatures ranging between $-3\text{ }^{\circ}\text{C}$ and $-12\text{ }^{\circ}\text{C}$ varied from -3% to -34% and from $+5\%$ to -5% for A1 and A2 coated configurations, respectively, whereas in the present work, the ice thickness reduction is more pronounced, ranging between -8% and -49% . On the other hand, the impingement length reduction with respect to the uncoated surfaces in the previous work [11] ranged between -35% and -100% for A1, and -12% and -76% for A2, which becomes less pronounced in the present work, ranging between $+3.7\%$ and -10% .

5. Conclusions

This work provides and discusses results of an icing wind tunnel (IWT) experimental campaign performed on a nacelle lip-skin belonging to the M28 Polskie Zakłady Lotnicze (PZL) vehicle. The test campaign reproduced the typical flight conditions of the M28 vehicle, which also correspond to the take-off and first climb conditions of an aircraft CS-25 class aviation. Tests were repeated after the application on the nacelle of a superhydrophobic coating (SHC), in order to study the effect of a low wettability surface on the ice accretion in real flight conditions. SHC performance seems to be encouraging across the entire spectrum of test conditions investigated. The maximum ice thickness reduction was recorded during the tests at lower temperature. Significant ice thickness and ice impingement reduction were also recorded in the tests aimed to evaluate the airspeed and the exposure time. The repeatability tests performed at higher airspeed show a good agreement between them, corroborating the overall quality of the carried-out measurements. Finally, the tests aimed to assess the LWC effect presents a moderate reduction in the ice thickness, matched to an increase in the impingement length but with a reduced length and number of the frozen rivulets.

Future works should focus to further explore the working envelope of SHC, investigating additional test conditions, particularly in terms of LWC and MVD. Future developments should also include the improvement of the measurement technique. The adopted method provided data of appropriate quality for the scope of the intended analysis. Nevertheless, for a deeper understanding of SHC behavior, it is necessary to adopt a measurement tech-

nology able to provide a more substantial amount of quantitative data. The employment of a 3D laser scanner is actually deemed as one of the best possible options. This research is especially relevant for Northern Europe, which is characterized by high humidity.

6. Patents

Data reported in this manuscript refer to coatings whose formulation is protected by the patent submission: F. Piscitelli, Italian Patent Application N. IT102021000032444, “Rivestimento superidrofobico e ghiacciofobico di un substrato, metodo per il suo ottenimento e substrato così rivestito”, 23 December 2021, and F. Piscitelli, Substrate superhydrophobic and icephobic coating, method for obtaining it and substrate thus coated, International Patent Application N° PCT/IB2022/062672 22 December 2022.

Author Contributions: Conceptualization, F.P.; methodology, F.P., S.P. and F.D.N.; investigation, F.P. and S.P.; manufacturing F.P. and F.D.N.; data curation, F.P., S.P. and F.D.N.; writing—original draft preparation, F.P.; writing—review and editing, F.P. All authors have read and agreed to the published version of the manuscript.

Funding: This research was funded by Clean Sky JTICS2- 2015-CPW02-AIR-02-07 as SAT-AM (More Affordable Small Aircraft Manufacturing) project.

Institutional Review Board Statement: Not applicable.

Informed Consent Statement: Not applicable.

Data Availability Statement: Not applicable.

Acknowledgments: The author would like to thank Antonio Chiariello for his management support, Antonio Ragni and Antonio Auletta for the interesting discussions and the IWT team for their valuable support during tests.

Conflicts of Interest: The authors declare no conflict of interest.

References

- Papadakis, M.; Breer, M.; Craig, N.; Liu, X. Experimental Water Droplet Impingement Data on Airfoils, Simulated Ice Shapes, an Engine Inlet and a Finite Wing. *NASA Contract. Rep.* **1994**, 4636–4816.
- Bidwell, C.S.; Mohler, S.R. Collection efficiency and ice accretion calculation for a sphere, a Swept MS (1)-317 Wing, a Swept NACA-0012 Wing Tip, an Axisymmetric Inlet and Boeing 737-300 Inlet. In Proceedings of the 33rd Aerospace Science Meeting and Exhibit sponsored by the AIAA, Reno, NV, USA, 9–12 January 1995; pp. 95–0755.
- Ismail, M.A.; Abdullah, M.Z. Applying Computational Fluid Dynamic to Predict the Thermal Performance of the Nacelle Anti-Icing System in Real Flight Scenarios. *Indian. J. Sci. Technol.* **2015**, *8*, 30. [CrossRef]
- Hua, J.; Liu, H.T. Fluid Flow and thermodynamic analysis of a wing anti-icing system. *Can. Aeronaut. Space J.* **2005**, *51*, 35–40. [CrossRef]
- Brown, J.M.; Raghunathan, S.; Watterson, J.K. Heat transfer correlation for anti-icing system. *J. Aircr.* **2002**, *39*, 65–70. [CrossRef]
- Raghunathan, S.; Benard, E.; Watterson, J.K.; Cooper, R.K.; Curran, R.; Price, M.; Yao, H.; Devine, R.; Crawford, B.; Riordan, D.; et al. Key aerodynamic technologies for aircraft engine nacelles. *Aeronaut. J.* **2006**, *110*, 265–288. [CrossRef]
- Brown, J.M. Investigation of Heat Transfer between a Staggered Array of Hot Air Jets and a Jet Engine Nacelle Lip Skin Surface. Ph.D. Thesis, Queens University Belfast, Belfast, UK, 1999.
- Syed, M.H.Y.; Ismail, M.A.; Azam, Q.; Rajendran, P.; Mazlan, N.M. Simulation Study of the Effect of Anti-Icing on the Nacelle Lip-skin Material IOP Conf. Ser. *Mater. Sci. Eng.* **2018**, *370*, 012011.
- Yang, Q.; Guo, X.; Dong, W.; Wang, A. Ice accretion and aerodynamic effects on a turbofan engine nacelle under takeoff conditions. *Aerosp. Sci. Technol.* **2022**, *126*, 107571–107584. [CrossRef]
- FA Regulation. *Airworthiness Standard: Transport Category Airplanes Part 25 Appendix C*; Federal Aviation Administration, Atlantic City International Airport: Atlantic City, NJ, USA, 1982.
- Piscitelli, F. Characterization in Relevant Icing Conditions of Two Superhydrophobic Coatings. *Appl. Sci.* **2022**, *12*, 3705. [CrossRef]
- Khai, L.C.; Ismail, M.A.; Azam, Q.; Mazlan, N.M. Experimental study on aerodynamic performance of nacelle lip-skin bias flow. *J. Mech. Sci. Technol.* **2020**, *34*, 1613–1621. [CrossRef]
- Hamid, H.A.; Yong, W.K.; Yusoff, H.; Ismail, M.A. CFD Impingement Flow Study on Temperature Profile of Concave Plate. *J. Adv. Res. Fluid. Mech.* **2022**, *95*, 1–16.
- Özgen, S.; Canibek, M. In-flight ice formation simulation on finite wings and air intakes. *Aeronaut. J.* **2012**, *116*, 337–362. [CrossRef]
- Papadakis, M.; Yeong, H.W.; Wong, S.C.; Wong, S.H. Comparison of experimental and computational ice shapes for an engine inlet. In Proceedings of the AIAA Atmospheric and Space Environments Conference, Toronto, ON, Canada, 2–5 August 2010.

16. Tian, L.; Li, L.; Hu, H.; Hu, H. Experimental Study of Dynamic Ice Accretion Process over Rotating Aeroengine Fan Blades. *J. Thermophys. Heat Trans.* **2022**, *37*, 353–364. [CrossRef]
17. Li, L.; Liu, Y.; Tian, L.; Hu, H.; Hu, H.; Liu, X.; Hogate, I.; Kohli, A. An experimental study on a hot-air-based anti-/de-icing system for aeroengine inlet guide vanes. *Appl. Therm. Eng.* **2020**, *167*, 114778–114790. [CrossRef]
18. Tian, L.; Liu, Y.; Li, L.; Hu, H. *An Experimental Study to Evaluate Hydro-/Ice-Phobic Coatings for Icing Mitigation over Rotating Aero-engine Fan Blades*; SAE Technical Paper; SAE International: Warrendale, PA, USA, 2019.
19. Piscitelli, F. Rivestimento Superidrofobico e Ghiacciofobico di un Substrato, Metodo per il suo Ottenimento e Substrato Così Rivestito. Italian Patent Application N. IT102021000032444, 23 December 2021.
20. Piscitelli, F. Substrate Superhydrophobic and Icephobic Coating, Method for Obtaining it and Substrate thus Coated. International Patent Application N° PCT/IB2022/062672, 22 December 2022.
21. ISO 4288; Geometrical Product Specifications (GPS)—Surface Texture: Profile Method—Rules and Procedures for the Assessment of Surface Texture. International Organization for Standardization: Geneva, Switzerland, 1996.
22. D7490-13; Standard Test Method for Measurement of the Surface Tension of Solid Coatings, Substrates and Pigments using Contact Angle Measurements. American Society for Testing and Materials: West Conshohocken, PA, USA, 2013.
23. ISO 2360:2017; Non-Conductive Coatings on Non-Magnetic Electrically Conductive Base Metals—Measurement of Coating Thickness—Amplitude-Sensitive Eddy-Current Method. International Organization for Standardization: Geneva, Switzerland, 2003.
24. Piscitelli, F.; Chiariello, A.; Dabkowski, D.; Corrado, G.; Marra, F.; Di Palma, L. Superhydrophobic Coatings as Anti-Icing Systems for Small Aircraft. *Aerospace* **2020**, *7*, 2. [CrossRef]
25. Piscitelli, F.; Tescione, F.; Mazzola, L.; Bruno, G.; Lavorgna, M. On a simplified method to produce hydrophobic coatings for aeronautical applications. *Appl. Surf. Sci.* **2019**, *472*, 71–81. [CrossRef]
26. Przybyszewski, B.; Kozera, R.; Krawczyk, Z.D.; Boczkowska, A.; Dolatabadi, A.; Amer, A.; Sztorch, B.; Przekop, R.E. A Wind Tunnel Experimental Study of Icing on NACA0012 Aircraft Airfoil with Silicon Compounds Modified Polyurethane Coatings. *Materials* **2021**, *14*, 5687. [CrossRef]
27. Gao, L.; Liu, Y.; Hu, H. An experimental investigation of dynamic ice accretion process on a wind turbine airfoil model considering various icing conditions. *Int. J. Heat. Mass. Transf.* **2019**, *133*, 930–939. [CrossRef]
28. Jin, J.Y.; Virk, M.S. Study of ice accretion and icing effects on aerodynamic characteristics of DU96 wind turbine blade profile. *Cold Reg. Sci. Technol.* **2019**, *160*, 119–127. [CrossRef]
29. Özgen, S.; Canıbek, M. Ice accretion simulation on multi-element airfoils using extended messinger model. *Heat. Mass. Transf.* **2009**, *45*, 305–322. [CrossRef]
30. Li, W.; Zhan, Y.; Yu, S. Applications of superhydrophobic coatings in anti-icing: Theory, mechanisms, impact factors, challenges and perspectives. *Prog. Org. Coat.* **2021**, *152*, 106117–106135. [CrossRef]
31. Varanasi, K.K.; Hsu, M.; Bhate, N.; Yang, W.; Deng, T. Spatial control in the heterogeneous nucleation of water. *Appl. Phys. Lett.* **2009**, *95*, 094101. [CrossRef]
32. Varanasi, K.K.; Deng, T.; Smith, J.D.; Hsu, M.; Bhate, N. Frost formation and ice adhesion on superhydrophobic surfaces. *Appl. Phys. Lett.* **2010**, *97*, 234102. [CrossRef]
33. Yin, L.; Zhu, L.; Wang, Q.; Ding, J.; Chen, Q. Superhydrophobicity of natural and artificial surfaces under controlled condensation conditions. *ACS Appl. Mater. Interfaces* **2011**, *3*, 1254–1260. [CrossRef] [PubMed]
34. Xu, W.J.; Song, J.L.; Sun, J.; Dou, Q.L. Characteristics of ice and frost formation on superhydrophobic surfaces on aluminum substrates. *J. Refrig.* **2011**, *32*, 9–13.

Disclaimer/Publisher’s Note: The statements, opinions and data contained in all publications are solely those of the individual author(s) and contributor(s) and not of MDPI and/or the editor(s). MDPI and/or the editor(s) disclaim responsibility for any injury to people or property resulting from any ideas, methods, instructions or products referred to in the content.

Review

Superhydrophobic Coating Solutions for Deicing Control in Aircraft

Michele Ferrari *  and Francesca Cirisano 

CNR-ICMATE National Research Council, Institute of Condensed Matter Chemistry and Technologies for Energy, Via De Marini, 6, 16149 Genova, Italy; francesca.cirisano@ge.icmate.cnr.it

* Correspondence: michele.ferrari@ge.icmate.cnr.it; Tel.: +39-0106475723; Fax: +39-0106475700

Abstract: The risk of accidents caused by ice adhesion on critical aircraft surfaces is a significant concern. To combat this, active ice protection systems (AIPS) are installed on aircraft, which, while effective, also increase fuel consumption and add complexity to the aircraft systems. Replacing AIPS with Passive Ice Protection Systems (PIPS) or reducing the energy consumption of AIPS could significantly decrease aircraft fuel consumption. Superhydrophobic (SH) coatings have been developed to reduce water adherence to surfaces and have the potential to reduce ice adhesion, commonly referred to as icephobic coatings. The question remains whether such coatings could reduce the cost associated with AIPS and provide durability and performance through suitable tests. In this paper, we then review current knowledge of superhydrophobic and icephobic coatings as potential passive solutions to be utilized alternatively in combination with active systems. We can identify physical parameters, coating composition, structure, roughness, and morphology, durability as properties not to be neglected in the design and development of reliable protection systems in aircraft maintenance.

Keywords: superhydrophobic; icephobic; active ice protection systems (AIPS); passive ice protection systems (PIPS)



Citation: Ferrari, M.; Cirisano, F. Superhydrophobic Coating Solutions for Deicing Control in Aircraft. *Appl. Sci.* **2023**, *13*, 11684. <https://doi.org/10.3390/app132111684>

Academic Editor: Filomena Piscitelli

Received: 25 September 2023

Revised: 18 October 2023

Accepted: 23 October 2023

Published: 25 October 2023



Copyright: © 2023 by the authors. Licensee MDPI, Basel, Switzerland. This article is an open access article distributed under the terms and conditions of the Creative Commons Attribution (CC BY) license (<https://creativecommons.org/licenses/by/4.0/>).

1. Introduction

The term deicing involves actions and procedures aimed to remove or clear ice after formation on critical structures in the environment, while anti-icing systems are instead intended to prevent ice growth and deposition. The aviation industry is strongly affected by this phenomenon reflected in both technological and safety issues.

Before aircraft take off, ice formation prevention procedures usually imply that anti and deicing fluids are commonly administered, even if their effectiveness diminishes rapidly as the aircraft accelerates [1] in addition to releasing harmful fluid components to the environment while, during flight, aircraft can employ heaters and inflatable guards to shield against ice.

Physical parameters like wettability, temperature or pressure describe the direct response of materials to environmental conditions.

The development of an anti-icing surface on a specific industrial coating patch or object has posed a persistent challenge for various industries, including aviation and wind power. To address this challenge, it is essential to perform surface modifications to incorporate the icephobic property into existing commercial coatings for practical applications.

Additionally, permanent hydrophobic coatings can decrease the ability of water to adhere to the aluminum surface, preventing freezing. However, it has been demonstrated in [2] that these coatings can also compromise the effectiveness of anti-icing fluids. According to a recent examination carried out by scientists from Canada, there is a possibility that the application of anti-icing fluid alongside hydrophobic coatings may hinder the formation of a protective film. Researchers at Skoltech [3] also conducted experiments to

assess the ability of aluminum surfaces used in aircraft skins to repel water and ascertain whether this has any impact on the effectiveness of these fluids.

Nevertheless, we can regard SH or icephobic coatings (PIPS) as an adjuvant in the inhibition of ice formation during the take-off, in fact eliminating or strongly reducing the use of fluids or chemicals which, in turn, could result as harmful to the environment.

The endurance of three distinct fluid types, all of which met the rigorous aerospace standards of SAE AMS1424 or AMS1428, was examined. These fluid types exhibited varying durations of endurance. To prepare for testing, aluminum plates underwent a process of sanding, polishing, and coating with a hydrophilic acrylic varnish, which yielded a transparent finish that could be either glossy or matte.

The results of the Canadian team's study differ from those of the researchers, as they found that the wetting ability of plates did not affect the effectiveness of anti-icing fluids. However, the researchers attribute this divergence to the surface tension and viscosity of the fluids. Additionally, the researchers acknowledged that surface roughness (S_a) may be a factor, as it takes longer for ice to accumulate on rough surfaces.

Also, temperature and pressure have been demonstrated to affect the shape of the supercooled water on the new icephobic coating. Mechanical tests like cutting, tape tests, pull-off tests and nanoindentation were carried out in [4] to assess the high durability of the icephobic coating. To claim that an icephobic surface is suitable for aeronautical application, it should be tested under flight conditions. This test is possible in an icing wind tunnel (IWT) that can mimic the icing or frosting process in the natural environment by spraying supercooled water droplets onto the substrates. Unfortunately, this facility is rather rare due to the high cost of the setup.

In [5] the effects on roughness at the micro/nanoscale by the pressure have been evidenced due to the impinging of supercooled water droplets, in fact, the pressures at water droplet impact can reach up to 10^5 Pa with the strong mechanical wearing of the coating during its application. Moreover, the Cassie–Baxter state is a condition to be maintained to keep the icephobic properties through the Euler stability of the roughness, the surface asperities resistance to buckling upon water drop impacts.

The huge work on structures and morphology including roughness on hierarchical scales is probably the most innovative approach in this field, considering the high level of manipulation at the micro-nano scale available.

In the last 20 years high water-repellent surfaces have attracted the scientific community due to their wide potential applications in various research and technological fields [6,7] (Figure 1). Lotus-leaf-inspired superhydrophobic surfaces (SHS) and Pitcher-plant-inspired slippery liquid-infused porous surfaces (SLIPS) are compared in this review work [8] providing the state-of-the-art bio-inspired icephobic coatings/surfaces aimed at aircraft icing mitigation Experiments [9] were carried out at Icing Research Tunnel of Iowa State University (i.e., ISU-IRT) facility aiming to evaluate SHS and SLIPS coatings effectiveness in decreasing or eliminating ice accretion and its impact over the surfaces of typical airfoil/wing models. Ice accretion was found to be hindered by both SHS and SLIPS where strong aerodynamic forces were present, while where these forces found a minimum like close to the airfoil stagnation line, ice formation was still found.

This method for preventing ice buildup on aerodynamic surfaces and wings has been successfully demonstrated by combining icephobes with reduced surface heating in the leading edge vicinity. This experimental study assessed the durability of icicle coatings when exposed to rainfall, and the potential applications for preventing aircraft icing. Additionally, it was re-evaluated the impact of ice on erosion and its associated consequences by analyzing variations in ice adhesion forces and surface morphology of eroded surfaces coated with SHS and SLIPS. The findings of this research provide valuable insight into the fundamental physics behind developing anti-/deicing strategies and robust solutions for mitigating aircraft icing.

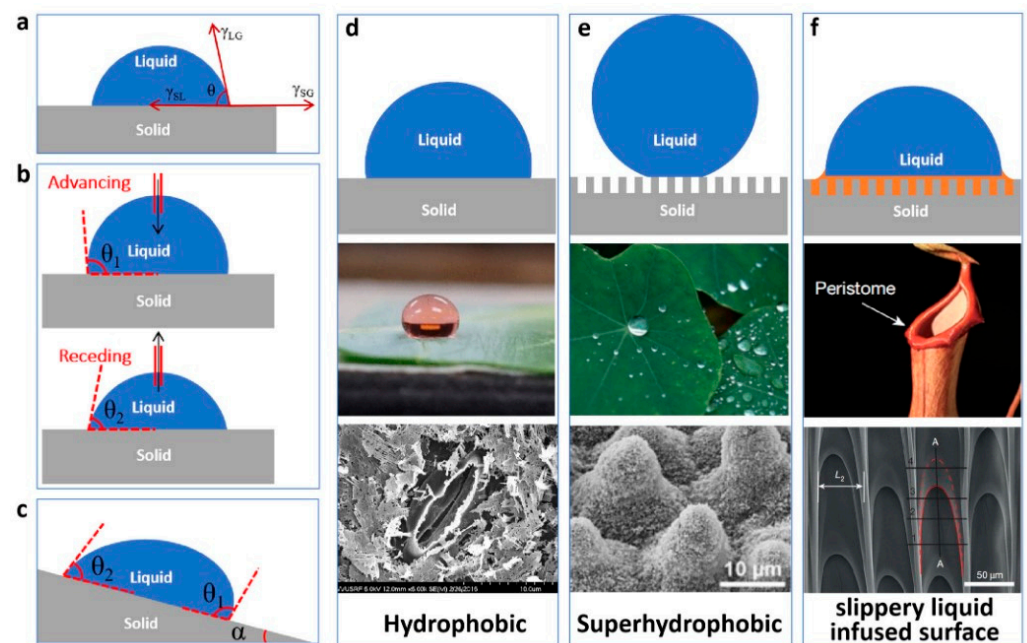


Figure 1. (a) Schematic diagram of contact angle and Young's equation. (b) Schematic diagram of dynamic contact angle measurement. (c) Schematic diagram of rolling angle measurement. (d) Hydrophobic model and its prototype in nature and electron micrograph. (e) Superhydrophobic model and its prototype in nature and electron micrograph. (f) Slipperyliquid-infused porous surfaces (SLIPS) model and its prototype in nature and electron micrograph. Reprinted with permission under the terms of the Creative Commons CC BY license from Li, Z.; Wang, X.; Bai, H.; Cao, M. *Advances in Bioinspired Superhydrophobic Surfaces Made from Silicones: Fabrication and Application*. *Polymers* 2023, 15, 543. <https://doi.org/10.3390/polym15030543> [10].

Nevertheless, the impact of surface coatings on the performances and behavior of the fluids should be thoroughly tested before their use in the industry. Once introduced, new materials for coatings developed for passive ice protection systems undergo for testing with deicing fluids in facilities like the Anti-icing Materials International Laboratory (AMIL) where, more than 30 years, interactions with the ground deicing/anti-icing fluids have been tested before approval for aeronautic application. In this work, current test methods, like the Water Spray Endurance Test (WSET) and Aerodynamic Acceptance Test (AAT), have been carried out on different, commercial and not commercial, surface coatings, with ground deicing/anti-icing fluids: The application of the coating resulted in a decreased spreading, wetting and the endurance time of the commercial fluids. Moreover, the superhydrophobic coating could also avoid aerodynamic drawbacks coming with the reference fluid [2]. The conclusions and methodology of this study were used in the development of sections of the SAE AIR6232 (Society of Automotive Engineers, Aerospace Information Report n°6232) Aircraft Surface Coating Interaction with the Aircraft Deicing/Anti-Icing Fluids standard.

Coating composition is related to its chemistry, to low energy materials, but also aimed to avoid the constraints given by environmental issues, raised by the dispersion of solids and fluids in the air and ground, hardly recoverable and unpredictable long-term accumulation effects.

Among new materials, the ice-repelling properties of superhydrophobic silicone rubber nanocomposite surfaces were created in [11] through either spin coating or spray-coating methods and examined through contact angle hysteresis (CAH), surface roughness, and icing conditions. Both the spin and spray-coated samples displayed a high contact angle (CA) ($>150^\circ$), a low contact angle hysteresis ($<6^\circ$), and a roll-off property. While the spin-coated sample had a significantly reduced ice adhesion strength, the ice adhesion strength on the spray-coated sample was surprisingly similar to that of the uncoated sample. This study highlights that a surface's icephobic properties may not directly correspond

to its superhydrophobicity, and further investigations, such as considering the effects of icing conditions, are necessary. Additionally, the ice-repelling behavior of the spray-coated sample was found to improve at lower levels of liquid water content (LWC) and under icing conditions characterized by smaller water droplet size.

The role of surface topology on superhydrophobic/icephobic properties has been also investigated by the authors in [12] where, despite high water-repellence with low heat transfer in superhydrophobic surfaces having been widely found for anti-icing purposes, at low temperatures, condensation phenomena occur with the result of more ice adhesion by wetting of the micro- and nanostructures. To address this issue, researchers have developed five different superhydrophobic coatings at the microscale by adjusting the weight ratio of surface-modified nanoparticles to unmodified ones. The strength of ice adhesion and the temperature at which ice nucleation occurs were examined, along with the impact of moisture condensation on ice adhesion. The mechanism and condition of ice strength and formation do not seem to be related to merely morphological aspects of the coating, evidencing the key but not unique role of the roughness in determining the surface features. The results address a more careful surface design underlying the top superhydrophobic coating.

Various studies [13–15] have designed strategies to create an anti-icing surface for specific industrial coating patches or objects carrying out surface modifications with the icephobic characteristic embedded into currently existing commercial coatings for real-world uses. The wide use of polyurethane-based products in the paint and coating industry suggested by a study [16] about the icephobicity of a micron-scaled hydrophobic heterogeneous treatment on Polyurethane Aerospace Coating, an icephobic coating (PPG Industries), evidencing the role of coating in postponing the formation of frost while reducing ice adhesion strength. A copolymer composed of hard and soft sections, poly(methyl methacrylate) and poly(lauryl methacrylate-2-hydroxy-3-(1-amino dodecyl)propyl methacrylate), respectively, a hydrophobic heterogeneity was obtained at the micron-scale at segregation level, resulting in the maintenance of the icephobic properties. The presence of distinct segments with opposite features provides a particular characteristic appearing in a wrinkled design of the coated layer (Figure 2).

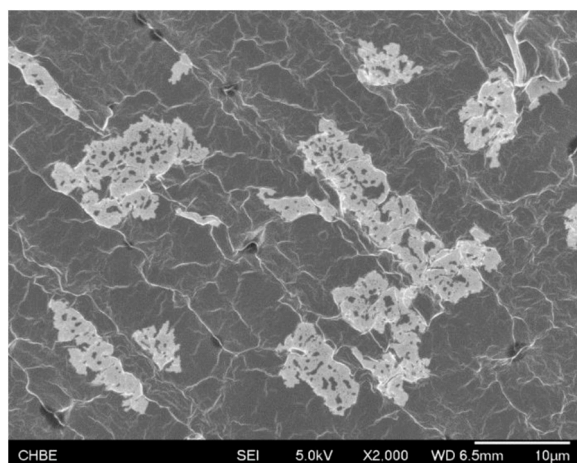


Figure 2. Scanning electron micrograph of the hydrophobic coating showing soft micro-domains embedded on the wrinkled surface. Adapted with permission from Formation of Icephobic Surface with Micron-Scaled Hydrophobic Heterogeneity on Polyurethane Aerospace Coating, Yeap-Hung Ng, Siok-Wei Tay, and Liang Hong, ACS Applied Materials & Interfaces 2018 10 (43), 37517–37528, DOI: 10.1021/acsami.8b13403. Copyright 2018 American Chemical Society [16].

The integration of icephobic solutions with active systems and their testing represents the transition period in which newly achieved coating systems begin to couple existing efficient, but energy-consuming devices.

The effectiveness of a series of coatings composed of amphiphilic silicone polyurethane (AmSiPU) was tested for its anti-icing capabilities [17,18]. While these types of coatings have been previously researched for their antifouling potential, their use for anti-icing purposes remains relatively unexplored. A range of amphiphilic polyurethane-based coatings were produced, containing both hydrophilic polyethylene glycol (PEG) and hydrophobic polydimethylsiloxane (PDMS) with variations in both molecular weight and composition. The surface of these coatings was analyzed, revealing the presence of both PDMS and PEG moieties and confirming their amphiphilic properties. The coatings were then tested for their ability to prevent ice adhesion, with particular attention given to the relationship between their anti-icing performance and water absorption and barrier properties.

The role of innovation aimed to limit accidents caused by ice adhesion on aircraft surfaces poses a significant weight, highlighting the need for AIPS on board. Nevertheless, the downside of AIPS is its added complexity and increased fuel consumption. A potential solution to this is to use PIPS or seek ways to decrease the energy consumption of the AIPS. Superhydrophobic coatings are one such innovative development that could help reduce water adherence on surfaces and subsequently, fuel consumption. The cost associated with AIPS could potentially be decreased by utilizing superhydrophobic or icephobic coatings. Such coatings can effectively decrease ice adhesion and are thus commonly used. The question remains whether these coatings will prove to be a solution for the cost issue at hand.

In these commentaries [19], the author makes a wide comparison among different ways to face ice adhesion-related problems and solutions. Superhydrophobic and icephobic coatings are currently being studied to determine their level of hydrophobicity. Various methods are being developed to adapt existing experimental data to be applied to aircraft. However, it is important to consider the durability of these coatings and, even though some of them have the potential to reduce AIPS power consumption, many do not possess adequate erosion resistance for practical use. To aid manufacturers, guidelines for aircraft erosion tests have been devised. Using superhydrophobic coatings, the extent to which AIPS power consumption can be reduced is dependent on the level of hydrophobicity utilized. Developing coatings that can resist erosion is the primary obstacle faced by manufacturers and designers and the demand for coatings that are superhydrophobic and icephobic arises from this need.

Critical components like leading edges, slats, or vertical tails are strongly affected by ice formation decreasing flight reliability and safety. This work [5] mainly proposed two aims focused on coating design with icephobic properties and, on the other side, developing an innovative tool for wettability assessment. While in the first case, the study addresses coating multifunctional properties including livery effect and resistance to adhesion and abrasion, in the second one the authors attempt to reproduce the thermodynamic conditions like pressure and temperature present at flight altitudes.

In these papers [20,21], the authors evaluated the performance of SHS in preventing ice formation as a function of their durability in terms of erosion coupled with active deicers (Figure 3).

Coupling icephobic coating with electromechanical deicers is one solution for facing ice growth on the surfaces of aircraft with long-recognized issues concerning the security, effectiveness and operational costs. Current dynamic ant-ice strategies, such as electromechanical de-icers, are regularly based on dissolving or breaking ice layers despite these dynamic approaches requiring significant energy for their operation. As passive solutions, SHS can show icephobic properties preventing ice accretion, and, even if their prevention is not completely found, they can be the basis for designing hybrid systems efficient in lowering energy demand for active electromechanical deicers.

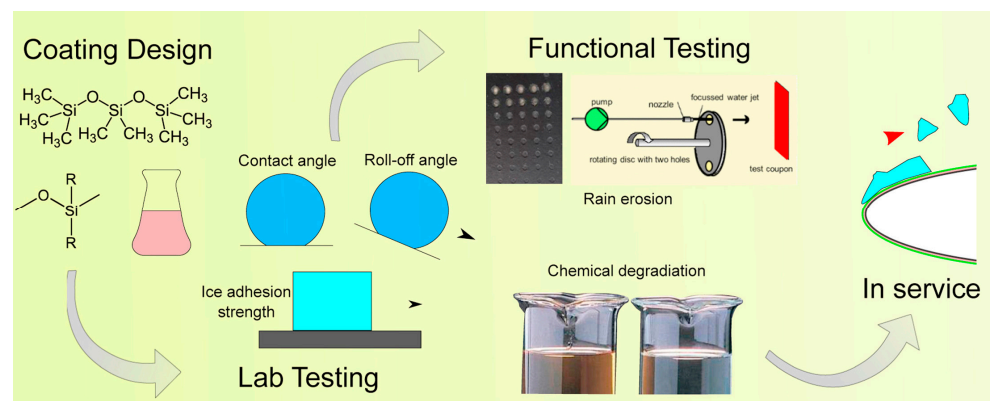


Figure 3. From synthesis to tests, a passive icephobic solution design path to hybrid systems. Reprinted from Progress in Aerospace Sciences, 105, Huang, X.; Tepylo, N.; Pommier-Budinger, V.; Budinger, M.; Bonaccorso, E.; Villedieu, P.; Bennani, L, A survey of icephobic coatings and their potential use in a hybrid coating/active ice protection system for aerospace applications, 74–97, Copyright (2019), with permission from Elsevier [21].

2. Superhydrophobic Surface with Icephobic Behaviour for General Purpose

In recent years, the research on the prevention of ice and frost has significantly grown since this problem affects numerous fields. Superhydrophobic surfaces, due to their low water wettability, are regarded as the most promising materials with anti-icing properties. As we shall see, this statement is partly erroneous because much depends on the actual conditions under which the coating will be exercised (aerospace, marine environment, energy systems). Much research that tries to find a solution to this problem provides results that need to be investigated through specific tests for the different industrial applications.

Chen et al. [22] prepared a macroscopic Al honeycomb structure by electrospray on an SHS with high mechanical strength and anti-icing behaviors. The coating on the honeycomb structure has $CA = 161.1$ and roll of angle (RoA) = 5.6° . The particular honeycomb structure combined with the low wettability can explain the results from the icing test, in fact, it was observed that at different temperatures below 0°C the complete freezing time increased for SHS and was better for the honeycomb structure. Also, the frost formation on the sample surface tilted at 60° and at $T = -20^\circ\text{C}$ was less on the SH honeycomb surface both compared to the sample taken as a reference and especially compared to the superhydrophobic on a smooth surface.

Another example is the work of Yu et al. [23] in which the authors affirm preparing an SHS with icephobic behavior. The titanium SHS was prepared via chemical immersion in copper solution and a successively annealing after that the surface showed a CA of about 158° . Icephobicity was tested just by observing the behavior of the water droplet on SH and reference surfaces cooled at -16°C or observing ice melting on the two surfaces. The authors observed that on SHS, water needs more time to freeze compared to reference and ice, once melted, formed a spherical water droplet able to roll off the surface (Figure 4).

Cheng et al. [24] reported the creation of a superhydrophobic surface with ultra-low ice adhesion without a specific application. For this reason, in this paper, the anti-icing tests did not follow standard protocol. The authors prepared an SHS based on a sprayed PDMS microsphere and OTS@SiO_2 np (OTS is octadecyl trichloro silane), on fluorocarbon resin (PDMS/SiO_2 based surface). SHS show $CA = 171^\circ$ and $Sa = 0.277\ \mu\text{m}$. The Sa was ten times lower with respect to the PDMS coating and in the same order of magnitude coating with only OTS@SiO_2 . From static and dynamic anti-icing tests with the surface at -10°C , it was observed that the PDMS/SiO_2 -based surface had good anti-icing ability as it was able to prolong the freezing time probably due to a greater CAH (not reported). Ice adhesion was further evaluated by freezing an ice block on the different surfaces and measuring the shear force to detach ice. The test produced a result in line with previous observations confirming

the anti-ice behavior of the prepared SHS. Also, the surface maintains its wettability after 100 mechanical abrasion cycles.

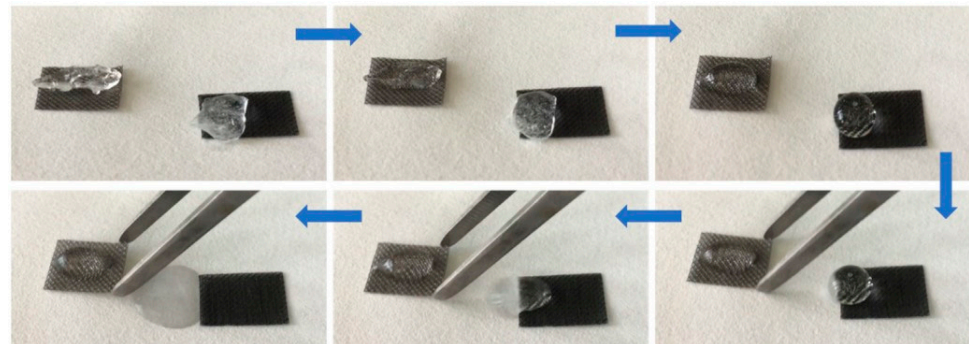


Figure 4. Successive snapshots of ice melting process for adhesion test, the original Ti mesh is on the left and the SSTM is on the right. Reprinted from Applied Surface Science, 476, T. Yu, S. Lu, W. Xu, R. Boukherroub, Preparation of superhydrophobic/superoleophilic copper coated titanium mesh with excellent ice-phobic and water-oil separation performance, 353–362, Copyright (2019), with permission from Elsevier [23].

These are just a few examples where we can see how surfaces are deemed icephobic but in a general context. In addition, the used tests to assess it are nonspecific and, in some cases, exclusively qualitative rather than quantitative.

In the next sections studies on coatings at different degrees of hydrophobicity will be reviewed also according to the test procedures they underwent including the use and the impact of deicing fluids on the stability and durability of their icephobic performances.

3. Superhydrophobic Surface with Icephobic Behaviour for Aircraft Applications

3.1. SHS Not Tested in Flight Conditions

In the literature, some papers aimed to explore the application of superhydrophobic coating in aeronautical fields conducting resistance and anti-icing tests in non-standard conditions. These works could be considered as preliminary and some of them, are indeed a first step of works that applied more stringent and adherence tests to what are the real conditions of use.

Piscitelli et al. presented two works [25,26] in which an SH coating was characterized on a lab scale. The SHS, in both papers, was prepared following the procedure in [27] and the SH coating was applied on different aeronautical substrates, in terms of material and roughness, and the icephobicity was tested by observing the shape of water-frozen droplets ($-27\text{ }^{\circ}\text{C}$) (Figure 5) and then the surface wettability. Cutting and tape tests according to ASTM procedure were performed to evaluate mechanical abrasion resistance. Furthermore, the work of adhesion and surface free energy of the prepared surface was calculated and correlated with sample surface roughness. The authors observed that the SH treatment was necessary to reach high CA and the roughness, regardless of the material, decreased after surface modification, and different roughness can allow the same CA. The works conclude by stating that prepared surfaces can reduce the contact area between ice and substrate and that adhesion work, obtained from surface free energy value, was reduced by more than 80%.

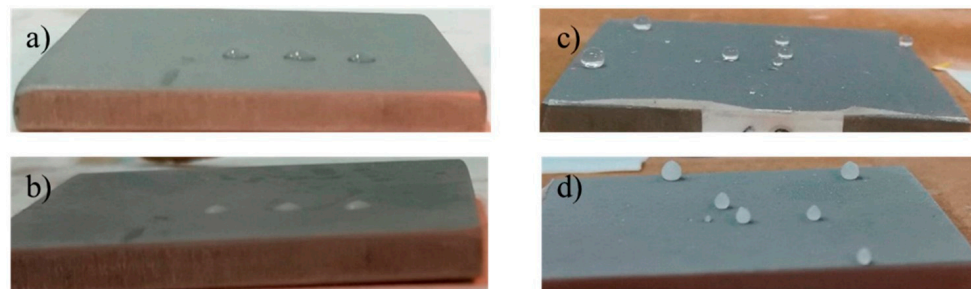


Figure 5. Pictures of samples acquired at $-27\text{ }^{\circ}\text{C}$. Reference with water droplets before (a) and after (b) the icing at $-27\text{ }^{\circ}\text{C}$; coated sample with water droplets before (c) and after (d) the icing at $-27\text{ }^{\circ}\text{C}$. Reprinted with permission under the terms of the Creative Commons CC BY license from F. Piscitelli, A. Chiariello, D. Dabkowski, G. Corrado, F. Marra, L. Di Palma, Superhydrophobic coatings as anti-icing systems for small aircraft, *Aerospace*. 7 (2020) [26].

Liu et al. [28] developed and tested different PDMS-based icephobic coatings for aircraft applications. In this study PDMS coating was fluorinated (F/PDMS) to increase the wettability ($\text{CA} = 124^{\circ}$) and, to enhance the CA up to 157° , fumed silica was added (F-PDMS/silica). An initial test used to study icephobicity was to deposit a water drop on a surface at a temperature of $-10\text{ }^{\circ}\text{C}$, from this test it was observed that the greater the CA, the smaller the contact area between ice and surface. On the other hand, a lower value was observed for the hydrophobic sample. This result was justified by the different roughness between the samples, SH F-PDMS/silica surface showed an average surface roughness of $7.3\text{ }\mu\text{m}$ while hydrophobic F-PDMS $1.6\text{ }\mu\text{m}$, with high values meaning high interlocking of the ice within the surface. To investigate operating conditions similar to those of a future application, wettability measurements were performed at a pressure of 0.5 bar and temperature of $-12\text{ }^{\circ}\text{C}$. In such conditions, the CA of the SHS decreases to 104° (reduction of air pockets). From these works, it can be observed that, although the purpose of use of the investigated surfaces is for aeronautical applications, the conducted tests do not follow standard specifications and are rather subjective. Comparing these works, it is also observed that surface roughness at macroscopic magnitudes is important to define ice adhesion but is not sufficient to define a surface as icephobic.

3.2. SHS Tested in Flight Conditions

Some works devoted to ice prevention employing superhydrophobic surfaces for aerospace applications draw incomplete or preliminary conclusions because the tests to which the materials are subjected are not in line with real application conditions. To date, the tests that most closely simulate real-world conditions are those involving the use of an Icing Wind Tunnel (IWT) in which is possible to reach the relevant droplet's impact velocity (50 m/s or higher) at low temperatures (up to $-30\text{ }^{\circ}\text{C}$) generating both rime and glaze ice or specific aging test according to standards. Fortunately, to date, the research employing these tests is increasing and this improves knowledge and the chances, through careful study, of finding a solution to the long-standing problem of ice accretion during flight.

Among the earliest works devoted to the study of the properties of superhydrophobic coatings for aeronautics applications using tests conducted under standard conditions (IWT and others) are those by Antonini et al. [29] and Tarquini et al. [30]. In [29] different surfaces, from hydrophilic to superhydrophobic, were analyzed in IWT (air speed 28 m/s , $T = -17\text{ }^{\circ}\text{C}$) varying icing conditions by acting on the nozzle for the liquid water clouds generation following Icing certification (FAR29, Appendix C—Icing Certification for icing condition requirements). The SH coating ($\text{CA} = 161^{\circ} \pm 2$) was obtained by depositing a thin layer of Teflon by spray coating technique on the wing surface (etched aluminum). To define how a surface was effective in reducing ice adhesion, values of heating power required to avoid ice formation were taken as quantitative parameters. They found that the use of SH coating for aluminum reference provides a reduction in heating power

up to 80% to keep the edge of the wing ice-free and a significant reduction of runback ice in high LWC and complete prevention in low LWC conditions. Furthermore, it was observed that the grown ice consists of isolated structures, features that facilitate their breakage and removal. Unfortunately, the present study did not provide data regarding the characteristics of the coating after the test. In [30] the authors tested two SH commercial materials (surface roughness 1.1 and 2.42 μm) and two common metals (baseline) (surface roughness 0.5 μm) to evaluate the icephobic properties in helicopter blades employing an Adverse Environment Rotor Test Stand facility (T up to $-25\text{ }^{\circ}\text{C}$ and about 60 m/s) following the Federal Aviation Administration (FAA) advisor circular. The authors found that at high LWC on SH-FAS material, the ice-shedding capability could be slightly enhanced compared to the other samples. However, the authors observed that the adhesion reduction for the two SH samples did not depend on wettability because similar CA show differently in rime ice conditions. Nevertheless, it was observed that SHS exhibited a reduced thickness of the grown ice (Figure 6) but on the other hand, it was pointed out that adhesion stress increases as roughness increases, and the SH samples started to deteriorate after four shedding tests.

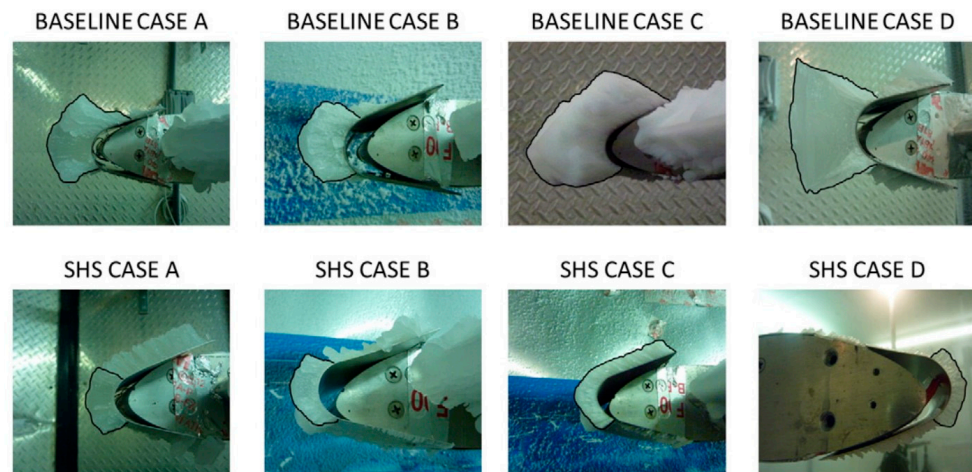


Figure 6. Ice shape pictures for both metallic and SHS materials, taken immediately before the shedding event. Case nomenclature is A, D glaze ice, B, mix condition and C rime. Ice shape profile has been enhanced to ease visual comparisons. SHS case A seems to have a lot of ice on the top surface not enhanced, but this is correct because that ice section is made only by light ice feathers, which would have been shed earlier and separately from the leading edge ice. Reprinted from *Cold Regions Science and Technology*, 100, S. Tarquini, C. Antonini, A. Amirfazli, M. Marengo, J. Palacios, Pages 50–58, Copyright (2014), with permission from Elsevier [30].

Also, Fortin et al. [31] tested different commercial hydrophobic and superhydrophobic ($\text{CA} = 152^{\circ}$) coatings under glaze and rime conditions in IWT. Different temperatures were settled to simulate different ice conditions at a constant speed of 21 m/s. From the test, it was observed that the SHS allowed to save energy equal to 33% for glaze ice and about 13% for rime concerning the anti-icing system without coating (reference). Also, the hydrophobic coating allowed for saving energy but in smaller quantities than SHS. From this preliminary work, the increase in hydrophobicity allowed reducing energy consumption for ice protection but no tests about the durability and resistance of SHS were conducted.

Piscitelli et al., over the years, proposed different studies in which they analyzed the yield of SH materials under real application conditions. In these works, [27,32] the SH coating was prepared by spray coating technique where several layers of nanometric hydrophobic silica dispersed in Tetrahydrofuran were deposited on different substrates with or without a polyurethane primer layer. In [27] the authors found that higher CA was reached when the silica dispersion was prepared by ultrasonication, in fact, superhydrophobic behavior was reached only after this step. Reference and SH-coated samples

($R_a = 0.3 \mu\text{m}$) were subjected to an aging test according to the MIL standard in which real flight conditions at 16,000 m in altitude were simulated (variation of humidity and temperature) for about 16 h, 10 times. After the aging test, the SH coating maintained its wettability in particular when a primer PU (Polyurethane) layer was applied and measurement of CA at -12°C and 0.5 bar showed a decrease in wettability losing superhydrophobicity ($<130^\circ$). An evolution of the work is found in [32] where an SH coating, produced following the procedure in [33], was applied on the NACA0015 (symmetrical airfoil with a 15% thickness to chord ratio developed by the National Advisory Committee for Aeronautics) wing profile has been subjected to an IWT test, the temperature ranged from -3 to -23°C at an altitude of 3000 m, LWC 0.3 g/m^3 and two-speed tests 50 and 95 m/s. Superhydrophobicity was maintained after the IWT test campaign but the effectiveness of the SH coating on ice prevention/reduction depended on the tested conditions (glace or rime and exposure time) and, in general, for long exposure time it could be considered as a support to an active system and not for use only as an anti-icing system.

Morita et al. [34] conducted validation tests in IWT on a hybrid anti-icing system (CA = 150° RoA = 8°) prepared by combining icephobic polytetrafluoroethylene (PTFE) coating and electrothermal heating (ICE-WIPS). The IWT test chosen conditions appeared in Federal regulation and they selected wind speed of 75 m/s, $T = -10/-8^\circ\text{C}$ and different LWC. The experiments provided raw data concerning the reduction in power consumption and it was observed that, in relationship to the existing heating system, the ICE-WIPS reduced power consumption by 30 to 70% depending on icing conditions. The work, however, did not provide data regarding the durability and the maintenance of properties thus resulting partly deficient for actual applications.

Brown et al. [35] recently developed an SH duplex coating system devoting a great deal of attention to its environmental durability. This material was obtained on stainless steel by depositing first TiO_2 powder by suspension plasma spray and secondly, a thin coating of diamond-like carbon network with SiO_2 by plasma enhanced chemical vapor deposition. The prepared coating showed CA = 159° , CAH = 3.8° and Sa = $10.3 \mu\text{m}$. The SH coating was exposed to icing/deicing cycling (IWT), rain erosion, and accelerated aging test, and the results were compared with those from tests performed on SH TiO_2 /stearic acid and commercial hydrophobic fluoropolymer. The IWT test conditions were $T = -10^\circ\text{C}$ with air speed of 43 m/s and LWC of 0.5 g/m^3 . At the end of the study, it was possible to affirm that the prepared SH coating was resistant to UV exposure, and could resist up to 6000 water droplets impact at 165 m/s and especially started to degrade after 170 icing/deicing cycles resulting in the coating with the best performance. However, the authors pointed out that, although the test in IWT was under severe conditions, deicing by melting and removal of ice through this method was less damaging than removing it by shearing force and that, if this situation could arise, the coating would degrade much faster. As above noted, the works just reported all apply specific test conditions that are very close to real ones even if they are often different from each other. In general, it is observed that SHS decreases the energy required to melt ice in AIPS and that the greater or lesser effectiveness depends on the type of formed ice.

Until now, we revised articles where wettability studies did not take into account the reported roughness values. In the following papers, however, this relationship has been carefully analyzed to draw more accurate conclusions after IWT testing.

Belaud et al. [36] investigated by IWT tests hydrophobic and superhydrophobic surfaces created on an aluminum alloy commonly used for aerospace components. The different wettability and roughness were obtained working on the Al alloy anodization in different media, sulphuric (SA) or oxalic acid (OA), and subsequently, each sample was functionalized by spraying a commercial hydrophobizing agent. OA samples were hydrophobic (max CA = 146° , RoA = 81°) with max surface roughness of $0.32 \mu\text{m}$, SA samples were superhydrophobic with CA of 162° and 170° , RoA of 32 and 4° , respectively, and surface roughness one order of magnitude higher than OA samples and smooth Al alloy reference (roughness like OA). IWT tests were performed following FAA specifi-

cations creating four different icing conditions (rime, mixed/rime, mixed/glaze, glaze) after each of them, ice adhesion strength was measured. Except for the glaze condition in which the adhesion strength remained unchanged for all surfaces (approx. 45 kPa), in the other three conditions, only the hydrophobic OA sample showed adhesion strength lower, 2–3 times, than the reference (Figure 7). This result was explained considering the different surface roughness between the samples supporting the theory that wettability alone is not synonymous with anti-ice.

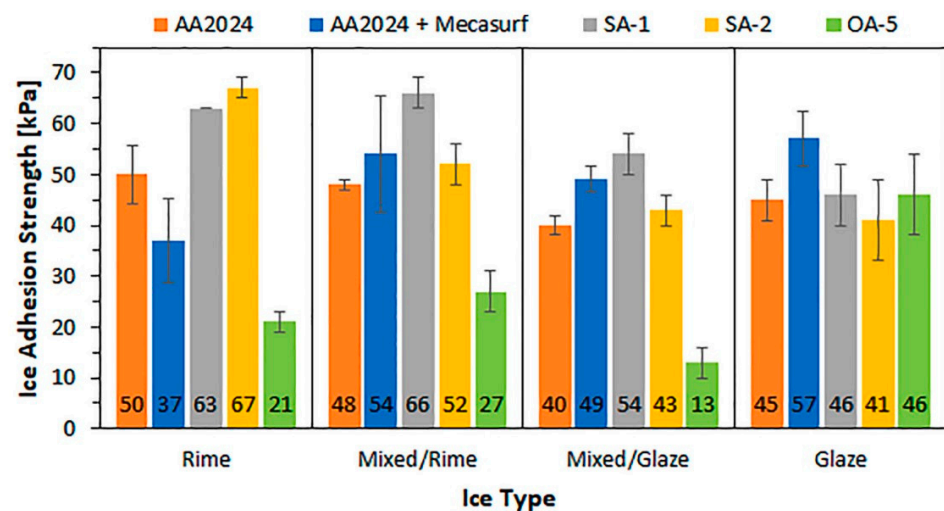


Figure 7. Ice adhesion strength of the anodized samples in rime ice, mixed/rime ice, mixed/glaze and glaze ice conditions with respect to the reference bare AA2024 surface. Reprinted from *Surface & Coatings Technology* journal, 405, C. Belaud, V. Vercillo, M. Kolb, E. Bonaccorso, Development of nanostructured icephobic aluminum oxide surfaces for aeronautic applications, 126652, Copyright (2021), with permission from Elsevier [36].

Another work supporting this theory is [11] in which the authors prepared, by different techniques (spin and spray coating) but the same mixture, two SHS with different surface roughness. Spin coated sample showed CA = 156°, CAH = 5° and Ra = 500 nm, spray coated sample showed CA = 165°, CAH = 4° and Ra = 8 μm. After the IWT test (T = −10 °C, wind speed 10 m/s, different LWC conditions and size of microdroplets) it was observed that although the samples had similar wettability and CAH, different ice adhesion strength values were registered. The spray-coated sample showed higher values, similar to the reference, compared to the spin-coated one evidencing the dominant effect of roughness on icephobicity. Furthermore, less stable wettability of spin coated sample with respect to spray coated one was observed, and icephobicity decreased after each icing/deicing cycle.

Continuing the search for a performance coating with icephobic behaviors for aerospace components, Mora et al. [37] proposed the use of quasicrystals (QCs) metallic materials. They are applied by means of high-velocity oxyfuel thermal spray Al-based QCs on common aeronautic materials. In particular, the work aimed to compare the QCs coating with PTFE, PU-based commercial paints and bare metal considering also the surface roughness. To do that, two QC materials were chosen and tested both in an “as deposited” state and after grinding with SiC paper to allow surface roughness similar to the reference. As deposited QCs materials showed different CA, for QC1 it was 158° with a CAH of 58°, for QC2 CA = 114° and CAH = 60°. All other reference materials showed contact angles less than 101° (PTFE). Ground QCs lost their wettability in fact CA for QC1 decreases to 57° and QC2 to 72°. IWT tests were performed both in glaze and rime ice conditions and ice accretion was evaluated. Under rime and glaze conditions the mass of ice accreted on all QCs coating was less than ice on standard metals. A different behavior was observed for the ice adhesion test, in this case, roughness played a critical role, the best results (low shear stress) were observed for the low roughness sample (PTFE and PU reference), and

lower values than as-deposited QCs were observed for ground QCs samples even lower than the value obtained for the aeronautic paint. The results thus lead to the statement that for ice adhesion, roughness played a role more important than wettability which seemed to be important in the mass of accreted ice, and finally that QCs materials are promising in terms of durability. Comparing these works, it can be affirmed that roughness is a key factor in the ice adhesion to the surface. Each work concludes by noting that samples with higher roughness, even if SH, show higher shear stress than the unmodified surfaces used as reference. It should be noted, however, that in all these cases the produced SHS shows a macroroughness on the order of microns, while in the only case where an SHS shows performant results, the roughness is below the micron (500 nm, CA = 156°). In conclusion, we can affirm that superhydrophobicity plays a key role only if it is accompanied by nano roughness that does not allow strong ice interlocking.

3.3. Hydrophobic and SLIP Surfaces with Icephobic Purpose Tested in Flight Conditions

It was observed from the literature that it is difficult to obtain SH surfaces with anti-ice behavior and durability; some authors directed their research toward other types of surfaces.

Rivero et al. [38] in the present study proposed three hydrophobic coatings, prepared by different techniques and materials, with anti-icing behavior to deepen the use of coatings for passive solutions in airplanes. The three coatings were tested in IWT (air speed 50 m/s, T = −8 °C, LWC 0.36 g/cm³) evaluating ice accretion and durability after some icing-deicing cycles. From these tests, it was observed, considering also reference material such as PTFE and Al substrate, that the anti-icing behavior was a combination of surface roughness and surface energy. Materials with similar roughness (coating 1 and PTFE) showed different ice adhesion and high roughness was more important with respect to low wettability. The best coating was that showing CA = 88° and Ra 0.19 μm but the results are far from a possible aeronautical application due to its low mechanical resistance.

SLIPS are a category of materials recently investigated for applications in aeronautical applications. Veronesi et al. [39] prepared and tested them in IWT to evaluate the ice accretion in rime and glaze conditions. Two different SLIPS were prepared, one was Al₂O₃-based and the other was SiO₂-based and both were infused in perfluoropolyether lubricant oils (two liquids that differ in terms of viscosity). IWT were conducted in different conditions but same velocity, 50 m/s, to obtain glaze and rime regimes. Al₂O₃-based and SiO₂-based SLIPS showed similar CA around 120° depending on the used lubricant oil and not on the substrate material. An important difference was the morphology of the samples: Al₂O₃-based coatings showed a flower-like structure, and SiO₂-based showed nanoparticles agglomerate with larger pores compared to alumina coatings. Both SLIPS displayed a decrease in ice accretion with respect to the uncoated surface, in particular, silica-based showed a reduction of up to 45% in glaze conditions. In rime, ice conditions not much improvement was observed compared with the reference.

Also, Vicente et al. [40] studied SLIPS as an anti-icing solution comparing them with self-prepared SHS. Both surfaces were formed by PVDF deposited by electrospinning technique and silicon oil was used as liquid to fill the porous PVDF structure and obtain the SLIPS. The prepared SH surfaces showed a linear correlation between CA and Sa, the highest value of CA (about 162°) was reached for the roughest sample (Sa = 700 nm). The SLIPS obviously showed low CA (106°) but the value of CAH (SHS CAH = 30°, SLIPS CAH = 19°) denoted how droplet mobility was better on this surface. Anti-icing behavior, on the best SHS and on SPLIPS, was tested in two conditions in IWT (air speed 70 m/s, T = −5/−15 °C, LWC 0.5 g/cm³) in order to produce glaze and rime ice, and adhesion test was performed using a centrifuge. PTFE and Al were used as a reference and in both glaze and rime conditions, as shown in Figure 8, SHS showed higher ice adhesion (especially in glaze conditions) than PTFE, while SLIPS achieved low ice adhesion in both conditions (four and seven times less of PTFE). SHS sample lost its property after only one cycle of

icing/deicing instead of SLIPS that resisted up to four cycles. The surface was still not resistant considering that Al and PTFE did not show degradation after the test.

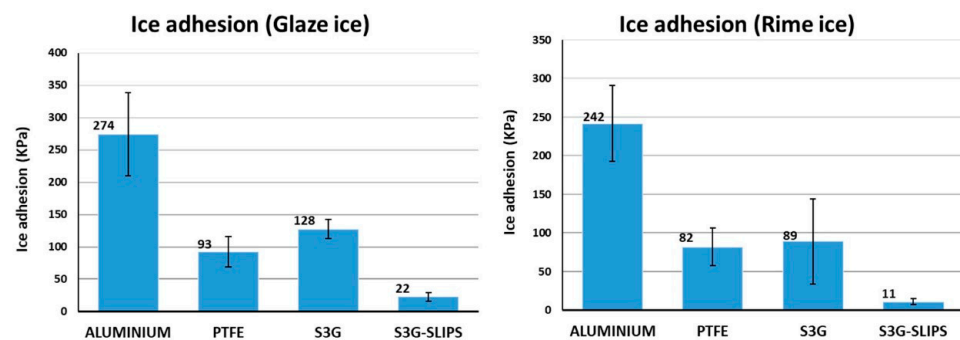


Figure 8. Graphs of ice adhesion tests after glaze and rime icing procedures in IWT. Reprinted with permission under the terms of the Creative Commons CC BY license from Vicente, A.; Rivero, P.J.; García, P.; Mora, J.; Carreño, F.; Palacio, J.F.; Rodríguez, R. Icephobic and Anticorrosion Coatings Deposited by Electrospinning on Aluminum Alloys for Aerospace Applications. *Polymers* 2021, 13, 4164 [40].

From these studies, it is possible to observe that SLIP surfaces are more performant compared to SHS due to the presence of lubricant in the microstructure that avoids water penetration and ice interlocking with the surface. Unfortunately, SLIPS seems to be not resistant to icing/deicing tests indicating that to date this solution is not applicable.

4. Deicing Fluids

Regardless of whether innovative coatings investigated as potential passive ice protection systems were hydrophobic, superhydrophobic, or SLIPS, they must resist the effects due to the application of deicing fluids and simultaneously that the fluids do not lose effectiveness when applied to surfaces. The problem with deicing/anti-icing fluids regards their composition because they are mainly composed of water, glycols, additives, and surfactants with potential adsorption to the surface and consequential loss of their initial highly hydrophobic properties. Villeneuve et al. [2] performed two current test methods used to qualify the ground deicing/anti-icing fluids on five different surface coatings, commercial and under development, and the results were used to develop a section of the SAE AUR6232 about fluids endurance time. They found that, depending on used deicing/anti-icing fluids, some surfaces could reduce the fluid endurance time that was regulated by law (Figure 9). The authors found no direct correlation between the CA and the endurance time and even when a positive result was observed, it was possible that the surface affected the fluid flow off establishing possible negative effects on aerodynamics. A later study setting out to explore this problem is more accurately described in [3]. In this paper, as opposed to [2], the authors provided detailed information about commercial anti-ice fluids (density, viscosity and surface tension) and employed surfaces (Sa, advancing and receding CA). Superhydrophilic and hydrophobic surfaces were used to test the ice protection of three commercially anti-icing fluids during the water spray endurance test. It was observed that surface wettability had no effect on the anti-icing fluid endurance time and that the results of ice accretion and durability were correlated with fluid viscosity and surface tension. The authors in particular stressed how surface roughness was important and must be considered for comparative studies since rough surfaces took longer to accumulate ice due to the presence of anti-ice fluid in the surface texture.

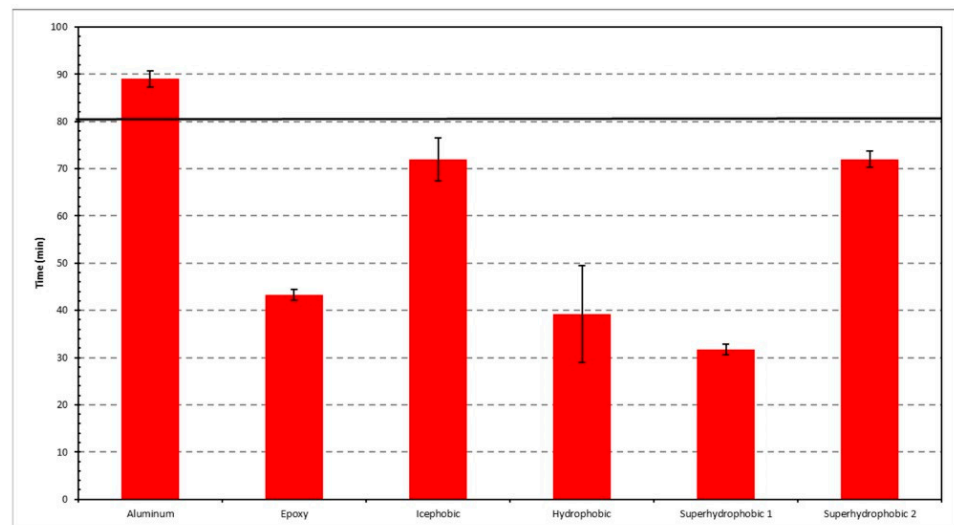


Figure 9. Endurance time for the different surfaces for Fluid B. Bold black line at 80 min is the minimum requirement as per AMS1428. Reprinted with permission under the terms of the Creative Commons CC BY license from Villeneuve, E.; Brassard, J.-D.; Volat, C. Effect of Various Surface Coatings on De-Icing/Anti-Icing Fluids Aerodynamic and Endurance Time Performances. *Aerospace* 2019, 6, 114. <https://doi.org/10.3390/aerospace6100114> [2].

On the other hand, Zhang et al. [41] investigated the negative effects of deicing fluids on coating performance. Commercial SHS and PTFE-based surfaces were chosen as representative icephobic materials and they were applied on test plates. Enamel coating was used as a reference material. Icephobic plates were immersed in two different commercial deicing fluids to simulate a situation where liquids remained on the airframe surfaces for different amounts of time before take-off. The authors observed that the two liquids had different impacts on the surface's wettability. Type-I deicing fluid showed low or no effect on the performance of SH and PTFE coating, on the other hand, Type-IV deicing fluid was capable of strongly contaminating surfaces by drastically reducing their icephobicity and consequently increasing their ice adhesion strength.

5. Conclusions

In this work, recent and fundamental literature has been revised on topics related to strategies to inhibit ice formation in aircraft as passive solutions or in combination with active systems. In the conclusion remarks, we can underline the high potential of SHS, which can be efficiently combined to reduce power consumption in an anti-icing active system. From the literature, some improvements should be addressed among physicochemical properties studies, where it can be observed that icephobicity is correlated with surface roughness, while wettability is not a comprehensive parameter to speculate about icephobic behavior. Moreover, studies addressing erosion resistance and ultraviolet degradation will be conducted, as they significantly affect the durability and overall stability of the treatment, potentially compromising the safety of the aircraft functions. Lack of methodology has been observed in studies on characterization and assessment of the icephobic coating performance, found not following the same protocols (methodology, shape form airfoils, how ice was introduced/grown on material) producing results that are not easily comparable and, in some cases, the test conditions are not reported. Furthermore, in some papers, details about surfaces such as roughness and CAH are not listed making comparison impossible. Future perspectives can be suggested considering the real application on aircraft with more insight into uniforming protocols and tests with de-icing/anti-icing fluids.

Author Contributions: The manuscript was written through the contributions of all authors. M.F.: conceptualization and supervision. F.C. and M.F.: writing—original draft. F.C. and M.F.: validation,

resources, investigation, writing—review and editing; F.C.: image processing. All authors have read and agreed to the published version of the manuscript.

Funding: This research received no external funding.

Data Availability Statement: Not applicable.

Conflicts of Interest: The authors declare no conflict of interest.

References

1. Tiwari, A. A Study of Icephobic Coatings, Part 1. Available online: <https://www.pcimag.com/articles/106963-a-study-of-icephobic-coatings-part-1> (accessed on 27 August 2023).
2. Villeneuve, E.; Brassard, J.D.; Volat, C. Effect of Various Surface Coatings on De-Icing/Anti-Icing Fluids Aerodynamic and Endurance Time Performances. *Aerospace* **2019**, *6*, 114. [CrossRef]
3. Grishaev, V.G.; Borodulin, I.S.; Usachev, I.A.; Amirfazli, A.; Drachev, V.P.; Rudenko, N.I.; Gattarov, R.K.; Bakulin, I.K.; Makarov, M.V.; Akhatov, I.S. Anti-Icing Fluids Interaction with Surfaces: Ice Protection and Wettability Change. *Int. Commun. Heat Mass Transf.* **2021**, *129*, 105698. [CrossRef]
4. Laforte, C.; Blackburn, C.; Perron, J. *A Review of Icephobic Coating Performances over the Last Decade*; SAE Technical Papers; SAE International: Warrendale, PA, USA, 2015; Volume 2015.
5. Mazzola, L. Aeronautical Livery Coating with Icephobic Property. *Surf. Eng.* **2016**, *32*, 733–744. [CrossRef]
6. Guo, Z.; Liu, W.; Su, B.-L. Superhydrophobic Surfaces: From Natural to Biomimetic to Functional. *J. Colloid Interface Sci.* **2011**, *353*, 335–355. [CrossRef] [PubMed]
7. Elzaabalawy, A.; Meguid, S.A. Advances in the Development of Superhydrophobic and Icephobic Surfaces. *Int. J. Mech. Mater. Des.* **2022**, *18*, 509–547. [CrossRef] [PubMed]
8. Ma, L.; Zhang, Z.; Gao, L.; Liu, Y.; Hu, H. Bio-Inspired Icephobic Coatings for Aircraft Icing Mitigation: A Critical Review. *Rev. Adhes. Adhes.* **2020**, *8*, 168–198. [CrossRef]
9. Gao, L.; Liu, Y.; Ma, L.; Hu, H. A Hybrid Strategy Combining Minimized Leading-Edge Electric-Heating and Superhydro-/Ice-Phobic Surface Coating for Wind Turbine Icing Mitigation. *Renew. Energy* **2019**, *140*, 943–956. [CrossRef]
10. Coclite, A.M.; Chen, L.; Zang, D.; Antonini, C.; Li, Z.; Wang, X.; Bai, H.; Cao, M. Advances in Bioinspired Superhydrophobic Surfaces Made from Silicones: Fabrication and Application. *Polymers* **2023**, *15*, 543. [CrossRef]
11. Momen, G.; Jafari, R.; Farzaneh, M. Ice Repellency Behaviour of Superhydrophobic Surfaces: Effects of Atmospheric Icing Conditions and Surface Roughness. *Appl. Surf. Sci.* **2015**, *349*, 211–218. [CrossRef]
12. Susoff, M.; Siegmund, K.; Pfaffenroth, C.; Hirayama, M. Evaluation of Icephobic Coatings—Screening of Different Coatings and Influence of Roughness. *Appl. Surf. Sci.* **2013**, *282*, 870–879. [CrossRef]
13. Ng, Y.H.; Tay, S.W.; Hong, L. Ice-Phobic Polyurethane Composite Coating Characterized by Surface Micro Silicone Loops with Crumpling Edges. *Prog. Org. Coat.* **2022**, *172*, 107058. [CrossRef]
14. Wu, X.; Silberschmidt, V.V.; Hu, Z.T.; Chen, Z. When Superhydrophobic Coatings Are Icephobic: Role of Surface Topology. *Surf. Coat. Technol.* **2019**, *358*, 207–214. [CrossRef]
15. Bakhshandeh, E.; Sobhani, S.; Jafari, R.; Momen, G. New Insights into Tailoring Physicochemical Properties for Optimizing the Anti-Icing Behavior of Polyurethane Coatings. *J. Appl. Polym. Sci.* **2023**, *140*, e54610. [CrossRef]
16. Ng, Y.H.; Tay, S.W.; Hong, L. Formation of Icephobic Surface with Micron-Scaled Hydrophobic Heterogeneity on Polyurethane Aerospace Coating. *ACS Appl. Mater. Interfaces* **2018**, *10*, 37517–37528. [CrossRef]
17. Upadhyay, V.; Galhenage, T.; Battocchi, D.; Webster, D. Amphiphilic Icephobic Coatings. *Prog. Org. Coat.* **2017**, *112*, 191–199. [CrossRef]
18. Martinelli, E.; Suffredini, M.; Galli, G.; Glisenti, A.; Pettitt, M.E.; Callow, M.E.; Callow, J.A.; Williams, D.; Lyall, G. Amphiphilic Block Copolymer/Poly(Dimethylsiloxane) (PDMS) Blends and Nanocomposites for Improved Fouling-Release. *Biofouling* **2011**, *27*, 529–541. [CrossRef]
19. Fortin, G. *Considerations on the Use of Hydrophobic, Superhydrophobic or Icephobic Coatings as a Part of the Aircraft Ice Protection System*; SAE Technical Papers; SAE: Warrendale, PA, USA, 2013; Volume 7. [CrossRef]
20. Consortium ICEAGE Project. *PROJECT FINAL REPORT Grant Agreement Number: CS-GA-2014-632630 Project Acronym: ICEAGE Project Title: Ice Phobic Coating Associated to Low Power Electromechanical De-Icers*; Cordis: Luxembourg, 2015.
21. Huang, X.; Tepylo, N.; Pommier-Budinger, V.; Budinger, M.; Bonaccorso, E.; Villedieu, P.; Bennani, L. A Survey of Icephobic Coatings and Their Potential Use in a Hybrid Coating/Active Ice Protection System for Aerospace Applications. *Prog. Aerosp. Sci.* **2019**, *105*, 74–97. [CrossRef]
22. Chen, X.; Hu, L.; Du, Y. Anti-Icing and Anti-Frost Properties of Structured Superhydrophobic Coatings Based on Aluminum Honeycombs. *Mater. Chem. Phys.* **2022**, *291*, 126683. [CrossRef]
23. Yu, T.; Lu, S.; Xu, W.; Boukherroub, R. Preparation of Superhydrophobic/Superoleophilic Copper Coated Titanium Mesh with Excellent Ice-Phobic and Water-Oil Separation Performance. *Appl. Surf. Sci.* **2019**, *476*, 353–362. [CrossRef]
24. Cheng, H.; Yang, G.; Li, D.; Li, M.; Cao, Y.; Fu, Q.; Sun, Y. Ultralow Icing Adhesion of a Superhydrophobic Coating Based on the Synergistic Effect of Soft and Stiff Particles. *Langmuir* **2021**, *37*, 12016–12026. [CrossRef]

25. Piscitelli, F. Superhydrophobic Coatings for Aeronautical Applications. In Proceedings of the 2020 IEEE International Workshop on Metrology for AeroSpace, MetroAeroSpace 2020-Proceedings, Pisa, Italy, 22–24 June 2020; pp. 282–287. [CrossRef]
26. Piscitelli, F.; Chiariello, A.; Dabkowski, D.; Corrado, G.; Marra, F.; Di Palma, L. Superhydrophobic Coatings as Anti-Icing Systems for Small Aircraft. *Aerospace* **2020**, *7*, 2. [CrossRef]
27. Piscitelli, F.; Tescione, F.; Mazzola, L.; Bruno, G.; Lavorgna, M. On a Simplified Method to Produce Hydrophobic Coatings for Aeronautical Applications. *Appl. Surf. Sci.* **2019**, *472*, 71–81. [CrossRef]
28. Liu, J.; Wang, J.; Mazzola, L.; Memon, H.; Barman, T.; Turnbull, B.; Mingione, G.; Choi, K.S.; Hou, X. Development and Evaluation of Poly(Dimethylsiloxane) Based Composite Coatings for Icephobic Applications. *Surf. Coat. Technol.* **2018**, *349*, 980–985. [CrossRef]
29. Antonini, C.; Innocenti, M.; Horn, T.; Marengo, M.; Amirfazli, a. Understanding the Effect of Superhydrophobic Coatings on Energy Reduction in Anti-Icing Systems. *Cold Reg. Sci. Technol.* **2011**, *67*, 58–67. [CrossRef]
30. Tarquini, S.; Antonini, C.; Amirfazli, A.; Marengo, M.; Palacios, J. Investigation of Ice Shedding Properties of Superhydrophobic Coatings on Helicopter Blades. *Cold Reg. Sci. Technol.* **2014**, *100*, 50–58. [CrossRef]
31. Fortin, G.; Adomou, M.; Perron, J. *Experimental Study of Hybrid Anti-Icing Systems Combining Thermoelectric and Hydrophobic Coatings*; SAE Technical Papers; SAE: Warrendale, PA, USA, 2011. [CrossRef]
32. Piscitelli, F. Characterization in Relevant Icing Conditions of Two Superhydrophobic Coatings. *Appl. Sci.* **2022**, *12*, 3705. [CrossRef]
33. Piscitelli, F. Substrate Superhydrophobic and Icephobic Coating, Method for Obtaining It and Substrate Thus Coated. International Patent Application N PCT/IB2022/062672, 22 December 2022.
34. Morita, K.; Kimura, S.; Sakaue, H. Hybrid System Combining Ice-Phobic Coating and Electrothermal Heating for Wing Ice Protection. *Aerospace* **2020**, *7*, 102. [CrossRef]
35. Brown, S.; Lengaigne, J.; Sharifi, N.; Pugh, M.; Moreau, C.; Dolatabadi, A.; Martinu, L.; Klemberg-Sapieha, J.E. Durability of Superhydrophobic Duplex Coating Systems for Aerospace Applications. *Surf. Coat. Technol.* **2020**, *401*, 126249. [CrossRef]
36. Belaud, C.; Vercillo, V.; Kolb, M.; Bonaccorso, E. Development of Nanostructured Icephobic Aluminium Oxide Surfaces for Aeronautic Applications. *Surf. Coat. Technol.* **2021**, *405*, 126652. [CrossRef]
37. Mora, J.; García, P.; Muelas, R.; Agüero, A. Hard Quasicrystalline Coatings Deposited by HVOF Thermal Spray to Reduce Ice Accretion in Aero-Structures Components. *Coatings* **2020**, *10*, 290. [CrossRef]
38. Rivero, P.J.; Rodríguez, R.J.; Larumbe, S.; Monteserín, M.; Martín, F.; García, A.; Acosta, C.; Clemente, M.J.; García, P.; Mora, J.; et al. Evaluation of Functionalized Coatings for the Prevention of Ice Accretion by Using Icing Wind Tunnel Tests. *Coatings* **2020**, *10*, 636. [CrossRef]
39. Veronesi, F.; Boveri, G.; Mora, J.; Corozzi, A.; Raimondo, M. Icephobic Properties of Anti-Wetting Coatings for Aeronautical Applications. *Surf. Coat. Technol.* **2021**, *421*, 127363. [CrossRef]
40. Vicente, A.; Rivero, P.J.; García, P.; Mora, J.; Carreño, F.; Palacio, J.F.; Rodríguez, R. Icephobic and Anticorrosion Coatings Deposited by Electrospinning on Aluminum Alloys for Aerospace Applications. *Polymers* **2021**, *13*, 4164. [CrossRef] [PubMed]
41. Zhang, Z.; Lusi, A.; Hu, H.; Bai, X.; Hu, H. An Experimental Study on the Detrimental Effects of Deicing Fluids on the Performance of Icephobic Coatings for Aircraft Icing Mitigation. *Aerosp. Sci. Technol.* **2021**, *119*, 107090. [CrossRef]

Disclaimer/Publisher’s Note: The statements, opinions and data contained in all publications are solely those of the individual author(s) and contributor(s) and not of MDPI and/or the editor(s). MDPI and/or the editor(s) disclaim responsibility for any injury to people or property resulting from any ideas, methods, instructions or products referred to in the content.

Article

Transparent Silicone–Epoxy Coatings with Enhanced Icephobic Properties for Photovoltaic Applications

Katarzyna Ziętkowska ^{1,*}, Bartłomiej Przybyszewski ^{1,2}, Dominik Grzęda ¹, Rafał Kozera ^{1,2},
Anna Boczkowska ^{1,2}, Malwina Liszewska ³, Daria Pakuła ⁴, Robert Edward Przekop ⁴ and Bogna Sztorch ⁴

- ¹ Faculty of Materials Science and Engineering, Warsaw University of Technology, ul. Woloska 141, 02-507 Warszawa, Poland; bartlomiej.przybyszewski.dokt@pw.edu.pl (B.P.); dominik.grzeda.dokt@pw.edu.pl (D.G.); rafal.kozera@pw.edu.pl (R.K.); anna.boczkowska@pw.edu.pl (A.B.)
- ² Technology Partners Foundation, ul. Pawinskiego 5A, 02-106 Warszawa, Poland
- ³ Institute of Optoelectronics, Military University of Technology, ul. Kaliskiego 2, 00-908 Warsaw, Poland; malwina.liszewska@wat.edu.pl
- ⁴ Faculty of Chemistry, Adam Mickiewicz University in Poznań, ul. Uniwersytetu Poznańskiego 8, 61-614 Poznań, Poland; darpak@amu.edu.pl (D.P.); robert.przekop@amu.edu.pl (R.E.P.); bogna.sztorch@amu.edu.pl (B.S.)
- * Correspondence: katarzyna.zietkowska.dokt@pw.edu.pl

Abstract: Recently, the photovoltaic technology has become very popular as a means to produce renewable energy. One of the problems that are still unsolved in this area of the industry is that photovoltaic panels are subject to a significant loss of efficiency due to the accumulation of dust and dirt. In addition, during the winter season, the accumulation of snow and ice also reduces or stops the energy production. The current methods of dealing with this problem are inefficient and pollute the environment. One way with high potential to prevent the build-up of dirt and ice is to use transparent coatings with self-cleaning and icephobic properties. In this work, the chemical modification of an epoxy–silicone hybrid resin using dually functionalized polysiloxanes was carried out. The icephobic properties (ice adhesion and freezing delay time of water droplets), hydrophobic properties (water contact angle, contact angle hysteresis, and roll-off angle), average surface roughness, and optical properties were characterized. It can be concluded that the performed chemical modification resulted in a significant improvement of the icephobic properties of the investigated coatings: ice adhesion decreased by 69%, and the freezing delay time increased by 17 times compared to those of the unmodified sample. The polysiloxanes also caused a significant reduction in the contact angle hysteresis and roll-off angle. The chemical modifications did not negatively affect the optical properties of the coatings, which is a key requirement for photovoltaic applications.

Keywords: icephobicity; hydrophobicity; ice adhesion; freezing delay time; polysiloxanes; transparent coatings; photovoltaics



Citation: Ziętkowska, K.; Przybyszewski, B.; Grzęda, D.; Kozera, R.; Boczkowska, A.; Liszewska, M.; Pakuła, D.; Przekop, R.E.; Sztorch, B. Transparent Silicone–Epoxy Coatings with Enhanced Icephobic Properties for Photovoltaic Applications. *Appl. Sci.* **2023**, *13*, 7730. <https://doi.org/10.3390/app13137730>

Academic Editor: Filomena Piscitelli

Received: 26 May 2023

Revised: 26 June 2023

Accepted: 29 June 2023

Published: 29 June 2023



Copyright: © 2023 by the authors. Licensee MDPI, Basel, Switzerland. This article is an open access article distributed under the terms and conditions of the Creative Commons Attribution (CC BY) license (<https://creativecommons.org/licenses/by/4.0/>).

1. Introduction

Over the past few years, the world of science and industry has focused a great deal of attention on coatings as structural and functional materials. Transparent coatings are of particular interest because of their multitude of applications. These coatings can be used on windows, car windows, aircraft subcomponents, skyscraper roofs, glass facades, and photovoltaic modules [1–3].

The photovoltaic technology is one of the most popular and growing means for the production of renewable energy. The technology converts sunlight directly into electricity. Photovoltaics finds a variety of applications such as in solar farms [4], systems to supply power in space [5], remote locations [6], buildings [7], etc. In 2020, there was a record increase of 23% in power generation from solar photovoltaic compared to 2019, translating into a 156 TWh increase in power generation [8,9].

As the market grows, there are new requirements for photovoltaic installations to be increasingly efficient and reliable. However, the performance of photovoltaic panels is directly affected by external atmospheric factors such as dust, pollution, UV radiation, snow, ice, and frost. The accumulation of pollutants on the surface of photovoltaic modules in the form of dust or sediment can reduce their efficiency and power output by up to several percent points. It is estimated that the decrease in output for contaminants with a thickness of 1 μm can be about 10% and for dust with a thickness of 3 μm can be up to 25% [10]. In addition, during winter and in cold regions, snow and ice are other obstacles to maintaining the high efficiency of photovoltaic power generation. The accumulation of snow or frost on installations usually results in a complete halt of power production [11]. The current methods of removing snow from PV installations include manual methods causing energy consumption and the use of polluting de-icing chemicals. However, the chemicals contribute to environmental pollution, and the manual labor includes risk factors of personal injury and the risk of damaging the PV module surfaces with sundry tools [12].

In recent years, a proposed strategy with great potential to deal with surface icing is the use of passive icephobic coatings. In the literature, studies of icephobicity focus on the low ice adhesion strength, the longest possible freezing time for water droplets, and the prevention of ice accumulation. In addition to the aforementioned icephobicity, coatings for photovoltaic panels should also exhibit self-cleaning properties (high value of the water contact angle and low value of the roll-off angle) and durability of their properties over time, while maintaining the required optical properties (transmittance and reflectance) [13]. The reasons limiting the use of durable, transparent coatings with self-cleaning and icephobic properties in industrial practice are their high manufacturing cost, difficulties in production scalability, and susceptibility to various types of degradation such as thermal and UV damage [14,15]. None of the solutions currently known from the literature is fully effective in preventing the fouling and icing of photovoltaic panels over the long term.

Epoxy resins and their hybrids are among the most popular resins used. In the available literature, only a few works about transparent coatings based on epoxy resins that exhibit durable self-cleaning and icephobic properties can be found. In [16], an epoxy surface water contact angle of 175° was obtained, but the authors did not perform optical measurements of the investigated coatings. In 2017, Z. Yang et al. [17] presented very promising results on transparent epoxy coatings with superhydrophobic and self-cleaning properties. The work detailed the influence of various factors on the durability of the water contact angle. Unfortunately, the effect of the applied coating modifications on the optical and icephobic properties was not presented. Roppolo et al. [18] also presented transparent epoxy coatings, which can be used as coatings on photovoltaic modules due to the uncomplicated, low-cost, and easily scalable manufacturing method. The modification of these coatings involved the addition of a mica-based mineral filler. In this work, no studies were conducted to evaluate the anti-icing properties.

One of the main groups of materials used in the growing fields of icephobicity and hydrophobicity is that of polysiloxanes and their derivatives. These materials have low surface energy, high durability, and low elastic modulus [19]. All these properties provide polysiloxanes with a high potential as anti-icing hydrophobic materials. In many works, coatings exhibiting a low surface energy are being studied for their anti-icing properties [20–23]. In 2020, Kozera et al. [24] performed a modification of an unsaturated polyester resin with double-organofunctionalized polysiloxanes. This modification resulted in an increase in the water contact angle and a decrease in ice adhesion compared to the unmodified matrix. According to literature reports, the adhesion of ice to surfaces based on polysiloxanes can achieve a value even below 1 kPa [19]. Bessonov et al. [25] also proved that polysiloxanes increase a surface hydrophobicity.

Transparent coatings intended for photovoltaic panel applications should meet several requirements that mainly include icephobic properties, self-cleaning properties, and of course, optical properties. To date, no solution in the literature simultaneously provides all of these properties. The research presented in this work is a first step in the design

of coatings for photovoltaic panel applications mainly focusing on obtaining ice-phobic properties. In this work, the modification of a transparent silicone–epoxy resin with original in-lab-synthesized chemical compounds from the group of doubly functionalized polysiloxanes was carried out. The chemical modifiers used in this work contain alkyl and oxirane groups in their structure to ensure compatibility with the selected polymer matrix and icephobic properties. The use of polysiloxanes containing two types of functional groups represents the novelty and uniqueness of this research. This work attempted to test the effect of individual functional groups on the properties of the matrix. The icephobic properties of the produced surfaces were characterized by determining two parameters: ice adhesion and the freezing delay time of water droplets. The dualistic approach in determining the anti-icing properties allowed for a more in-depth analysis of this phenomenon. The hydrophobic properties of the surface were characterized by its water contact angle measured at room temperature and at temperatures below 0 °C, contact angle hysteresis, and roll-off angle. Roughness tests and optical measurements were also included. The relationship between icephobic and hydrophobic properties is presented as well.

2. Materials and Methods

2.1. Coatings

The coating material used in the present study was a silicon–epoxy hybrid resin, SILIKOPON[®] ED, from Evonik (Essen, Germany). SILIKOPON[®] ED is characterized by good chemical and excellent corrosion resistance. It is suitable for ultra-high solids coatings. Applications include industrial and anti-corrosion coatings, uses in offshore/marine areas, structural steel, rail cars, tank construction, concrete walls and floors, and commercial transport coatings. This resin has a viscosity of 1500 mPas at 25 °C. SILIKOPON[®] ED cures at ambient temperature in combination with amino silanes. The hardener used in this paper was Q-sil AMEO (3-aminopropyltriethoxysilane) from Oqema (Mönchengladbach, Germany). The mixing ratio SILIKOPON[®] ED/Q-sil AMEO was 4.5:1.

The substances used in the modifier synthesis were silicon compounds (trime-thylsiloxy-terminated polymethylhydrosiloxanes (PMHS)) and olefins (hexene, octane, allyl-glycidyl ether) purchased from Linegal Chemicals (Warsaw, Poland); a solvent (toluene) from Avantor Performance Materials Poland S.A. (Gliwice, Poland); and chloroform-d, toluene-d₈, and a Karstedt catalyst from Sigma Aldrich Poland, (Poznan, Poland). In the process, toluene was dried and purified with the MB SPS 800 Solvent Drying System and stored under an argon atmosphere in Rotaflo Schlenk flasks.

2.2. Synthesis of the Chemical Modifiers

Mixtures of allyl glycidyl ether (AGE) (0.168 mol) and hexene (HEX) (0.336 mol) in a molar ratio of 1:2 and of allyl glycidyl ether (0.168 mol) and octene (OCT) (0.336 mol) in a molar ratio of 1:2 were added to a solution of trimethylsiloxy-terminated polymethylhydrosiloxanes 992 (30 g, 0.504 mol) in toluene and allyl glycidyl ether (0.100 mol) and hexene (0.403 mol) in a molar ratio of 1:4, and of allyl glycidyl ether (0.100 mol) and octene (0.403 mol) in a molar ratio of 1:4. The mixture was constantly stirred and heated to 70 °C. Then, the Karstedt's catalyst solution (10^{-a} eq Pt/mol SiH) was added. The reaction mixture was heated in reflux and stirred until the full conversion of Si–H (controlled by FT-IR). After confirming the complete conversion of the mixture, post-reaction evaporation was performed on a slow-speed vacuum evaporator.

2.3. Analysis of the Chemical Modifiers

Using Bruker Ascend 400 and Ultra Shield 300 spectrometers (both from Bruker Polska, Warszawa, Poland), the nuclear magnetic resonance (NMR) ¹H, ¹³C, and ²⁹Si spectra were recorded (at 25 °C using CDCl₃ as a solvent). Chemical shifts were reported in pm for ¹H and ¹³C concerning the residual solvent (CHCl₃) peaks.

Fourier transform-infrared (FT-IR) spectra were obtained using a Nicolet iS 50 Fourier transform spectrophotometer (Thermo Fisher Scientific, Walsham, MA, USA) equipped with a diamond ATR unit with a resolution of 0.09 cm^{-1} .

2.4. Preparation of the Samples

Four types of in-house synthesized modifiers (MOD) were used. The chemical modifiers were added in the amounts of 2 wt.%. The composition of the prepared samples and the number of modifiers used are shown in Table 1. The procedure for preparing the mixtures was as follows. The chemical modifiers were added to the silicone–epoxy resin in appropriate amounts and mixed using a magnetic stirrer. Furthermore, the hardener Q-sil was added in a ratio of 1:4.5 to the resin.

Table 1. Compositions of the prepared epoxy–silicone samples and their modifiers.

Sample No.	MOD Type	PHS	Olefin 1	Olefin 2	Molar Ratio
1 (REF)	-	-	-	-	-
2	MOD 1/2 wt.%	PHS992	AGE	OCT	1:2
3	MOD 2/2 wt.%	PHS992	AGE	OCT	1:4
4	MOD 3/2 wt.%	PHS992	AGE	HEX	1:2
5	MOD 4/2 wt.%	PHS992	AGE	HEX	1:4

The coatings were manufactured using the spin coating method. The spin coater SPIN150i from POLOS was used. The transparent coatings were applied on glass substrates with the size of $30\text{ mm} \times 30\text{ mm}$. The glasses were rinsed with acetone before applying the resin. The spin coating process was divided into four stages: dispensing, spreading, edge bead removal (EBR), and drying. The parameters of each stage are shown in Table 2. The applied polymer coatings were cured at room temperature for 24 h.

Table 2. The parameters of the spin coating steps.

Stage	Spin Speed [rpm]	Spin Accel. [rpm/s]	Spin Time [s]
Dispense	100	1000	10
Spread	2000	1000	20
EBR	500	1000	10
Dry	4000	1000	40

2.5. Determination of the Optical Properties

The optical properties of samples were characterized using a Cary 7000 UV-Vis-NIR Universal Measurement Spectrophotometer (Agilent Inc., Santa Clara, CA, USA). The samples were measured at room temperature in the 350–2500 nm spectral range with an increment of 4 nm. Transmittance and reflectance were measured using an integrating sphere module. The absorptance was calculated assuming the sum of transmittance, reflectance, and absorptance was 100%.

2.6. Determination of Roughness

The roughness tests were performed using a non-contact 3D surface profiler Slynx Sensofar from Sensofar Metrology (Barcelona, Spain). The Ra parameter, i.e., the average roughness of the surface profile was determined. The final values are the average of five different measuring points on the surfaces.

2.7. Determination of Hydrophobicity

The wettability of the surfaces was determined by measuring the water contact angles (WCA), the water contact angles at reduced temperatures, the contact angles hysteresis (CAH), and the roll-off angles (RoA). The measurements were performed using an OCA15 goniometer from DataPhysics Instruments (Filderstadt, Germany) with software SCA20,

equipped with a chamber designed for testing at reduced temperatures. The volume of the water droplets for the WCA and CAH measurements was 5 μL , and that for the RoA measurements was 10 μL . The contact angle hysteresis was determined using the needle-in method. The WCA was measured at room temperature and at temperatures of 0 $^{\circ}\text{C}$, -5°C , -10°C , and -15°C . The final WCA and RoA values are the average of five different measuring points on the surfaces.

2.8. Determination of Freezing Delay Time (FDT)

The freezing delay time (FDT) of water droplets, which is one of the parameters describing the icephobicity of a surface, was determined using an OCA15 goniometer (DataPhysics Instruments, Germany) with software SCA20, equipped with a chamber designed for testing at reduced temperatures. The test was conducted at -15°C and lasted a maximum of 4 h. The volume of the water droplets was 5 μL .

2.9. Determination of Ice Adhesion Strength (IA)

The ice adhesion (IA) was determined using the universal testing machine Zwick/Roel Z050 (from Zwick Roell, Ulm, Germany). During the measurement, the shear strength between the ice and the surface of the sample was determined. The tests of ice adhesion were carried out at room temperature, at a relative humidity of 50%. A detailed description of this method was presented in our earlier work [24].

3. Results

3.1. Characterization of the Polysiloxanes Derivatives

Functionalized polysiloxanes were obtained by hydrosilylation with hexene, octene, and allyl glycidyl ether. The reactions were carried out in the presence of a platinum Karstedt's catalyst. To confirm the full conversion of the substrates, NMR and FT-IR analyses were performed, and the disappearance of the characteristic signals at 2141 and 889 cm^{-1} was observed. This disappearance is caused by the stretching and bending of the Si-H group, respectively. Based on the ^1H NMR analysis, the conversion for all compounds was $>99\%$. The structure and purity of the modifiers were also confirmed by ^1H NMR, ^{13}C NMR, and ^{29}Si NMR analyses.

Figures 1–4 show the schemes of the product structures confirmed by NMR. The following signals were assigned:

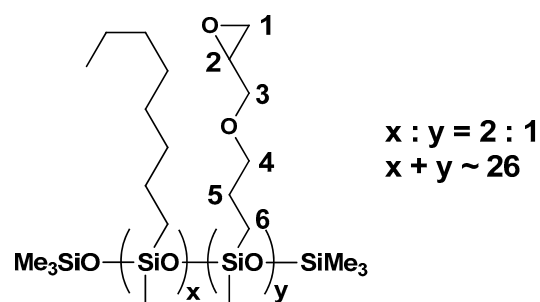


Figure 1. The scheme of the structure of the MOD1 modifier (MOD1—poly((methyloctylsiloxane)-co-(3-glycidyloxypropyl)(methyl)siloxane), trimethoxysilyl-terminated).

^1H NMR (400 MHz, CDCl_3): δ (ppm) = 3.70–3.67 (m, position 3), 3.47–3.41 (m, positions 3 and 4), 3.14 (m, position 2), 2.79–2.78 (m, position 1), 2.61–2.60 (m, position 1), 1.66–1.60 (m, position 5), 1.34–1.27 (m, octyl $-\text{CH}_2-$), 0.90–0.88 (m, octyl $-\text{CH}_3$), 0.53–0.50 (m, SiCH_2-), 0.15–0.05 (SiMe, SiMe_3)

^{13}C NMR (101 MHz, CDCl_3): δ (ppm) = 74.35, 72.16, 71.53, 69.71, 50.96, 44.43 (AGE), 33.65, 33.58, 32.13, 29.58, 29.51 (OCT), 23.38, 23.23, 23.11, (AGE), 22.85, 17.83, 17.55, 14.24 (OCT), 13.66 (AGE), 2.00, 1.61, -0.18 , -0.29 , -0.54 (SiMe, SiMe_3);

^{29}Si NMR (79.5 MHz, CDCl_3): δ (ppm) = -21.24 –(-22.95) (SiMe, SiMe_3).

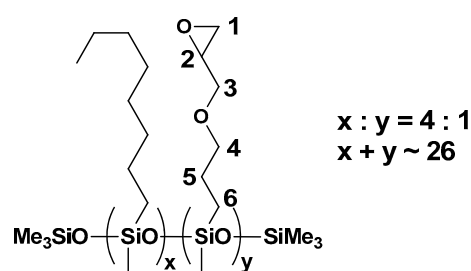


Figure 2. The scheme of the structure of the MOD2 modifier (MOD2—poly((methyloctylsiloxane)-co-(3-glycidoxypropyl)(methyl)siloxane), trimethoxysilyl-terminated).

^1H NMR (400 MHz, CDCl_3): δ (ppm) = 3.68–3.65 (m, position 3), 3.48–3.38 (m, positions 3 and 4), 3.13 (m, position 2), 2.78–2.76 (m, position 1), 2.60–2.58 (m, position 1), 1.67–1.59 (m, position 5), 1.34–1.27 (m, octyl $-\text{CH}_2-$), 0.90–0.86 (m, octyl $-\text{CH}_3$), 0.51–0.48 (m, SiCH_2-), 0.13–0.03 (SiMe, SiMe_3)

^{13}C NMR (101 MHz, CDCl_3): δ (ppm) = 74.42, 72.17, 71.53, 50.96, 44.45 (AGE), 33.69, 33.52, 32.16, 29.56, 29.47 (OCT), 23.40, 23.26, 23.12, (AGE), 22.87, 17.86, 17.58, 14.25 (OCT), 13.68 (AGE), 2.01, 1.62, -0.16 , -0.19 , -0.27 , -0.53 (SiMe, SiMe_3);

^{29}Si NMR (79.5 MHz, CDCl_3): δ (ppm) = -21.30 –(-22.96) (SiMe, SiMe_3).

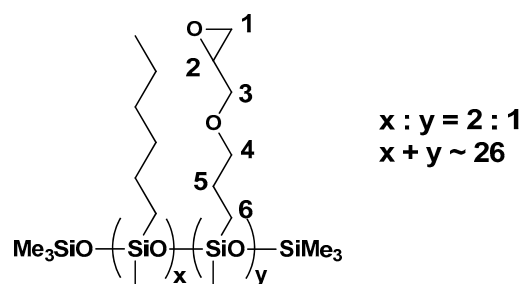


Figure 3. The scheme of the structure of the MOD3 modifier (MOD3—poly((hexylmethylsiloxane)-co-(3-glycidoxypropyl)(methyl)siloxane), trimethoxysilyl-terminated).

^1H NMR (400 MHz, CDCl_3): δ (ppm) = 3.68–3.65 (m, position 3), 3.47–3.34 (m, positions 3 and 4), 3.13–3.11 (m, position 2), 2.78–2.76 (m, position 1), 2.59–2.58 (m, position 1), 1.64–1.60 (m, position 5), 1.33–1.26 (m, hexyl $-\text{CH}_2-$), 0.88–0.86 (m, hexyl $-\text{CH}_3$), 0.51–0.48 (m, SiCH_2-), 0.13–0.03 (s, SiMe, SiMe_3)

^{13}C NMR (101 MHz, CDCl_3): δ (ppm) = 74.31, 71.53, 50.97, 44.44 (AGE), 33.65, 33.57, 32.12, 29.58, 29.51, (HEX) 23.37, 23.23, 23.18, 23.10 (AGE), 22.85, 17.82, 17.66, 17.55, 14.25 (HEX) 13.66, 13.44 (AGE), 2.01, 1.61, -0.19 , -0.29 , -0.46 (SiMe, SiMe_3)

^{29}Si NMR (79.5 MHz, CDCl_3): δ (ppm) = -20.99 –(-21.26) (SiMe, SiMe_3).

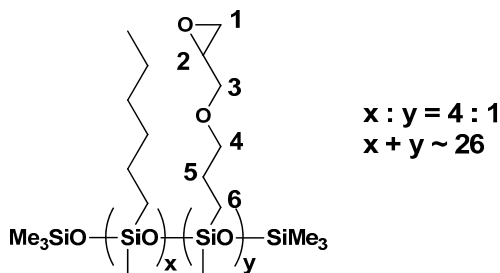


Figure 4. The scheme of the structure of the MOD4 modifier (MOD4—poly((hexylmethylsiloxane)-co-(3-glycidoxypropyl)(methyl)siloxane), trimethoxysilyl-terminated).

^1H NMR (400 MHz, CDCl_3): δ (ppm) = 3.70–3.67 (m, position 3), 3.51–3.40 (m, positions 3 and 4), 3.15–3.13 (m, position 2), 2.80–2.78 (m, position 1), 2.62–2.60 (m, position 1),

1.68–1.62 (m, position 5), 1.34–1.30 (m, hexyl -CH₂-), 0.92–0.89 (m, hexyl -CH₃), 0.54–0.51 (m, SiCH₂-), 0.11–0.07 (s, SiMe, SiMe₃);

¹³C NMR (101 MHz, CDCl₃): δ (ppm) = 74.35 (position 4), 71.52 (position 3), 50.95 (position 2), 44.41 (position 1), 33.29, 33.22, 31.81, 23.18, 23.06, 22.79, 17.84, 17.77, 17.57, 14.25 (-CH₂-), 1.97, 1.61, -0.20, -0.31, -0.47 (SiMe, SiMe₃).

²⁹Si NMR (79.5 MHz, CDCl₃): δ (ppm) = -21.28–(-21.36) (SiMe, SiMe₃).

3.2. Optical Properties

The measured optical properties of the fabricated coatings and neat glass are presented in Figure 5. The transmittance of the MOD1, MOD2, MOD3, and MOD4 samples was similar to the transmittance of glass in the tested range (Figure 5a). The differences in values were about 2%. The reference sample had a lower transmittance than the other samples. The reflectance of the measured samples was similar and ranged from 6% to 9% over the tested range (Figure 5b). The reference sample had a broad absorptance band of about 1000 nm. The other measured samples had an absorptance not greater than 4% within the tested range (Figure 5c).

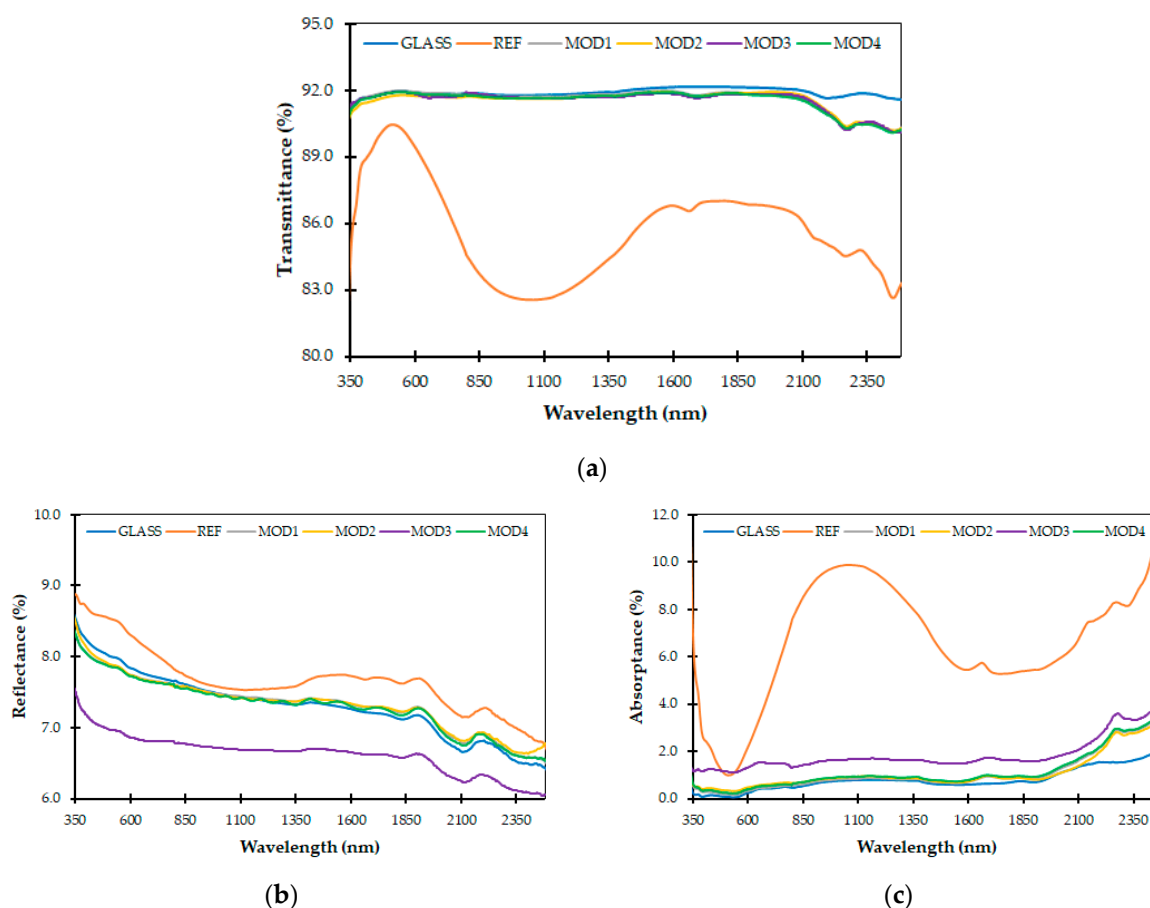


Figure 5. Transmittance (a), reflectance (b), and absorbance (c) spectra of the samples and glass.

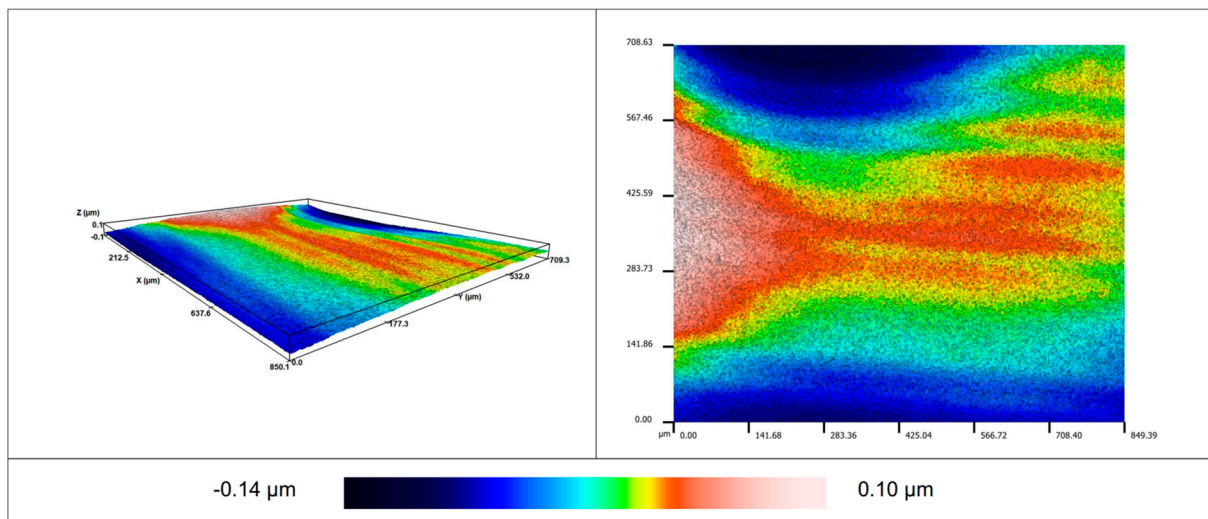
3.3. Roughness of the Surface

Table 3 presents the values of the Ra parameter, which indicates the average roughness of the surface profile. The reference sample obtained a value of 2 ± 0.1 nm. Figure 6a shows a visualization of the surface of the reference sample acquired with the profilometer. Analyzing the obtained results, it can be seen that the chemical modification with polysiloxanes increased the surface roughness of the silicone–epoxy samples. The range of the Ra values for the modified samples was from 5 nm to 21 nm. The highest increase in the Ra values was recorded for the MOD2-modified sample (Figure 6b). Furthermore, it can be seen that

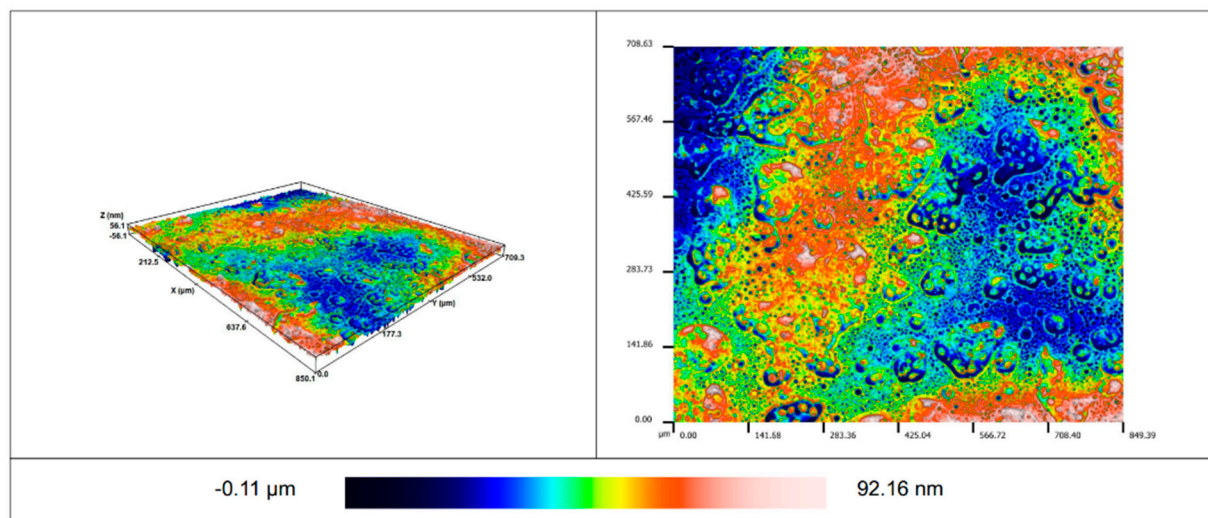
the polysiloxanes containing the OCT functional group displayed higher Ra parameter values compared to the polysiloxanes containing the HEX functional group. In addition, a higher amount of OCT/HEX functional groups also resulted in higher Ra parameter values compared to a lower amount of these groups.

Table 3. The hydrophobicity and roughness parameters of the silicone–epoxy coatings.

Sample No.	MOD Type	Core of MOD	Olefin 1	Olefin 2	Molar Ratio	Ra [nm]	WCA [°]	CAH [°]	RoA [°]
1 (REF)		-	-	-	-	2 ± 0.1	80 ± 1	22 ± 2	75 ± 8
2	MOD1	PWS992	AGE	OCT	01:02	12 ± 1.1	84 ± 1	9 ± 1	50 ± 3
3	MOD2	PWS992	AGE	OCT	01:04	21 ± 1.9	89 ± 1	7 ± 2	55 ± 9
4	MOD3	PWS992	AGE	HEX	01:02	5 ± 0.5	88 ± 2	9 ± 1	35 ± 6
5	MOD4	PWS992	AGE	HEX	01:04	7 ± 0.4	90 ± 1	11 ± 2	32 ± 14



(a)



(b)

Figure 6. The visualization of the surface of (a) the reference sample; (b) the MOD2–modified sample.

3.4. Hydrophobic Properties

The surface hydrophobicity of the produced samples was determined by measuring three parameters: water contact angle (WCA), contact angle hysteresis (CAH), and roll-off angle (RoA). The values of these parameters are presented in Table 3.

The reference sample, an unmodified epoxy–silicone resin, obtained a WCA of $80 \pm 1^\circ$ and hence may be considered hydrophilic ($\text{WCA} < 90^\circ$). Analyzing the WCA values of the coatings after the chemical modification, it can be concluded that the double functionalization of polysiloxanes caused an increase in the WCA values. Nevertheless, the increase was not significant. The range of the WCA values for the modified samples was from 84° to 90° . Taking into account the measurement uncertainty, it can be concluded that the samples modified with the MOD2, MOD3, and MOD4 additives presented surfaces at the boundary between hydrophilicity and hydrophobicity, obtaining WCA values close to 90° . The lowest increase in WCA compared to the reference sample was recorded for the sample modified with MOD1. Figure 7 shows a picture of a water droplet applied on the surface of a MOD4-modified sample, which achieved the highest WCA value.



Figure 7. The picture of a water droplet applied on the surface of a MOD4-modified sample.

The unmodified sample achieved a CAH value of $22 \pm 2^\circ$. The chemical modifications caused a significant decrease in this parameter. All modified samples obtained similar results, and the CAH range was from 7° to 11° . The lowest value was recorded for the sample modified with MOD2 polysiloxane, for which CAH decreased by 59% compared to that of the reference coating.

The RoA parameter also significantly decreased after modification with polysiloxanes. The reference sample obtained an RoA of $75 \pm 8^\circ$, and the modified samples achieved RoA values in the range from 32° to 55° . The lowest RoA values were obtained for MOD3- and MOD4-modified samples, with a reduction of about 55% compared to the RoA of the reference sample.

In summary, double-functionalized polysiloxanes showed increased water contact angle values (despite not crossing the boundary between hydrophobicity and hydrophilicity) and a significant reduction in contact angle hysteresis and roll-off angle values for all types of modifications.

Water Contact Angle at Temperatures Below 0°C

Figure 8 shows the values of WCA measured at four temperatures below 0°C to determine how a temperature reduction affected the surface hydrophobicity.

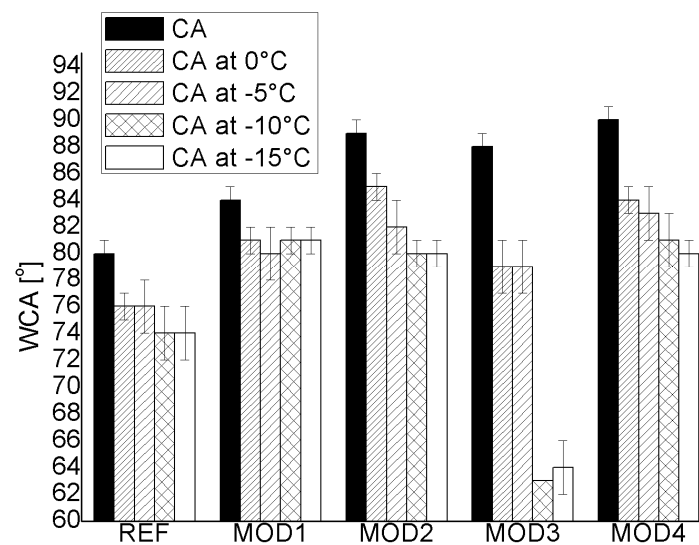


Figure 8. The water contact angles at room temperature and at temperatures below 0 °C of the epoxy–silicone samples.

Analyzing the results, it can be seen that the reference sample as well as all modified samples recorded a decrease in the WCA values at reduced temperatures compared to the values determined at room temperature. In addition, for some of the modifications, a relationship can be observed, i.e., the lower the test temperature, the lower the WCA values. The highest reduction in WCA, i.e., a reduction in the hydrophobic properties of the surface, was recorded for the sample modified with MOD3; at the temperatures of -10 °C and -15 °C , the WCA value decreased by 27% compared to the WCA value at room temperature. On the other hand, the highest hydrophobic stability at low temperatures was shown by the sample modified with polysiloxane MOD1, obtaining only a decrease in WCA equal to about 5% compared to the room temperature value. Moreover, for this sample, no further decrease in WCA was observed with the decreasing temperature, the WCA values determined at temperatures from 0 °C to -15 °C being either the same or close to each other. The reference sample also experienced a low decrease in the WCA values at reduced temperatures, as the reduction was equal to 8% compared to the WCA determined at room temperature. Other samples modified with the MOD2 and MOD4 additives showed a similar decrease in WCA of about 10% compared to the values determined at room temperature. Fu et al. [26] also observed that the wettability changes with ambient temperature and that the higher the WCA at ambient temperature, the higher the decrease in the value of this parameter at reduced temperatures. In addition, He et al. [27] found that for a modified superhydrophobic surface at -10 °C , the WCA value would decrease by about 8° compared to the value at room temperature. Moreover, some reports proposed that the surface free energy increases at low temperatures, which is related to the decrease in WCA [28,29].

3.5. Icephobic Properties

Figure 9 presents the obtained values of ice adhesion and freezing delay time for the investigated coatings. These two parameters allowed determining the anti-icing behavior of the epoxy–silicone samples.

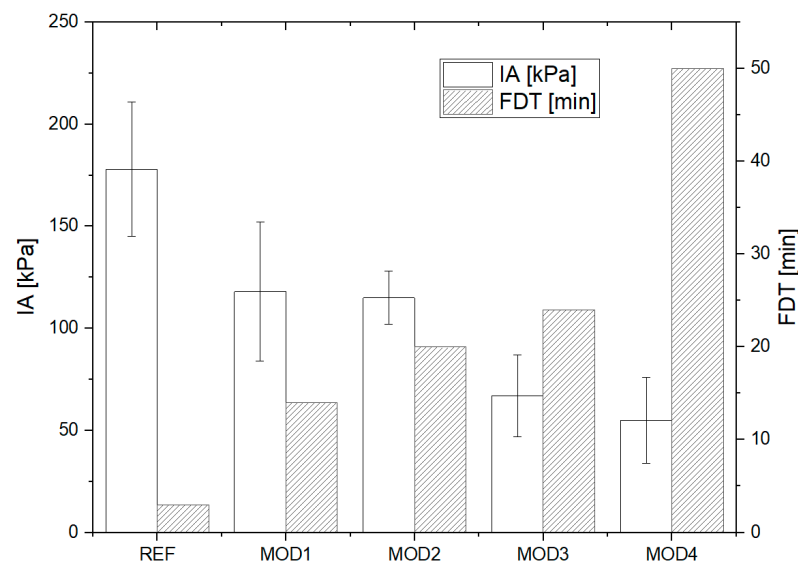


Figure 9. The ice adhesion and the freezing delay time of the epoxy–silicone samples at $-15\text{ }^{\circ}\text{C}$.

3.5.1. Ice Adhesion Strength

The ice adhesion determines the force needed for ice to break away from the surface. The lower the ice adhesion value, the more the surface is icephobic. The reference sample without chemical modification achieved the IA value of 178 ± 33 kPa. The samples modified with polysiloxanes obtained IA values in the range from 55 kPa to 118 kPa; so, all chemical modifications caused a decrease in the value of this parameter. The MOD4 sample showed the highest decrease, as the reduction in the IA values was as much as 69% compared to the IA of the reference sample. The MOD3 sample also achieved a very large decrease in IA values similar to the MOD4 sample, as the reduction was equal to 62% compared to the IA of the unmodified coating. The other modified MOD1 and MOD2 samples also recorded positive results, as the IA values for these samples were reduced by 34% and 35%, respectively, compared to the reference value. Another important aspect is that the MOD3 and MOD4 samples recorded IA values below 100 kPa. It is considered that surfaces exhibit low ice adhesion when the detachment force for ice is lower than 100 kPa. From such surfaces, ice is detached under the influence of natural forces such as wind, gravity, or ambient vibration [30]. The effectiveness of improving the anti-icing properties by using the chemical modification of the polymer matrix with double-functionalized polysiloxanes was proven in a work [31], achieving an IA reduction of 51% compared to the IA of the unmodified epoxy resin.

3.5.2. Freezing Delay Time

The FDT recorded for the reference sample was 3 min. The other modified coatings showed values for this parameter from 14 min to 50 min. Thus, it can be concluded that the addition of functionalized polysiloxanes increased the FDT and consequently improved the anti-icing properties of the surface of the epoxy–silicone coatings. The longest FDT was recorded for the sample MOD4, which also obtained the lowest ice adhesion value. The FDT for this sample increased 17 times compared to that of the unmodified sample; the FDT for the MOD 4 sample was 50 min. The other samples also showed a significant increase in the FDT, as the time values for these samples increased 5, 6, and 8 times. A previous work [32] also observed an increase in the FDT after modification with polysiloxanes of a polymer resin.

3.5.3. Summary of the Icephobic Properties

Comparing the results of the ice adhesion and the freezing delay time of water droplets, a direct correlation between these parameters can be seen. The lower the ice adhesion value

the sample showed, the higher the value of the freezing delay time. Among the samples tested, the sample MOD4 showed the highest icephobic properties. This sample displayed the lowest ice adhesion and the longest freezing delay time for water droplets.

4. Discussion

4.1. Influence of the Chemical Groups on Wettability and Icephobicity

Modifications with polysiloxanes functionalized with the AGE and HEX functional groups yielded the best icephobic results (the lowest ice adhesion value and the highest freezing delay time of water droplets). The modifications with polysiloxanes functionalized with the AGE and OCT functional groups achieved inferior results compared to those obtained using the AGE and HEX groups, but also achieved a significant improvement in the anti-icing properties compared to the unmodified sample. In addition, the higher content of the HEX functional group relative to the AGE functional group (i.e., 4:1) made it possible to obtain a significantly higher freezing delay time of water droplets and a slightly lower ice adhesion value compared to samples with a lower content of the HEX functional group relative to the AGE group (i.e., 2:1). In the case of modifications with polysiloxanes with the OCT functional group, the above relationship was not observed, and the values of the parameters of the icephobic properties were similar to each other. In summary, the polysiloxanes functionalized with the HEX functional group provided better icephobic properties to the epoxy–silicone surface compared to the polysiloxanes functionalized with the OCT functional group. In addition, the sample with the higher content of HEX functional groups recorded the best icephobic properties.

Regarding the hydrophobic properties, it can be said that the polysiloxanes functionalized with the AGE and HEX functional groups were characterized by higher WCA values and lower RoA values compared to analogous polysiloxanes functionalized with the AGE and OCT functional groups. It should be added that the WCA values were not diametrically different from each other, as the three modifications yielded very similar WCA values; only the sample modified with polysiloxane functionalized with the AGE and OCT groups in a ratio of 1:2 obtained a lower WCA value of 84°. It should be added that this value is not diametrically different from the other values of the modified samples, which also did not cross the boundary between hydrophobicity and hydrophilicity. As for the RoA values, the differences between the above polysiloxanes were significant. Comparing the WCA and RoA values of samples modified with polysiloxanes functionalized with the same functional groups but in different molar ratios, it can be concluded that they were very close to each other. The CAH values of all modified samples were in a similar range. In summary, the polysiloxanes functionalized with the HEX functional group provided better hydrophobic properties to the epoxy–silicone surface compared to the polysiloxanes functionalized with the OCT functional group.

Among the samples tested, the highest stability of the WCA values at reduced temperature was recorded for the sample modified with polysiloxane functionalized with the AGE and OCT groups in a ratio of 1:2, while the lowest stability was recorded for the sample modified with polysiloxane functionalized with the AGE and HEX groups in a ratio of 1:2. Polysiloxanes with higher ratios of the AGE functional group to the OCT/HEX groups showed very similar relationships. Thus, it can be concluded that polysiloxanes functionalized with the OCT functional group lead to a better stability of the WCA values of silicone–epoxy surfaces compared to polysiloxanes functionalized with the HEX functional group.

4.2. Relationship between Wettability and Icephobicity

In many reports in the literature, hydrophobic and icephobic properties are related [33–37]. Figure 10 shows the relationship between ice adhesion and the hydrophobic parameters water contact angle and roll-off angle. The values of contact angle hysteresis were similar for all chemical modifications; so, they will not be collated in the following discussion.

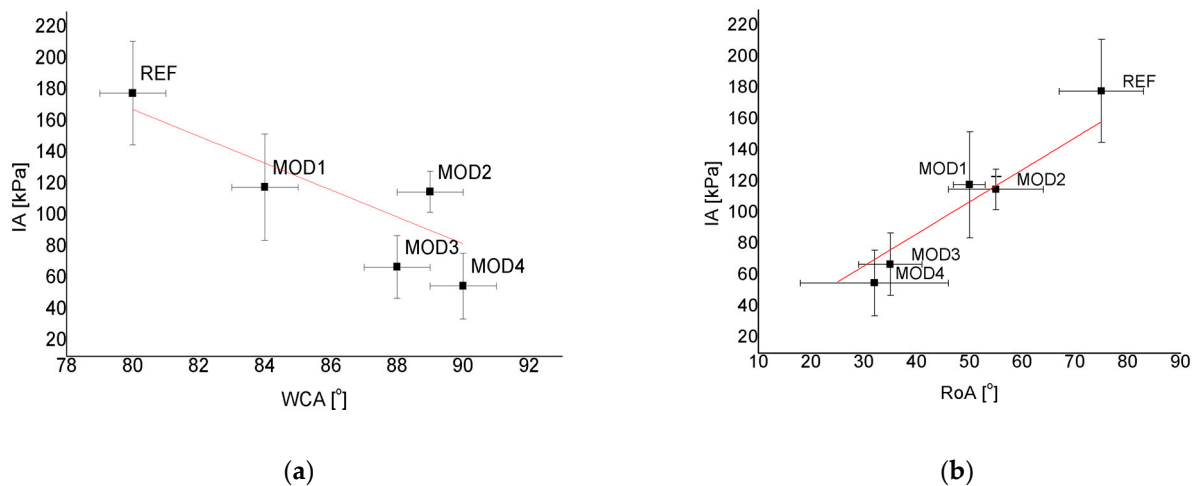


Figure 10. Relationship of IA as a function of (a) WCA determined at room temperature; (b) RoA.

Analyzing the relationship between IA and WCA, it can be concluded that as the value of WCA increased, the value of IA decreased. This was related to the change in surface free energy. In previous works [26,38], it was proven that this relationship has a strong influence on the icephobic properties. Only the MOD2-modified sample showed a deviation from this relationship, but it also recorded a significant decrease in the IA values compared to the reference sample. This sample obtained a very similar IA value as the MOD1-modified sample, despite obtaining a higher WCA value. This was likely influenced by the surface roughness. The MOD2-modified sample recorded twice the value of the Ra parameter, which may have offset the effect of the increased water contact angle, i.e., reduced surface energy. It was proven in many works that an increased roughness can significantly affect ice adhesion through the formation of a mechanical connection between the emerging ice and the rough substrate (ice anchoring) [37–39]. The second relationship between the icephobic and hydrophobic parameters was that as the value of RoA decreased, the value of IA also decreased.

The lowest possible values of IA and RoA and the highest value of WCA are key features that coatings intended for photovoltaic panels, among others, must present. The respective values of these parameters guarantee the surface's icephobicity. In further studies, the authors of this work will focus on surface texturization to obtain higher values of the WCA and lower values of the RoA parameters to achieve self-cleaning properties for the investigated coatings.

5. Conclusions

- The silicone–epoxy coatings produced in the entire tested spectral range showed similar optical properties (T, R, A) to those of glass. They can be potentially used in photovoltaic panels.
- The chemical modification with polysiloxanes resulted in an increase in surface roughness compared to the unmodified coating.
- The chemical modification with polysiloxanes contributed to an increase in hydrophobicity, with most samples achieving WCA values close to 90°.
- The use of polysiloxanes resulted in a significant reduction in the CAH and RoA values compared to those of the unmodified coating.
- The WCA values at reduced temperatures decreased for all applied modifications compared to the WCA values determined at room temperature. In addition, it was observed that the lower the ambient temperature, the lower the WCA value.
- Double-functionalized polysiloxanes in the epoxy–silicone matrix led to a significant improvement in the anti-icing properties, a reduction in ice adhesion, and an increased

freezing delay time of water droplets in comparison to the unmodified silicone–epoxy resin.

- The synergistic effect of the AGE and HEX functional groups at the polysiloxane core yielded better icephobic and hydrophobic results compared to those obtained with the AGE and OCT functional groups when using a silicone–epoxy matrix.
- Two relationships were observed for the modifications used. As the WCA values increased and as the RoA values decreased, the IA values were reduced.

Author Contributions: Conceptualization, K.Z. and B.P.; methodology, K.Z., B.S. and D.G.; validation, K.Z., B.P., M.L. and D.P.; formal analysis, K.Z.; investigation, K.Z. and D.G.; resources, D.G., M.L., B.S., R.K. and D.P.; data curation, K.Z.; writing—original draft preparation, K.Z.; writing—review and editing, K.Z. and B.P.; visualization, K.Z.; supervision, A.B. and R.E.P.; funding acquisition, B.P. All authors have read and agreed to the published version of the manuscript.

Funding: This research was funded by the National Centre for Research and Development (NCBR), grant number LIDER/15/0089/L-12/20/NCBR/2021.

Institutional Review Board Statement: Not applicable.

Informed Consent Statement: Informed consent was obtained from all subjects involved in the study.

Data Availability Statement: Data sharing not applicable.

Conflicts of Interest: The authors declare no conflict of interest.

References

1. Lyu, J.; Wu, B.; Wu, N.; Peng, C.; Yang, J.; Meng, Y.; Xing, S. Green preparation of transparent superhydrophobic coatings with persistent dynamic impact resistance for outdoor applications. *Chem. Eng. J.* **2021**, *404*, 126456. [CrossRef]
2. Ji, Z.; Liu, Y.; Du, F. Rational design of superhydrophobic, transparent hybrid coating with superior durability. *Prog. Org. Coat.* **2021**, *157*, 106294. [CrossRef]
3. Siddiqui, A.R.; Li, W.; Wang, F.; Ou, J.; Amirfazli, A. One-step fabrication of transparent superhydrophobic surface. *Appl. Surf. Sci.* **2021**, *542*, 148534. [CrossRef]
4. Gorjian, S.; Bousi, E.; Özdemir, E.; Trommsdorff, M.; Kumar, N.M.; Anand, A.; Kant, K.; Chopra, S.S. Progress and challenges of crop production and electricity generation in agrivoltaic systems using semi-transparent photovoltaic technology. *Renew. Sustain. Energy Rev.* **2022**, *158*, 112126. [CrossRef]
5. Bermudez-Garcia, A.; Voarino, P.; Raccurt, O. Environments, needs and opportunities for future space photovoltaic power generation: A review. *Appl. Energy* **2021**, *290*, 116757. [CrossRef]
6. Gorjian, S.; Sharon, H.; Ebadi, H.; Kant, K.; Scavo, F.B.; Tina, G.M. Recent technical advancements, economics and environmental impacts of floating photovoltaic solar energy conversion systems. *J. Clean. Prod.* **2021**, *278*, 124285. [CrossRef]
7. Zahedi, R.; Seraji, M.A.N.; Borzuei, D.; Moosavian, S.F.; Ahmadi, A. Feasibility study for designing and building a zero-energy house in new cities. *Sol. Energy* **2022**, *240*, 168–175. [CrossRef]
8. IEA. *Solar PV (IEA)*; IEA: Paris, France, 2021.
9. Kant, K.; Pitchumani, R. Fractal textured glass surface for enhanced performance and self-cleaning characteristics of photovoltaic panels. *Energy Convers. Manag.* **2022**, *270*, 116240. [CrossRef]
10. Klugmann-Radziemska, E. Degradation of electrical performance of a crystalline photovoltaic module due to dust deposition in northern Poland. *Renew. Energy* **2015**, *78*, 418–426. [CrossRef]
11. Priyadarshini, B.G.; Sharma, A.K. Design of multi-layer anti-reflection coating for terrestrial solar panel glass. *Bull. Mater. Sci.* **2016**, *39*, 683–689. [CrossRef]
12. Borrebæk, P.O.A.; Jelle, B.P.; Zhang, Z. Avoiding snow and ice accretion on building integrated photovoltaics—Challenges, strategies, and opportunities. *Sol. Energy Mater. Sol. Cells* **2020**, *206*, 110306. [CrossRef]
13. Boutamart, M.; Briche, S.; Nouneh, K.; Rafqah, S.; Agzenai, Y. Transparent and Self-Cleaning Surfaces Based on Nanocomposite Sol-Gel Coatings. *ChemistrySelect* **2020**, *5*, 8522–8531. [CrossRef]
14. Tarquini, S.; Antonini, C.; Amirfazli, A.; Marengo, M.; Palacios, J. Investigation of ice shedding properties of superhydrophobic coatings on helicopter blades. *Cold Reg. Sci. Technol.* **2014**, *100*, 50–58. [CrossRef]
15. Mozumder, M.S.; Mourad, A.-H.I.; Pervez, H.; Surkatti, R. Recent developments in multifunctional coatings for solar panel applications: A review. *Sol. Energy Mater. Sol. Cells* **2019**, *189*, 75–102. [CrossRef]
16. Alamri, H.; Al-Shahrani, A.; Bovero, E.; Khaldi, T.; Alabedi, G.; Obaid, W.; Al-Taie, I.; Fihri, A. Self-cleaning superhydrophobic epoxy coating based on fibrous silica-coated iron oxide magnetic nanoparticles. *J. Colloid Interface Sci.* **2018**, *513*, 349–356. [CrossRef]

17. Yang, Z.; Wang, L.; Sun, W.; Li, S.; Zhu, T.; Liu, W.; Liu, G. Superhydrophobic epoxy coating modified by fluorographene used for anti-corrosion and self-cleaning. *Appl. Surf. Sci.* **2017**, *401*, 146–155. [CrossRef]
18. Roppolo, I.; Shahzad, N.; Sacco, A.; Tresso, E.; Sangermano, M. Multifunctional NIR-reflective and self-cleaning UV-cured coating for solar cell applications based on cycloaliphatic epoxy resin. *Prog. Org. Coat.* **2014**, *77*, 458–462. [CrossRef]
19. Zhuo, Y.; Xiao, S.; Amirfazli, A.; He, J.; Zhang, Z. Polysiloxane as icephobic materials—The past, present and the future. *Chem. Eng. J.* **2021**, *405*, 127088. [CrossRef]
20. Zhu, L.; Xue, J.; Wang, Y.; Chen, Q.; Ding, J.; Wang, Q. Ice-phobic Coatings Based on Silicon-Oil-Infused Polydimethylsiloxane. *ACS Appl. Mater. Interfaces* **2013**, *5*, 4053–4062. [CrossRef]
21. Wang, H.; He, G.; Tian, Q. Effects of nano-fluorocarbon coating on icing. *Appl. Surf. Sci.* **2012**, *258*, 7219–7224. [CrossRef]
22. Huang, Y.; Hu, M.; Yi, S.; Liu, X.; Li, H.; Huang, C.; Luo, Y.; Li, Y. Preparation and characterization of silica/fluorinated acrylate copolymers hybrid films and the investigation of their icephobicity. *Thin Solid Films* **2012**, *520*, 5644–5651. [CrossRef]
23. Li, J.; Zhao, Y.; Hu, J.; Shu, L.; Shi, X. Anti-icing Performance of a Superhydrophobic PDMS/Modified Nano-silica Hybrid Coating for Insulators. *J. Adhes. Sci. Technol.* **2012**, *26*, 665–679. [CrossRef]
24. Kozera, R.; Przybyszewski, B.; Żołyńska, K.; Boczkowska, A.; Sztorch, B.; Przekop, R.E. Hybrid Modification of Unsaturated Polyester Resins to Obtain Hydro- and Icephobic Properties. *Processes* **2020**, *8*, 1635. [CrossRef]
25. Bessonov, I.V.; Kopitsyna, M.N. New Prepregs Based on Unsaturated Polyester Resins Modified with Polysiloxane Oligomers. *Int. Polym. Sci. Technol.* **2016**, *43*, 49–56. [CrossRef]
26. Fu, Q.; Wu, X.; Kumar, D.; Ho, J.W.C.; Kanhere, P.D.; Srikanth, N.; Liu, E.; Wilson, P.; Chen, Z. Development of Sol–Gel Icephobic Coatings: Effect of Surface Roughness and Surface Energy. *ACS Appl. Mater. Interfaces* **2014**, *6*, 20685–20692. [CrossRef]
27. He, M.; Wang, J.; Li, H.; Song, Y. Super-hydrophobic surfaces to condensed micro-droplets at temperatures below the freezing point retard ice/frost formation. *Soft Matter* **2011**, *7*, 3993–4000. [CrossRef]
28. Wang, C.-F.; Su, Y.-C.; Kuo, S.-W.; Huang, C.-F.; Sheen, Y.-C.; Chang, F.-C. Low-Surface-Free-Energy Materials Based on Polybenzoxazines. *Angew. Chem. Int. Ed.* **2006**, *45*, 2248–2251. [CrossRef]
29. David, C. Interfaces and the driving force of hydrophobic assembly. *Nature* **2005**, *437*, 640–647.
30. Ibáñez-Ibáñez, P.F.; Ruiz-Cabello, F.J.M.; Cabrerizo-Vílchez, M.A.; Rodríguez-Valverde, M.A. Mechanical Durability of Low Ice Adhesion Polydimethylsiloxane Surfaces. *ACS Omega* **2022**, *7*, 20741–20749. [CrossRef]
31. Ziętkowska, K.; Kozera, R.; Przybyszewski, B.; Boczkowska, A.; Sztorch, B.; Pakuła, D.; Marciniak, B.; Przekop, R.E. Hydro- and Icephobic Properties and Durability of Epoxy Gelcoat Modified with Double-Functionalized Polysiloxanes. *Materials* **2023**, *16*, 875. [CrossRef]
32. Kozera, R.; Przybyszewski, B.; Krawczyk, Z.D.; Boczkowska, A.; Sztorch, B.; Przekop, R.E.; Barbucha, R.; Tański, M.; Garcia-Casas, X.; Borrás, A. Hydrophobic and Anti-Icing Behavior of UV-Laser-Treated Polyester Resin-Based Gelcoats. *Processes* **2020**, *8*, 1642. [CrossRef]
33. Emelyanenko, K.A.; Emelyanenko, A.M.; Boinovich, L.B. Water and Ice Adhesion to Solid Surfaces: Common and Specific, the Impact of Temperature and Surface Wettability. *Coatings* **2020**, *10*, 648. [CrossRef]
34. He, Z.; Zhuo, Y.; Zhang, Z.; He, J. Design of Icephobic Surfaces by Lowering Ice Adhesion Strength: A Mini Review. *Coatings* **2021**, *11*, 1343. [CrossRef]
35. He, Z.; Vâgenes, E.T.; Delabahan, C.; He, J.; Zhang, Z. Room Temperature Characteristics of Polymer-Based Low Ice Adhesion Surfaces. *Sci. Rep.* **2017**, *7*, 42181. [CrossRef]
36. Li, X.; Zhao, Y.; Li, H.; Yuan, X. Preparation and icephobic properties of polymethyltrifluoropropylsiloxane–polyacrylate block copolymers. *Appl. Surf. Sci.* **2014**, *316*, 222–231. [CrossRef]
37. Wang, Y.; Liu, J.; Li, M.; Wang, Q.; Chen, Q. The icephobicity comparison of polysiloxane-modified hydrophobic and superhydrophobic surfaces under condensing environments. *Appl. Surf. Sci.* **2016**, *385*, 472–480. [CrossRef]
38. Kulinich, S.A.; Farhadi, S.; Nose, K.; Du, X.W. Superhydrophobic surfaces: Are they really ice-repellent? *Langmuir* **2011**, *27*, 25–29. [CrossRef]
39. Bharathidasan, T.; Kumar, S.V.; Bobji, M.S.; Chakradhar, R.P.S.; Basu, B.J. Effect of wettability and surface roughness on ice-adhesion strength of hydrophilic, hydrophobic and superhydrophobic surfaces. *Appl. Surf. Sci.* **2014**, *314*, 241–250. [CrossRef]

Disclaimer/Publisher’s Note: The statements, opinions and data contained in all publications are solely those of the individual author(s) and contributor(s) and not of MDPI and/or the editor(s). MDPI and/or the editor(s) disclaim responsibility for any injury to people or property resulting from any ideas, methods, instructions or products referred to in the content.

Article

A Study on the Sensitivities of an Ice Protection System Combining Thermoelectric and Superhydrophobic Coating to Icing Environment Parameters

Lei Yu ^{1,2,3,*}, Yuan Wu ^{1,2,3}, Huanyu Zhao ^{1,2,3} and Dongyu Zhu ^{1,2,3}¹ AVIC Aerodynamic Research Institute, No. 1 Yangshan Road, Huanggu District, Shenyang 110034, China² China-Italy Belt and Road Joint Laboratory on Green Aviation Technology, No. 172 Hangzhou Road, Shenbei New District, Shenyang 110021, China³ Liaoning Provincial Key Laboratory of Aircraft Ice Protection, No. 172 Hangzhou Road, Shenbei New District, Shenyang 110021, China

* Correspondence: aerowater@163.com; Tel.: +86-15840169527

Abstract: The hybrid Ice Protection System combining thermoelectric and superhydrophobic coating is efficient and benefits from low-energy consumption. In order to explore the application details of superhydrophobic coating, this paper investigated the sensitivities of the Ice Protection System parameters including the range of the superhydrophobic coating, heating range and power to icing environmental parameters. In this paper, an icing wind tunnel test was adopted to study the performance of this Ice Protection System under different icing conditions, as well as the influence of the superhydrophobic coating range, heating range and power variation on ice protection. The results showed that the superhydrophobic coating is effective only when it covers the droplet impingement area, with the heating power requirement emerging as a critical design consideration that is extremely sensitive to environmental temperature changes. Additionally, median volumetric diameter determines the protection area to be protected, while liquid water content variation has little effect on the designed Ice Protection System in contrast.

Keywords: ice; ice protection system; superhydrophobic

Citation: Yu, L.; Wu, Y.; Zhao, H.; Zhu, D. A Study on the Sensitivities of an Ice Protection System Combining Thermoelectric and Superhydrophobic Coating to Icing Environment Parameters. *Appl. Sci.* **2023**, *13*, 6607. <https://doi.org/10.3390/app13116607>

Academic Editors: Angelo Luongo and Filomena Piscitelli

Received: 24 March 2023

Revised: 23 May 2023

Accepted: 27 May 2023

Published: 29 May 2023



Copyright: © 2023 by the authors. Licensee MDPI, Basel, Switzerland. This article is an open access article distributed under the terms and conditions of the Creative Commons Attribution (CC BY) license (<https://creativecommons.org/licenses/by/4.0/>).

1. Introduction

Icing on key parts of an aircraft, such as wings, tails and engines, poses a threat to flight safety [1]. To tackle this issue, various ice protection systems have been developed and widely used, including thermal, pneumatic, electro-mechanic and anti-/de-icing fluid systems [2,3]. Although these ice protection systems have been effective, the increasing emphasis on safety requirements and limited aircraft energy capacity have exposed the conflict between the two. For instance, the hot-air ice protection system utilizes engine-generated hot air that affects engine power. In adverse weather conditions, when the hot air is insufficient, surface heating cannot ensure the complete evaporation of impinging water droplets, and part of the supercooled water impinging on the surface will freeze and form runback ice after flowing over the protected area [4]. That is the major cause of the ATR72 accident in Roselawn in 1994 [5]. The thermoelectric ice protection system has been widely used in helicopter blades, windshields, instruments, etc. However, with components such as wings and tails, due to the limited power supply of the aircraft, it typically operates periodically or continuously provides less heat only to maintain water on the surface in its liquid state [6], resulting in weak ice protection. Pneumatic, electro-mechanic ice protection system and anti-/de-icing fluid would negatively impact aerodynamic performance or add extra weight.

With advances in material technology, researchers attempted to develop a kind of icephobic coating that can passively reduce or delay ice formation without energy consumption. However, almost all coatings could not achieve the desired goal [7–9]. Alternatively,

hydrophobic or superhydrophobic coatings have been used to decrease the power required for ice protection by facilitating droplet removal when subjected to shear flow. In 2007, Kimura et al. [10] tested a mixture of acrylic urethane resin and polytetrafluoroethylene named AIS, and the results showed less difference in performance when no heating was performed. There was less ice on the AIS, but the test did not reflect whether it was due to the icephobic or hydrophobic properties. In 2009, Cao et al. [11] examined the ice formation process of supercooled water drops on surfaces with different hydrophobic characteristics and confirmed that the hydrophobic property had a significant impact on icing. In subsequent studies, Antonini et al. [12] investigated the reasons why superhydrophobic coatings reduce energy consumption and determined that they reduced water droplet aggregation on the surface and promote water droplets' falling off the surface, resulting in fewer droplets freezing. Mangini et al. [13], by comparing runback ice formed on a hydrophilic surface and a superhydrophobic surface, believed that surface wetting state played an important role in the icing process. Yin et al. [14] found that the decreasing contact angle would lead to an increase in the angle needed for droplet inclined rolling. The movement of water droplets on the surface deteriorates rapidly under the condition of high relative humidity and low temperature. In 2011, Fortin et al. [15] combined thermoelectric and hydrophobic coatings and evaluated the behavior of various hydrophobic coatings under glaze and rime icing conditions. The energy savings achieved were about 33% for glaze ice and about 13% for rime ice compared to ice protection systems used with no coating [15]. In 2017, Pauw et al. [16] studied the behavior of superhydrophobic coating on an airfoil model equipped with a thermal ice protection system and found no ice formation when maintaining the superhydrophobic coating surface temperature above 4 °C, while the ice protection system surface with no coating needs at least 70 °C in the same condition. They inferred that there would be no ice formation if the impingement area was covered with a superhydrophobic coating and the temperature was maintained above 6 °C.

The literature suggests two main perspectives: (1) Coatings with better superhydrophobic behavior, characterized by larger contact-angles and smaller roll-off-angles, achieve superior anti-icing performance. To address this perspective, novel coatings must be developed. (2) Combining thermoelectric and superhydrophobic coatings represents an efficient and low-energy consumption method for preventing ice formation. This perspective requires research into the design methods for the combined use of these coatings, which is a focus of this study. The literature has focused on the anti-icing mechanisms of superhydrophobic coatings, the reason why it reduces energy consumption, the effectiveness of different superhydrophobic coatings and the reduction of energy consumption. However, less attention has been paid to the engineering problems associated with the application of superhydrophobic coatings, such as their layout and internal heating area. To address these issues, similar to the design of thermoelectric and hot-air anti-icing systems, it is crucial to investigate the effects of various parameters of the anti-icing system, including the heating range and the layout of superhydrophobic coatings, under different icing conditions. This research provides valuable insights into the design of anti-icing system parameters specific to different icing conditions and offers actionable methods for the design and development of anti-icing systems that combine thermoelectric and superhydrophobic coatings.

This study provides fundamental research data to guide the future design of the Ice Protection System with a superhydrophobic coating (IPS). The data include the sensitivities of IPS to icing environmental parameters, as well as protective effects at different IPS parameters. The IPS parameters include the superhydrophobic coating range, heating range and power. Moreover, the environment parameters include median volumetric diameter (MVD), liquid water content (LWC) and environment temperature. These data can help guide the design of this type of IPS in the future.

2. Experimental Methodology

2.1. Experimental Setup

The tests were conducted in a FL-61 icing wind tunnel at the AVIC Aerodynamic Research Institute. As shown in Figure 1, FL-61 facility is a closed loop circuit refrigerated wind tunnel with a test section size of $0.6 \text{ m} \times 0.6 \text{ m} \times 2.7 \text{ m}$, driven by a 5200 kW main compressor and a 2500 kW auxiliary compressor. This facility can simulate altitude effect on ice accretion up to 7000 m. The maximum wind speed achievable in the test section is up to 240 m/s. Refrigeration of the air flow is achieved via a heat exchanger located upstream of the third corner, with the minimum temperature attainable being $-40 \text{ }^\circ\text{C}$. The system accuracy is $\pm 2 \text{ }^\circ\text{C}$ when the temperature falls below $-30 \text{ }^\circ\text{C}$ and $\pm 0.5 \text{ }^\circ\text{C}$ within the range of $-30 \text{ }^\circ\text{C}$ to $5 \text{ }^\circ\text{C}$. The cloud uniformity in the test section is within $\pm 20\%$. The tunnel is equipped with both a thermoelectric de-icing supply and a hot-air de-icing system supply making it capable of ice protection system tests.

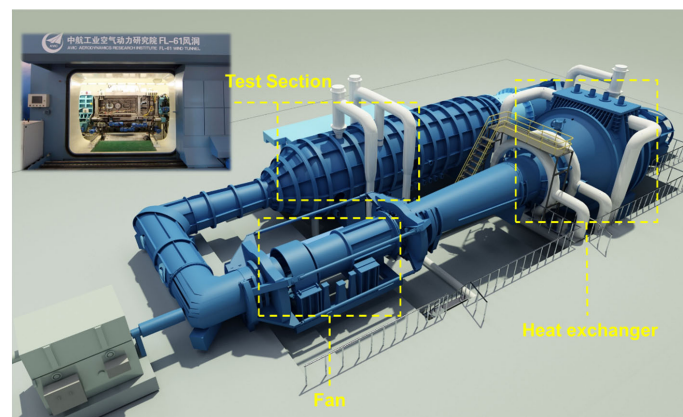


Figure 1. FL-61 icing wind tunnel.

This facility is calibrated annually and conforms to the SAE Aerospace Recommended Practice 5905 document. An additional calibration of LWC's spatial uniformity in the test section was performed before this experiment. One typical cloud uniformity result was shown in Figure 2.

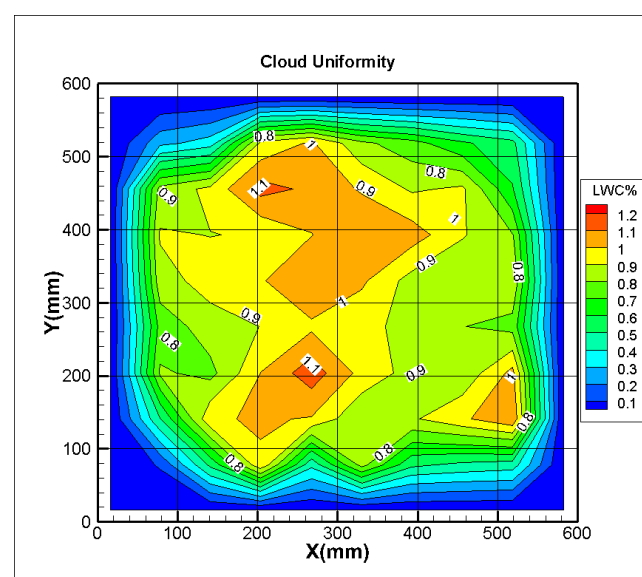


Figure 2. Icing cloud uniformity ($V = 90 \text{ m/s}$, $\text{LWC} = 1 \text{ g/m}^3$, $\text{MVD} = 20 \text{ }\mu\text{m}$).

2.2. Test Model

The model used in this study was a 2 D NACA0012 airfoil model with a sweep angle of 15°, as shown in Figure 3a. The NACA0012 airfoil is frequently utilized in aerodynamics research. Its upper and lower surfaces’ symmetrical characteristics facilitate comparative analysis of these regions. Therefore, it sees widespread employment in the research shown above. The model had a chord of 500 mm and a span of 600 mm, suspended in the test section. This model size was selected based on the maximum allowable size within the FL-61 icing wind tunnel. As shown in Figure 3b, five electric heating sheets were installed chordwise within the leading edge of the model to simulate the thermoelectric ice protection system, with each sheet’s heating power controlled separately via voltage control. All sheets covered the whole spanwise area. White lines drawn in the leading edge signified the position of the heating sheets. Additionally, lines were drawn in the rear spaced 2 cm apart, serving as a visual measure of icing extent, as shown in Figure 3a. The parameters of each sheet are shown in Table 1. Sheets A, B and C covered the droplet impingement area analyzed using numerical simulation methods during the initial stage, while sheets D and E were reserved for further heating purposes. The heating sheet distribution, with a narrow sheet in the leading edge and large sheets in the rear, was designed referencing aircraft ice protection system layout. In order to measure the model surface temperature, 9 thermocouples were arranged in the leading edge of the middle section spanwise of the model with the positions of each thermocouple detailed in Table 2. Due to possible significant temperature variations near the stagnation point of the leading edge, three thermocouples were arranged on sheet A. As the temperature gradient changed continuously after the leading edge, two thermocouples were positioned approximately 1/3 and 2/3 along sheet B and C, respectively, with one additional thermocouple on each of the sheets D and E. These thermocouples measured temperature fluctuations twice a second, with an accuracy of approximately ±0.5 °C after calibration.

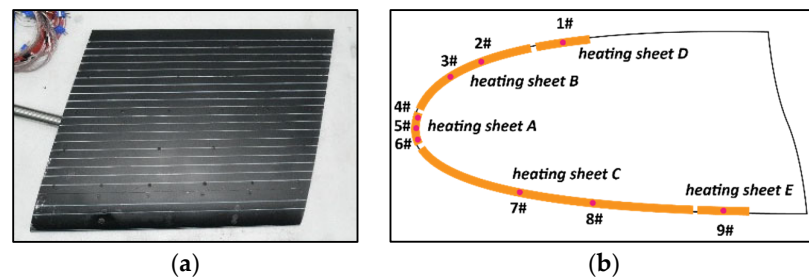


Figure 3. Test model. (a) Test model (top view), (b) Heating sheets and thermocouples layout.

Table 1. Heating sheets parameters.

No.	Arc Length (mm)	Thermocouples Number
A	12	4# 5# 6#
B	35	2# 3#
C	80	7# 8#
D	20	1#
E	20	9#

Table 2. Thermocouples position.

No.	1#	2#	3#	4#	5#	6#	7#	8#	9#
Arc length from the leading edge (mm)	51	31	21	3	0	3	36	61	101

Superhydrophobic coatings (Figure 4) were fabricated with laser sources on aluminum (Al) alloy foils (from BondHus, 6061 Al) with a thickness of 300 µm. A fs laser having

a wavelength of 1030 nm, a pulse length of 800 fs, average power up to 40 W and beam diameter of around 30 μm was used as the laser source. SEM-image is shown in Figure 3b. Contact-angle 150.14° and roll-off-angle 6.63° were measured using a video-based optical contact-angle measurement device.

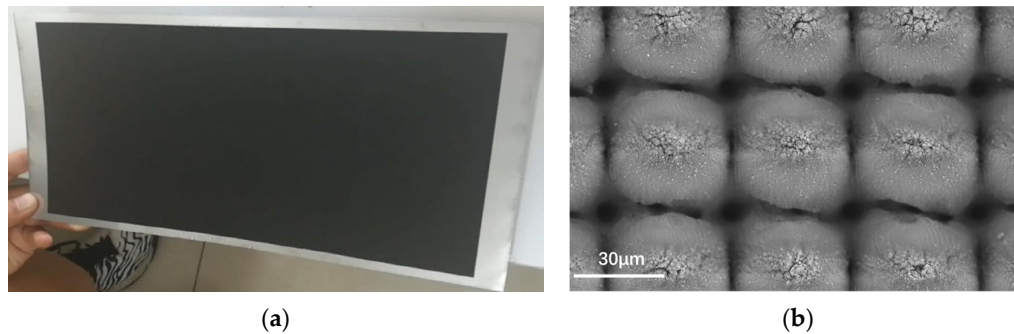


Figure 4. Superhydrophobic coating. (a) Coating appearance. (b) SEM-images of the coating.

2.3. Test Conditions

In this experiment, three typical temperatures were selected to simulate glaze ice (-7°C), mixed ice (-10°C) and rime ice (-15°C) at a speed of 90 m/s. The other icing cloud parameters selected were MVD 20, 30 and 40 μm , combined with LWC 0.5, 1, 1.3 and 1.5 g/m^3 . These parameters represent the typical icing conditions outlined in 14 CFR parts 25, Appendix C (<https://www.ecfr.gov/current/title-14/chapter-I/subchapter-C/part-25/appendix-Appendix%20C%20to%20Part%2025> (accessed on 23 March 2023)). Heating sheet area was designed using the numerical simulation method under the speed of 90 m/s, an angle of attack ranging from 0° to 4° , MVD 20 μm and a static temperature of -7°C . Pre-tests were conducted indicating that a minimum power density of 5 kW/m^2 was required to prevent ice forming on the leading edge with a coating.

The test was divided into two parts. The first part (shown in Table 3) explored the sensitivities of a designed superhydrophobic coating range, heating range and power of IPS to icing environmental parameters. The purpose was to evaluate the performance when IPS encountered an icing environment beyond the system's designated capabilities. Each case maintained the same velocity of 90 m/s, angle of attack of 0° and a testing time of 180 s, while varying MVD, LWC and environmental temperature. Sheets A, B and C were powered on and were covered with superhydrophobic coating, as a basic configuration.

Table 3. Test condition for part 1.

Case	MVD μm	LWC g/m^3	Temperature $^\circ\text{C}$	Heating Power Density kW/m^2
1	20	1	-7	5
2	30	1	-7	5
3	40	1.3	-7	5
4	20	0.5	-7	5
5	20	1.5	-7	5
6	20	1.5	-10	5 & 7.5
7	20	1.5	-15	10 & 12

The second part studied the performance of various IPS parameters such as coating ranges, heating ranges and powers dealing with a fixed icing environment parameter. The purpose was to explore the potential for further power reduction through optimization. Four types of IPS layout were examined (Figure 5). Type (1) represented the baseline configuration with both the heating sheet range and superhydrophobic coating range identical to the droplet impingement area. It was expected that supercooled droplets impacting the coating would immediately fall off and there would be no runback water

after the heating protection area. Type (2) decreased the range of heating area, expecting an increase in heating power density but the reduced heating area would reduce the total heating power consumption. Type (3) increased both the range of heating area and superhydrophobic coating area equally, intending to reduce the total heating power consumption with increased protection area but less power. Type (4) examined whether the water would fall off after the heating protection area. The superhydrophobic coating was positioned after the droplet impingement area with high heating power supplied to ensure the water temperature on the coating remained above freezing point. Type (1)–(3) targeted ways to reduce power consumption. As shown in Equation (1), type (2) decreased heating area but increased heating power density slightly trying to minish heating power compared with type (1). In contrast, type (3) decreased heating power density but increased heating area slightly, trying to minish heating power compared with type (1). That is why the reserved heating sheets D and E which expand the heating area were chosen with artificially different sizes than sheets B or C. Type (4) was designed to determine where droplets fell off, compared with Type (1).

$$\text{Heating power} = \text{heating power density} \times \text{heating area} \tag{1}$$

The tests were conducted at a velocity of 90 m/s, angle of attack of 0°, MVD 20 μm, LWC 1 g/m³ and a test duration of 180 s. The heating power, the range of heating area and the range of superhydrophobic coating area represented with sheet A, B, C, D, E are shown in Table 4.

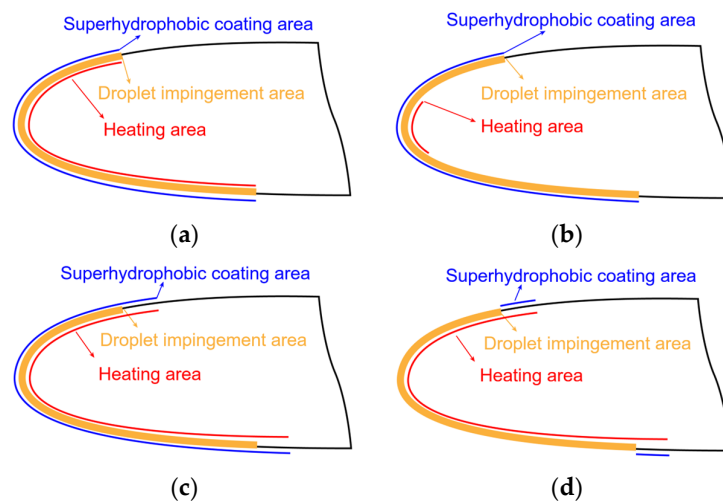


Figure 5. Four types of layouts of ice protection system. (a) Type (1). (b) Type (2). (c) Type (3). (d) Type (4).

Table 4. Test condition for part 2.

Case/Type	Heating Power W					Heating Power Density kW/m ²	Coating Area
	Sheet A	Sheet B	Sheet C	Sheet D	Sheet E		
8/type (2)	150	×	×	×	×	21	A B C
9/type (3)	Goes from high to low, details shown below						A B C D E
10/type (4)	72	210	510	120	120	10	D E

2.4. Test Procedure and Temperature Processing Method

The test procedure followed the steps below: (1) the wind tunnel temperature was set at target value; (2) the velocity was set to target value; (3) heating system was switched on and allowed the model surface temperature to reach a steady state condition; (4) spray

system was activated to generate liquid water cloud, and this time was set to 0; (5) test run for 180 s, after which wind tunnel fan and spray systems were switched off; (6) pictures of model were taken immediately. Throughout the test, temperatures of the model surface were continuously monitored.

Take case 1 results as an example to explain the temperature data processing method. Figure 6 indicates that time 0 s denotes step (4). Due to the cloud, the surface temperature decreased to a lower value, reaching a steady state once again at approximately time 100 s. The final value of each thermocouple was calculated by averaging out the surface temperatures collected between 120 and 170 s.

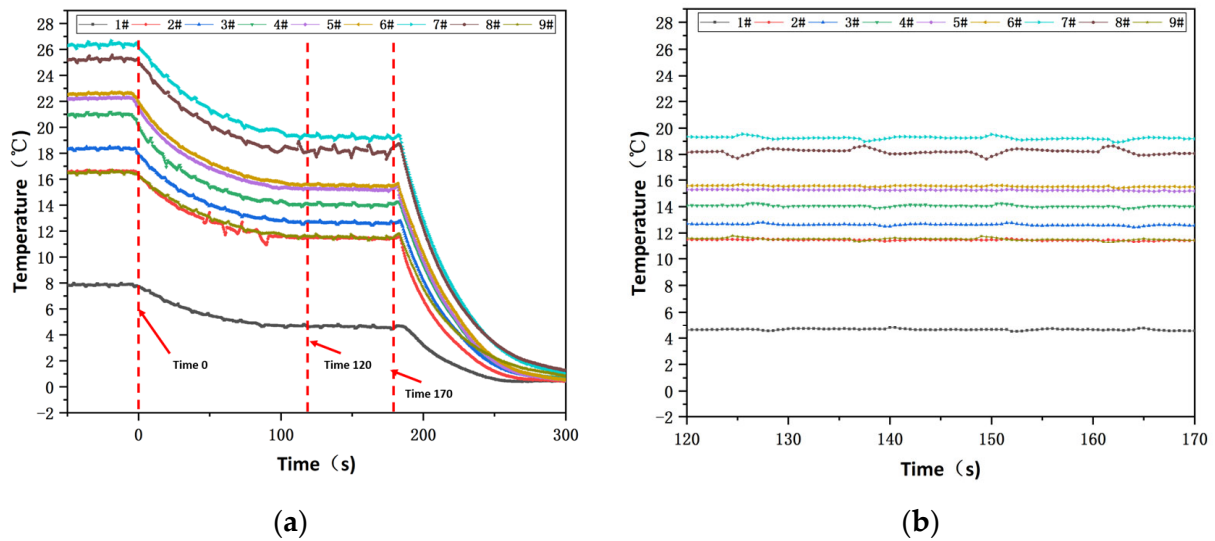


Figure 6. Surface temperature history in case 1. (a) Complete history. (b) Time 120 s to 170 s.

3. Results and Discussion

3.1. Sensitivity to Icing Environment Parameters

3.1.1. MVD

The protection area of basic configuration was designed based on MVD 20 μm . Comparing cases 1~3, the IPS prevented ice from forming when MVD was 30 μm . When MVD increased to 40 μm , ice appeared after the protection area but without rivulet characteristics, shown in Figure 7. An additional ice formation test under the same icing condition (Figure 8) showed that icing range exceeded the upper limit of the heating area (sheet B in this test). Thus, it could be inferred that the ice formation was due to the droplet impingement of MVD 40 μm that surpassed the protection range rather than runback water.

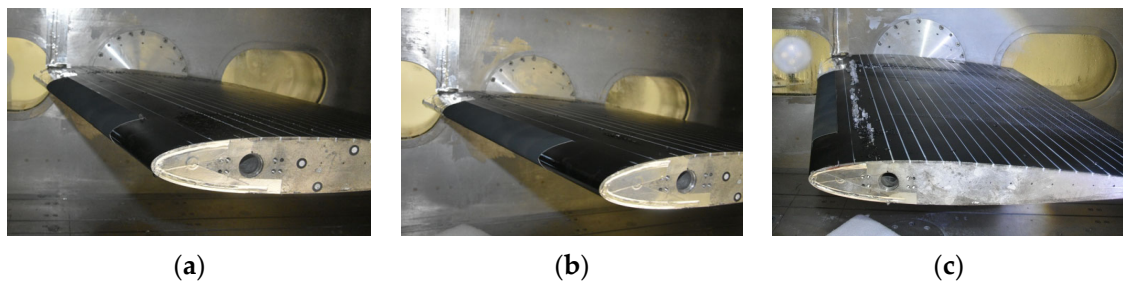


Figure 7. Test results of various MVDs. (a) MVD 20 μm . (b) MVD 30 μm . (c) MVD 40 μm .



Figure 8. Ice formation test in case 3 condition.

The surface temperature decreased when MVD increased from 20 μm to 40 μm , as shown in Figure 9. The lower surface temperature showed a linear decrease, while the upper surface temperature exhibited multiple decreasing trends, with the lower surface experiencing the most significant reduction. A maximum temperature decrease of 1.81 $^{\circ}\text{C}$ (about 9.93%) was observed when MVD increased from 20 μm to 30 μm and 3.47 $^{\circ}\text{C}$ (about 19.03% compared to MVD 20 μm) when MVD increased from 20 μm to 40 μm .

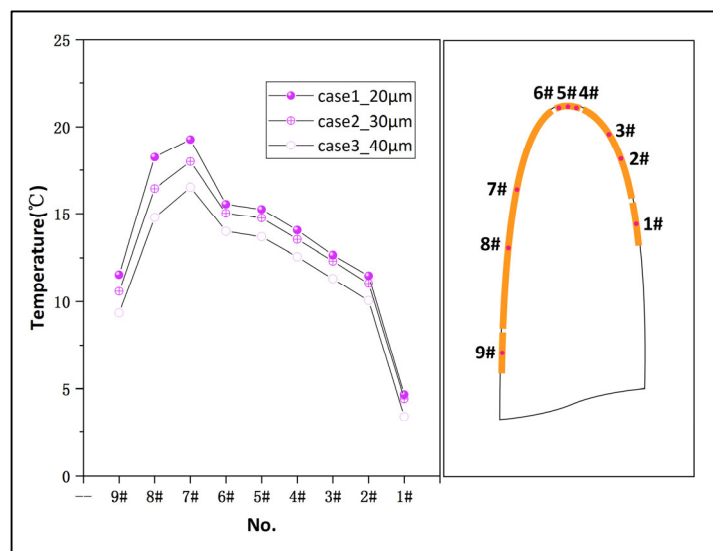


Figure 9. Comparison of surface temperature with different MVDs.

The test utilized a symmetrical NACA0012 airfoil tested at 0 $^{\circ}$ angle of attack. The difference in temperature between the upper and lower surfaces in this configuration resulted from their dissimilar protection areas. As such, an asymmetrical distribution of the protection areas of the upper and lower surfaces ultimately led to differences in temperature variation as MVD increased.

According to the results of this test, MVD affects the droplet impingement limit and becomes a factor to be considered in the design of IPS. An increase in MVD leads to an increase in water collected on the surface, which necessitates a simultaneous enhancement of the protection power required, as reflected in the decrease of surface temperature under the condition of constant heating power in this test.

In order to demonstrate the efficiency and low-energy consumption of IPS with a coating, a reference test of IPS without coatings was conducted under the same condition as case 1. The heating power densities of 5 kW/m^2 and 10 kW/m^2 were provided to prevent ice formation. As shown in Figure 10, runback ice formed after the heating area on the test model without coatings even when the heating power density was 10 kW/m^2 which was

twice as the power provided in case 1. IPS with a coating prevented runback ice formation and reduced power consumption by more than 50%.

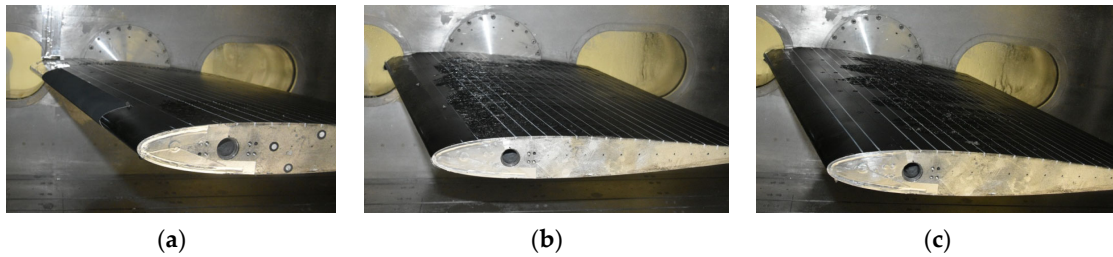


Figure 10. Test results of IPS with and without a coating in case 1 test condition. (a) The 5 kW/m² with a coating. (b) The 5 kW/m² without a coating. (c) The 10 kW/m² without a coating.

3.1.2. LWC

Through a comparative analysis of the test results for cases 1, 4 and 5, it was determined that a designed IPS prevented ice formation on the surface when LWC varied from 0.5 to 1.5 g/m³. As shown in Figure 11, the surface temperature decreased significantly when LWC increased from 0.5 to 1 g/m³ but did not decrease further when LWC increased further to 1.5 g/m³. The surface temperature of case 3, with LWC set to 1.3 g/m³, was lower than that of case 5 with LWC set to 1.5 g/m³ but revealed a temperature decrease compared to case 5. Since case 5 involved an increase in MVD to 40 μm, it could be reasoned that the decrease in surface temperature resulted from the combined effects of LWC and MVD.

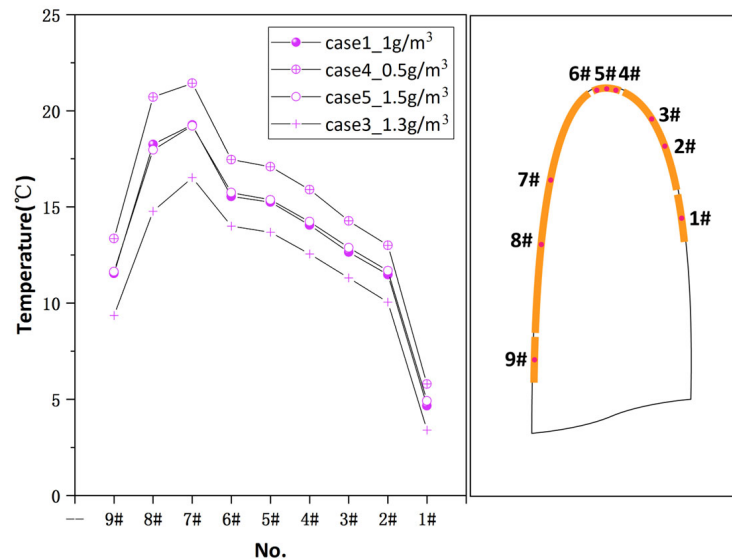


Figure 11. Comparison of surface temperature with different LWCs.

Based on the results of the tests, it was inferred that more power was required for heating with the increase of LWC, but once the LWC increased to a certain critical value, the power required would plateau. However, when coupled with an increased MVD, an expansion of droplet impingement area accompanied by more liquid water would lead to a considerable increase in power requirement.

3.1.3. Environment Temperature

IPS heating power density of 5 kW/m² was determined under an environment temperature of −7 °C. When the temperature dropped down to −10 °C and −15 °C, the power density 7.5 kW/m² and 12 kW/m², respectively, were required to protect the surface from icing, as test results suggest in Table 5 and as shown in Figure 12. In comparison to LWC and MVD, IPS was more sensitive to environment temperature. Therefore, when

environment temperature drops, IPS must immediately provide more heating power for ice protection.

Table 5. Heating power details in different environment temperatures.

Case \ Temp (°C)	Heating Power W					Heating Power Density kW/m ²	Valid or Invalid
	Sheet A	Sheet B	Sheet C	Sheet D	Sheet E		
Case 1 \ -7 °C	36	105	255	×	×	5	Valid
Case 6 \ -10 °C	36	105	255	×	×	5	Invalid
Case 6 \ -10 °C	54	158	383	×	×	7.5	Valid
Case 7 \ -15 °C	72	210	510	×	×	10	Invalid
Case 7 \ -15 °C	87	252	612	×	×	12	Valid

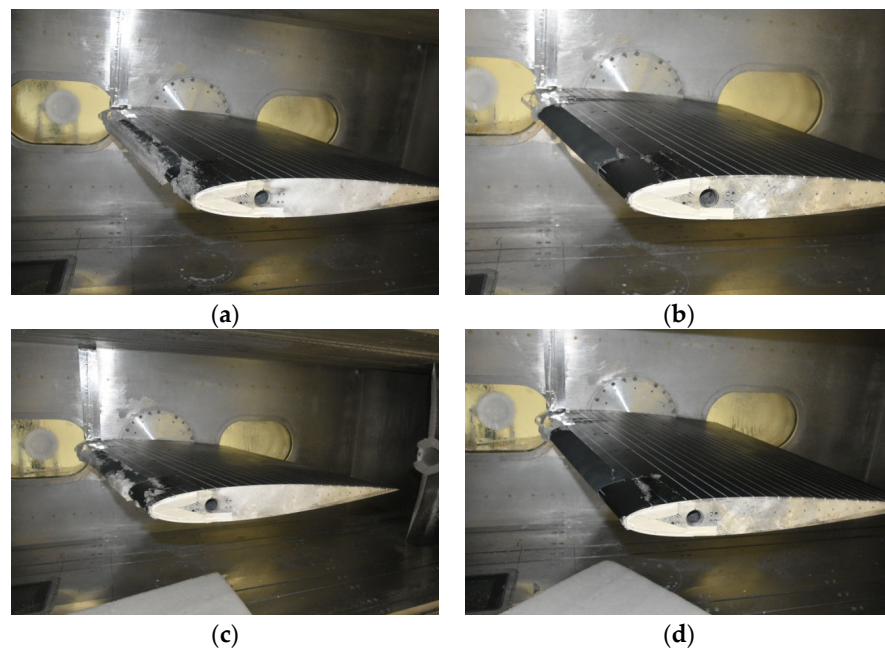


Figure 12. Test results of various environment temperatures. (a) Case 6 (5 kW/m²). (b) Case 6 (7.5 kW/m²). (c) Case 7 (10 kW/m²). (d) Case 7 (12 kW/m²).

In this test, when the temperature dropped from -7 °C down to -10 °C and -15 °C, the needed IPS heating power density went from 5 kW/m² to 7.5 kW/m² and 12 kW/m². Based on the results, the required heating power density was fitted linearly with the environment temperatures:

$$q = -0.877(T - 273.15) - 1.193 \quad (2)$$

where T is environment temperature, with units in Kelvin (K), and q is heating power density, with units in kW/m².

It is noteworthy that the thermocouples used for surface temperature measurement were positioned inside the model, rather than on the superhydrophobic coating surface. As a result, the surface temperature of the coating, which is crucial in IPS evaluation, would be lower than the measured temperature due to the heat transfer properties of superhydrophobic coatings. In the test, as shown in Figure 13, a heating power density of 10 kW/m² at environment temperature -15 °C (case 7) maintained an internal temperature virtually identical to that provided by a heating power density of 7.5 kW/m² at environment temperature of -10 °C (case 6) but could not prevent ice formation. It could be inferred that

the coating surface temperature dropped below the freezing point. Therefore, it is necessary to study the heat transfer qualities between the airfoil skin and superhydrophobic coating in the future.

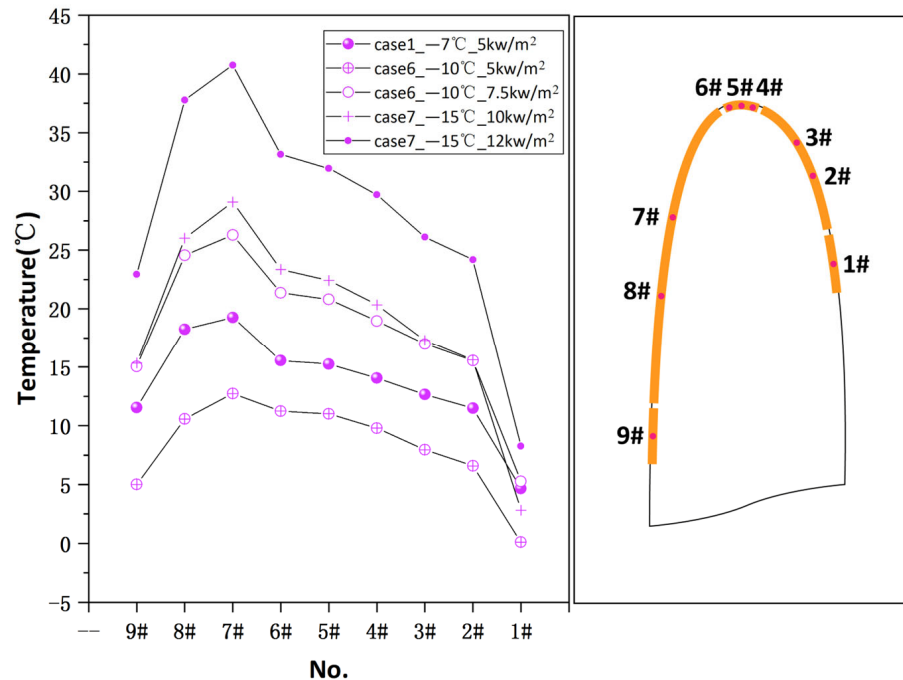


Figure 13. Comparison of surface temperature with different environment temperatures and heating power densities.

3.2. IPS Parameters Effect

3.2.1. Heating Range and Powers

Case 8 entailed the activation of only sheet A with a considerable increase in power of 150 W to simulate Type (2) previously defined. Results (Figure 14) showed that this design could not prevent ice formation even near the stagnation point. The high power applied to sheet A led to a leading edge surface temperature approximately equal to that of Type (1) in case 1, as shown in Figure 15, but with a temperature fall rapidly after the heating area. It could be inferred that the temperature of the superhydrophobic surface here should have fallen below the freezing point. As a result, it is not advisable to reduce the heating area range since this could adversely impact efficient heat distribution in addition to the superhydrophobic coating’s poor heat transfer. The surface temperature on the superhydrophobic surface must be kept above the freezing point.



Figure 14. Leading edge ice formation when only sheet A was turned on.

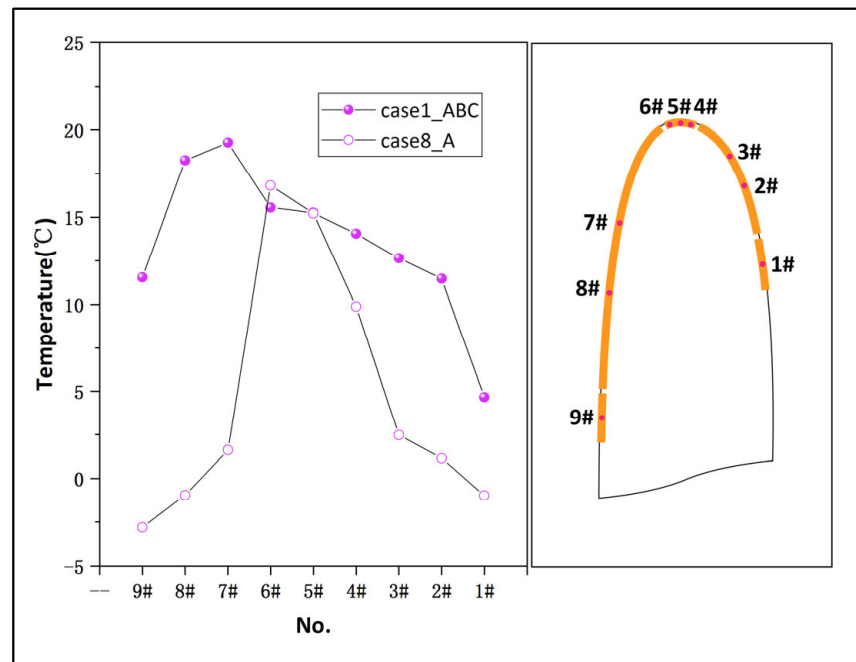


Figure 15. Comparison of surface temperature with sheet A on and sheets A/B/C all on.

3.2.2. Coating Range

Type (3) layout was tested in case 9, where all the heating sheets A/B/C/D/E were turned on and covered with superhydrophobic coatings. Each heating sheet was provided with the same power density which decreased gradually during the test until ice formation occurred. Heating power details are shown in Table 6. On the first attempt, a power density of 5 kW/m² was chosen based on the minimum power density obtained from the pre-tests described above. This was evidently sufficient to prevent ice formation due to the additional sheets D and E. However, when the provided power density fell to 4 kW/m², ice appeared on the leading edge, as shown in Figure 16. The ice protection results are shown in Table 6. At a power density of 4.5 kW/m², the total power of sheets A/B/C/D/E was 466 W, whereas the total power at a power density of 5 kW/m² with sheets A/B/C on was 396 W. Increased coating range led to a decrease in heating power density but not in the total power.

Table 6. Heating power details in case 9.

	Heating Power W					Total Power W	Heating Power Density kW/m ²	Valid or Invalid
	Sheet A	Sheet B	Sheet C	Sheet D	Sheet E			
1st try	36	105	255	60	60	516	5	Valid
2nd try	33	95	230	54	54	466	4.5	Valid
3rd try	29	84	204	48	48	413	4	Invalid
Case 1 (reference)	36	105	255	×	×	396	5	Valid

It can be seen from this part of the study that increasing the range of superhydrophobic coating and heating, while decreasing the heating power density of heating sheets, cannot lead to a reduction in total heating power consumption. Efficient distribution of heating power remains the key consideration in IPS design, even with a superhydrophobic coating.



Figure 16. Ice formation on the leading edge at a power density of 4 kW/m^2 .

3.2.3. Water Fall-off Position

Type (4) layout was tested in case 10. Sheets A/B/C/D/E were provided a high heating power density of 10 kW/m^2 to ensure that the water on the protection surface remained in its liquid state. Only sheets D and E were covered with superhydrophobic coating to investigate whether it led to runback water falling off beyond the droplet impingement limit. Aluminum plates covered the sheets A/B/C region to prevent steps between the two regions. Results in Figure 17 showed no ice formation on the heating protected surface, but runback ice formed thereafter. It indicates that the water collected on the sheets A/B/C region did not completely fall off the surface while passing through the sheets D/E region. In case 1, when superhydrophobic coatings covered the sheets A/B/C region, no runback ice formed, indicating that all liquid water fell off within the impingement area. It could be inferred from the comparison of the two test results that it was the droplet impingement area covered with the superhydrophobic coating that effectively impacted droplets falling off.

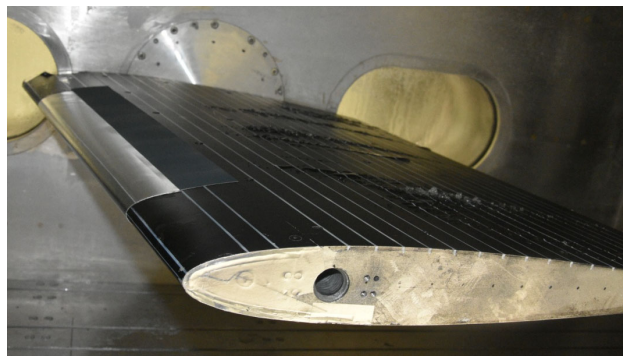


Figure 17. Runback ice forms after droplet impingement limit.

4. Conclusions

This paper investigated the sensitivity of the superhydrophobic coating range, heating range and power to icing environmental parameters. Based on the results of the tests, the following conclusions were derived:

1. IPS with a coating prevented runback ice formation and reduced the power consumption by more than 50% compared to IPS with no coatings.
2. IPS is highly sensitive to environment temperature. A designed IPS might not work well when environment temperature is beyond the design point.
3. IPS is sensitive to MVD which determines the area that needs to be protected and is less sensitive to LWC. Nonetheless, increased MVD and LWC at the same time may demand enhancing the IPS's heating power.
4. The droplet impingement area is where the superhydrophobic coating works. The coating cannot promote all the water falling off when situated outside the impinge-

ment area. Therefore, the superhydrophobic coating needs to cover the droplet impingement area only.

5. Sufficient heating power is required to keep the surface temperature of the superhydrophobic coating above the freezing point. Effective heat distribution on the surface is critical to IPS design.

In general, when applying the new IPS method that combines thermoelectric and superhydrophobic coatings to an aircraft, the design of its protection range requires no additional consideration compared to conventional designs. In terms of energy consumption, it is necessary to ensure that the surface temperature is above 0 °C or slightly higher for optimal anti-icing performance. However, the addition of superhydrophobic coatings may result in a decrease in the heat transfer efficiency. Thus, the measured and adjustable temperature inside the model needs to be a little higher than the temperature one wants to achieve on the surface of the superhydrophobic coating. Detailed research on the heat transfer process and temperature variations is likely to be necessary in the future.

Author Contributions: Conceptualization, L.Y. and D.Z.; Methodology, L.Y.; Software, Y.W.; Validation, Y.W. and H.Z.; Data curation, H.Z.; Writing—original draft, L.Y.; Writing—review & editing, L.Y.; Supervision, D.Z.; Project administration, D.Z. All authors have read and agreed to the published version of the manuscript.

Funding: This research was funded by the National Key R&D Program of China, grant number 2022YFE0203700.

Data Availability Statement: Not applicable.

Acknowledgments: We acknowledge the Liaoning Provincial Key Laboratory of Aircraft Ice Protection, Joint Research Center for Advanced Materials and Anti-icing of Tsinghua University (SMSE)-AVIC ARI and the China-Italy Joint Laboratory on Green Aviation Technology for the support for this research.

Conflicts of Interest: The authors declare no conflict of interest.

References



1. Thomas, S.K.; Cassoni, R.P.; MacArthur, C.D. Aircraft Anti-Icing and De-Icing Techniques and Modeling. *J. Aircr.* **1996**, *33*, 841–854. [CrossRef]
2. Papadakis, M.; Wong, S.H. Parametric Investigation of a Bleed Air Ice Protection System. In Proceedings of the 44th AIAA Aerospace Sciences Meeting and Exhibit, Reno, NV, USA, 9–12 January 2006; p. 1013.
3. Wright, W.B.; Keith, T.G. Numerical Simulation of Icing, Deicing and Shedding. In Proceedings of the 29th Aerospace Sciences Meeting, Reno, NV, USA, 7–10 January 1991; p. 665.
4. Alegre, N.; Hammond, D. Experimental Setup for the Study of Runback Ice at Full Scale. *J. Aircr.* **2011**, *48*, 1978–1983. [CrossRef]
5. Gent, R.W.; Ford, J.M.; Miller, D.R. *SLD Research in the UK*; SAE International: Montreal, QC, Canada, 2003.
6. Rosen, K.M.; Potash, M.L. 40 years of helicopter ice protection experience at Sikorsky Aircraft. In Proceedings of the AIAA 19th Aerospace Sciences Meeting, St. Louis, MO, USA, 12–15 January 1981.
7. Fortin, G.; Beisswenger, A.; Perron, J. Centrifuge Adhesion Test to Evaluated Icephobic Coatings. In Proceedings of the 2nd Atmospheric and Space Environment, Toronto, ON, Canada, 2–5 August 2010.
8. Laforte, C.; Beisswenger, A. Icephobic Material Centrifuge Adhesion Test. In Proceedings of the 11th International Workshop on Atmospheric Icing on Structures, Montreal, QC, Canada, 12–16 June 2005.
9. Fortin, G.; Perron, J. Spinning Rotor Blade Tests in Icing Wind Tunnel, American Institute of Aeronautics and Astronautics. In Proceedings of the 1st Atmospheric and Space Environment, San Antonio, TX, USA, 22–25 June 2009.
10. Kimura, S.; Yamagishi, Y.; Sakabe, A.; Adachi, T.; Shimanuki, M. A new surface coating for prevention of icing on airfoils. In Proceedings of the SAE Aircraft and Engine Icing International Conference, Seville, Spain, 24–27 September 2007.
11. Cao, L.; Jones, A.K.; Sikka, V.K.; Wu, J.; Gao, D. Anti-icing superhydrophobic coatings. *Langmuir* **2009**, *25*, 12444–12448. [CrossRef] [PubMed]
12. Antonini, C.; Innocenti, M.; Horn, T.; Marengo, M.; Amirfazli, A. Understanding the effect of superhydrophobic coating on energy reduction in anti-icing systems. *Cold Reg. Sci. Technol.* **2011**, *67*, 58–67.
13. Mangini, D.; Antonini, C.; Marengo, M.; Amirfazli, A. Runback Ice Formation Mechanism on Hydrophilic and Superhydrophobic Surfaces. *Cold Reg. Sci. Technol.* **2015**, *109*, 53–60. [CrossRef]
14. Yin, L.; Zhu, L.; Wang, Q.; Ding, J.; Chen, Q. Superhydrophobicity of Natural and Artificial Surfaces under Controlled Condensation Conditions. *ACS Appl. Mater. Interfaces* **2011**, *3*, 1254–1260. [CrossRef] [PubMed]

15. Fortin, G.; Adomou, M.; Perron, J. *Experimental Study of Hybrid Anti-Icing Systems Combining Thermoelectric and Hydrophobic Coatings*; SAE International: Montreal, QC, Canada, 2011.
16. De Pauw, D.; Dolatabadi, A. Effect of Superhydrophobic Coating on the Anti-Icing and Deicing of an Airfoil. *J. Aircr.* **2017**, *54*, 490–499. [CrossRef]

Disclaimer/Publisher's Note: The statements, opinions and data contained in all publications are solely those of the individual author(s) and contributor(s) and not of MDPI and/or the editor(s). MDPI and/or the editor(s) disclaim responsibility for any injury to people or property resulting from any ideas, methods, instructions or products referred to in the content.

Review

A Review on Ultrafast Laser Enabled Excellent Superhydrophobic Anti-Icing Performances

Lizhong Wang¹, Huanyu Zhao², Dongyu Zhu², Li Yuan², Hongjun Zhang¹, Peixun Fan¹ and Minlin Zhong^{1,*}

¹ Laser Materials Processing Research Center, Key Laboratory for Advanced Materials Processing Technology (Ministry of Education), Joint Research Center for Advanced Materials & Anti-Icing of Tsinghua University (SMSE)-AVIC ARI, School of Materials Science and Engineering, Tsinghua University, Beijing 100084, China; wlz20@mails.tsinghua.edu.cn (L.W.)

² Liaoning Provincial Key Laboratory of Aircraft Ice Protection, AVIC Aerodynamics Research Institute, Shenyang 110034, China

* Correspondence: zhml@tsinghua.edu.cn

Abstract: Fabricating and developing superhydrophobic anti-icing surfaces have been a research hotspot for eliminating undesired icing issues. Among various fabricating strategies, ultrafast laser micro-nano fabrication is regarded as a greatly promising technique owing to its advantages of high geometric accuracy, highly flexible microstructure or dimension availability, no contact, and no material limitation. A number of diverse micro-nanostructured superhydrophobic surfaces have been developed by ultrafast lasers and demonstrated extraordinary anti-icing properties. They are collectively known as ultrafast laser-fabricated superhydrophobic anti-icing surfaces (ULSAs). In this article, we reviewed the recent advances in ULSAs from micro-nano structure fabricating to anti-icing performances and to potential applications. The surface wettability and mechanisms of ultrafast laser micro-nano fabrication are first introduced, showing the strong ability of ultrafast laser for fabricating superhydrophobic surfaces. Then the deepened understanding of the relationship between superhydrophobicity and icephobicity is discussed in detail, including Cassie–Baxter stability, surface durability and environmental adaptability. Eventually, the passive anti-icing technique, the passive/active combined anti-icing technique and their practical applications are presented together with current challenges and future prospects.

check for
updates

Citation: Wang, L.; Zhao, H.; Zhu, D.; Yuan, L.; Zhang, H.; Fan, P.; Zhong, M. A Review on Ultrafast Laser Enabled Excellent Superhydrophobic Anti-Icing Performances. *Appl. Sci.* **2023**, *13*, 5478. <https://doi.org/10.3390/app13095478>

Academic Editor: José A. Jiménez

Received: 28 March 2023

Revised: 10 April 2023

Accepted: 23 April 2023

Published: 28 April 2023



Copyright: © 2023 by the authors. Licensee MDPI, Basel, Switzerland. This article is an open access article distributed under the terms and conditions of the Creative Commons Attribution (CC BY) license (<https://creativecommons.org/licenses/by/4.0/>).

Keywords: ultrafast laser; superhydrophobic; anti-icing

1. Introduction

Icing phenomena have brought tremendous troubles in many fields such as telecommunication, transportation, energy, etc. [1–4]. Especially in aviation applications, the formed and accumulated ice on airplanes greatly damages aerodynamic properties [5–7]. It has been shown that mm-thick ice on airfoils will result in about 30% loss of lift force per unit area, eventually causing catastrophic accidents [8,9]. In recent years, many crashes related to icing have taken place. To eliminate ice formation and build-up, some conventional anti/deicing technologies such as electrothermal, pneumatic, and ultrasonic deicing have been developed and widely used [10–12]. This notwithstanding, such active deicing strategies tend to be extremely wasteful of energy, are of low-efficiency, and not environmentally friendly [13]. These drawbacks overwhelmingly restrict their applications in situations such as for diminutive airplanes from drones to warcraft and some industrial applications from pipelines to power lines [14,15]. Therefore, novel anti/deicing technologies are in urgent need of researching and developing to meet the application demands.

Inspired by the water repellency of the lotus in nature, superhydrophobic surfaces (SHSs) have been one of the most promising candidates for achieving passive anti/deicing [16,17]. With extremely high contact angles of $>150^\circ$ and low sliding angles of $<10^\circ$, SHSs can significantly reduce the solid-liquid contact area to repel external water droplets in time

and thus keep surfaces dry [18–20]. The unique properties have attracted a flurry of researchers and engineers to pay great attention to moving SHSs toward anti-icing applications [21–24]. Figure 1 shows the increasing number of published articles on the topic of “anti-icing” and “superhydrophobic anti-icing” in recent years. Among these, papers about superhydrophobic anti-icing account for about one-quarter of all publications, showing their dominant role. However, with the deepening of research, it is found that superhydrophobic surfaces cannot always eliminate icing issues and have greater ice adhesion strengths than smooth pristine surfaces in some cases [25,26]. With regard to mechanisms, superhydrophobicity is mainly attributed to a large number of trapped air pockets among micro-nanostructures, where a triple-phase solid-liquid-gas interface will be constructed. However, the air pockets are very fragile. Once they are broken, greater ice adhesion will be generated owing to the mechanical locking between ice and micro-nanostructures. In this case, the micro-nanostructures also provide more ice nucleation sites to promote the icing process [27–29]. These negative results have given rise to a number of debates on whether SHSs are advantageous for anti-icing applications. Kreder et al. compared different types of anti-icing surfaces, including superhydrophobic surfaces, slippery surfaces, and hydrated surfaces. They emphasized the decisive role of surface structures on anti-icing properties [30]. To further understand the relationship between superhydrophobicity and icephobicity and explore the optimized superhydrophobic anti-icing surfaces, fabricating and easily controlling micro-nanostructures is of great significance.

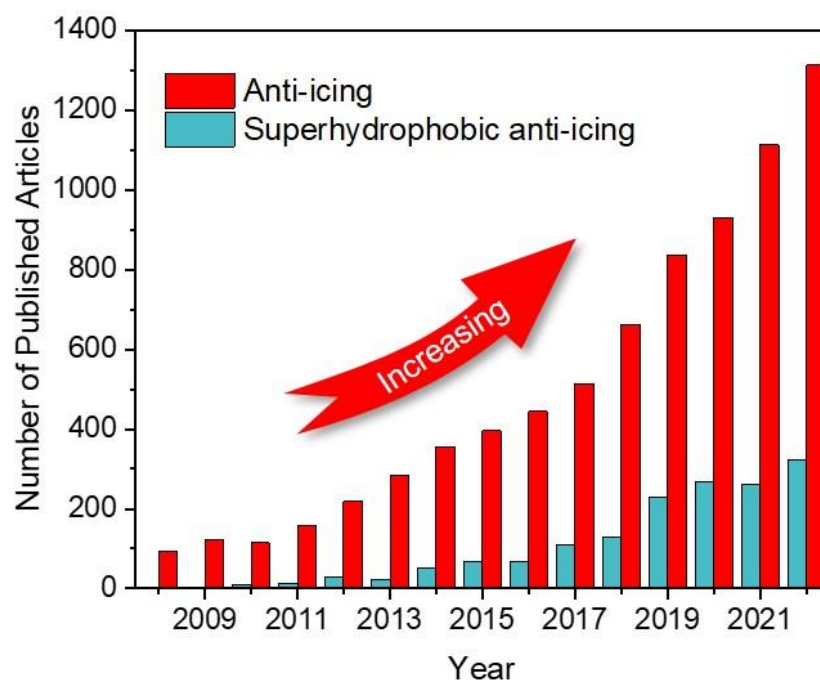


Figure 1. Number of published articles per year indexed by Web of Science. The keywords for searching are “anti-icing” and “superhydrophobic anti-icing”.

To date, many state-of-the-art strategies have been developed to fabricate micro-nanostructures, including chemical etching, machining, 3D printing, sol–gel methods, laser processing, and others [31–35]. Among these, ultrafast laser micro-nano fabricating, as a novel top-down processing strategy, shows the superior advantages of nm-accuracy, contact-free, and highly programmable processing without material dependence. This method is not only easy for fabricating surface micro-nanostructures but also greatly promising for practical applications [36–39] (Table 1). Meanwhile, compared to other conventional lasers with continuous wave and short pulses, ultrafast lasers have an ultrashort pulse width from several tens of femtoseconds to tens of picoseconds, which is equivalent to or shorter than the heat conduction time of an electron lattice. Hence, a smaller

heat-affected zone and higher processing quality could be realized [40,41]. Generally, the surface structures formed by ultrafast laser irradiation can be divided into two types: laser-ablated structures (arrayed microstructures) and laser-induced structures (random and/or periodic nanostructures) [42,43]. The former's geometry is mainly determined by the ablation process with intense laser energy interaction with materials and can be closely controlled by user-defined structure shapes. The most typical representative of the latter, the laser-induced periodic surface structure (LIPPS), is formed by linearly polarized laser radiation with fluences slightly above the ablation threshold [44]. By varying laser processing conditions such as wavelength, pulse duration, power density, incidence angle, scanning speed, and processing environments, the morphologies of LIPPS could also be closely controlled. Adopting the above two structures, microscale and nanoscale structures on surfaces could be easily and tunably fabricated with ultrafast lasers. In the meantime, during laser ablation, the plasma plume contains abundant energetic species, which reunite and rapidly deposit on microstructures to form nanostructures, thus constituting the hierarchical micro-nanostructures [45–47]. The fabrication of various micro/nanostructures enabled by ultrafast lasers has paved a solid pathway to preparing SHSs. Although most materials such as metals and ceramics are intrinsically hydrophilic so that the superhydrophilic interfaces are produced after laser processing, the superhydrophobicity can be easily achieved by surface chemical modification, including vapor deposition, solution immersing, spinning coating, and so on [48–50]. Many reports and advances have been produced in fabricating SHSs and controlling their superhydrophobic states by ultrafast lasers [51,52]. Compared to the SHSs fabricated by other methods, laser-fabricated superhydrophobic surfaces have shown tremendous advantages in durability, stability, and repeatability as well as high tunability [53–56]. Many reviews have summarized laser-fabricated superhydrophobic surfaces in various application scenarios [40,42,57]. Specifically, research articles about ultrafast laser-fabricated superhydrophobic anti-icing surfaces (ULSASs) have sprung up in recent years [58–61], as shown in Figure 2. However, to our best knowledge, related reviews and perspectives are rarely reported. In response to the special issue “Superhydrophobic and Icephobic Coatings”, it is of significance and value to summarize recent progress in ULSASs and to propose current challenges and future prospects.

Table 1. Comparison of common micro-nanofabrication techniques in terms of fabrication rate, accuracy, structural tunability, applicable materials, and large-scale fabricating.

Methods	Accuracy	Structural Tunability	Applicable Materials	Large-Scale Fabricating	Refs.
Ultrafast laser processing	nm	✓	Any materials	✓	[62–64]
Chemical treatment	nm	×	Metals	✓	[65–67]
Photolithography	nm	✓	Silicon	×	[68,69]
Template methods	nm	✓	Polymer, metal	✓	[70–72]
Machining	μm	✓	Any materials	✓	[73,74]
3D printing *	μm	✓	Polymer, metal, ceramics	×	[35,75]
Sol-gel methods	nm	×	Polymer	✓	[76,77]

* Here, we take two-photon lithography (TPL) as the representative of 3D printing.

In this review, we focus on ultrafast laser enabled superhydrophobic anti-icing performances and draw examples from surface fabrication, anti-icing mechanisms, and advances and applications, as shown in Figure 3. The fundamental wettability and ultrafast laser micro-nano fabricating examples are discussed first, elucidating the structural diversity and tunability of ultrafast laser fabricating. Adopting ultrafast laser-fabricated SHSs, some novel and interesting phenomena involving icing and melting processes are discussed with a deepened understanding of the relationship between superhydrophobicity and icephobicity. We clarify that superhydrophobicity is one necessary but insufficient condition of icephobicity and present three common failure factors of superhydrophobic anti-icing surfaces, including Cassie–Baxter stability, surface durability, and environmental adaptivity.

The next section introduces the recent progress of ULSASs in the three aspects of passive anti-icing, passive/active combined anti-icing, and their practical outdoor applications in detail. Combining the storylines from fabrication to mechanisms and then to applications, we present current challenges in moving ULSASs toward practical applications. Finally, we give a conclusion and provide prospects for the future development of ULSASs.

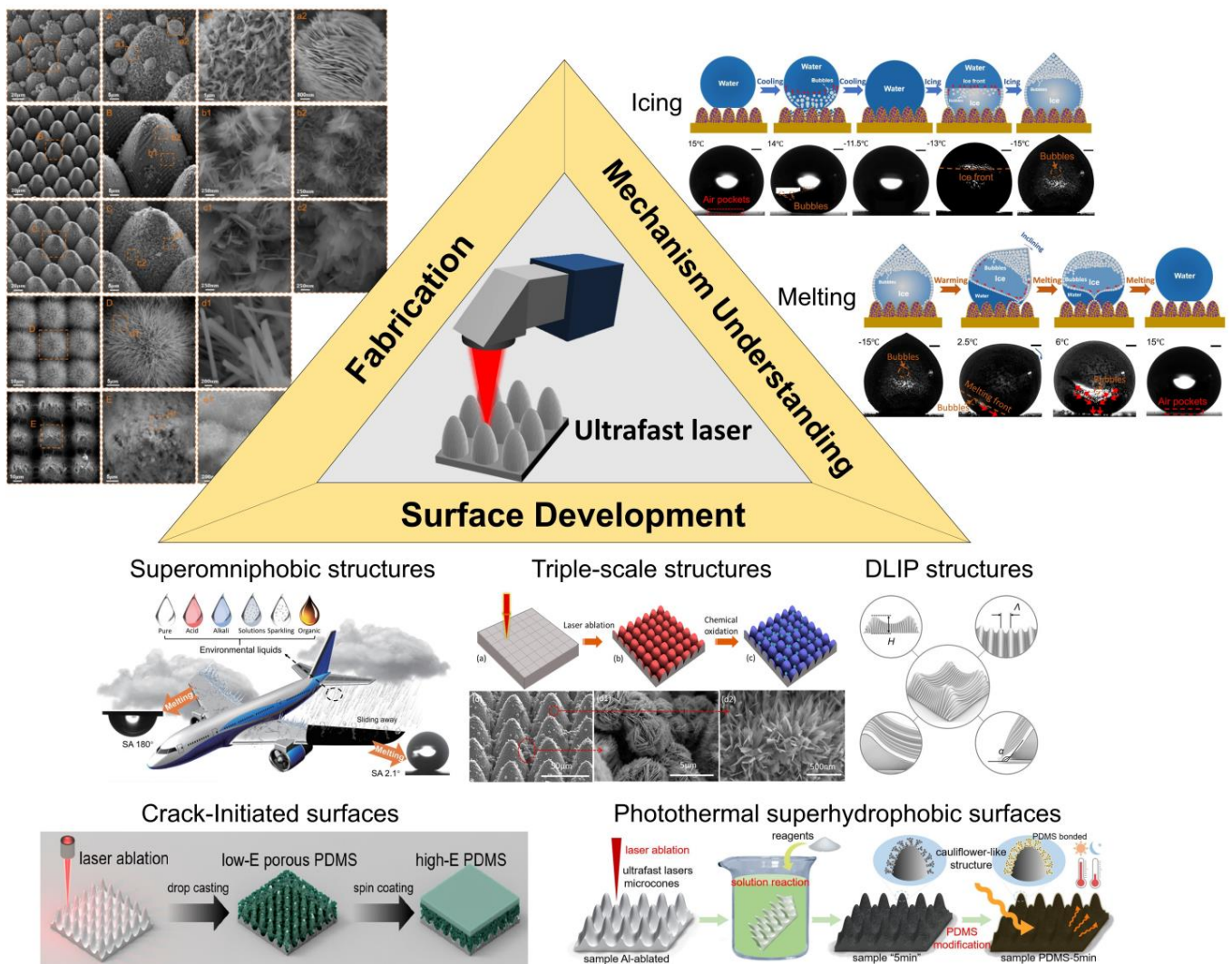


Figure 2. Ultrafast laser-fabricated superhydrophobic anti-icing surfaces: fabrication, mechanism understanding and surface development. Reproduced with permission from [78], copyright (2022) Springer; reproduced with permission from [79], copyright (2022) Nature Publishing Group; reproduced with permission from [80], copyright (2020) American Chemical Society; reproduced with permission from [81], copyright (2023) American Chemical Society; reproduced with permission from [6], copyright (2023) American Chemical Society; reproduced with permission from [82], copyright (2022) Elsevier.

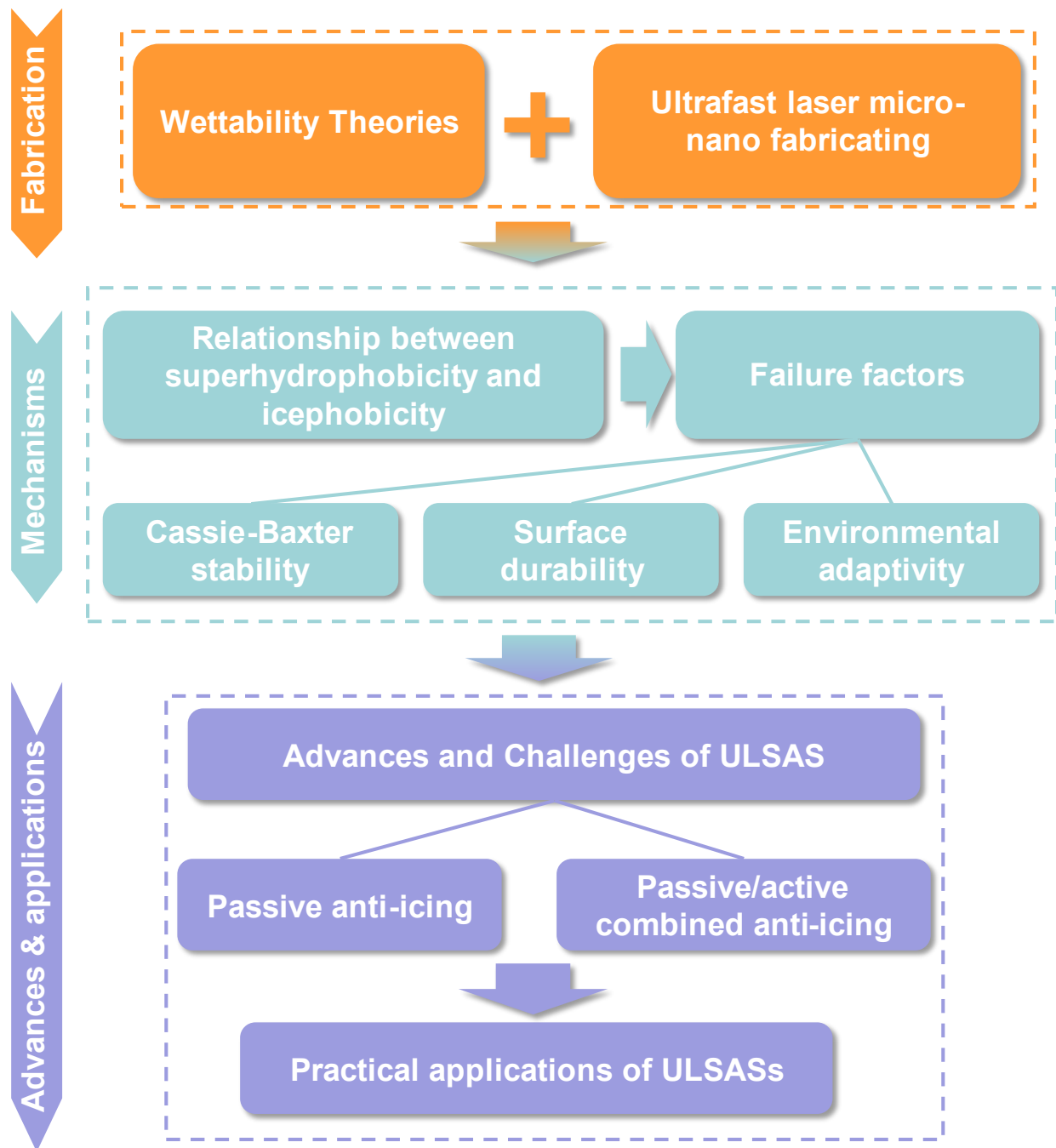


Figure 3. Flow chart describing the arrangement and order of each part in this review.

2. Ultrafast Laser-Fabricating Micro-Nanostructured Superhydrophobic Surfaces

2.1. Wettability and Superhydrophobicity

Surface wettability represents the ability of liquids to spread on surfaces. When the spreading reaches the equilibrium, droplets statically rest on surfaces and form an angle, namely, contact angle θ (CA). From thermodynamics, CA is the characterization of three-phase interfacial free energies. Back in 1805, the relationship between them has been well described by Young's equation [83], as shown in Figure 4a:

$$\cos\theta = (\gamma_{sv} - \gamma_{ls})/\gamma_{lv} \quad (1)$$

where γ_{sv} , γ_{ls} and γ_{lv} denote the interface tensions of solid-vapor, liquid-solid, and liquid-vapor, respectively. Although Young's equation establishes the qualitative relationship

between interfacial energies and wettability, it is not appropriate for describing rough surfaces in the real world. Wenzel et al. introduced the roughness factor r and took the apparent contact angle θ^* to characterize surface wettability [84], as shown in the following equation:

$$\cos\theta^* = r \cdot (\gamma_{sv} - \gamma_{ls}) / \gamma_{lv} = r \cdot \cos\theta \quad (2)$$

where the roughness factor r is the ratio of the actual solid-liquid contact area to the nominal contact area. However, the model is limited to the occasion that liquids completely penetrate micro-nano valleys and cannot explain some common wetting phenomena in nature such as the rolling droplets on lotuses. Cassie and Baxter further introduced the contact fractions of liquid-solid f_{ls} and liquid-vapor f_{lv} to describe the mixed triple-phase interfaces [85]. Considering $f_{ls} + f_{lv} = 1$, the Cassie–Baxter equation is expressed by:

$$\cos\theta^* = f_{ls} \cdot \cos\theta - 1 + f_{ls} \quad (3)$$

Generally, droplets on superhydrophobic surfaces show a large CA and low adhesion strength. Contact angle hysteresis is one of the most common evaluation standards of droplet adhesion. The maximum and minimum static CAs are defined as the advancing angle θ_{adv} and receding angle θ_{rec} , respectively. The difference between θ_{adv} and θ_{rec} is the contact angle hysteresis (CAH), as shown in Figure 4a. Smaller CAHs mean smaller adhesion forces exist between interfaces so that droplets can move on surfaces more easily. In this case, surfaces have better liquid-repellency [86,87]. In nature, superhydrophobic phenomena exist widely. For example, luxuriant micropapillae covered by low-surface-energy epicuticular wax endow lotuses with excellent superhydrophobic and anti-fouling properties [88] (Figure 4(d1,d2)), and needle-shaped micro-nano setae combined with wax make water striders walk on rivers freely [89] (Figure 4(e1,e2)). Meanwhile, diverse micro-nanostructure arrangements also bring about many unique superhydrophobic properties, such as the high droplet adhesion on rose petals enabled by single-tier microstructures (Figure 4(f1,f2)) [90], directional adhesion on rice leaves [88] and butterflies enabled by directional microgrooves [91] (Figure 4(g1,g2,h1,h2)), and the anti-fogging properties on mosquito eyes enabled by elaborate nanonipples [92] (Figure 4(i1,i2)).

2.2. Ultrafast Laser Micro-Nano Fabricating

As discussed above, ultrafast lasers have many incomparable advantages in micro-nanofabrication. These advantages are not only ascribed to the convenience and programmability of processing methods but also attributed to the complicated light-matter interactions [39,93]. Generally, ultrafast lasers are defined as lasers with ultrashort pulse duration from several tens of femtoseconds to tens of picoseconds [94]. Figure 5a shows the timescales and intensity of the main phenomena during and after irradiating a solid with a femtosecond laser. The light-matter interacting processes could be divided mainly into three types: electronic excitation, nonequilibrium phase transformation, and morphology formation [95], as illustrated in Figure 5a. Overall, in most cases, electronic excitation occurs during the laser pulse (fs—ps), and nonequilibrium phase transformations take place on the picosecond timescale (about ps—100 ps). The timescale of morphology formation reaches up to nanoseconds (about ns—100 ns). There also exist some differences when processing different materials. For semiconductors or dielectrics, the irradiated laser on the one hand can prompt the generation of high-concentration free electrons across the bandgap, which might further induce non-thermal melting. Meanwhile, on the other hand, the laser also provides the excited electrons with more energy, triggering the switching to the plasma state or producing a coulomb explosion. When reaching the electron lattice equilibration, rapid heating at a rate of $>10^{14}$ K/s occurs to further lead to homogeneous melting or the formation of a supercritical fluid [96]. Many new surface morphologies or metastable phases are produced in extreme environments. After the temperature decreases below material melting points, the melts start to solidify or resolidify to form surface micro-nanostructures. For metals, laser-induced electron heating dominates, resulting in

localized high-temperature melting. However, the high thermal conductivities of metals can additionally result in a high supercooling state, where some unexpected structures or defects will be constructed, such as some amorphous structures or nanocrystals [97,98].

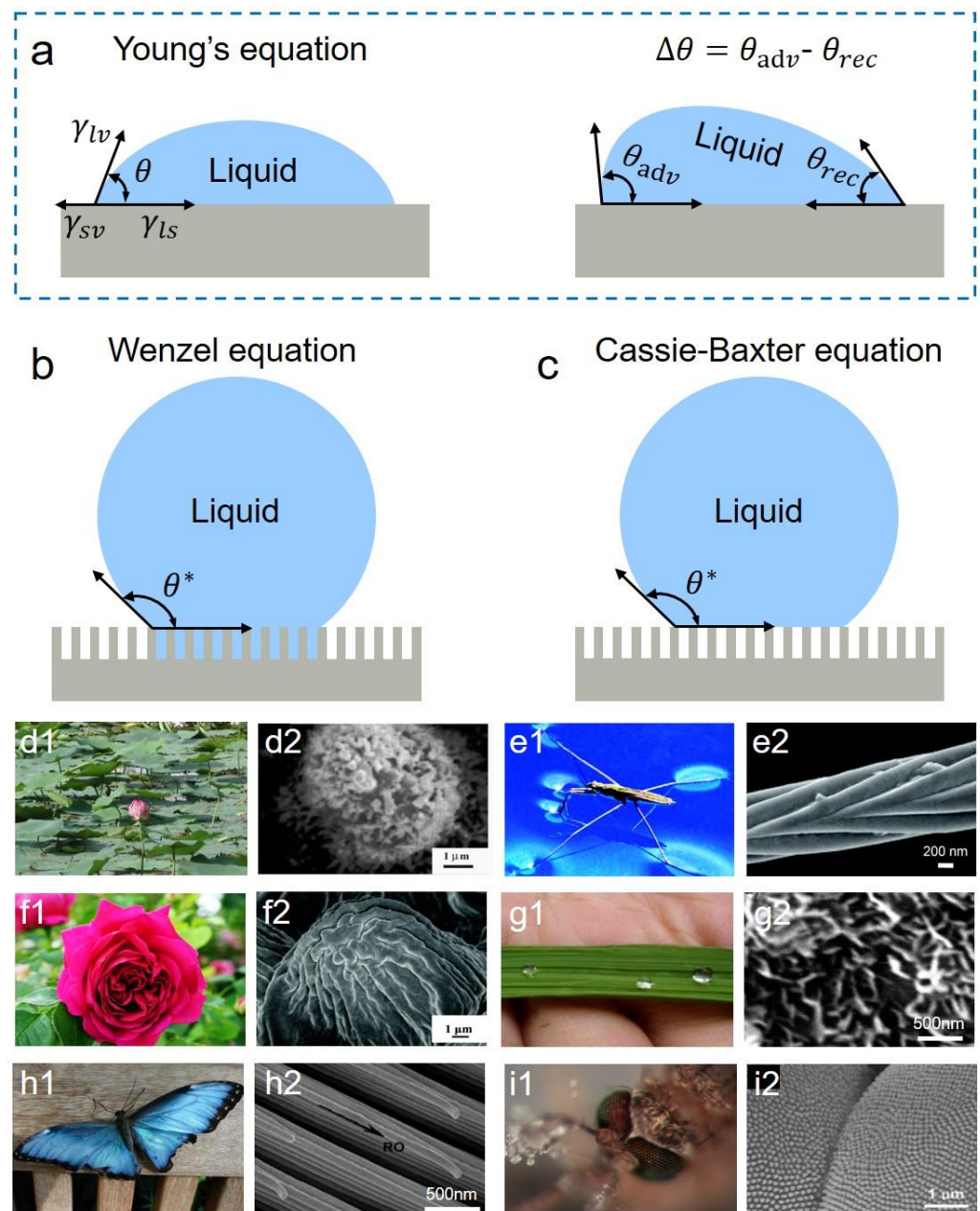


Figure 4. Three classical wetting states and the superhydrophobic phenomena in nature. (a–c) Schematics of the three states: (a) Young’s equation; (b) Wenzel equation; (c) Cassie–Baxter equation. (d–i) Creatures with superhydrophobicity: (d1,d2) lotus leaves (reproduced with permission from [88]. Copyright (2007) Elsevier); (e1,e2) water striders (reproduced with permission from [89]. Copyright (2007) American Chemical Society); (f1,f2) rose petals (reproduced with permission from [90]. Copyright (2008) American Chemical Society); (g1,g2) rice leaves (reproduced with permission from [88]. Copyright (2007) Elsevier); (h1,h2) butterflies (reproduced with permission from [91]. Copyright (2018) American Chemical Society); (i1,i2) mosquito eyes (reproduced with permission from [92]. Copyright (2007) John Wiley and Sons).

Following the interaction mechanisms between ultrafast lasers and matter, numerous diverse micro-nanostructures can be easily fabricated and can be further tuned by varying

laser processing parameters or adjusting processing environments. Some common laser parameters include laser wavelengths, pulse duration, pulse repetition frequency, pulse input number, laser fluence, and so on [39,99]. Here, we take two important parameters (laser pulse duration and pulse input number) as examples to introduce their effects on micro-nanostructures. Generally, different laser pulse durations result in different heat affected zones, eventually affecting the processing quality. As shown in Figure 5b, with the shortening of pulse duration from 10^{-9} to 10^{-15} , the processing quality gradually improves as a result of the smaller heat-affected zone [94]. This phenomenon is mainly attributed to the pulse durations of ultrafast laser (picosecond and femtosecond laser) being shorter than the electron-lattice relaxation time ($\sim 10^{-12}$ s). Hence, less heat is transferred, causing a smaller thermal effect. For the pulse input number, the micro-nanostructure sizes and morphologies are directly influenced. Figure 5c exhibits the evolution of micro-nanostructures with the pulse input number. It is found that the particles can be flexibly controlled not only in the wide range of nanoscale, sub-microscale, fine-microscale, microscale, and coarse-microscale but also with various structural sizes, including heights and intervals [100].

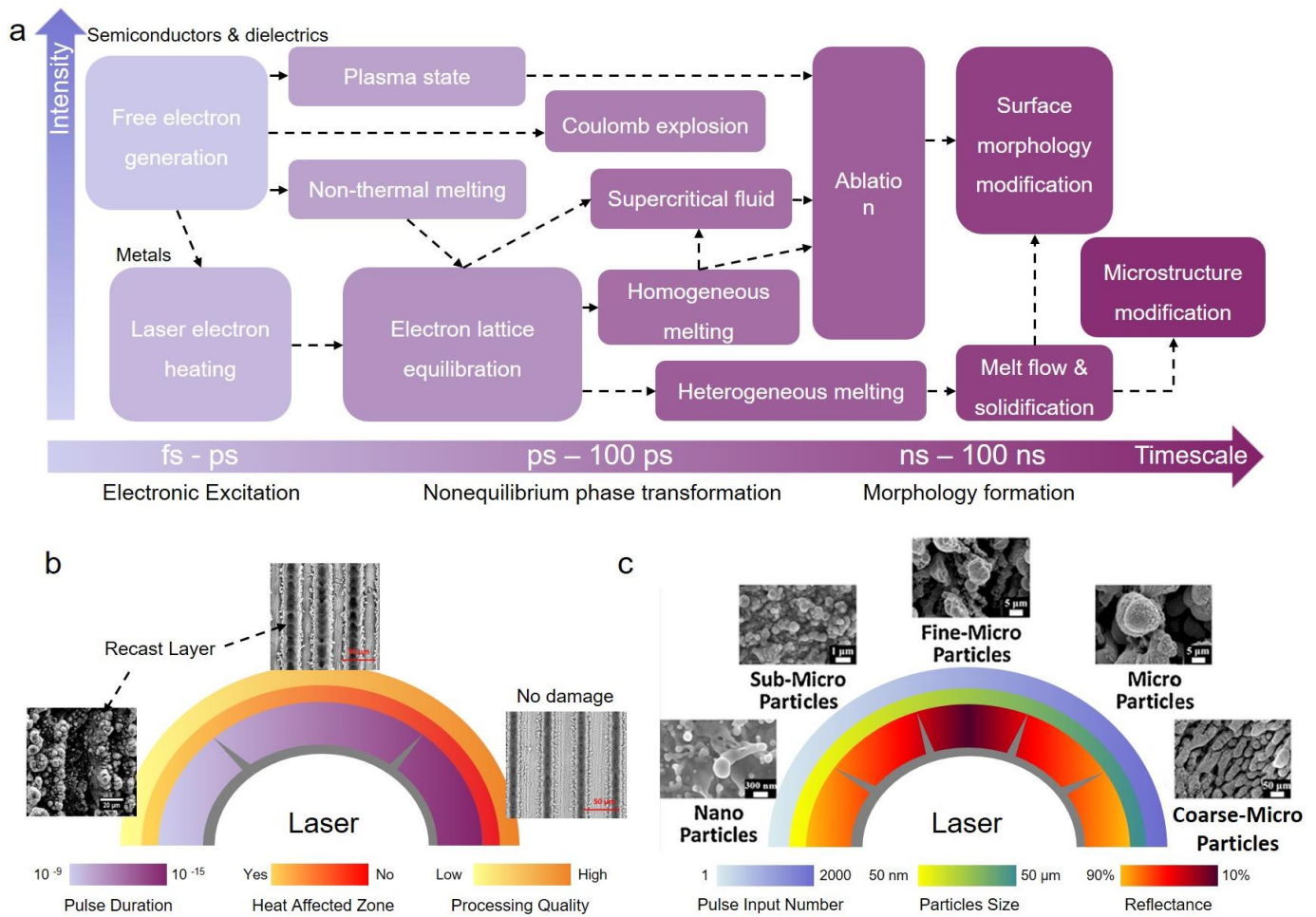


Figure 5. Mechanisms and morphologies of ultrafast laser micro-nano fabrication. (a) Timescales and intensity of main phenomena during and after irradiating a solid with a femtosecond laser. (b) Evolution of surface morphologies and processing quality with the laser wavelength (reproduced with permission from [101] (copyright (2021) Elsevier) and [102] (copyright (2019) Elsevier)). (c) Evolution of micro-nanostructure sizes with the laser pulse input number (reproduced with permission from [100]. Copyright (2015) Elsevier).

Besides the fundamental laser parameters, processing environments also play a significant role in structural morphologies and chemical elements. For example, we once adopted a femtosecond laser to process Ag samples in air and Argon atmosphere [103]. It was found that more nanoparticle clusters and less oxide were generated in Argon. In the meantime, by ablating NiFe in the NH₃ atmosphere, we also fabricated more abundant nanoclusters than in the air [104]. These discoveries confirm that the processing atmosphere has a great influence on micro-nanostructure morphologies.

Based on diverse processing parameters and environments, ultrafast laser-fabricated micro-nanostructures could be easily tuned to further realize the fine control for superhydrophobic states. Long et al. achieved the superhydrophobic state tunability from the Wenzel state to the CB state by simply changing the laser scanning speeds on the copper material [51]. The superhydrophobic state evolution was ascribed to the changes in microstructure sizes and nanostructure amounts, where lower scanning speeds could induce deeper microstructures and more abundant nanostructures to contribute to the CB state. Yin et al. discovered the controllable wettability on Polyimide film via femtosecond laser thermal accumulation engineering [105]. By regulating local thermal accumulation effects, different micro-nanostructures were induced, realizing the wettability changes from superhydrophobicity (~3.6°) to superhydrophobicity (~151.6°). Zheng et al. adopted a femtosecond laser to fabricate a temperature-response ceramic surface with switchable wettability [106]. Superhydrophobic and superhydrophilic interfaces were reversibly and repeatedly transitioned after alternate heating treatments. It was confirmed that laser-induced micro-nanostructures contributed to the removal and re-absorption of organic compounds, thus resulting in the wettability transition.

3. Anti-Icing Mechanisms of SHSs

Adopting diverse and tunable micro-nanostructures fabricated by ultrafast lasers, a large number of applications have been explored [48,107,108]. Among that, ULSAs have been extensively researched in recent years. Many new phenomena have been discovered to deepen the understanding of superhydrophobic anti-icing properties. In this section, we combine recent reports and our understanding to explain the relationship between superhydrophobicity and icephobicity and give the analysis of common failure factors of superhydrophobic anti-icing surfaces.

3.1. Relationship between Superhydrophobicity and Icephobicity

In terms of the interfacial states between droplets and micro-nanostructures, droplets on superhydrophobic surfaces mainly exhibit two states: Cassie-Baxter (CB) and Wenzel. Although droplets in both states have CAs exceeding 150°, their icephobicity performs differently [5]. Icephobicity works only when droplets are supported by air pockets to retain the CB state. However, once air pockets are broken, droplets will rapidly penetrate into the valleys and be stuck by surrounding micro-nanostructures. In this case, the SHSs not only lose their icephobicity but also bring about more icing danger such as easy-icing and ice difficult-removal [109]. Chen et al. reported that the Wenzel ice on SHSs even showed over four times higher ice adhesion strengths than on hydrophilic surfaces [25]. Hence, superhydrophobicity is not equal to icephobicity but is one necessary but not insufficient condition.

To ensure the icephobicity of superhydrophobic surfaces, droplets should retain the CB state but not the Wenzel state. Nonetheless, much research indicates droplets tend to passively transit from the CB state to the Wenzel state under external disturbances [79,110,111], such as freezing, vibration, external pressure, and so on. Affected by the energy barrier between the Wenzel state and the CB state, the spontaneously reversible transition was once regarded as impossible. Many experts have systematically investigated the icing and melting processes on different micro-nanostructured superhydrophobic surfaces [79]. Although some found ultralow ice adhesion strengths for mL-scale ice columns, the transition from the CB state to the Wenzel state still inevitably occurred when the droplet size

diminished to the μL -scale. Figure 6 shows the icing and melting processes of droplets on laser-fabricated superhydrophobic surfaces. Compared to other SHSs, it was discovered that droplets on laser-fabricated SHSs possessed a significantly delayed icing ability, which contributed to more bubbles dissolving in supercooled droplets and further dissolving out in ice droplets. During melting processes, these bubbles could spontaneously and rapidly impact downwards under the Marangoni effect, leading to the recovery of the CB state. The dewetting transitions were closely related to surface structures, which further affected the superhydrophobicity, the delayed icing time, and the liquid retraction resistance forces. Although it was confirmed that laser-induced micro-nanostructures could well ensure the robustness of dewetting transitions, the room-temperature superhydrophobicity was still overwhelmingly different from the low-temperature icephobicity owing to complex interfacial interactions at low temperatures [112]. To ensure the anti-icing properties of SHSs, extraordinary superhydrophobicity is undoubtedly one of the most significant conditions, but there are still many other factors that need to be guaranteed. As follows, three main failure factors of superhydrophobic anti-icing surfaces are discussed.

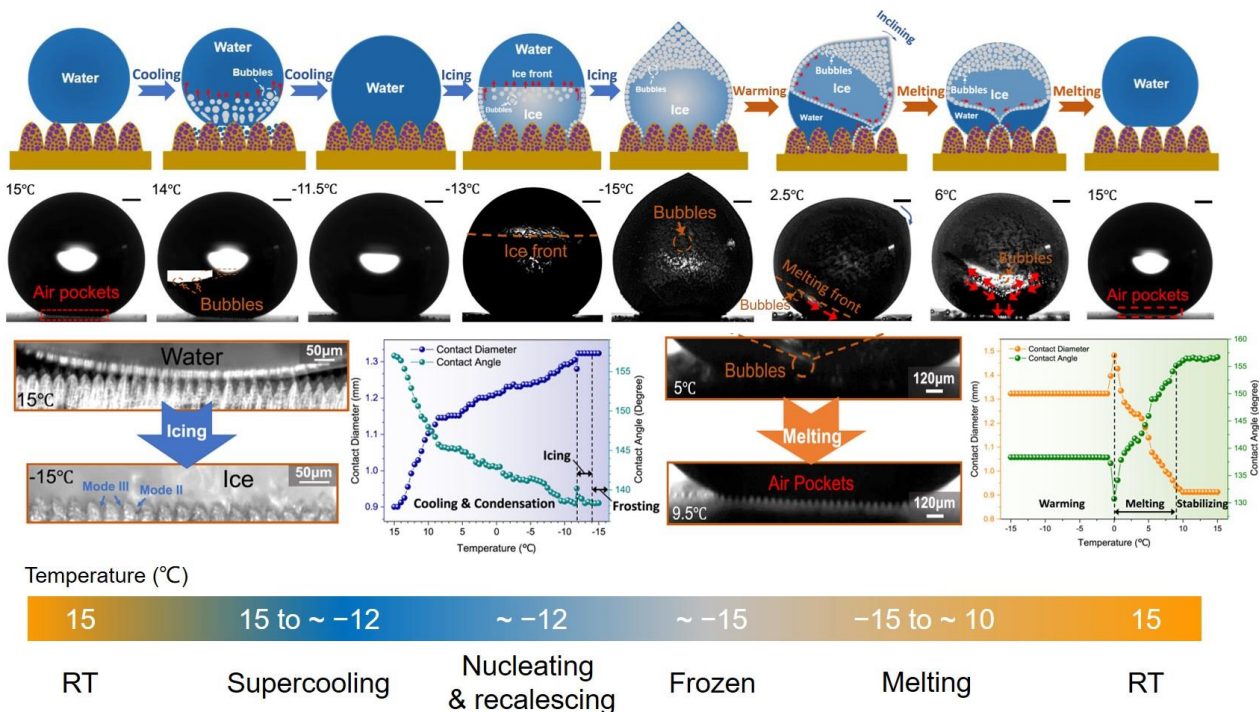


Figure 6. Icing and melting processes on the superhydrophobic surfaces fabricated by ultrafast laser (reproduced with permission from [79], copyright (2022) Nature Publishing Group).

3.2. Failure Factors of Superhydrophobic Anti-Icing Surfaces

3.2.1. Cassie–Baxter Stability

The CB stability represents the ability of SHSs to withstand the impalement of air pockets by droplets [113,114]. In room-temperature environments, the CB stability is evaluated by the Laplace pressure of droplets, namely, $P = 2\gamma/R_d$, where γ is the liquid surface tension and R_d is the radius of droplets. Higher CB stability means that SHSs can withstand higher Laplace pressure to retain the CB state of droplets. The critical Laplace pressure P_C is generally determined by two criteria [80,115]: (i) the critical Laplace pressure for the CA at the moment of droplet transiting from the superhydrophobic state to the hydrophobic state (P_{CCA}); and (ii) the critical Laplace pressure for the contact diameter at the moment of the triple-phase line stops retracting (P_{CCD}). In terms of the two criteria, P_C is expressed by:

$$\begin{cases} P_C = P_{CCA}, & \text{if } P_{CCA} < P_{CCD} \\ P_C = P_{CCD}, & \text{if } P_{CCA} > P_{CCD} \end{cases} \quad (4)$$

Many researches have confirmed that some finely designed ultrafast laser-fabricated SHSs show superior CB stability at room temperature owing to highly controllable and robust micro-nanostructures [115–117]. It is widely accepted that SHSs with higher P_C could show better anti-icing properties. Pan et al. combined ultrafast laser ablation and chemical oxidation to fabricate two types of three-tier micro-nanostructures: the microcone-microflower-nanosheet (MNSF) and the microcone-microflower-nanograss (MNGF) [80]. The two surfaces showed ultrahigh room-temperature CB stability with the highest critical Laplace pressure of ~ 1450 Pa among all the published reports (Figure 7a,b). However, although the two surfaces showed similar CB stability at room temperature, there still existed significant differences in their anti-icing properties. For example, the ice adhesion strength on MNGF was only 1.7 kPa while that on the MNSF reached 16.9 kPa (Figure 7c). The results indicated that room-temperature P_C was not appropriate for evaluating the low-temperature Cassie–Baxter stability. Focusing on this problem, related calculation models based on icing phenomena were recently established to evaluate the low-temperature CB stability of SHSs with air pocket pressure (Figure 8a,b) [118]. It was found that both microstructure morphologies and temperatures had a great influence on the air pocket pressure. Among these, the open-cell microstructures had higher air pocket pressure at low temperatures than the semi-open or closed microstructures, thus showing higher CB stability. As demonstrated in Figure 8c,d, the anti-icing properties corresponded well to the air pocket stability induced by microstructures, where the SHSs with more open-cell structures showed better and robust anti-icing properties. Hence, to avoid the failure of superhydrophobic anti-icing surfaces, open-cell structures should be adopted to maintain the low-temperature CB stability.

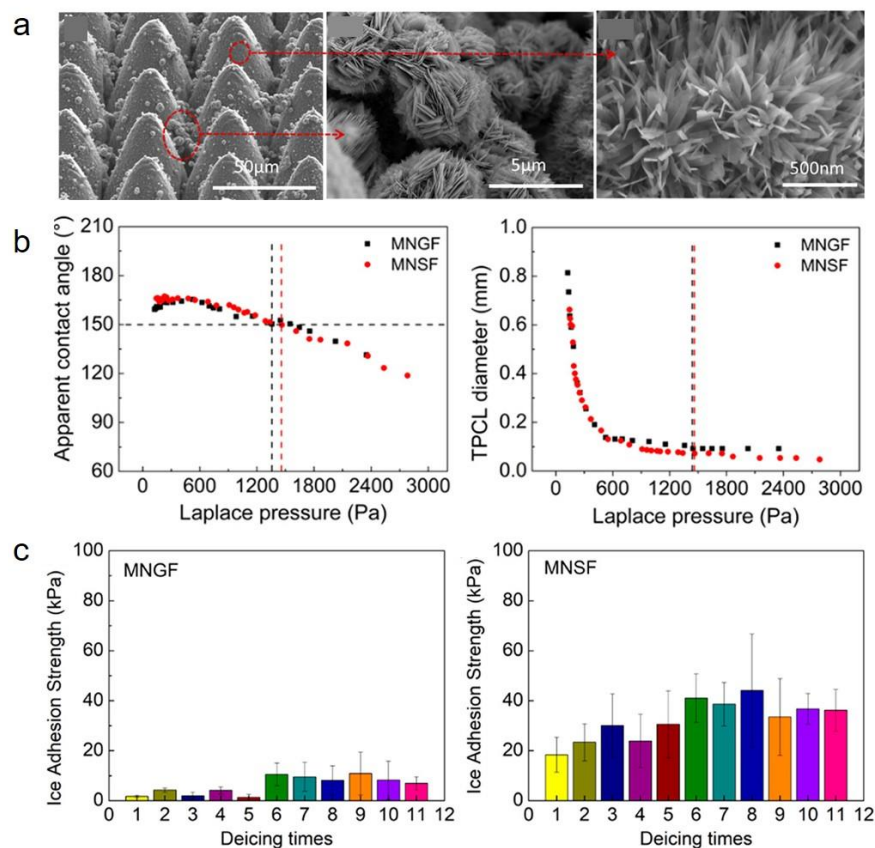


Figure 7. Morphologies (a), CB stability (b) and ice adhesion strengths (c) of laser-fabricated superhydrophobic surfaces. MNGF denotes the surface with microcone-microflower-nanosheet structures while MNSF denotes the surface with microcone-microflower-nanograss structures. The SEM images in (a) are from the MNGF surfaces. (Reproduced with permission from [80]. Copyright (2020) American Chemical Society.)

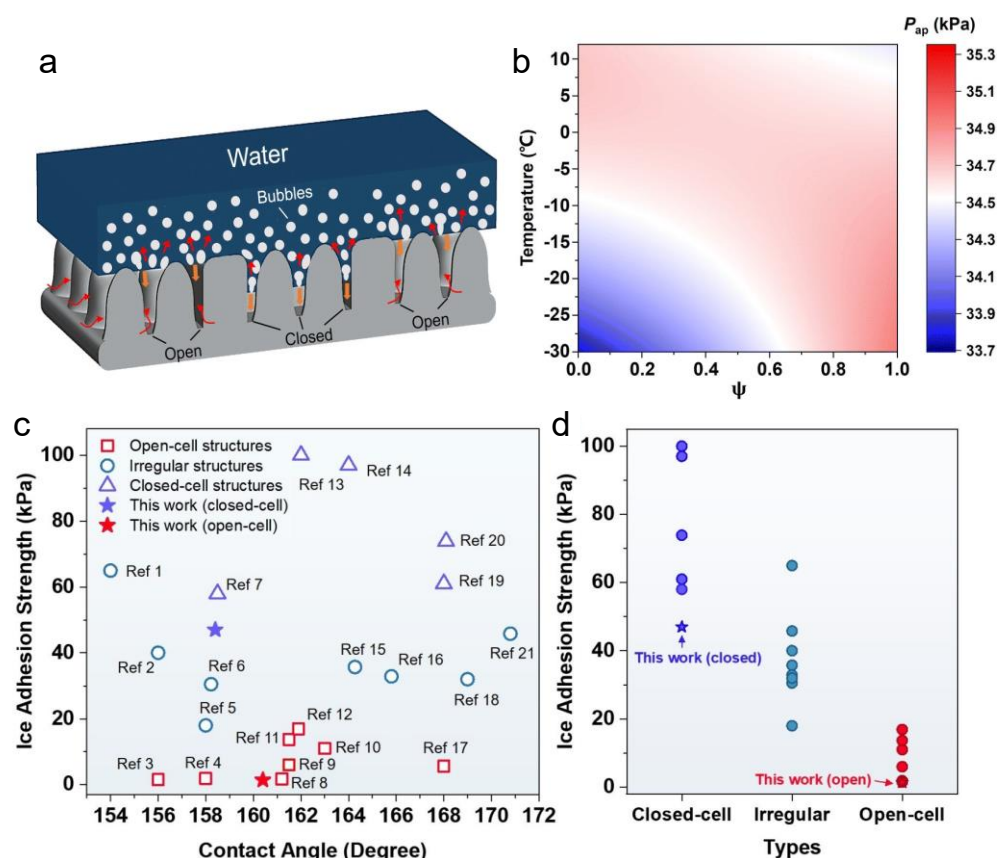


Figure 8. Effect of air pocket stability at low temperatures on anti-icing performances. (a) Schematics displaying the triple-phase interface changes during icing processes. (b) Phase diagram of air pocket pressure at different temperatures and on the surfaces with different closed/open area ratios. (c) Comparison of ice adhesion strengths on different surfaces with different structural types and contact angles. (d) Comparison of ice adhesion strengths on the surfaces with different structural types. (Reproduced with permission from [118]. Copyright (2023) Royal Society of Chemistry.)

3.2.2. Surface Durability

Surface durability plays a key role in long-term practical applications. Among these, micro-nanostructures and low-surface-energy coatings are two crucial factors. For micro-nanostructures, it is well-known that the structures on SHSs are generally fragile and can be abraded easily when subjected to external shear forces [119]. To improve structural durability, much research has conducted [120,121]. In the best-known study, Wang et al. used armor-like microstructures combined with nanoparticles to realize ultrahigh superhydrophobic durability [87]. However, based on the above analysis, the introduction of armor-like microstructures would result in a decrease in air pocket pressure at low temperatures, eventually causing the failure of anti-icing properties. Hence, the closed-cell structures are not icephobic-durable (Figure 9a). Both room-temperature durability and icephobic durability need to be met for long-term anti-icing applications. Designing the micro-nanostructures to make this comprise is of significance.

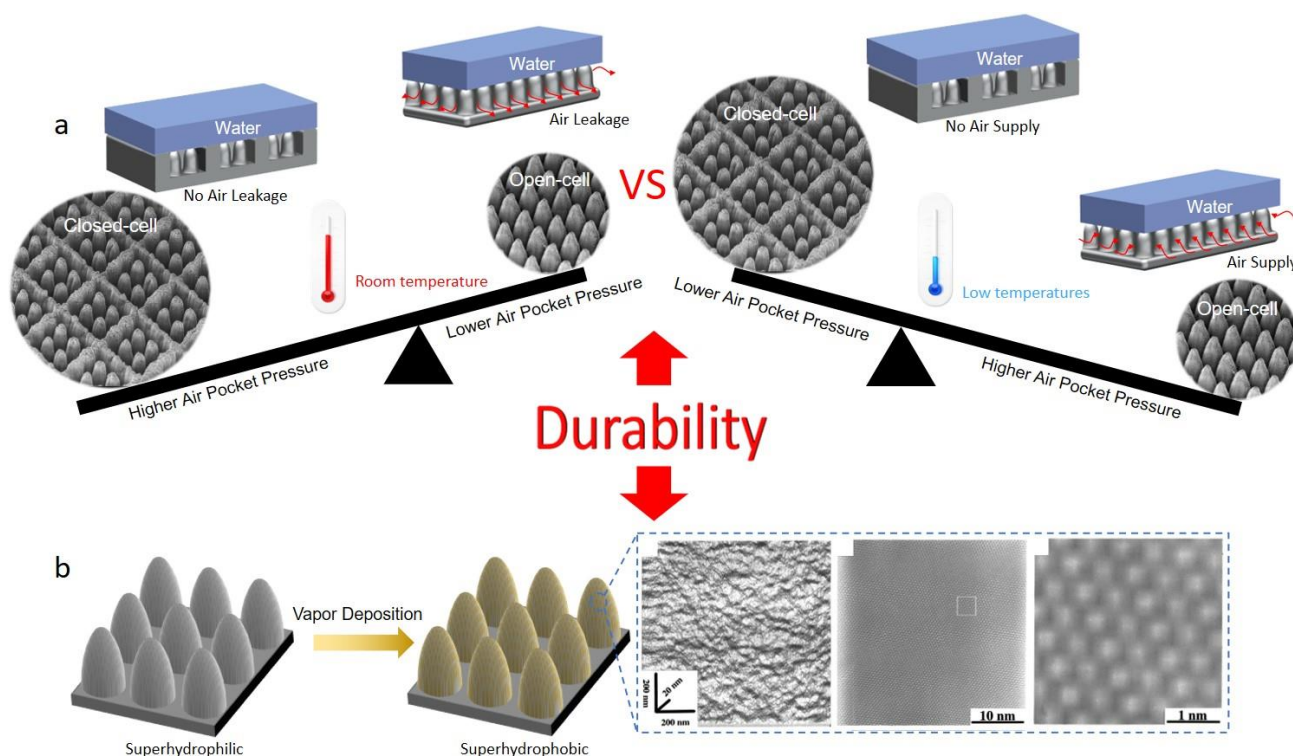


Figure 9. Two key factors influencing surface durability. (a) Surface structure types (Reproduced with permission from [118]. Copyright (2023) Royal Society of Chemistry.) (b) Low-surface-energy coatings (Reproduced with permission from [122]. Copyright (1999) American Chemical Society.)

For low-surface-energy coatings, durability is related only to intrinsically hydrophilic materials, such as metals, ceramics, etc. The most common coating substance is fluorosilanes, which can be easily coated on micro-nanostructures by the methods of vapor deposition or solution immersing [123]. Although excellent superhydrophobicity could be achieved with the methods, the durability of such coatings is usually poor owing to the single molecular layer thickness of the coated fluorosilanes by bonding with hydroxyl groups [82]. Nishino et al. measured the surface roughness of the coating on glass [122], where *n*-Perfluoroicosane ($C_{20}F_{42}$, one of the low-surface-energy substances) was vapor deposited. They found that the vapor-deposited layer was single crystal-like with a maximum roughness of only 8 Å (Figure 9b). Under external abrasion, the coatings can be easily peeled off to expose the inner hydrophilic sites, eventually leading to the failure of anti-icing properties. Therefore, research on chemical synthesis and coating materials still needs to be made in developing novel durable low-surface-energy coatings.

3.2.3. Environmental Adaptivity

Numerous complex and unexpected disturbances exist in practical application environments, including high-speed droplet impact, dust accretion, strong wind, etc. [124]. In this case, superhydrophobic anti-icing surfaces fail more easily compared to static laboratory environments. We take the common dynamic impact as an example to elucidate the influences of environments on anti-icing properties. Figure 10a,b show the comparison of four typical dynamic tests: water jet impacting, solid particle impacting, supercooled droplet impinging, and icing wind tunnel tests [81]. It can be observed that there are tremendous differences for different test conditions. For icing wind tunnel tests (a widely adopted method to simulate real aviation environments), the droplet sizes and impacting velocities are generally in the range of $\sim 20\text{--}100\ \mu\text{m}$ and $\sim 10\text{--}100\ \text{m/s}$. The dynamic pressures in icing wind tunnel tests reach up to over 1 Mpa, which is more than an order of magnitude higher than those in other tests. Under continuous, high-speed, high-pressure and tiny droplet impact, superhydrophobic anti-icing surfaces tend to fail extremely easily.

Figure 10c shows the icing processes of the superhydrophobic anti-icing surfaces fabricated by the DLIP. The surfaces, which could easily repel supercooled droplets ($-5\text{ }^{\circ}\text{C}$; diameter: $\sim 2\text{ }\mu\text{m}$; impact speed: 3.4 m/s) at the substrate temperature of $-25\text{ }^{\circ}\text{C}$, not only failed in 0.5 min in the icing wind tunnel tests but also even resulted in more ice accretion than pristine smooth surfaces. We ascribed the phenomenon to the preferentially bottom freezing when supercooled tiny droplets contacted surfaces. Within several milliseconds, the ice embryo nucleated and generated a strong adhesion to the substrate instead of rebounding (Figure 10d). Meanwhile, subsequent high-pressure droplets continuously impacted the surfaces to further increase the ice adhesion and lead to ice accretion.

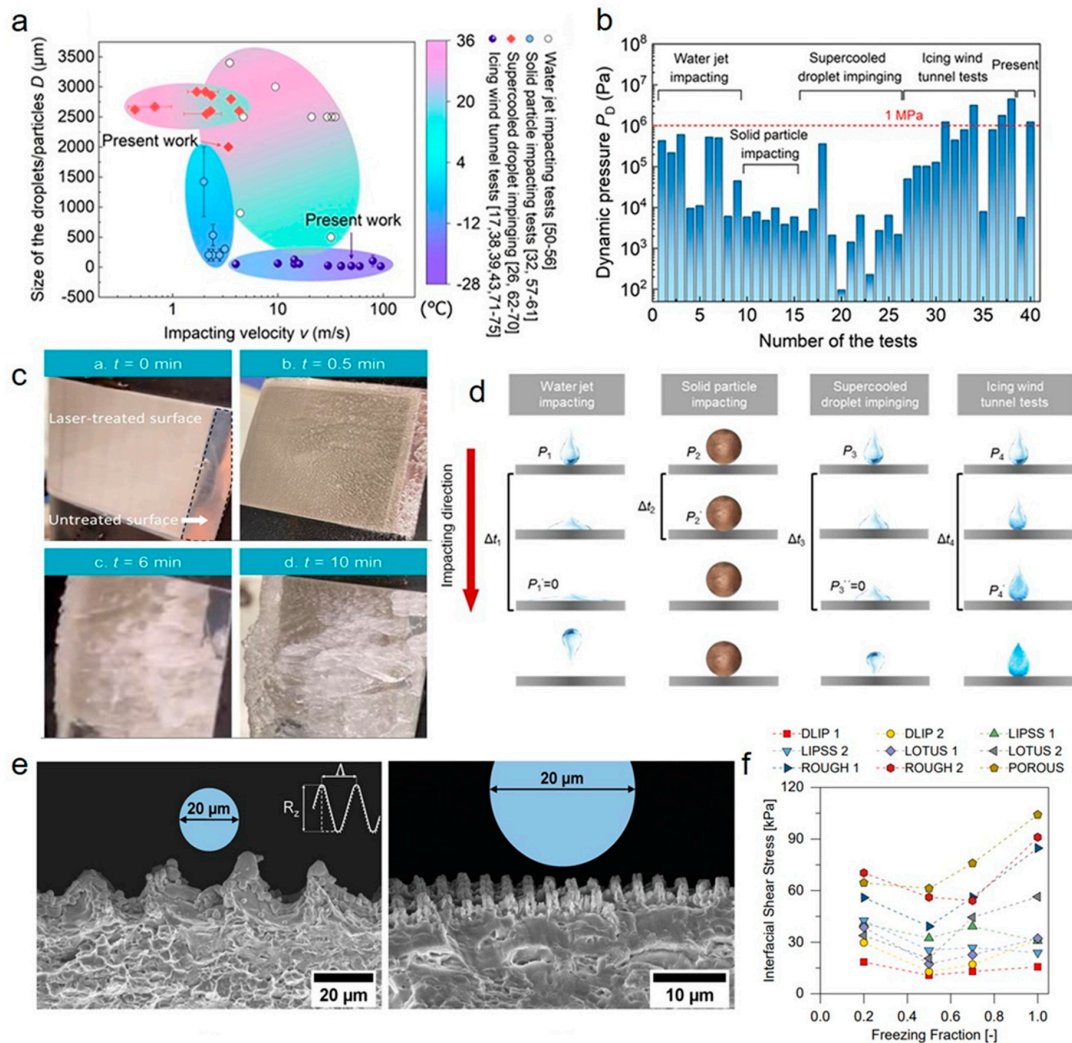


Figure 10. Influence of environmental disturbances on anti-icing performances. (a) Summarization of the relationships between the size of the droplets/particles and the impacting velocity from the four dynamic experiments: water-jet impacting, solid-particle impacting, supercooled-droplet impinging, and icing wind tunnel tests. (b) Dynamic impact pressure when the droplets/particles contact the target surfaces. (c) Image sequences of the icing processes on SHSs in icing wind tunnel tests. (d) Schematic diagrams showing the physical processes at dynamic impacting (Reproduced with permission from [81]. Copyright (2023) American Chemical Society.) (e) Comparison of structural sizes with droplet sizes. (f) Interfacial shear stress versus freezing fraction (Reproduced with permission from [125]. Copyright (2020) John Wiley and Sons.)

To ensure that superhydrophobic anti-icing surfaces have qualified environmental adaptivity, Vercillo et al. explored the design rules of ULSAs by testing various micro-nanostructures in icing wind tunnel conditions [125]. Two dominant but opposite factors

were summarized: stress concentrations and surface contact area. They found that although micro-nanostructures with small sizes had a smaller solid-liquid contact area, the structures also induced lower stress concentration. For those with larger sizes, higher stress concentration but a larger contact area was produced. It was concluded that the laser-fabricated structures should be with a spatial period of one order of magnitude smaller than the mean volume diameter (MVD) and with abundant nanostructures (Figure 10e). They also confirmed that the ice types, i.e., freezing fraction, had a strong influence on anti-icing properties, where droplets could freeze faster at higher freezing fractions and were also more difficult to remove (Figure 10f).

4. Advances and Challenges of ULSASs

Based on the above understanding, we summarize recent advances of ULSASs and proposed corresponding challenges in this section. Two typical types of SHS anti-icing technologies are discussed, including passive superhydrophobic anti-icing surfaces and passive/active combined superhydrophobic anti-icing surfaces. For ease of understanding, the challenges are presented by following their respective progress. Finally, current attempts and explores of ULSASs in their practical applications are introduced and discussed.

4.1. Passive Superhydrophobic Anti-Icing Surfaces

4.1.1. Delayed Icing/Frosting

Five stages are divided into the whole icing processes: supercooling, nucleating, recalescing, freezing, and solid cooling [79,126]. The delayed icing time generally denotes the duration time of the first three stages, which start in the original cooling from room temperatures and end in the occurrence of recalescence. Among these stages, avoiding ice embryo nucleation is the key to delaying icing [127].

Nucleation processes are divided into two types: homogeneous nucleation and heterogeneous nucleation [128]. The former generally takes place in environments without any disturbance and is completed by structure fluctuation and energy fluctuation. However, in practical environments, heterogeneous nucleation generally takes the dominant [129]. The nucleation rate of liquids can be expressed by:

$$R(T) = R_{\text{bulk}}(T)V + R_{\text{lv}}(T)S_{\text{lv}} + R_{\text{ls}}(T)S_{\text{ls}} \quad (5)$$

where $R(T)$, $R_{\text{bulk}}(T)$, $R_{\text{lv}}(T)$ and $R_{\text{ls}}(T)$ are the nucleation rates of the total, the bulk, the liquid-vapor interface, and the liquid-solid interface, respectively; S_{lv} and S_{ls} are the contact areas of the liquid-vapor interface and the liquid-solid interface, respectively; V is the liquid volume, and T is the surface temperature. Compared to $R_{\text{ls}}(T)$, the value of $R_{\text{lv}}(T)$ is very small. Hence the total nucleation rate $R(T)$ is mainly dependent of $R_{\text{ls}}(T)$ and S_{ls} [5]. Among them, $R_{\text{ls}}(T)$ is determined by the heterogeneous nucleation energy barrier, which is expressed by:

$$\Delta G_{\text{het}} = \frac{16\pi\gamma_{\text{lv}}^3}{3\Delta G_{\text{v}}^2} \cdot \frac{(2 + \cos\theta)(1 - \cos\theta)^2}{4} \quad (6)$$

where ΔG_{het} is the energy barrier of heterogeneous nucleation; γ_{lv} is the liquid-vapor interface energy; ΔG_{v} is the Gibbs free energy per unit volume; and θ is the contact angle of the ice embryo on a surface. The value of ΔG_{het} is proportional to the contact angles, where higher contact angles could induce a higher heterogeneous nucleation energy barrier, further slowing down the nucleation rate. However, as discussed above, superhydrophobic delayed icing properties work only when the CB state is retained. Once droplets transit to the Wenzel state, the significantly increased solid-liquid contact area will greatly accelerate the icing proceedings. Hence, maintaining the CB stability at low temperatures is of great importance. Many researches reveal that it is mainly affected by surface wettability and micro-nanostructure morphologies [11,30]. Undoubtedly, wettability is the key factor that influences delayed icing properties. However, the above analysis confirms

that the micro-nanostructure topologies play a more important role in low-temperature air pocket stability [118]. To explore the optimal ULSASs, numerous state-of-the-art micro-nanostructures have been developed. Pan et al. combined femtosecond laser ablation and chemical etching to fabricate the triple-scale micro-nanostructures on copper and aluminum alloy materials [130], where the open microcone arrays were covered by densely distributed submicroflowers and nanograss (Figure 11a). It was found that the triple-scale micro-nanostructures showed a significantly longer delayed icing time of 52 min 39 s, longer than on smooth surfaces (8 min 15 s) and double-scale structured SHSs (34 min 38 s). Ge et al. fabricated a hybrid micro-nanostructure with square pillars integrated Siberian–Cocklebur-like microstructures on PTFE by controlling femtosecond laser parameters [131], as shown in Figure 11b. They found that the surfaces not only had excellent superhydrophobicity but also exhibited significantly enhanced delayed icing time. Xing et al. adopted a picosecond laser to fabricate the cauliflower-like protrusions with nanostructures on the open micro-gratings [132], as shown in Figure 11c. They revealed that the laser-processed multi-tier micro-nanostructures moderated the heat loss to delay the icing process. Summarizing recently reported data on ULSASs [61,129,131,133–136], Figure 12 shows the delayed icing times versus different droplet volumes and materials. Compared to organic and inorganic ULSASs, most metallic surfaces have better delayed icing properties. This is attributed to the differences of the formed micro-nanostructures on different materials owing to different light-matter interaction mechanisms (discussed in Section 2.2). Some chemical component changes during ablating also account for the differences.

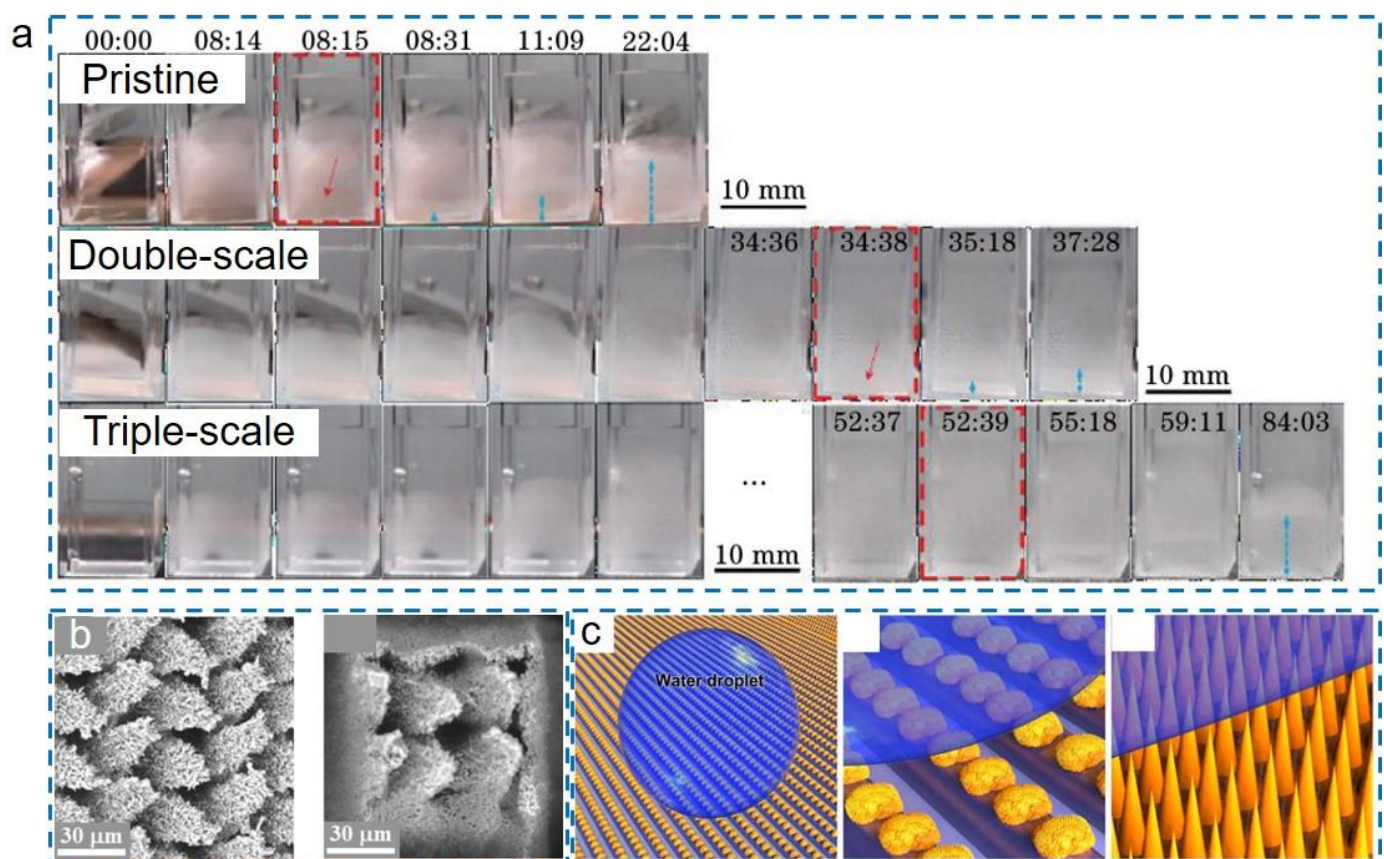


Figure 11. Delayed icing properties of ULSASs. (a) Image sequence of icing processes on the pristine copper surface, the double-scale structured ULSAS, and triple-scale structured ULSASs (reproduced

with permission from [130]. Copyright (2021) Chinese Laser Press). (b) SEM images of the hybrid micro-nanostructure with square pillars integrated Siberian-Cocklebur-like microstructures (reproduced with permission from [131]. Copyright (2020) Elsevier). (c) Schematics showing the cauliflower-like protrusions with nanostructures on the micro-gratings (reproduced with permission from [132]. Copyright (2020) Elsevier).

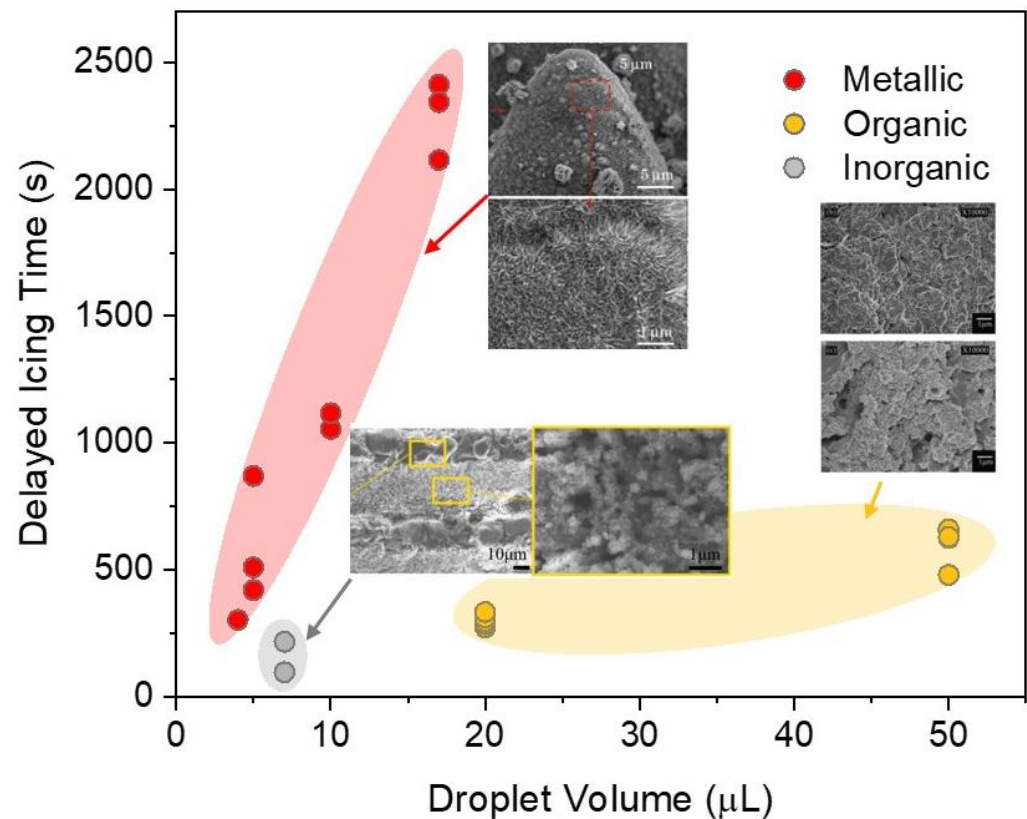


Figure 12. Delayed icing times on ULSAs versus different droplet volumes and materials. The test temperature of all data was $-10\text{ }^{\circ}\text{C}$. Data were from the references [61,129,131,133–136].

In contrast to droplet freezing, frosting is a more complicated process, involving more phase transformations [137–139]. Generally, two types of frosting modes are included: desublimation frosting and condensation frosting [140]. Desublimation frosting involves the gas-solid phase change and occurs mostly when the surface temperature is lower than the triple point of water. In condensation frosting, vapor first condenses onto surfaces, and then condensates freeze to form frosts when surface temperatures decrease below the icing point [4]. On hydrophobic surfaces, the required supersaturation degree for desublimation frosting is an order of magnitude larger than on hydrophilic surfaces [137]. Therefore, in practical applications, the delayed frosting on SHSs generally represents the delayed condensation frosting. Numerous studies have been made on understanding the mechanisms of condensation frosting on SHSs and developing related anti-frosting surfaces [24,68,141,142]. The most remarkable is the discovery of droplet jumping on SHSs induced by the decreased Laplace pressure and droplet coalescence [21,24]. Taking advantage of the spontaneous droplet jumping, condensates could be swept off the surfaces in time before freezing. However, some remaining droplets can still freeze to inevitably form frosts. To diminish the frosting ratio, two strategies have been mainly developed: (i) designing and optimizing micro-nanostructures to inhibit the growth of frost layers; (ii) designing the chemical components of surfaces to enhance droplet jumping. For ULSAs, the first strategy is adopted more frequently. By adjusting the microstructure sizes and morphologies, the frost growing extent and spreading directions could be well con-

trolled. Many experts have investigated frosting behaviors on ULSASs. He et al. adjusted laser fluence and pulse repetition frequency to fabricate different micro-nanostructures and investigated the relationship between surface morphologies and anti-frosting properties [143]. They found the smaller tip area and the larger nanostructures were preferred for delaying frosting. Long et al. fabricated 3D conical microtextures covered with nanowires on copper materials [144]. In condensation environments, the fine structures could contribute to the departure of condensate droplets, thus realizing the dropwise condensation and delaying frosting. Although much effort has been expended on developing diverse laser-induced micro-nanostructures for anti-frosting, which type of structures performed better was still unclear. In 2023, we classified all micro-nanostructures into two types: open-cell and closed-cell structures [118]. By comparing the condensation frosting processes on the two structures, it was found that more small condensate droplets emerged on the closed-cell structures since the microframes provided more nucleation sites (Figure 13). The delayed frosting time decreased as the area ratio of closed structures increased, indicating open structures performed better than closed structures. This conclusion could greatly guide the structural design of ULSASs for better anti-frosting properties.

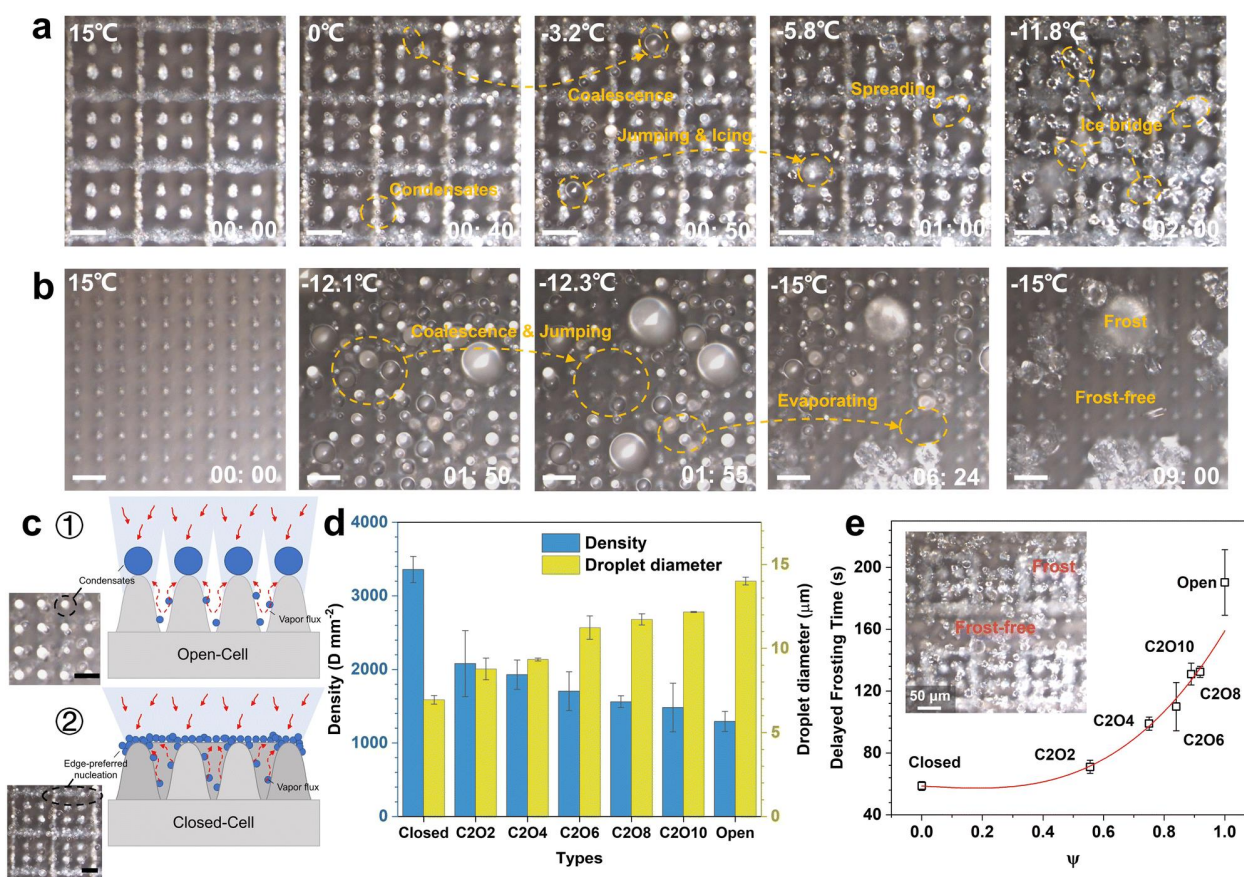


Figure 13. Delayed frosting phenomena on the ULSASs with different microstructures. (a,b) The frosting processes on the closed-cell microstructures and open-cell microstructures. (c) Schematics describing the differences of condensates nucleating and growing on different microstructures. (d) The densities and diameters of condensate droplets on the ULSASs with different microstructures. (e) Delayed frosting times versus different microstructures. (reproduced with permission from [118]. Copyright (2023) Royal Society of Chemistry).

Although much progress has been made in delaying icing/frosting of ULSASs, the icing/frosting cannot still be completely avoided. Especially in some extremely low-temperature and high-humidity environments, numerous droplets initiate and adhere to the micro-nano valleys, and then rapidly freeze [145,146]. How to inhibit the icing/frosting

on ULSASs in extremely freezing environments is a great challenge, which needs to be further explored in structures, chemistry, and other areas.

4.1.2. Ultralow Ice Adhesion Strengths

Besides delaying ice embryo nucleation, lowering ice adhesion strengths is also one of the most important properties of ULSASs [147]. In some severe icing environments (e.g., ice wind tunnel conditions), freezing processes inevitably occur on SHSs [81]. How to lower ice adhesion strengths is the key for avoiding ice accretion.

Centrifuge adhesion tests and push-off adhesion tests are the two most common methods [148,149]. The former determines the adhesion strengths by measuring the maximum shear forces or pulling forces at the moment of ice shedding during the centrifugal rotating while the latter records the maximum shear forces of the ice column detachment by the horizontal pushing. Although the reported ice adhesion strengths in literature cannot be compared accurately owing to the differences in test methods, it is widely regarded that the surfaces with ice adhesion strengths below 100 kPa are icephobic surfaces, and the ice adhesion strength of 20 kPa is the benchmark for passive anti-icing surfaces, where ice could be removed by wind blow or slight vibration [30,150]. To date, many ULSASs have been designed and fabricated with ultralow ice adhesion strengths [37,125,151–153]. Milles et al. tested the ice adhesion strengths of different ULSASs under various icing conditions and found that the cross-like DLIP pattern with the size of 2.6 μm showed the lowest ice adhesion strengths of 6~10 kPa [154]. As shown in Figure 14a, the accumulated ice layer on laser-structured surfaces could be easily removed by vibration. Considering that the solidification of environmental-related mixed liquids always took place in practical applications, we adopted a femtosecond laser to fabricate the superomniphobic surface showing excellent repellent ability for multiple liquids from deionized water to mixed solutions and then to organic liquids [78]. Figure 14b shows the ice adhesion strengths of different liquids on the designed surfaces. It was found that our fabricated surfaces had ultralow ice adhesion strengths for various liquids. Even after multiple deicing cycles, the ice adhesion strengths could be maintained below 20 kPa. However, some challenges still exist [11,30], such as poor icephobic durability (discussed in the next section), the poor environmental adaptivity, and the difficulty of large-scale fabrication. These issues greatly limit ULSASs for practical applications.

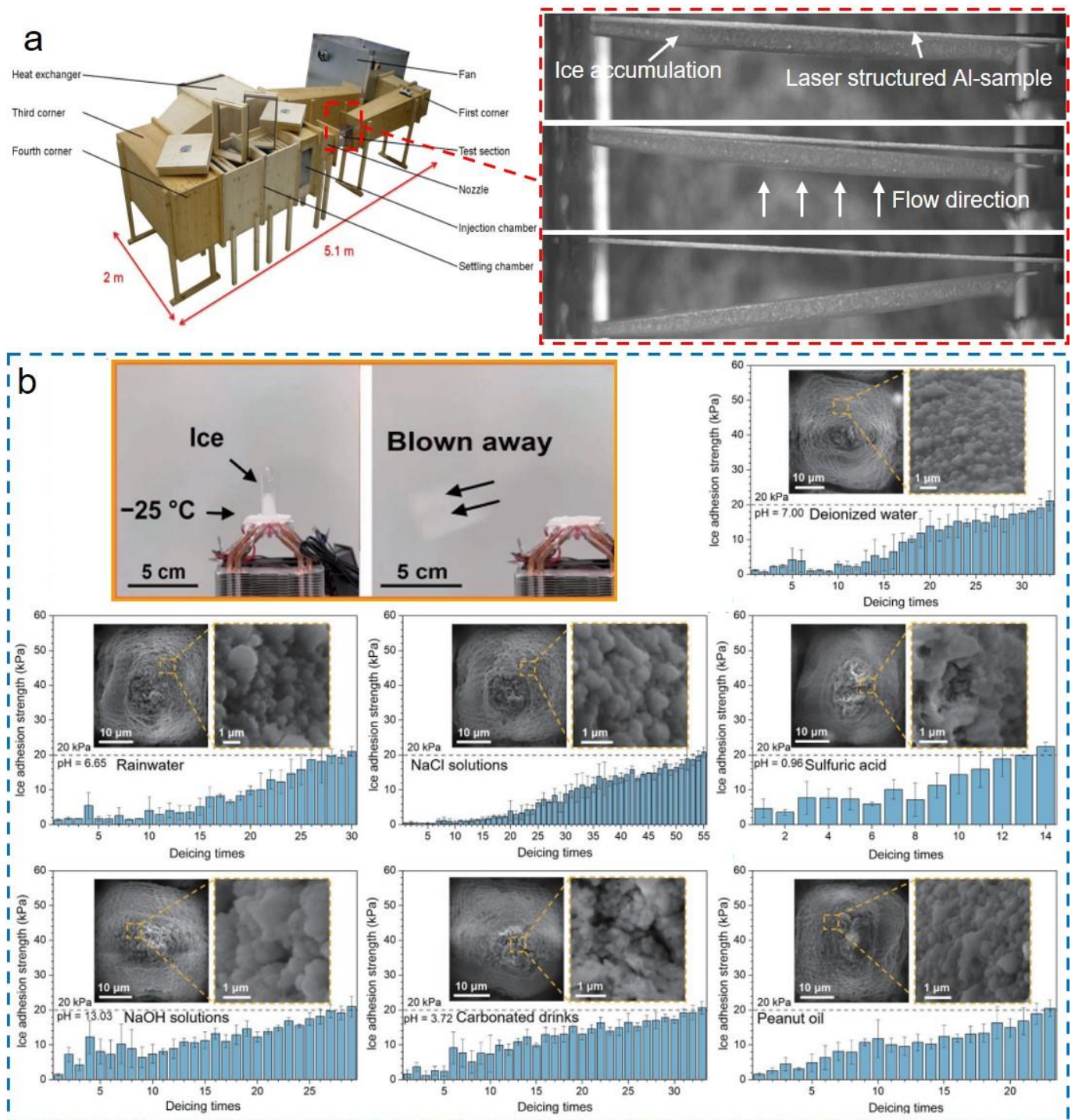


Figure 14. Low ice adhesion on the ULSASs. (a) Images of the ice easy-removal of ULSASs with vibration. Ice was formed and accumulated in the icing wind tunnel condition (reproduced with permission from [154]. Copyright (2021) MDPI). (b) Low ice adhesion of ULSASs for different liquids (reproduced with permission from [78]. Copyright (2022) Springer).

4.1.3. Durable Icephobicity

Icephobic durability directly determines the lifespan of ULSASs in practical applications. Based on the discussion in Section 3.2.2, to enhance the icephobic durability, both the micro-nanostructure durability and the coating durability need to be enhanced.

On SHSs, microstructures work as the robust skeleton while nanostructures endow surfaces with better superhydrophobicity [155]. Although the closed microstructures could

greatly enhance the room-temperature superhydrophobic durability, the open microstructures exhibit higher icephobic durability at low temperatures [118]. Hence, maintaining the open structures and further introducing more durable nanostructures become a good strategy for improving the micro-nanostructure durability. Chen et al. utilized ultrafast laser ablation and chemical oxidation to fabricate the micro-nano-nanowire triple-scale structures, where the $\text{Cu}(\text{OH})_2$ nanowires with an average length of 6–8 μm and a width of 50 nm in situ grew on the microcones (Figure 15a). After continuous deicing tests, it was found that the surface icephobicity was progressively enhanced with an increase in deicing cycles, showing a unique property that the surfaces could become more and more icephobic after wear. The phenomenon was mainly ascribed to the side nanowires and the flat microcones constructing the moderate top roughness after the top nanowires were damaged, which decreased the ice-solid contact area and further led to the lower ice adhesion strengths. The lowest ice adhesion strength on the prepared surfaces reached 12.2 kPa and could maintain 17.3 kPa even after 60 deicing cycles. To date, it is the lowest ice adhesion strength after so many deicing cycles among all reported ULSASs [156].

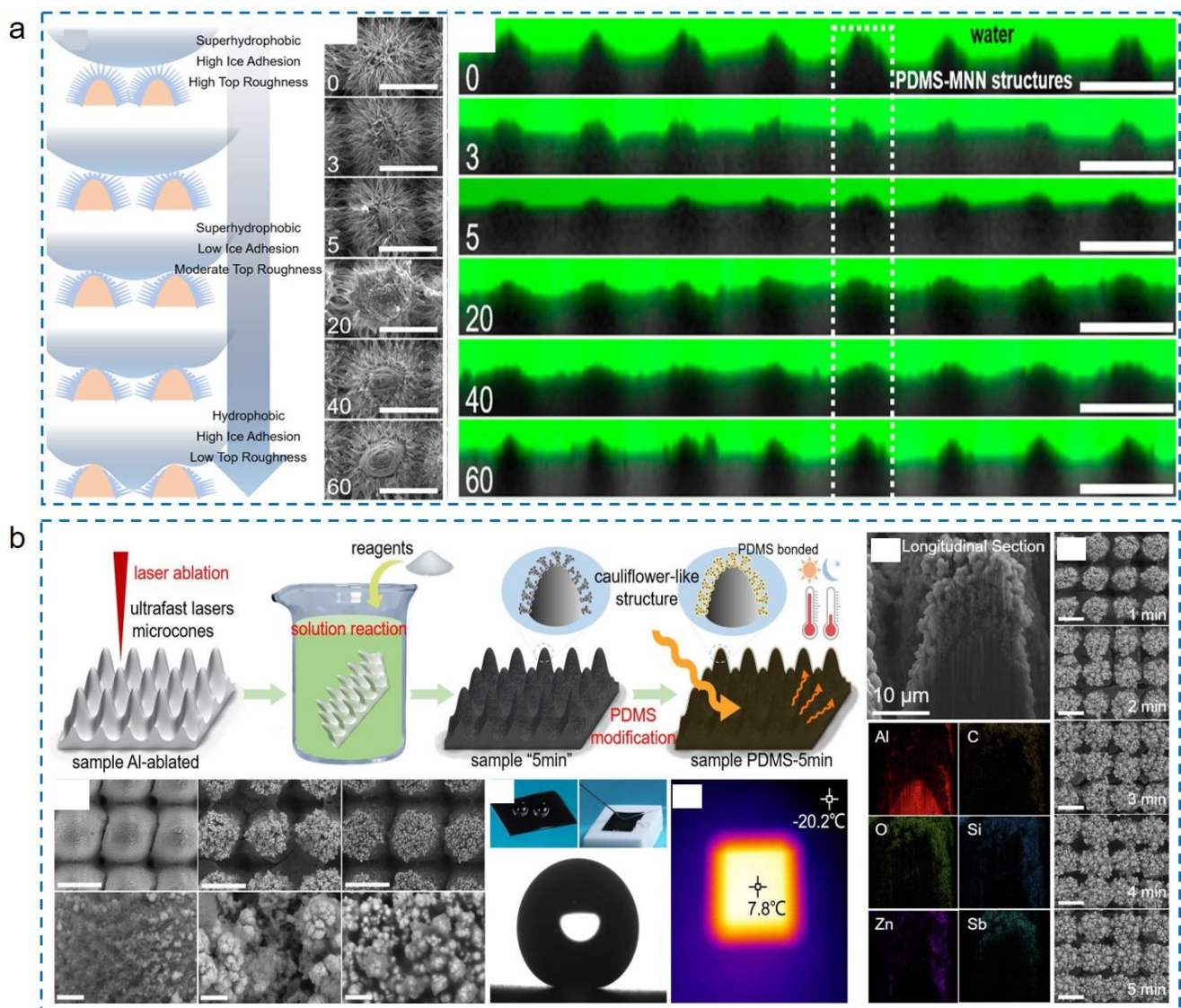


Figure 15. Enhanced icephobic durability. (a) Enhanced micro-nanostructure durability by fabricating the micro-nano-nanowire triple-scale structures (reproduced with permission from [156]. Copyright (2022) American Chemical Society). (b) Enhanced low-surface-energy coating durability by using the method of PDMS spin coating (reproduced with permission from [82]. Copyright (2022) Elsevier).

To provide more durable low-surface-energy coatings, many durable coating materials have been developed and tested [157–159]. Among these, PDMS materials show great application potential owing to strong bonding strength and an easy preparation process. Many durable superhydrophobic surfaces have been fabricated by the PDMS spin coating method instead of the vapor deposition of fluorosilanes [157,160,161]. Based on these properties, Chen et al. fabricated a cauliflower-like micro-nanostructure combined with PDMS coatings by taking advantage of ultrafast laser ablation and wet chemical reactions [82]. As shown in Figure 15b, the prepared surfaces exhibited excellent superhydrophobicity and highly effective photothermal properties. Adopting FIB and EDS techniques to analyze the cross-sectional elements, it was found that the PDMS solutions could cover and bond the cauliflower-like structures well, forming an integrated structure. The infiltrated depth of PDMS in micro-nanostructures could reach the μm -scale, which meant that the low-surface-energy coating could still be preserved to maintain the qualified superhydrophobicity after structure damage. With the robust coatings and abundant micro-nanostructures, surface icephobicity could be well maintained after 25 abrasion cycles or 1.5-hour water impact or 500 tape peeling cycles.

Overall, the improvement of micro-nanostructures and low-surface-energy coatings contributes well to the enhancement of icephobic durability. However, most of the reported surfaces are far away from real industrial applications. Further developing durable icephobic surfaces to meet various demands is still needed.

4.2. Passive/Active Combined Superhydrophobic Anti-Icing Surfaces

In some severe application scenarios, the single passive anti-icing of SHSs is still limited to eliminating ice formation and accretion. Combining with other active anti-icing technologies to achieve passive/active combined anti-icing could overcome the disadvantages [162–165]. Among various hybrid anti-icing methods, electrothermal/superhydrophobic and photothermal/superhydrophobic anti-icing surfaces have been developed most widely. Here we introduce the main advances in the two methods.

4.2.1. Electrothermal/Superhydrophobic Anti-Icing Surfaces

In terms of different heating methods, electrothermal/superhydrophobic anti-icing surfaces are divided into two main types [166,167]: one is achieved by directly installing heating elements under SHSs; the other is enabled by electricity power input to transform from electricity to heat. The former has no requirement for the electrical conductivity of SHSs while the latter requires surfaces with good conductivity and electro-to-heat conversion performances. Alamri et al. used an ultrafast laser to fabricate the hierarchical micro-nanostructures on the NACA 0012 airfoil [151]. After chemical treatment, the surfaces showed strong water repellence with a contact angle of $163^\circ \pm 6^\circ$ and a roll-off angle of $8^\circ \pm 6^\circ$. Combining the SHSs and their bottom-heating elements (Figure 16a), the electrothermal/superhydrophobic deicing tests were conducted in the icing wind tunnel environment (TAS (true air speed) = 65 m s^{-1} ; SAT (static air temperature) = $-10^\circ\text{C}/-20^\circ\text{C}$; LWC (liquid water content) = 0.2 g m^{-3} and AoA (angle of attack) = 3°). Figure 16b shows the plot of the required deicing time as a function of heating power density. The power density and time of deicing on the reference surfaces were significantly higher than on the laser-fabricated SHSs. For the SATs of -10°C and -20°C , the deicing power densities on the reference surfaces reached up to ~ 2.1 and $\sim 2.5 \text{ W cm}^{-2}$, respectively, while those on the SHSs decreased to ~ 0.5 and $\sim 1.1 \text{ W cm}^{-2}$, respectively. Sun et al. also compared the electrothermal/superhydrophobic deicing properties of pristine surfaces and laser-fabricated SHSs in the icing wind tunnel conditions (TAS = $0\sim 200 \text{ m/s}$; SAT = -35°C ; LWC = $0.2\sim 3.9 \text{ g m}^{-3}$) [168]. They found that although external heating could avoid icing on the heating zone of the pristine surface, the runback ice would be accreted more severely at the trailing edge of airfoils. In contrast to the icing phenomena on pristine surfaces, the liquid water could quickly roll away from the laser-fabricated SHSs to prevent the runback icing (Figure 16c).

For the second electrothermal deicing technology, some new phases with electrothermal properties are usually added to substrates to reinforce the thermal conductivity and electro-to-heat conversion ability. The common electrothermal materials include carbon-based materials (e.g., graphene, carbon nanotube, etc.), Ag-based materials, and some conducting polymers [169]. Xue et al. mixed multi-walled carbon nanotubes (MWCNT) and N-methylpyrrolidone solutions to prepare the MWCNT/PEI nanocomposite film [170]. An ultrafast laser was adopted to fabricate the micro-nanostructures, realizing the superhydrophobicity with a contact angle of 156.6°. Under 12 V, the three-dimensional conductive network constructed by MWCNT could rapidly rise the temperature to 109 °C within 370 s. With excellent electrothermal and superhydrophobic properties, ice on the surfaces could completely melt in 170 s (Figure 16d).

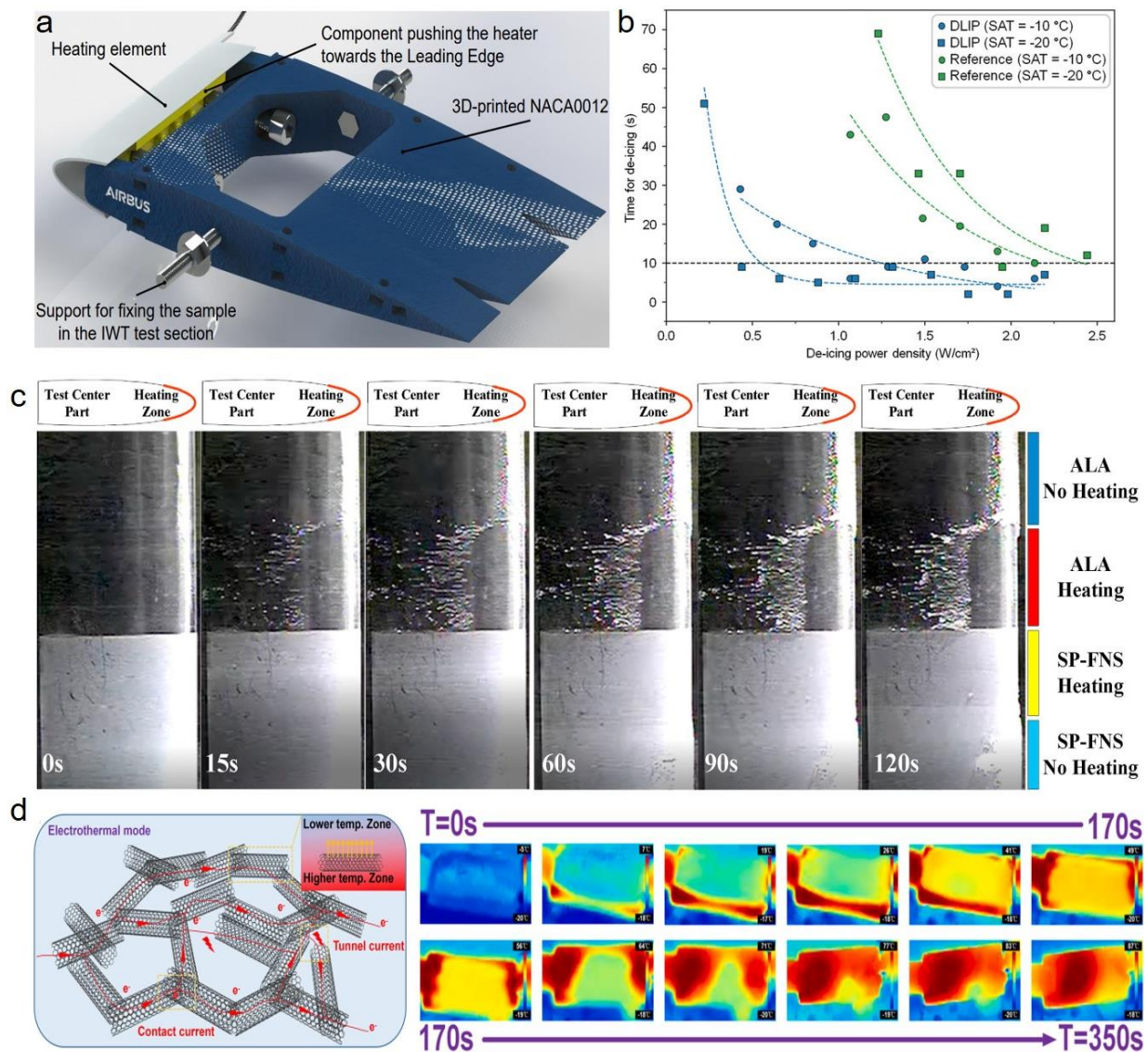


Figure 16. Electrothermal/superhydrophobic combined anti-icing surfaces. (a) Schematics showing the NACA0012 support and the heating element. (b) Comparison of the deicing time and deicing power on pristine surfaces and ULSAs (reproduced with permission from [151]. Copyright (2020) John Wiley and Sons). (c) Image sequences of electrothermal deicing on different surfaces in the icing wind tunnel conditions (reproduced with permission from [168]. Copyright (2021) Elsevier). (d) Schematic showing the electrothermal mechanisms when the current is directly applied on materials, and the thermographic image sequences of electrothermal deicing processes on ULSAs (reproduced with permission from [170]. Copyright (2023) Elsevier).

4.2.2. Photothermal/Superhydrophobic Anti-Icing Surfaces

In contrast to electrothermal deicing methods, the photothermal/superhydrophobic anti-icing technology mainly utilizes solar energy in nature to convert into heat, eventually realizing passive/active combined deicing [171]. It is an environmentally friendly deicing technique without consuming any fossil fuel. Based on the photothermal conversion principles, photothermal SHSs can also be divided into two types: (i) the SHSs with structural light traps [82,172]; and (ii) the SHSs with the new phases that own the high solar-to-heat conversion efficiency [163,173,174]. Adopting various micro-nanostructures and the generated new matters enabled by ultrafast lasers, the two types of methods have been widely explored. Zhao et al. were inspired by moth eyes to fabricate the biomimetic micro-nanostructures with a femtosecond laser [175], as shown in Figure 17a. The surfaces were composed of micro-mountain arrays with micro-nanoparticles, which constructed a well-structured light trap. Under one-sun illumination, the surface temperature can rise rapidly and exceed $80\text{ }^{\circ}\text{C}$ in 300 s. Even a large ice cube could melt and shed off the surfaces within 240 s under sunlight. Zhang et al. considered that the adhered condensates in extremely high-humidity conditions could hinder the photothermal properties and induce condensation freezing. Hence, they fabricated hierarchically structured materials by ultrafast pulsed laser deposition (PLD) technology (Figure 17b) [176]. The generated iron oxide during laser irradiation was deposited densely on substrates, not only constructing the strong light traps but also further contributing to the photothermal conversion by the thermoplasmonic effect of iron oxide nanoparticles. In the extreme environment with a temperature of $-50\text{ }^{\circ}\text{C}$ and a supersaturation degree of ~ 260 , the photothermal anti-icing properties of the surfaces could be well maintained and the equilibrium temperature could exceed $0\text{ }^{\circ}\text{C}$ under one-sun illumination owing to their superior condensate self-removing and high photothermal conversion capability.

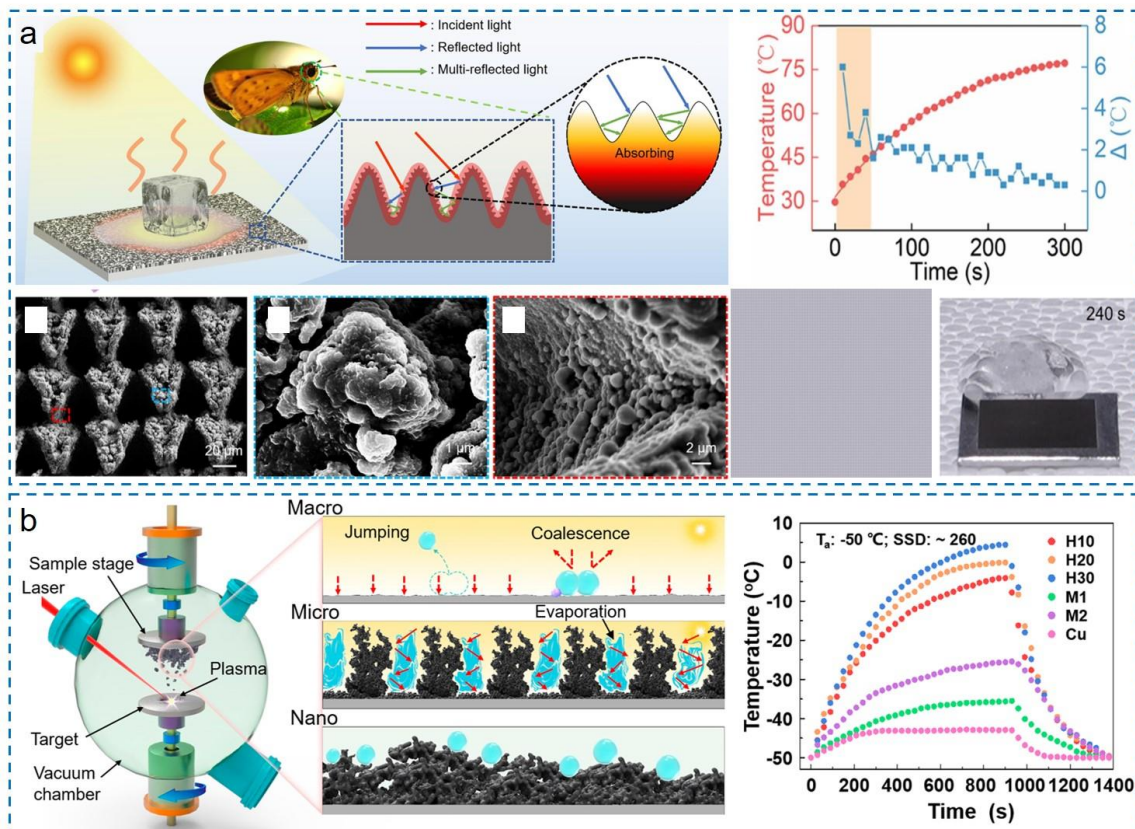


Figure 17. Photothermal/superhydrophobic anti-icing surfaces. (a) Highly effective photothermal/superhydrophobic anti-icing properties enabled by the biomimetic laser-fabricated structures

(reproduced with permission from [175]. Copyright (2021) Elsevier B.V.). (b) Solar anti-icing surfaces with enhanced condensate self-jumping in extremely low-temperature and high-humidity environments (reproduced with permission from [176]. Copyright (2021) PNAS).

Compared to the single passive superhydrophobic anti-icing method, the passive/active combined anti-icing methods could better withstand complicated and volatile environments. However, how to realize low-cost large-scale fabrication is still a key problem for practical applications [11,13]. Meanwhile, different application scenarios also propose more requirements, such as the specific surface roughness and the bonding between surfaces and heating elements in the aviation field.

4.3. Exploiting Superhydrophobic Anti-Icing Surfaces in Real Applications

Based on the excellent anti-icing properties of ULSASs, many outdoor tests have been conducted to exploit their feasibility for practical applications. Vercillo et al. installed a laser-fabricated superhydrophobic Ti64 metal sheet on an A350 port-side slat for a real flight test [177]. The total flight duration was 171.2 h, traveling mostly across Europe and experiencing two long flights to New Zealand and the Philippines. By measuring the contact angle changes and roughness, they found that surface superhydrophobicity was mostly lost after the flight. The degrading of superhydrophobicity was mainly ascribed to the failure of the low-surface-energy coating under long-time UV exposure. Boinovich et al. conducted outdoor tests with laser-fabricated SHSs [178]. The test went from September 2016 to the end of March 2019 in Moscow, where regular snowfalls, sleet, and freezing rain accompanied by high humidity and frequent air temperature changes occurred frequently. They found that the bare aluminum surfaces had significant pitting corrosion in outdoor conditions, which greatly increased the snow/ice adhesion. For the SHSs, their icephobicity could be well maintained after continuous long-time rain and could effectively keep snow from accumulating when the wind speed exceeded 3–5 m/s, as shown in Figure 18. Even at a lower wind speed, the buildup of snow cups could still induce the spontaneous shedding of snow by their gravity. Although the practical test results also revealed some problems and limitations of ULSASs, these attempts and advances provided tremendous reference values for guiding ULSASs designs and accelerating their applications.

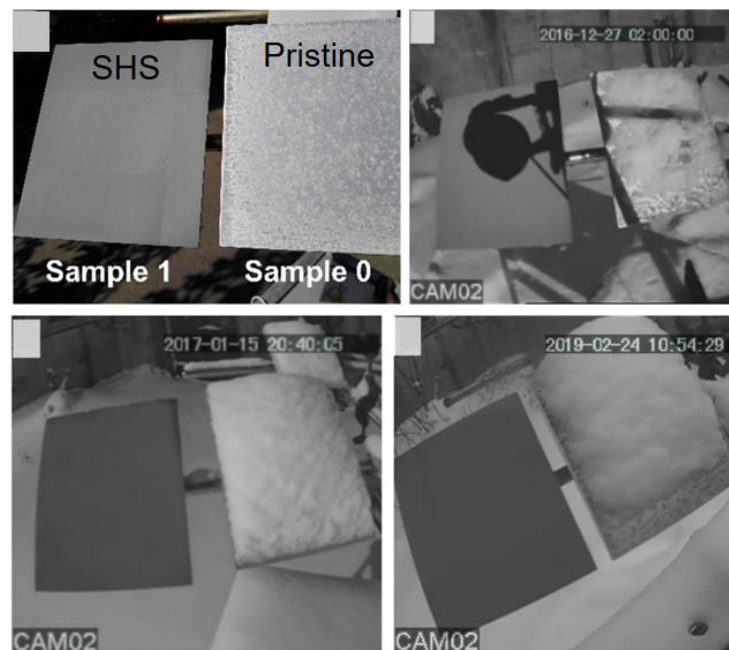


Figure 18. Long-term outdoor anti-icing tests of ULSASs and pristine surfaces (reproduced with permission from [178]. Copyright (2019) American Chemical Society).

5. Conclusions

Ultrafast lasers, as powerful and promising manufacturing tools, have colossal value in accelerating the development and applications of superhydrophobic anti-icing surfaces. To eliminate the undesired ice, much attention has been paid to ultrafast laser-fabricated superhydrophobic anti-icing surfaces (ULSASs), and related research has been comprehensively conducted in recent years. Here, we summarized the recent development of ULSASs, mainly including three aspects: fabricating, mechanisms, and advances and challenges. With respect to fabricating, we introduced fundamental wettability. Combining exquisite micro-nanostructures and low-surface-energy matters, biomimetic superhydrophobicity can be endowed on various substrate materials. Next, the advantages and mechanisms of ultrafast laser micro-nano fabricating were explained. Compared to other micro-nano fabricating strategies, the ultrafast laser-fabricating method possesses the significant advantages of being highly programmable, having the nm-accuracy, being contact-free, and with non-limitation for materials. Based on the light-matter interaction, many unique micro-nanostructures have been widely developed, providing more opportunities and possibilities for exploring the superhydrophobic anti-icing mechanisms and applications. In mechanisms, we introduced some recent discoveries and thus extended understanding of anti-icing on the laser-fabricated micro-nanostructures, and further elucidated the relationship between superhydrophobicity and icephobicity that superhydrophobicity is one necessary but not insufficient condition of icephobicity. Meanwhile, three common failure mechanisms of ULSASs were analyzed, including Cassie–Baxter stability, surface durability, and environmental adaptivity. Essentially, structures and coatings were two crucial factors to avoid the failure of ULSASs. In advances and challenges, we summarized the recent progress and the respective challenges of ULSASs in passive anti-icing, passive/active combined anti-icing, and some practical outdoor applications. The passive anti-icing of ULSASs mainly lies in delaying icing time, decreasing ice adhesion strengths, and achieving durable anti-icing, while the passive/active combined anti-icing technologies were introduced with the electrothermal- or photothermal-assisted methods. However, in contrast to lab-scale freezing environments, the practical application environments were more complicated and volatile, which brings tremendous challenges for the performances of ULSASs (icephobicity, durability, stability, etc.) and their engineering feasibility (large-scale fabrication, surface installation, device matching, etc.). As for the future development of ULSASs, the following opportunities are envisioned:

- Further investigations and deepened understanding of icing-related phenomena on superhydrophobic surfaces need to be explored.
- More design and optimization of structures and chemical coatings are demanded for developing more durable ULSASs.
- More novel ultrafast laser-fabrication technologies and more advanced ultrafast laser instruments are expected to meet the strictly industrial application requirements.

Author Contributions: Writing—original draft preparation, L.W.; writing—review and editing, H.Z. (Huanyu Zhao), D.Z., L.Y. and H.Z. (Hongjun Zhang); supervision, P.F. and M.Z. All authors have read and agreed to the published version of the manuscript.

Funding: We acknowledge funding support from the National Key R&D Program of China (Grant No. 2017YFB1104300 and 2022YFE0203700, M.Z.), the Tsinghua University Initiative Scientific Research Program (Grant No. 2018Z05JZY009, M.Z.), and the National Natural Science Foundation of China (Grant Nos. 51575309 and 51210009, M.Z.).

Institutional Review Board Statement: Not applicable.

Informed Consent Statement: Not applicable.

Data Availability Statement: Data is contained within the article.

Acknowledgments: We acknowledge the Liaoning Provincial Key Laboratory of Aircraft Ice Protection, Joint Research Center for Advanced Materials & Anti-icing of Tsinghua University (SMSE)-AVIC ARI, and the China-Italy Joint Laboratory on Green Aviation Technology for the support for this research.

Conflicts of Interest: The authors declare no conflict of interest.

References

1. Wong, T.-S.; Kang, S.H.; Tang, S.K.Y.; Smythe, E.J.; Hatton, B.D.; Grinthal, A.; Aizenberg, J. Bioinspired self-repairing slippery surfaces with pressure-stable omniphobicity. *Nature* **2011**, *477*, 443–447. [CrossRef] [PubMed]
2. Schutzius, T.M.; Jung, S.; Maitra, T.; Graeber, G.; Köhme, M.; Poulikakos, D. Spontaneous droplet trampolining on rigid superhydrophobic surfaces. *Nature* **2015**, *527*, 82–85. [CrossRef] [PubMed]
3. Golovin, K.; Dhyani, A.; Thouless, M.D.; Tuteja, A. Low-interfacial toughness materials for effective large-scale deicing. *Science* **2019**, *364*, 371–375. [CrossRef] [PubMed]
4. Hou, Y.; Yu, M.; Shang, Y.; Zhou, P.; Song, R.; Xu, X.; Chen, X.; Wang, Z.; Yao, S. Suppressing Ice Nucleation of Supercooled Condensate with Biphilic Topography. *Phys. Rev. Lett.* **2018**, *120*, 075902. [CrossRef] [PubMed]
5. Shen, Y.; Wu, X.; Tao, J.; Zhu, C.; Lai, Y.; Chen, Z. Icephobic materials: Fundamentals, performance evaluation, and applications. *Prog. Mater. Sci.* **2019**, *103*, 509–557. [CrossRef]
6. Chen, C.; Fan, P.; Zhu, D.; Tian, Z.; Zhao, H.; Wang, L.; Peng, R.; Zhong, M. Crack-Initiated Durable Low-Adhesion Trilayer Icephobic Surfaces with Microcone-Array Anchored Porous Sponges and Polydimethylsiloxane Cover. *ACS Appl. Mater. Interfaces* **2023**, *15*, 6025–6034. [CrossRef]
7. Grizen, M.; Tiwari, M.K. Icephobic Surfaces. In *Ice Adhesion: Mechanism, Measurement and Mitigation*; Scrivener Publishing LLC: Beverly, MA, USA, 2020.
8. Schultz, P.; Politovich, M.K. Toward the improvement of aircraft icing forecasts for the continental United States. *Weather. Forecast.* **1992**, *7*, 491–500. [CrossRef]
9. Cebeci, T.; Kafyke, F. Aircraft Icing. *Annu. Rev. Fluid Mech.* **2003**, *35*, 11–21. [CrossRef]
10. Chu, F. *Condensed and Melting Droplet Behavior on Superhydrophobic Surfaces*; Springer Nature: Berlin, Germany, 2020.
11. Huang, W.; Huang, J.; Guo, Z.; Liu, W. Icephobic/anti-icing properties of superhydrophobic surfaces. *Adv. Colloid Interface Sci.* **2022**, *304*, 102658. [CrossRef]
12. Esmeryan, K.D. From Extremely Water-Repellent Coatings to Passive Icing Protection—Principles, Limitations and Innovative Application Aspects. *Coatings* **2020**, *10*, 66. [CrossRef]
13. Wang, F.; Zhuo, Y.; He, Z.; Xiao, S.; He, J.; Zhang, Z. Dynamic Anti-Icing Surfaces (DAIS). *Adv. Sci.* **2021**, *8*, 2101163. [CrossRef] [PubMed]
14. Li, Y.; Ma, W.; Kwon, Y.S.; Li, W.; Yao, S.; Huang, B. Solar Deicing Nanocoatings Adaptive to Overhead Power Lines. *Adv. Funct. Mater.* **2022**, *32*, 2113297. [CrossRef]
15. Jiang, S.; Diao, Y.; Yang, H. Recent advances of bio-inspired anti-icing surfaces. *Adv. Colloid Interface Sci.* **2022**, *308*, 102756. [CrossRef] [PubMed]
16. Chen, F.; Wang, Y.; Tian, Y.; Zhang, D.; Song, J.; Crick, C.R.; Carmalt, C.J.; Parkin, I.P.; Lu, Y. Robust and durable liquid-repellent surfaces. *Chem. Soc. Rev.* **2022**, *51*, 8476–8583. [CrossRef]
17. Zhang, W.; Wang, D.; Sun, Z.; Song, J.; Deng, X. Robust superhydrophobicity: Mechanisms and strategies. *Chem. Soc. Rev.* **2021**, *50*, 4031–4061. [CrossRef]
18. Liu, Y.; Moevius, L.; Xu, X.; Qian, T.; Yeomans, J.M.; Wang, Z. Pancake bouncing on superhydrophobic surfaces. *Nat. Phys.* **2014**, *10*, 515–519. [CrossRef]
19. Jin, M.; Shen, Y.; Luo, X.; Tao, J.; Xie, Y.; Chen, H.; Wu, Y. A combination structure of microblock and nanohair fabricated by chemical etching for excellent water repellency and icephobicity. *Appl. Surf. Sci.* **2018**, *455*, 883–890. [CrossRef]
20. Zhang, H.; Zhang, X.; He, F.; Lv, C.; Hao, P. How micropatterns affect the anti-icing performance of superhydrophobic surfaces. *Int. J. Heat Mass Transf.* **2022**, *195*, 123196. [CrossRef]
21. Lv, C.; Hao, P.; Zhang, X.; He, F. Dewetting Transitions of Dropwise Condensation on Nanotexture-Enhanced Superhydrophobic Surfaces. *ACS Nano* **2015**, *9*, 12311–12319. [CrossRef]
22. Tian, X.; Verho, T.; Ras, R.H.A. Moving superhydrophobic surfaces toward real-world applications. *Science* **2016**, *352*, 142–143. [CrossRef]
23. Lee, S.H.; Seong, M.; Kwak, M.K.; Ko, H.; Kang, M.; Park, H.W.; Kang, S.M.; Jeong, H.E. Tunable Multimodal Drop Bouncing Dynamics and Anti-Icing Performance of a Magnetically Responsive Hair Array. *ACS Nano* **2018**, *12*, 10693–10702. [CrossRef]
24. Yan, X.; Huang, Z.; Sett, S.; Oh, J.; Cha, H.; Li, L.; Feng, L.; Wu, Y.; Zhao, C.; Orejon, D.; et al. Atmosphere-mediated superhydrophobicity of rationally designed micro/nanostructured surfaces. *ACS Nano* **2019**, *13*, 4160–4173. [CrossRef]
25. Chen, J.; Liu, J.; He, M.; Li, K.; Cui, D.; Zhang, Q.; Zeng, X.; Zhang, Y.; Wang, J.; Song, Y. Superhydrophobic surfaces cannot reduce ice adhesion. *Appl. Phys. Lett.* **2012**, *101*, 111603. [CrossRef]
26. Varanasi, K.K.; Deng, T.; Smith, J.D.; Hsu, M.; Bhate, N. Frost formation and ice adhesion on superhydrophobic surfaces. *Appl. Phys. Lett.* **2010**, *97*, 234102. [CrossRef]

27. Kulinich, S.; Farhadi, S.; Nose, K.; Du, X.-W. Superhydrophobic Surfaces: Are They Really Ice-Repellent? *Langmuir ACS J. Surf. Colloids* **2011**, *27*, 25–29. [CrossRef]
28. Li, Y.; Quéré, D.; Lv, C.; Zheng, Q. Monostable superrepellent materials. *Proc. Natl. Acad. Sci. USA* **2017**, *114*, 3387–3392. [CrossRef]
29. Tang, W.; Liu, L.; Ruan, Q.; Wu, Z.; Yang, C.; Cui, S.; Ma, Z.; Fu, R.K.Y.; Tian, X.; Chu, P.K.; et al. Dynamic changes of hydrophobic behavior during icing. *Surf. Coat. Technol.* **2020**, *397*, 126043. [CrossRef]
30. Kreder, M.J.; Alvarenga, J.; Kim, P.; Aizenberg, J. Design of anti-icing surfaces: Smooth, textured or slippery? *Nat. Rev. Mater.* **2016**, *1*, 15003. [CrossRef]
31. Fan, K.; Jin, Z.; Zhu, X.; Wang, Q.; Sun, J. A facile electrochemical machining process to fabricate superhydrophobic surface on iron materials and its applications in anti-icing. *J. Dispers. Sci. Technol.* **2021**, *42*, 457–464. [CrossRef]
32. Dong, Z.; Vuckovac, M.; Cui, W.; Zhou, Q.; Ras, R.H.A.; Levkin, P.A. 3D Printing of Superhydrophobic Objects with Bulk Nanostructure. *Adv. Mater.* **2021**, *33*, 2106068. [CrossRef]
33. Guo, P.; Zheng, Y.; Wen, M.; Song, C.; Lin, Y.; Jiang, L. Icephobic/Anti-Icing Properties of Micro/Nanostructured Surfaces. *Adv. Mater.* **2012**, *24*, 2642–2648. [CrossRef] [PubMed]
34. Fu, Q.T.; Liu, E.J.; Wilson, P.; Chen, Z. Ice nucleation behaviour on sol–gel coatings with different surface energy and roughness. *Phys. Chem. Chem. Phys. Pccp* **2015**, *17*, 21492–21500. [CrossRef]
35. Dong, Z.; Schumann, M.F.; Hokkanen, M.J.; Chang, B.; Welle, A.; Zhou, Q.; Ras, R.H.A.; Xu, Z.; Wegener, M.; Levkin, P.A. Superoleophobic Slippery Lubricant-Infused Surfaces: Combining Two Extremes in the Same Surface. *Adv. Mater.* **2018**, *30*, 1803890. [CrossRef] [PubMed]
36. Ngo, C.-V.; Chun, D.-M. Control of laser-ablated aluminum surface wettability to superhydrophobic or superhydrophilic through simple heat treatment or water boiling post-processing. *Appl. Surf. Sci.* **2018**, *435*, 974–982. [CrossRef]
37. Raja, R.S.S.; Selvakumar, P.; Babu, P.D. A novel fabrication of superhydrophobic surfaces on aluminium substrate by picosecond pulsed laser. *J. Mech. Sci. Technol.* **2020**, *34*, 1667–1674. [CrossRef]
38. Samanta, A.; Wang, Q.; Shaw, S.K.; Ding, H. Nanostructuring of laser textured surface to achieve superhydrophobicity on engineering metal surface. *J. Laser Appl.* **2019**, *31*, 022515. [CrossRef]
39. Fan, P.; Pan, R.; Zhong, M. Ultrafast Laser Enabling Hierarchical Structures for Versatile Superhydrophobicity with Enhanced Cassie–Baxter Stability and Durability. *Langmuir* **2019**, *35*, 16693–16711. [CrossRef]
40. Chen, Z.; Yang, J.; Liu, H.; Zhao, Y.; Pan, R. A short review on functionalized metallic surfaces by ultrafast laser micromachining. *Int. J. Adv. Manuf. Technol.* **2022**, *119*, 6919–6948. [CrossRef]
41. Phillips, K.C.; Gandhi, H.H.; Mazur, E.; Sundaram, S.K. Ultrafast laser processing of materials: A review. *Adv. Opt. Photon.* **2015**, *7*, 684–712. [CrossRef]
42. Fadeeva, E.; Chichkov, B. Biomimetic Liquid-Repellent Surfaces by Ultrafast Laser Processing. *Appl. Sci.* **2018**, *8*, 1424. [CrossRef]
43. Yang, X.; Song, R.; He, L.; Wu, L.; He, X.; Liu, X.; Tang, H.; Lu, X.; Ma, Z.; Tian, P. Optimization mechanism and applications of ultrafast laser machining towards highly designable 3D micro/nano structuring. *RSC Adv.* **2022**, *12*, 35227–35241. [CrossRef]
44. Bonse, J.; Gräf, S. Maxwell Meets Marangoni—A Review of Theories on Laser-Induced Periodic Surface Structures. *Laser Photonics Rev.* **2020**, *14*, 2000215. [CrossRef]
45. Jiang, G.; Tian, Z.; Wang, L.; Luo, X.; Chen, C.; Hu, X.; Peng, R.; Zhang, H.; Zhong, M. Anisotropic Hemiwicking Behavior on Laser Structured Prismatic Microgrooves. *Langmuir* **2022**, *38*, 6665–6675. [CrossRef]
46. Jiang, G.; Tian, Z.; Luo, X.; Chen, C.; Hu, X.; Wang, L.; Peng, R.; Zhang, H.; Zhong, M. Ultrathin aluminum wick with dual-scale microgrooves for enhanced capillary performance. *Int. J. Heat Mass Transf.* **2022**, *190*, 122762. [CrossRef]
47. Fan, P.; Bai, B.; Zhong, M.; Zhang, H.; Long, J.; Han, J.; Wang, W.; Jin, G. General Strategy toward Dual-Scale-Controlled Metallic Micro–Nano Hybrid Structures with Ultralow Reflectance. *ACS Nano* **2017**, *11*, 7401–7408. [CrossRef]
48. Liu, W.; Luo, X.; Chen, C.; Jiang, G.; Hu, X.; Zhang, H.; Zhong, M. Directional anchoring patterned liquid-infused superamphiphobic surfaces for high-throughput droplet manipulation. *Lab A Chip* **2021**, *21*, 1373–1384. [CrossRef]
49. Sabbah, A.; Youssef, A.; Damman, P. Superhydrophobic Surfaces Created by Elastic Instability of PDMS. *Appl. Sci.* **2016**, *6*, 152. [CrossRef]
50. Cao, Y.; Lu, Y.; Liu, N.; Li, Y.; Wang, P.; Dai, C.; Wei, Y. Multi-applicable, durable superhydrophobic anti-icing coating through template-method and chemical vapor deposition. *Surf. Interfaces* **2022**, *32*, 102100. [CrossRef]
51. Long, J.; Fan, P.; Gong, D.; Jiang, D.; Zhang, H.; Li, L.; Zhong, M. Superhydrophobic Surfaces Fabricated by Femtosecond Laser with Tunable Water Adhesion: From Lotus Leaf to Rose Petal. *ACS Appl. Mater. Interfaces* **2015**, *7*, 9858–9865. [CrossRef]
52. Long, J.; Pan, L.; Fan, P.; Gong, D.; Jiang, D.; Zhang, H.; Li, L.; Zhong, M. Cassie-State Stability of Metallic Superhydrophobic Surfaces with Various Micro/Nanostructures Produced by a Femtosecond Laser. *Langmuir* **2016**, *32*, 1065–1072. [CrossRef]
53. Cai, M.; Liu, W.; Luo, X.; Chen, C.; Pan, R.; Zhang, H.; Zhong, M. Three-Dimensional and In Situ-Activated Spinel Oxide Nanoporous Clusters Derived from Stainless Steel for Efficient and Durable Water Oxidation. *ACS Appl. Mater. Interfaces* **2020**, *12*, 13971–13981. [CrossRef] [PubMed]
54. Hu, X.; Tian, Z.; Luo, X.; Chen, C.; Jiang, G.; Wang, L.; Peng, R.; Zhang, H.; Zhong, M. Wetting behavior of gallium-based room temperature liquid metal (LM) on nanosecond-laser-structured metal surfaces. *Surf. Interfaces* **2022**, *32*, 102180. [CrossRef]
55. Luo, X.; Tian, Z.; Chen, C.; Jiang, G.; Hu, X.; Wang, L.; Peng, R.; Zhang, H.; Zhong, M. Laser-textured High-throughput Hydrophobic/Superhydrophobic SERS platform for fish drugs residue detection. *Opt. Laser Technol.* **2022**, *152*, 108075. [CrossRef]

56. Liu, W.; Fan, P.; Cai, M.; Luo, X.; Chen, C.; Pan, R.; Zhang, H.; Zhong, M. An integrative bioinspired venation network with ultra-contrasting wettability for large-scale strongly self-driven and efficient water collection. *Nanoscale* **2019**, *11*, 8940–8949. [CrossRef]
57. Correa, D.S.; Almeida, J.M.P.; Almeida, G.F.B.; Cardoso, M.R.; De Boni, L.; Mendonça, C.R. Ultrafast Laser Pulses for Structuring Materials at Micro/Nano Scale: From Waveguides to Superhydrophobic Surfaces. *Photonics* **2017**, *4*, 8. [CrossRef]
58. Tang, B.-H.; Wang, Q.; Han, X.-C.; Zhou, H.; Yan, X.-J.; Yu, Y.; Han, D.-D. Fabrication of anti-icing/de-icing surfaces by femtosecond laser. *Front. Chem.* **2022**, *10*, 1073473. [CrossRef]
59. Wang, H.; He, M.; Liu, H.; Guan, Y. One-Step Fabrication of Robust Superhydrophobic Steel Surfaces with Mechanical Durability, Thermal Stability, and Anti-icing Function. *ACS Appl. Mater. Interfaces* **2019**, *11*, 25586–25594. [CrossRef]
60. Volpe, A.; Gaudio, C.; Di Venere, L.; Licciulli, F.; Giordano, F.; Ancona, A. Direct Femtosecond Laser Fabrication of Superhydrophobic Aluminum Alloy Surfaces with Anti-icing Properties. *Coatings* **2020**, *10*, 587. [CrossRef]
61. Xia, A.; He, L.; Qie, S.; Zhang, J.; Li, H.; He, N.; Hao, X. Fabrication of an Anti-Icing Aluminum Alloy Surface by Combining Wet Etching and Laser Machining. *Appl. Sci.* **2022**, *12*, 2119. [CrossRef]
62. Cai, M.; Fan, P.; Long, J.; Han, J.; Lin, Y.; Zhang, H.; Zhong, M. Large-Scale Tunable 3D Self-Supporting WO₃ Micro-Nano Architectures as Direct Photoanodes for Efficient Photoelectrochemical Water Splitting. *ACS Appl. Mater. Interfaces* **2017**, *9*, 17856–17864. [CrossRef]
63. Eklund, P.C.; Pradhan, B.K.; Kim, U.J.; Xiong, Q.; Fischer, J.E.; Friedman, A.D.; Holloway, B.C.; Jordan, K.; Smith, M.W. Large-Scale Production of Single-Walled Carbon Nanotubes Using Ultrafast Pulses from a Free Electron Laser. *Nano Lett.* **2002**, *2*, 561–566. [CrossRef]
64. Yuan, D.; Li, J.; Huang, J.; Wang, M.; Xu, S.; Wang, X. Large-Scale Laser Nanopatterning of Multiband Tunable Mid-Infrared Metasurface Absorber. *Adv. Opt. Mater.* **2022**, *10*, 2200939. [CrossRef]
65. Zhang, Y.; Zhang, Z.; Yang, J.; Yue, Y.; Zhang, H. Fabrication of superhydrophobic surface on stainless steel by two-step chemical etching. *Chem. Phys. Lett.* **2022**, *797*, 139567. [CrossRef]
66. Guo, F.; Duan, S.; Wu, D.; Matsuda, K.; Wang, T.; Zou, Y. Facile etching fabrication of superhydrophobic 7055 aluminum alloy surface towards chloride environment anticorrosion. *Corros. Sci.* **2021**, *182*, 109262. [CrossRef]
67. Talesh Bahrami, H.R.; Ahmadi, B.; Saffari, H. Preparing superhydrophobic copper surfaces with rose petal or lotus leaf property using a simple etching approach. *Mater. Res. Express* **2017**, *4*, 055014. [CrossRef]
68. Ma, C.; Chen, L.; Wang, L.; Tong, W.; Chu, C.; Yuan, Z.; Lv, C.; Zheng, Q. Condensation droplet sieve. *Nat. Commun.* **2022**, *13*, 5381. [CrossRef]
69. Shi, S.; Lv, C.; Zheng, Q. Temperature-regulated adhesion of impacting drops on nano/microtextured monostable superrepellent surfaces. *Soft Matter* **2020**, *16*, 5388–5397. [CrossRef]
70. Niu, H.; Zhang, H.; Yue, W.; Gao, S.; Kan, H.; Zhang, C.; Zhang, C.; Pang, J.; Lou, Z.; Wang, L.; et al. Micro-Nano Processing of Active Layers in Flexible Tactile Sensors via Template Methods: A Review. *Small* **2021**, *17*, 2100804. [CrossRef]
71. Gong, D.; Long, J.; Fan, P.; Jiang, D.; Zhang, H.; Zhong, M. Thermal stability of micro-nano structures and superhydrophobicity of polytetrafluoroethylene films formed by hot embossing via a picosecond laser ablated template. *Appl. Surf. Sci.* **2015**, *331*, 437–443. [CrossRef]
72. He, Q.; Xu, Z.; Li, A.; Wang, J.; Zhang, J.; Zhang, Y. Study on hydrophobic properties of fluororubber prepared by template method under high temperature conditions. *Colloids Surf. A Physicochem. Eng. Asp.* **2021**, *612*, 125837. [CrossRef]
73. Zhu, J.; Hu, X. A novel and facile fabrication of superhydrophobic surfaces on copper substrate via machined operation. *Mater. Lett.* **2017**, *190*, 115–118. [CrossRef]
74. Zhao, Y.; Yan, Z.; Zhang, H.; Yang, C.; Cheng, P. Promote anti- /de- frosting by suppressing directional ice bridging. *Int. J. Heat Mass Transf.* **2021**, *165*, 120609. [CrossRef]
75. Dong, Z.; Levkin, P.A. 3D Microprinting of Super-Repellent Microstructures: Recent Developments, Challenges, and Opportunities. *Adv. Funct. Mater.* **2023**, *2213916*. [CrossRef]
76. Luo, X.; Weng, Y.; Wang, S.; Du, J.; Wang, H.; Xu, C. Superhydrophobic and oleophobic textiles with hierarchical micro-nano structure constructed by sol-gel method. *J. Sol-Gel Sci. Technol.* **2019**, *89*, 820–829. [CrossRef]
77. Kim, J.-H.; Mirzaei, A.; Kim, H.W.; Kim, S.S. Novel superamphiphobic surfaces based on micro-nano hierarchical fluorinated Ag/SiO₂ structures. *Appl. Surf. Sci.* **2018**, *445*, 262–271. [CrossRef]
78. Wang, L.; Tian, Z.; Luo, X.; Chen, C.; Jiang, G.; Hu, X.; Peng, R.; Zhang, H.; Zhong, M. Superomniphobic surfaces for easy-removals of environmental-related liquids after icing and melting. *Nano Res.* **2023**, *16*, 3267–3277. [CrossRef]
79. Wang, L.; Tian, Z.; Jiang, G.; Luo, X.; Chen, C.; Hu, X.; Zhang, H.; Zhong, M. Spontaneous dewetting transitions of droplets during icing & melting cycle. *Nat. Commun.* **2022**, *13*, 378. [CrossRef]
80. Pan, R.; Zhang, H.; Zhong, M. Triple-Scale Superhydrophobic Surface with Excellent Anti-Icing and Icephobic Performance via Ultrafast Laser Hybrid Fabrication. *ACS Appl. Mater. Interfaces* **2020**, *13*, 1743–1753. [CrossRef]
81. Tian, Z.; Wang, L.; Zhu, D.; Chen, C.; Zhao, H.; Peng, R.; Zhang, H.; Fan, P.; Zhong, M. Passive Anti-Icing Performances of the Same Superhydrophobic Surfaces under Static Freezing, Dynamic Supercooled-Droplet Impinging, and Icing Wind Tunnel Tests. *ACS Appl. Mater. Interfaces* **2023**, *15*, 6013–6024. [CrossRef]
82. Chen, C.; Tian, Z.; Luo, X.; Jiang, G.; Hu, X.; Wang, L.; Peng, R.; Zhang, H.; Zhong, M. Cauliflower-like micro-nano structured superhydrophobic surfaces for durable anti-icing and photothermal de-icing. *Chem. Eng. J.* **2022**, *450*, 137936. [CrossRef]

83. Young, T. An essay on the cohesion of fluids philosophical transactions. *R. Soc. Publ.* **2022**, *95*, 65–87.
84. Wenzel, R.N. Resistance of solid surfaces to wetting by water. *Trans. Faraday Soc.* **1936**, *28*, 988–994. [CrossRef]
85. Cassie, A.B.D.; Baxter, S. Wettability of porous surfaces. *Trans. Faraday Soc.* **1944**, *40*, 546–551. [CrossRef]
86. Lafuma, A.; Quéré, D. Superhydrophobic states. *Nat. Mater.* **2003**, *2*, 457–460. [CrossRef]
87. Wang, D.; Sun, Q.; Hokkanen, M.J.; Zhang, C.; Lin, F.-Y.; Liu, Q.; Zhu, S.-P.; Zhou, T.; Chang, Q.; He, B.; et al. Design of robust superhydrophobic surfaces. *Nature* **2020**, *582*, 55–59. [CrossRef]
88. Guo, Z.; Liu, W. Biomimic from the superhydrophobic plant leaves in nature: Binary structure and unitary structure. *Plant Sci.* **2007**, *172*, 1103–1112. [CrossRef]
89. Feng, X.-Q.; Gao, X.; Wu, Z.; Jiang, L.; Zheng, Q.-S. Superior Water Repellency of Water Strider Legs with Hierarchical Structures: Experiments and Analysis. *Langmuir* **2007**, *23*, 4892–4896. [CrossRef]
90. Feng, L.; Zhang, Y.; Xi, J.; Zhu, Y.; Wang, N.; Xia, F.; Jiang, L. Petal Effect: A Superhydrophobic State with High Adhesive Force. *Langmuir* **2008**, *24*, 4114–4119. [CrossRef]
91. Li, P.; Zhang, B.; Zhao, H.; Zhang, L.; Wang, Z.; Xu, X.; Fu, T.; Wang, X.; Hou, Y.; Fan, Y.; et al. Unidirectional Droplet Transport on the Biofabricated Butterfly Wing. *Langmuir* **2018**, *34*, 12482–12487. [CrossRef]
92. Gao, X.; Yan, X.; Yao, X.; Xu, L.; Zhang, K.; Zhang, J.; Yang, B.; Jiang, L. The Dry-Style Antifogging Properties of Mosquito Compound Eyes and Artificial Analogues Prepared by Soft Lithography. *Adv. Mater.* **2007**, *19*, 2213–2217. [CrossRef]
93. Franta, B.; Mazur, E.; Sundaram, S.K. Ultrafast laser processing of silicon for photovoltaics. *Int. Mater. Rev.* **2018**, *63*, 227–240. [CrossRef]
94. Chichkov, B.N.; Momma, C.; Nolte, S.; von Alvensleben, F.; Tünnermann, A. Femtosecond, picosecond and nanosecond laser ablation of solids. *Appl. Phys. A* **1996**, *63*, 109–115. [CrossRef]
95. Wolfgang, K.; Joerg, K. Femtosecond pulse laser ablation of metallic, semiconducting, ceramic, and biological materials. In Proceedings of the Laser Materials Processing: Industrial and Microelectronics Applications, Vienna, Austria, 3–8 April 1994; pp. 600–611.
96. Ihlemann, J.; Wolff, B.; Simon, P. Nanosecond and femtosecond excimer laser ablation of fused silica. *Appl. Phys. A* **1992**, *54*, 363–368. [CrossRef]
97. Ahmmed, K.M.T.; Grambow, C.; Kietzig, A.-M. Fabrication of Micro/Nano Structures on Metals by Femtosecond Laser Micromachining. *Micromachines* **2014**, *5*, 1219–1253. [CrossRef]
98. von der Linde, D.; Sokolowski-Tinten, K.; Bialkowski, J. Laser–solid interaction in the femtosecond time regime. *Appl. Surf. Sci.* **1997**, *109–110*, 1–10. [CrossRef]
99. Fan, P.; Bai, B.; Jin, G.; Zhang, H.; Zhong, M. Patternable fabrication of hyper-hierarchical metal surface structures for ultrabroad-band antireflection and self-cleaning. *Appl. Surf. Sci.* **2018**, *457*, 991–999. [CrossRef]
100. Fan, P.; Zhong, M.; Bai, B.; Jin, G.; Zhang, H. Tuning the optical reflection property of metal surfaces via micro–nano particle structures fabricated by ultrafast laser. *Appl. Surf. Sci.* **2015**, *359*, 7–13. [CrossRef]
101. Rajan, R.A.; Ngo, C.-V.; Yang, J.; Liu, Y.; Rao, K.S.; Guo, C. Femtosecond and picosecond laser fabrication for long-term superhydrophilic metal surfaces. *Opt. Laser Technol.* **2021**, *143*, 107241. [CrossRef]
102. Rajab, F.H.; Liu, Z.; Li, L. Long term superhydrophobic and hybrid superhydrophobic/superhydrophilic surfaces produced by laser surface micro/nano surface structuring. *Appl. Surf. Sci.* **2019**, *466*, 808–821. [CrossRef]
103. Luo, X.; Liu, W.; Chen, C.; Jiang, G.; Hu, X.; Zhang, H.; Zhong, M. Femtosecond laser micro-nano structured Ag SERS substrates with unique sensitivity, uniformity and stability for food safety evaluation. *Opt. Laser Technol.* **2021**, *139*, 106969. [CrossRef]
104. Cai, M.; Pan, R.; Liu, W.; Luo, X.; Chen, C.; Zhang, H.; Zhong, M. Pulsed laser-assisted synthesis of defect-rich NiFe-based oxides for efficient oxygen evolution reaction. *J. Laser Appl.* **2020**, *32*, 022032. [CrossRef]
105. Yin, K.; Wang, L.; Deng, Q.; Huang, Q.; Jiang, J.; Li, G.; He, J. Femtosecond Laser Thermal Accumulation-Triggered Micro-/Nanostructures with Patternable and Controllable Wettability Towards Liquid Manipulating. *Nano-Micro Lett.* **2022**, *14*, 97. [CrossRef]
106. Zheng, J.; Yang, B.; Wang, H.; Zhou, L.; Zhang, Z.; Zhou, Z. Temperature-Responsive, Femtosecond Laser-Ablated Ceramic Surfaces with Switchable Wettability for On-Demand Droplet Transfer. *ACS Appl. Mater. Interfaces* **2023**, *15*, 13740–13752. [CrossRef]
107. Cai, Y.; Luo, X.; Liu, Z.; Qin, Y.; Chang, W.; Sun, Y. Product and process fingerprint for nanosecond pulsed laser ablated superhydrophobic surface. *Micromachines* **2019**, *10*, 177. [CrossRef]
108. Zhong, M.; Fan, P. Ultrafast Laser Enabling Versatile Fabrication of Surface Micro-nano Structures. In *Laser Micro-Nano-Manufacturing and 3D Microprinting*; Hu, A., Ed.; Springer International Publishing: Cham, Switzerland, 2020; pp. 75–112.
109. Shen, Y.; Xie, X.; Tao, J.; Chen, H.; Cai, Z.; Liu, S.; Jiang, J. Mechanical Equilibrium Dynamics Controlling Wetting State Transition at Low-Temperature Superhydrophobic Array-Microstructure Surfaces. *Coatings* **2021**, *11*, 522. [CrossRef]
110. Shi, S.; Lv, C.; Zheng, Q. Drop Impact on Two-Tier Monostable Superrepellent Surfaces. *ACS Appl. Mater. Interfaces* **2019**, *11*, 43698–43707. [CrossRef]
111. Wu, H.; Yang, Z.; Cao, B.; Zhang, Z.; Zhu, K.; Wu, B.; Jiang, S.; Chai, G. Wetting and Dewetting Transitions on Submerged Superhydrophobic Surfaces with Hierarchical Structures. *Langmuir* **2017**, *33*, 407–416. [CrossRef]
112. Tavakoli, F.; Kavehpour, H.P. Cold-Induced Spreading of Water Drops on Hydrophobic Surfaces. *Langmuir* **2015**, *31*, 2120–2126. [CrossRef]

113. Han, X.; Wang, M.; Yan, R.; Wang, H. Cassie State Stability and Gas Restoration Capability of Superhydrophobic Surfaces with Truncated Cone-Shaped Pillars. *Langmuir* **2021**, *37*, 12897–12906. [CrossRef]
114. Wang, W.; Zhang, Y.; Chen, T.; Sun, X.; Mei, X.; Cui, J. Wettability and Stability of Wetting States for the Surfaces with Reentrant Structures. *J. Phys. Chem. C* **2020**, *124*, 28479–28487. [CrossRef]
115. Pan, R.; Cai, M.; Liu, W.; Luo, X.; Chen, C.; Zhang, H.; Zhong, M. Extremely high Cassie-Baxter state stability of superhydrophobic surfaces via precisely tunable dual-scale and triple-scale micro-nano structures. *J. Mater. Chem. A* **2019**, *7*, 18050–18062. [CrossRef]
116. Luo, X.; Pan, R.; Cai, M.; Liu, W.; Chen, C.; Jiang, G.; Hu, X.; Zhang, H.; Zhong, M. Atto-Molar Raman detection on patterned superhydrophilic-superhydrophobic platform via localizable evaporation enrichment. *Sens. Actuators B Chem.* **2021**, *326*, 128826. [CrossRef]
117. Pan, R.; Cai, M.; Liu, W.; Luo, X.; Chen, C.; Zhang, H.; Zhong, M. Ultrafast laser hybrid fabrication of hierarchical 3D structures of nanorods on microcones for superhydrophobic surfaces with excellent Cassie state stability and mechanical durability. *J. Laser Appl.* **2020**, *32*, 022047. [CrossRef]
118. Wang, L.; Jiang, G.; Tian, Z.; Chen, C.; Hu, X.; Peng, R.; Zhang, H.; Fan, P.; Zhong, M. Superhydrophobic microstructures for better anti-icing performances: Open-cell or closed-cell? *Mater. Horiz.* **2023**, *10*, 209–220. [CrossRef]
119. Li, X.-M.; Reinhoudt, D.; Crego-Calama, M. What do we need for a superhydrophobic surface? A review on the recent progress in the preparation of superhydrophobic surfaces. *Chem. Soc. Rev.* **2007**, *36*, 1350–1368. [CrossRef] [PubMed]
120. Qing, Y.; Shi, S.; Lv, C.; Zheng, Q. Microskeleton-Nanofiller Composite with Mechanical Super-Robust Superhydrophobicity against Abrasion and Impact. *Adv. Funct. Mater.* **2020**, *30*, 1910665. [CrossRef]
121. Zeng, Q.; Zhou, H.; Huang, J.; Guo, Z. Review on the recent development of durable superhydrophobic materials for practical applications. *Nanoscale* **2021**, *13*, 11734–11764. [CrossRef] [PubMed]
122. Nishino, T.; Meguro, M.; Nakamae, K.; Matsushita, M.; Ueda, Y. The Lowest Surface Free Energy Based on –CF₃ Alignment. *Langmuir* **1999**, *15*, 4321–4323. [CrossRef]
123. Liu, L.; Charlton, L.; Song, Y.; Li, T.; Li, X.; Yin, H.; He, T. Scaling resistance by fluoro-treatments: The importance of wetting states. *J. Mater. Chem. A* **2022**, *10*, 3058–3068. [CrossRef]
124. Li, R.; Tian, S.; Tian, Y.; Wang, J.; Xu, S.; Yang, K.; Yang, J.; Zhang, L. An Extreme-Environment-Resistant Self-Healing Anti-Icing Coating. *Small* **2022**, *19*, 2206075. [CrossRef] [PubMed]
125. Vercillo, V.; Tonnichia, S.; Romano, J.-M.; García-Girón, A.; Aguilar-Morales, A.I.; Alamri, S.; Dimov, S.S.; Kunze, T.; Lasagni, A.F.; Bonaccorso, E. Design Rules for Laser-Treated Icephobic Metallic Surfaces for Aeronautic Applications. *Adv. Funct. Mater.* **2020**, *30*, 1910268. [CrossRef]
126. Walker, C.; Lerch, S.; Reiningger, M.; Eghlidi, H.; Milionis, A.; Schutzius, T.M.; Poulikakos, D. Desublimation Frosting on Nanoengineered Surfaces. *ACS Nano* **2018**, *12*, 8288–8296. [CrossRef]
127. Bai, G.; Gao, D.; Liu, Z.; Zhou, X.; Wang, J. Probing the critical nucleus size for ice formation with graphene oxide nanosheets. *Nature* **2019**, *576*, 437–441. [CrossRef]
128. Matsumoto, M.; Saito, S.; Ohmine, I. Molecular dynamics simulation of the ice nucleation and growth process leading to water freezing. *Nature* **2002**, *416*, 409. [CrossRef]
129. Long, J.; Wu, Y.; Gong, D.; Fan, P.; Jiang, D.; Zhang, H.; Zhong, M. Femtosecond laser fabricated superhydrophobic copper surfaces and their anti-icing properties. *Zhongguo Jiguang/Chin. J. Lasers* **2015**, *42*, 156–163. [CrossRef]
130. Pan, R.; Zhang, H.; Zhong, M. Ultrafast Laser Hybrid Fabrication and Ice-Resistance Performance of a Triple-Scale Micro/Nano Superhydrophobic Surface. *Chin. J. Lasers-Zhongguo Jiguang* **2021**, *48*, 0202009. [CrossRef]
131. Ge, C.; Yuan, G.; Guo, C.; Ngo, C.-V.; Li, W. Femtosecond laser fabrication of square pillars integrated Siberian-Cocklebur-like microstructures surface for anti-icing. *Mater. Des.* **2021**, *204*, 109689. [CrossRef]
132. Xing, W.; Li, Z.; Yang, H.; Li, X.; Wang, X.; Li, N. Anti-icing aluminum alloy surface with multi-level micro-nano textures constructed by picosecond laser. *Mater. Des.* **2019**, *183*, 108156. [CrossRef]
133. Hong, Z.; Wang, W.; Ma, Z.; Lu, M.; Pan, S.; Shi, E.; Chen, Z.; Zhang, C. Anti-icing ceramics surface induced by femtosecond laser. *Ceram. Int.* **2022**, *48*, 10236–10243. [CrossRef]
134. Wan, Y.; Yan, C.; Yu, H.; Wang, B. Anti-Icing Performance of Superhydrophobic Surface with Square-Ring Structure Prepared by Nanosecond Laser. *Adv. Eng. Mater.* **2021**, *23*, 2100190. [CrossRef]
135. Gaddam, A.; Sharma, H.; Karkantonis, T.; Dimov, S. Anti-icing properties of femtosecond laser-induced nano and multiscale topographies. *Appl. Surf. Sci.* **2021**, *552*, 149443. [CrossRef]
136. Zhao, M.; Yin, Y.; He, Q.; Zhao, X. Anti-icing capability of textured silicone rubber surfaces via laser processing. *Mater. Manuf. Process.* **2021**, *36*, 979–986. [CrossRef]
137. Boreyko, J.B.; Collier, C.P. Delayed Frost Growth on Jumping-Drop Superhydrophobic Surfaces. *ACS Nano* **2013**, *7*, 1618–1627. [CrossRef]
138. Sun, X.; Rykaczewski, K. Suppression of Frost Nucleation Achieved Using the Nanoengineered Integral Humidity Sink Effect. *ACS Nano* **2017**, *11*, 906–917. [CrossRef]
139. Kim, P.; Wong, T.-S.; Alvarenga, J.; Kreder, M.J.; Adorno-Martinez, W.E.; Aizenberg, J. Liquid-Infused Nanostructured Surfaces with Extreme Anti-Ice and Anti-Frost Performance. *ACS Nano* **2012**, *6*, 6569–6577. [CrossRef] [PubMed]
140. Lo, C.-W.; Sahoo, V.; Lu, M.-C. Control of Ice Formation. *ACS Nano* **2017**, *11*, 2665–2674. [CrossRef] [PubMed]

141. Dou, R.; Chen, J.; Zhang, Y.; Wang, X.; Cui, D.; Song, Y.; Jiang, L.; Wang, J. Anti-icing Coating with an Aqueous Lubricating Layer. *ACS Appl. Mater. Interfaces* **2014**, *6*, 6998–7003. [CrossRef]
142. Chen, J.; Dou, R.; Cui, D.; Zhang, Q.; Zhang, Y.; Xu, F.; Zhou, X.; Wang, J.; Song, Y.; Jiang, L. Robust Prototypical Anti-icing Coatings with a Self-lubricating Liquid Water Layer between Ice and Substrate. *ACS Appl. Mater. Interfaces* **2013**, *5*, 4026–4030. [CrossRef]
143. He, J.-G.; Zhao, G.-L.; Dai, S.-J.; Li, M.; Zou, G.-S.; Wang, J.-J.; Liu, Y.; Yu, J.-Q.; Xu, L.-F.; Li, J.-Q.; et al. Fabrication of Metallic Superhydrophobic Surfaces with Tunable Condensate Self-Removal Capability and Excellent Anti-Frosting Performance. *Nanomaterials* **2022**, *12*, 3655. [CrossRef]
144. Long, J.; Zhou, P.; Huang, Y.; Xie, X. Enhancing the Long-Term Robustness of Dropwise Condensation on Nanostructured Superhydrophobic Surfaces by Introducing 3D Conical Microtextures Prepared by Femtosecond Laser. *Adv. Mater. Interfaces* **2020**, *7*, 2000997. [CrossRef]
145. Byun, S.; Jeong, H.; Kim, D.R.; Lee, K.-S. Frost layer growth behavior on ultra-low temperature surface with a superhydrophobic coating. *Int. Commun. Heat Mass Transf.* **2021**, *128*, 105641. [CrossRef]
146. Park, H.; Ahmadi, F.; Boreyko, J. Using Frost to Promote Cassie Ice on Hydrophilic Pillars. *Phys. Rev. Lett.* **2021**, *127*, 044501. [CrossRef]
147. Mittal, K.L.; Choi, C.H. *Ice Adhesion—Mechanism, Measurement and Mitigation*; John Wiley & Sons: Hoboken, NJ, USA, 2020.
148. Fortin, G.; Beisswenger, A.; Perron, J. Centrifuge Adhesion Test to Evaluate Icephobic Coatings. In Proceedings of the AIAA Atmospheric and Space Environments Conference, Toronto, ON, Canada, 2–5 August 2010.
149. Irajizad, P.; Al-Bayati, A.; Eslami, B.; Shafquat, T.; Nazari, M.; Jafari, P.; Kashyap, V.; Masoudi, A.; Araya, D.; Ghasemi, H. Stress-localized durable icephobic surfaces. *Mater. Horiz.* **2019**, *6*, 758–766. [CrossRef]
150. Work, A.; Lian, Y. A critical review of the measurement of ice adhesion to solid substrates. *Prog. Aerosp. Sci.* **2018**, *98*, 1–26. [CrossRef]
151. Alamri, S.; Vercillo, V.; Aguilar-Morales, A.I.; Schell, F.; Wetterwald, M.; Lasagni, A.F.; Bonaccorso, E.; Kunze, T. Self-Limited Ice Formation and Efficient De-Icing on Superhydrophobic Micro-Structured Airfoils through Direct Laser Interference Patterning. *Adv. Mater. Interfaces* **2020**, *7*, 2001231. [CrossRef]
152. Li, J.; Zhou, Y.; Wang, W.; Xu, C.; Ren, L. Superhydrophobic Copper Surface Textured by Laser for Delayed Icing Phenomenon. *Langmuir* **2020**, *36*, 1075–1082. [CrossRef]
153. Belaud, C.; Vercillo, V.; Kolb, M.; Bonaccorso, E. Development of nanostructured icephobic aluminium oxide surfaces for aeronautic applications. *Surf. Coat. Technol.* **2021**, *405*, 126652. [CrossRef]
154. Milles, S.; Vercillo, V.; Alamri, S.; Aguilar, A.; Kunze, T.; Bonaccorso, E.; Lasagni, A. Icephobic Performance of Multi-Scale Laser-Textured Aluminum Surfaces for Aeronautic Applications. *Nanomaterials* **2021**, *11*, 135. [CrossRef]
155. Pan, R.; Zhong, M. Fabrication of superwetting surfaces by ultrafast lasers and mechanical durability of superhydrophobic surfaces. *Chin. Sci. Bull.* **2019**, *64*, 1268–1289. [CrossRef]
156. Chen, C.; Tian, Z.; Luo, X.; Jiang, G.; Hu, X.; Wang, L.; Peng, R.; Zhang, H.; Zhong, M. Micro–Nano–Nanowire Triple Structure-Held PDMS Superhydrophobic Surfaces for Robust Ultra-Long-Term Icephobic Performance. *ACS Appl. Mater. Interfaces* **2022**, *14*, 23973–23982. [CrossRef]
157. Wu, S.; Du, Y.; Alsaid, Y.; Wu, D.; Hua, M.; Yan, Y.; Yao, B.; Ma, Y.; Zhu, X.; He, X. Superhydrophobic photothermal icephobic surfaces based on candle soot. *Proc. Natl. Acad. Sci. USA* **2020**, *117*, 11240–11246. [CrossRef]
158. Jin, Y.; He, Z.; Guo, Q.; Wang, J. Control of Ice Propagation by Using Polyelectrolyte Multilayer Coatings. *Angew. Chem. Int. Ed.* **2017**, *56*, 11436–11439. [CrossRef]
159. Niu, W.; Chen, G.Y.; Xu, H.; Liu, X.; Sun, J. Highly Transparent and Self-Healable Solar Thermal Anti-/Deicing Surfaces: When Ultrathin MXene Multilayers Marry a Solid Slippery Self-Cleaning Coating. *Adv. Mater.* **2022**, *34*, 2108232. [CrossRef]
160. Sun, W.; Lv, K.; Lou, Y.; Zeng, D.; Lin, X. Highly durable superhydrophobic surfaces based on a protective frame and crosslinked PDMS-candle soot coatings. *Mater. Res. Express* **2022**, *9*, 096401. [CrossRef]
161. Guo, X.-J.; Zhang, D.; Xue, C.-H.; Liu, B.-Y.; Huang, M.-C.; Wang, H.-D.; Wang, X.; Deng, F.-Q.; Pu, Y.-P.; An, Q.-F. Scalable and Mechanically Durable Superhydrophobic Coating of SiO₂/Polydimethylsiloxane/Epoxy Nanocomposite. *ACS Appl. Mater. Interfaces* **2023**, *15*, 4612–4622. [CrossRef] [PubMed]
162. Wang, P.; Yao, T.; Li, Z.; Wei, W.; Xie, Q.; Duan, W.; Han, H. A superhydrophobic/electrothermal synergistically anti-icing strategy based on graphene composite. *Compos. Sci. Technol.* **2020**, *198*, 108307. [CrossRef]
163. Jiang, G.; Chen, L.; Zhang, S.; Huang, H. Superhydrophobic SiC/CNTs Coatings with Photothermal Deicing and Passive Anti-Icing Properties. *Acs Appl. Mater. Interfaces* **2018**, *10*, 36505–36511. [CrossRef]
164. Xie, Z.; Wang, H.; Geng, Y.; Li, M.; Deng, Q.; Tian, Y.; Chen, R.; Zhu, X.; Liao, Q. Carbon-Based Photothermal Superhydrophobic Materials with Hierarchical Structure Enhances the Anti-Icing and Photothermal Deicing Properties. *ACS Appl. Mater. Interfaces* **2021**, *13*, 48308–48321. [CrossRef]
165. Xie, H.; Wei, J.; Duan, S.; Zhu, Q.; Yang, Y.; Chen, K.; Zhang, J.; Li, L.; Zhang, J. Non-fluorinated and durable photothermal superhydrophobic coatings based on attapulgite nanorods for efficient anti-icing and deicing. *Chem. Eng. J.* **2022**, *428*, 132585. [CrossRef]
166. Wang, L.; Zhang, H.; Zhu, D.; Yuan, L.; Zhong, M. Anti-Icing Research and Development of Superhydrophobic Surfaces. *Aerodyn. Res. Exp.* **2022**, *34*, 1–26.

167. Chu, Z.; Jiao, W.; Huang, Y.; Ding, G.; Zhong, X.; Yan, M.; Zheng, Y.; Wang, R. FDS-Modified SiO₂/rGO Wrinkled Films with a Micro-Nanoscale Hierarchical Structure and Anti-Icing/Deicing Properties under Condensation Condition. *Adv. Mater. Interfaces* **2020**, *7*, 1901446. [CrossRef]
168. Sun, H.; Lin, G.; Jin, H.; Bu, X.; Cai, C.; Jia, Q.; Ma, K.; Wen, D. Experimental investigation of surface wettability induced anti-icing characteristics in an ice wind tunnel. *Renew. Energy* **2021**, *179*, 1179–1190. [CrossRef]
169. Hao, T.; Zhu, Z.; Yang, H.; He, Z.; Wang, J. All-Day Anti-Icing/Deicing Film Based on Combined Photo-Electro-Thermal Conversion. *ACS Appl. Mater. Interfaces* **2021**, *13*, 44948–44955. [CrossRef]
170. Xue, Y.; Wang, Y.; Wang, Y.; Liang, W.; Wang, F.; Zhu, D.; Zhao, H. Functionalized superhydrophobic MWCNT/PEI nanocomposite film with anti-icing and photo-/electrothermal deicing properties. *Mater. Chem. Phys.* **2023**, *297*, 127385. [CrossRef]
171. Ma, L.; Wang, J.; Zhao, F.; Wu, D.; Huang, Y.; Zhang, D.; Zhang, Z.; Fu, W.; Li, X.; Fan, Y. Plasmon-mediated photothermal and superhydrophobic TiN-PTFE film for anti-icing/deicing applications. *Compos. Sci. Technol.* **2019**, *181*, 107696. [CrossRef]
172. Fan, P.X.; Wu, H.; Zhong, M.L.; Zhang, H.J.; Bai, B.F.; Jin, G.F. Large-scale cauliflower-shaped hierarchical copper nanostructures for efficient photothermal conversion. *Nanoscale* **2016**, *8*, 14617–14624. [CrossRef]
173. Ma, W.; Li, Y.; Chao, C.Y.H.; Tso, C.Y.; Huang, B.; Li, W.; Yao, S. Solar-assisted icephobicity down to $-60\text{ }^{\circ}\text{C}$ with superhydrophobic selective surfaces. *Cell Rep. Phys. Sci.* **2021**, *2*, 100384. [CrossRef]
174. Zhou, L.; Liu, A.; Zhou, L.; Li, Y.; Kang, J.; Tang, J.; Han, Y.; Liu, H. Facilely Fabricated Self-Lubricated Photothermal Coating with Long-Term Durability and External-Replenishing Property for Anti-Icing/Deicing. *ACS Appl Mater Interfaces* **2022**, *14*, 8537–8548. [CrossRef]
175. Zhao, W.; Xiao, L.; He, X.; Cui, Z.; Fang, J.; Zhang, C.; Li, X.; Li, G.; Zhong, L.; Zhang, Y. Moth-eye-inspired texturing surfaces enabled self-cleaning aluminum to achieve photothermal anti-icing. *Opt. Laser Technol.* **2021**, *141*, 107115. [CrossRef]
176. Zhang, H.; Zhao, G.; Wu, S.; Alsaid, Y.; Zhao, W.; Yan, X.; Liu, L.; Zou, G.; Lv, J.; He, X.; et al. Solar anti-icing surface with enhanced condensate self-removing at extreme environmental conditions. *Proc. Natl. Acad. Sci. USA* **2021**, *118*, e2100978118. [CrossRef]
177. Vercillo, V. Durable Laser Patterned Metal Surfaces with Enhanced Icephobic Properties for Aerospace Applications. Ph.D. Thesis, Technische Universität Dresden, Dresden, Germany, 2020.
178. Boinovich, L.B.; Emelyanenko, A.M.; Emelyanenko, K.A.; Modin, E.B. Modus Operandi of Protective and Anti-icing Mechanisms Underlying the Design of Longstanding Outdoor Icephobic Coatings. *ACS Nano* **2019**, *13*, 4335–4346. [CrossRef] [PubMed]

Disclaimer/Publisher’s Note: The statements, opinions and data contained in all publications are solely those of the individual author(s) and contributor(s) and not of MDPI and/or the editor(s). MDPI and/or the editor(s) disclaim responsibility for any injury to people or property resulting from any ideas, methods, instructions or products referred to in the content.

Article

Erosion Resistant Hydrophobic Coatings for Passive Ice Protection of Aircraft

Naiheng Song *  and Ali Benmeddour

Aerospace Research Center, National Research Council of Canada, 1200 Montreal Road,
Ottawa, ON K1A 0R6, Canada

* Correspondence: naiheng.song@nrc-cnrc.gc.ca; Tel.: +1-613-9988970

Abstract: Novel polymeric coatings, namely slippery polyurethane (SPU) coatings, with high surface hydrophobicity and superior erosion resistance against high speed solid particles and water droplets were successfully developed to protect the leading edge of fast moving aerodynamic structures, such as aircraft wings and rotor blades, against ice accretion. The coatings comprise newly synthesized surface-modifying polymers (SMPs) bearing fluorinated and polydimethylsiloxane branches at a loading level of 1–5 wt.%, based on the total resin solid, which showed good compatibility with the erosion-resistant polyurethane matrix (PU-R) and rendered effective surface hydrophobicity and slipperiness to the coatings, as evidenced by the high water contact angles of 100–115°. The coatings can be easily be sprayed or solution cast and cured at ambient temperature to provide highly durable thin coating films. X-ray photoelectron spectroscopy (XPS) investigation showed concentration of fluorine on the surface. The presence of 1–5 wt.% of SMPs in the polyurethane matrix slightly reduced the tensile modulus but had no significant impact on the tensile strength. All coating films exhibited good thermal stability with no material softening or degradation after heating at 121 °C for 24 h. DSC heating scans revealed no thermal transitions in the temperature range of –80 °C to 200 °C. Ice adhesion strength (IAS) tests using a static push rig in a cold room of –14 °C showed IAS as low as 220 kPa for the SPU coatings, which is much lower than that of PU-R (i.e., about 620 kPa). Sand erosion tests using 50 µm angular alumina particles at an impinging speed of 150 m/s and an impinging angle of 30° revealed very low erosion rates of ca. 100 µg/g sand for the coatings. Water droplet erosion tests at 175 m/s using 463 µm droplets with 42,000 impingements every minute showed no significant coating removal after 20 min of testing. The combination of the high surface hydrophobicity, low ice adhesion strength and superior erosion resistance makes the SPU coatings attractive for ice protection of aircraft structures, where the coatings' erosion durability is of paramount importance.

Keywords: icing protection; hydrophobic coating; surface modifying polymer; ice adhesion strength; erosion resistance



Citation: Song, N.; Benmeddour, A. Erosion Resistant Hydrophobic Coatings for Passive Ice Protection of Aircraft. *Appl. Sci.* **2022**, *12*, 9589. <https://doi.org/10.3390/app12199589>

Academic Editor: Filomena Piscitelli

Received: 11 July 2022

Accepted: 16 September 2022

Published: 24 September 2022

Publisher's Note: MDPI stays neutral with regard to jurisdictional claims in published maps and institutional affiliations.



Copyright: © 2022 by the authors. Licensee MDPI, Basel, Switzerland. This article is an open access article distributed under the terms and conditions of the Creative Commons Attribution (CC BY) license (<https://creativecommons.org/licenses/by/4.0/>).

1. Introduction

Aircraft icing by super-cooled water droplets poses a major hazard for aviation [1]. For aircraft flying in cold regions, ice may form and accrete quickly on certain surfaces, particularly on the leading edge of a wing, the tail and the engine intakes, causing increased drag and weight and decreased thrust and lift, all of which are detrimental to aircraft performance. To mitigate the risks associated with icing, in addition to navigating away from the hazardous regions or grounding the aircraft [2,3], which is not always possible due to difficulties in accurately forecasting the hazardous freezing layers, commercial jets are commonly equipped with active anti-icing technologies, such as passing hot bleeding air from engine compressors through icing prone areas, forcing freezing point depressant fluid out of porous panels, and using electro-thermal ice protection systems or pneumatic de-ice boots [4]. However, despite the effectiveness of these systems, they are not applicable

to most small and light aircraft, such as helicopters, remotely piloted aircraft systems (RPAS) and next generation air taxis, due to system complexity, added weight and power requirement. As a result, intensive efforts have been made around the world to develop prospective icing protective measures, especially passive icephobic coatings that can minimize in-flight icing and ice adhesion and/or facilitate ice removal with minimal externally applied forces.

In the pursuit of effective icephobic coatings for aircraft ice protection, various coating designs have been explored, including superhydrophobicity, lubricant or freezing point depressant infusion, hydrated surfaces and low shear modulus coatings [5,6]. However, although numerous coatings have been developed to show substantially reduced ice adhesion strength (IAS), they all suffer critical shortcomings that limit their practical application. For example, superhydrophobic coatings are known to have low work of adhesion to liquid water; many studies [7,8] have shown that a superhydrophobic surface could delay water freezing, reduce IAS and facilitate thermal de-icing. However, their downsides are significant, including low resistance to condensation and frosting, poor mechanical integrity and difficulty in quality control and repair [9–11]. For lubricant- or freezing point depressant-infused surfaces, a very low IAS of <50 kPa has been achieved [12–14]. Nevertheless, such coatings have not shown the high mechanical robustness and fluids resistance required for aircraft applications. More importantly, the infused lubricant or freezing point depressant is susceptible to depletion due to the high-speed impact of water droplets as well as due to repeated icing/de-icing cycles [15]. The hydratable coatings take advantage of the strong coating–water interactions that keep a portion of water non-freezing at sub-zero temperatures, thereby providing a water-lubricated slippery surface layer to depress ice formation and accretion [16–19]. However, the water up-take may swell and plasticize the coating, leading to reduced mechanical strength. Low shear modulus coatings (e.g., soft silicone elastomers) have recently drawn great attention due to their ability to afford extremely low IAS of less than 5 kPa [20–22]. Such low IAS values are highly attractive, but the high softness typically relates to high dust pick-up, deformation under air pressure and low erosion resistance against high-speed solid particles and rain droplets, making it difficult to use these types of materials for aircraft icing protection.

For a protective coating to be used on an aircraft, in addition to high icephobicity, it must meet comprehensive property requirements, such as workability, heat and low temperature resistance, weatherability, erosion durability and reparability. Among these, erosion resistance is the most important, since the coating applied to the leading edge of a wing or helicopter rotor blades, where icing tends to occur and cause the most negative impact on aircraft operation, may experience excessive wear due to the high-speed (e.g., 100–300 m/s) impact of sand, airborne dust, rain droplets and hail. To mitigate erosion damage, shield materials such as metal strips or caps made of nickel, titanium and stainless steel, as well as polymeric erosion protective tapes, are typically applied to the leading edges. Although studies have been carried out to understand the environment and surface properties in relation to IAS, and ceramic erosion-resistant coatings have been investigated for icing protection [23,24], the effectiveness of metals and ceramic coatings is limited due to their low ice adhesion reduction factor (e.g., <2) and poor applicability on large curved surfaces. In addition, erosion resistant polymeric coatings with reduced ice adhesion strength remain unknown.

Thus, it is the objective of this study to develop highly robust icephobic polymer coatings suitable for aircraft ice protection at leading edges, which have not only high icephobicity and superior erosion resistance, but also excellent thermal and mechanical properties, along with easy applicability on large curved surfaces. To this end, surface modification of a highly erosion resistant coating, namely PU-R, was carried out by introducing new surface-modifying polymers (SMPs) into the coating formulation, thereby producing novel slippery polyurethane (SPU) coatings with high surface hydrophobicity. The PU-R is a high solid, 2-part, solvent-borne aliphatic polyurethane coating developed at the National Research Council Canada. The coating demonstrated superior erosion resistance against

both high-speed solid particles and rain droplets, outperforming commercial aircraft top-coat and erosion protective tapes [25]. It is expected that the resulting SPU coatings could retain the exceptional erosion resistance of PU-R while exhibiting improved icephobicity to mitigate the hazards caused by icing on the leading edge surfaces of aircraft wings and helicopter rotor blades.

2. Materials and Methods

2.1. Materials

Desmodur[®] Z4470 BA (Z4470, NCO% = 11.9%, functionality ~3.5, Covestro, Leverkusen, Germany), anhydrous N,N-dimethylformamide (DMF, Sigma-Aldrich, St. Louis, MO, USA), 1H,1H,2H,2H-perfluoro-1-octanol (PFOA, Career Henan Chemicals, Zhengzhou, China), Terathane[®] PTMEG-650 (average Mw of 650 g/mol, Invista, Wichita, KS, USA), MCR-C18 (monocarbinol terminated polydimethylsiloxane, average Mw of 5000 g/mol, Gelest Inc., Bucks County, PA, USA) and dibutyltin dilaurate (DBTDL, Sigma-Aldrich) were used in the as-received conditions. Fiberglass plates (FR-4, 2 × 2 × 1/4 in) were purchased from Curbell plastics. Aeordur HS 2118 CF primer (Akzo Nobel, Amsterdam, The Netherlands) was purchased from Hypercoat-Downing Ltd., Mississauga, ON, Canada, X-9032/G401 Nix Stix[®] release agent was acquired from Stoner Molding Solutions. The matrix coating, namely PU-R, is a 2-part solvent-borne polyurethane elastomer coating developed at the National Research Council Canada for erosion protection of helicopter rotor blades against high-speed solid particles and rain droplets. Its formulation will be published elsewhere.

2.2. Methods

For property studies, coating and free-standing thin film samples were prepared by casting the coating solutions onto a fiberglass substrate (FR-4, 2 × 2 × 1/4 in) and into an aluminum mold (4.5 × 4.5 in) pre-treated with X-9032/G401 Nix Stix[®] release agent, respectively, followed by drying and curing at ambient conditions. Through controlling the amount of coating solutions cast, all the coatings on FR-4 and free-standing thin films have comparable thicknesses of ca. 0.35 mm.

Differential scanning calorimetry (DSC) was performed on DSC Q2000 (TA Instruments, New Castle, DE, USA) in nitrogen at specific heating and cooling profiles. FT-IR spectroscopy was recorded on Nicolet 6700 (Thermo Fisher Scientific, Waltham, MA, USA) equipped with Smart iTR[™] attenuated total reflectance (ATR) sampling accessory. Test samples were measured in the form of thin films that were pressed against a diamond plate with single bounce mode. The complex viscosity (η) of the coatings were measured by a DHR-2 rheometer (TA Instrument Co.) at 25 °C using a cone-plate geometry (40 mm, 0.9786°). The strain was set to be 5.85% and the angular frequency was set to be 10 rad/s. The X-ray photoelectron spectroscopy (XPS) data were collected using a Kratos AXIS Ultra DLD spectrometer with a monochromated Al K-alpha beam (1486.6 eV) under high vacuum (5×10^{-9} Torr). The binding energy scale was charge corrected by shifting the main peak of the C 1s spectrum to 284.8 eV. The electron collection lens aperture was set to sample a 700 $\mu\text{m} \times 300 \mu\text{m}$ spot, the largest possible, and at least two spots were measured for each sample to ensure the compositional information was representative of the average for the surface. The charge neutralizer was used in all measurements because the samples are non-conductive. The data were analyzed using CasaXPS (version 2.3.17PR1.1).

Tensile properties of thin films were measured on Instron model 5565 tensile tester equipped with pneumatic grips according to standard ASTM D412. Dumbbell-shaped film coupons were die cut using a DIN-53504-S3A type cutting die (ODC tooling & molds). All samples were conditioned at 23 ± 2 °C and $50 \pm 5\%$ RH for at least 24 h before testing. Due to the fact that slippage at the grip areas occurred during testing, benchmarks of 10 ± 1 mm distance (LO) in the middle of the dumbbell-shaped samples were drawn and followed during testing to obtain true elongation at break. The rate of grip separation was 500 mm/min. After rupture, the distance (LF) between the benchmarks was measured

within ca. 1 min for the calculation of tensile set. The Shore A hardness of the thin films was measured using a Rex DD-4 digital durometer with an OS-1 operating stand.

Solid particle erosion tests were performed according to ASTM Standard G76-04 using angular alumina particles of ca. 50 μm (AccuBRADE 50, part No.: AP106, S.S. White Technologies, Petersburg, FL, USA) as the erodent. During testing, the alumina particles were fed into a compressed air carrier stream from a pressurized vibrator-controlled hopper, which was allowed to pass through a silicon carbide nozzle with an inner diameter of 1.14 mm and directed towards the test sample at a preset impingement angle of 30° with respect to the test sample surface. The impingement speed of the ejected alumina particles was 150 m/s, which was controlled through adjusting the pressure of compressed air. The particle flux was regulated at 3–5 g/min by changing the vibrating amplitude of the hopper. The stand-off distance was maintained constant at 50 \pm 1 mm. After each 4 min of testing, the test sample was removed from the erosion rig and measured for its weight using an analytical balance with an accuracy of \pm 0.01 mg. At the same time, the weight of the consumed erodent was measured. Then the sample was returned to the test rig and erosion testing was resumed. The erosion rates were calculated by dividing the mass loss of the coatings with the mass of solid particles consumed. The maximum particle loads were estimated by dividing the amount of sand required to fail the coating sample (e.g., penetration) with the eroded area (i.e., approximately a circle of ca. 10 mm diameter).

The water droplet erosion (WDE) resistance of the coated samples were evaluated according to ASTM Standard G73 using a testing rig that was equipped with a working chamber, a vacuum system, a compressed air driven turbine and a water droplet generating system. During testing, two test coated coupons having mass differences of less than 0.1 g were mounted on the opposite ends of a rotating disc, with one as the comparative control and the other as the test sample. The disc was rotated at a specific speed while water droplets were formed in the test chamber on a path of the test coupons. A 30–50 mbar vacuum was maintained during the test to avoid temperature rise caused by friction between the rotating disc and air. In this study, the disc was rotated at a rate of 7000 rpm, corresponding to a water droplet impingement velocity of 175 m/s. The impingement angle was 90°. The average size of water droplets produced using a 400 μm shower head was about 463 μm . The test coupon underwent about 42,000 individual water droplet impingements during each minute of testing. For the test coupon preparation, AA2024 specimens (0.32" \times 0.97" \times 0.12") were first treated using Akzo Nobel's Metaflex® SP 1050 pretreatment, followed by priming using Aerodur HS 2118 primer (ca. 30 μm thick). The coatings of this study were applied by dispensing ca. 0.10 g of the coating solutions on the primed surface, followed by drying and curing at ambient conditions for 7 days. The coating layers had an average thickness of ca. 0.35 mm.

Static and dynamic water contact angles (CAs) were measured on an Automated Goniometer (Model 290, Ramé-hart Instrument Co., Succasunna, NJ, USA). For static contact angles, a water droplet of 4 μL was dispensed on the coating surface using an automated dispenser. The contact angles were analyzed by the Dropimage Advanced software. The measurement of dynamic contact angles, i.e., the advancing and receding angles, was performed using the volume addition and subtraction method, with each volume step being 2 μL and a delay time of 0.5 s. The maximum contact angle during volume addition was taken as the advancing angle, while the contact angle where the drop edges started to slide during volume subtraction was recorded as the receding angle.

Ice adhesion of the coatings was examined using the push-rig schematically shown in Figure 1 [26]. The set-up comprises a "pusher" shaft connected to a load cell, which, in turn, is connected to a threaded rod that provides lateral movement of the assembly into the test sample. The threaded rod was manually turned to drive the pusher against the ice block enclosed by a PTFE lined aluminum mold. Output from the load cell was recorded and the maximum force required to detach the ice block from the coating surface is used to calculate IAS. The aluminum mold has a dimension of 3" \times 3" \times 5/16", the PTFE has a thickness of 3/8" and the cavity for ice block preparation is 1" \times 1" \times 5/16". To prepare

the test sample, the PTFE lined aluminum mold was clamped tightly to the coating surface, with a rubber cushion (1/16" thick) sandwiched between the two. De-ionized water was filled into the cavity and the assembly was then kept in a cold room at $-14\text{ }^{\circ}\text{C}$ to freeze the water overnight. Figure 1 also shows the PTFE-lined aluminum mold and the preparation of the ice cube on the coating surface. Both the test sample preparation and the push rig test were performed in a cold room that was kept constantly at $-14\text{ }^{\circ}\text{C}$.

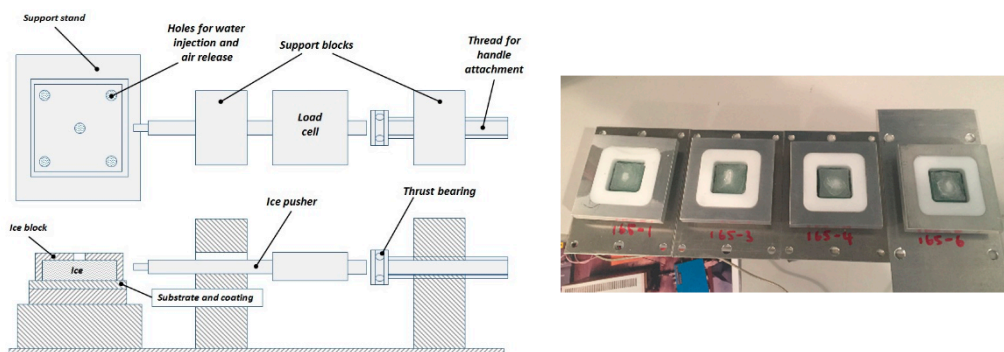


Figure 1. Schematic drawings of the push rig for ice adhesion test (left) and a picture of test specimens with ice formed in a cavity of PTFE-lined aluminum mold on top of coating surfaces (Right).

2.3. Preparation of Surface-Modifying Polymers (SMPs) and Durable Hydrophobic Polyurethane (SPU) Coatings

Synthesis of SMP-1: 1H,1H,2H,2H-perfluoro-1-octanol (PFOA, 6.5 g) and dibutyltin dilaurate (DBTDL, 0.3 g) were added to a solution of Desmodur[®] Z4470 BA (10.0 g) in 25 mL of anhydrous N,N-dimethylformamide (DMF). The mixture was heated to $60\text{ }^{\circ}\text{C}$ and stirred under nitrogen for 2 h before Terathane[®] PTMEG-650 (3.7 g) in 10 mL of anhydrous DMF was added, dropwise. The resulting reaction mixture was stirred at $60\text{ }^{\circ}\text{C}$ for another 3 h. After cooling to room temperature, the viscous reaction solution was precipitated in 300 mL of de-ionized water/methanol (4/1, v/v). The sticky solid formed was washed twice with warm de-ionized water (300 mL) and once with methanol (200 mL), then dried at $75\text{ }^{\circ}\text{C}$ in a convection oven for 72 h to yield 16.0 g of a clear rubbery product (yield 80%).

Synthesis of SMP-2: PFOA (6.2 g), MCR-C18 (4.1 g) and DBTDL (0.5 g) were added to a solution of Desmodur[®] Z4470BA (10.0 g) in 30 mL of anhydrous DMF. The mixture was heated to $60\text{ }^{\circ}\text{C}$ and stirred under nitrogen for 4 h before Terathane[®] PTMEG-650 (3.7 g) in 10 mL of anhydrous DMF was added. The reaction mixture was stirred at $60\text{ }^{\circ}\text{C}$ for another 3 h. After cooling to room temperature, the viscous reaction solution was precipitated in 300 mL of de-ionized water/methanol (4/1, v/v) and the resulting sticky solid was washed twice with warm de-ionized water (300 mL) and once with methanol (200 mL), then dried at $80\text{ }^{\circ}\text{C}$ in a convection oven for 72 h to yield 21.6 g of an opaque gel product (yield 90%).

Synthesis of SMP-3: PFOA (5.9 g), MCR-C18 (8.1 g) and DBTDL (0.5 g) were added to a solution of Desmodur[®] Z4470BA (10.0 g) in 30 mL of anhydrous DMF. The mixture was heated to $60\text{ }^{\circ}\text{C}$ and stirred under nitrogen for 4 h before Terathane[®] PTMEG-650 (3.7 g) in 10 mL of anhydrous DMF was added. The reaction mixture was stirred at $60\text{ }^{\circ}\text{C}$ for another 3 h. After cooling to room temperature, the viscous reaction solution was precipitated in 300 mL of de-ionized water/methanol (4/1, v/v) and the resulting sticky solid was washed twice with warm de-ionized water (300 mL) and once with methanol (200 mL), then dried at $80\text{ }^{\circ}\text{C}$ in a convection oven for 72 h to yield 23.8 g of an opaque gel product (yield 86%).

Preparation of SPU coating and thin film samples: SPU coating solutions were prepared by formulating the SMPs (i.e., SMP-1 to SMP-3) into the erosion-resistant polyurethane coating PU-R at levels of 1.0, 3.0 and 5.0 wt.%, respectively, based on the total resin solid. The coating solutions (ca. 1.50 g) were cast on fiberglass substrates (FR-4, $2 \times 2 \times 1/4$ in), followed by drying and curing at ambient conditions for 7 days to produce coatings with a dry film thickness of ca. 0.35 mm. The coating samples for water droplet erosion tests were prepared by casting ca. 0.10 g of coating solution on aluminum specimen (Al 2024 alloy,

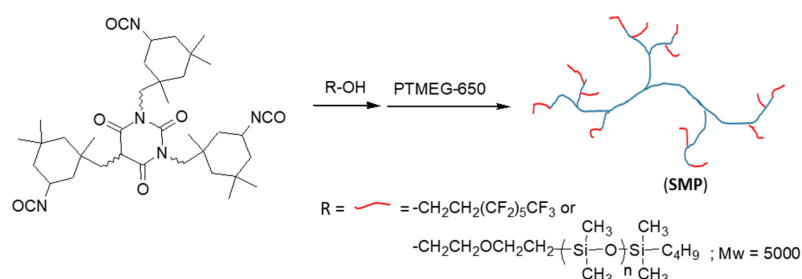
0.31 × 0.85 × 0.12 in), pre-coated with a chromate-free Aeordur HS 2118 CF primer (ca. 40 μm thick). The coatings were dried and cured at ambient conditions for 7 days before testing. For thin film samples, ca. 7.62 g of coating solutions were cast into an aluminum mold (4.5 × 4.5 in) pre-treated with X-9032/G401 Nix Stix[®] release agent. The coating solutions were allowed to flow and level naturally. After drying and curing at room temperature for 1 day, the resulting thin films (ca. 0.35 mm thick) were removed from the mold and allowed to further cure at ambient conditions for 6 more days before testing.

3. Results and Discussion

3.1. Synthesis of SMPs and SPU Coatings

To mitigate icing and ice accretion on the leading edge surfaces of aircraft wings and helicopter rotor blades without sacrificing erosion durability against high-speed solid particles and rain droplets, it would be straightforward and ideal to modify the existing erosion resistant coatings to render the surface with icephobicity. To this end, effort was first made by introducing various commercial surface modifying agents such as polyether-modified polydimethylsiloxane (e.g., BYK-306, BYK), fluorinated copolymers (e.g., Capstone[™] FS-83, Chemours), hydrophobic fumed silica (e.g., Aerosil[®] R 812, Evonik), PTFE micropowders (e.g., Zonyl[®] MP 1100, Chemours) and PEGylated polydimethylsiloxane (e.g., DBE-224, Gelest) into the erosion resistant PU-R coating at different levels in hoping to achieve hydrophobic and slippery surfaces that can delay ice formation or reduce ice adhesion strength. Unfortunately, limited success was achieved. None of these additives led to coatings with high surface hydrophobicity. Furthermore, foam stabilization and phase separation were observed when some of the additives (e.g., FS-83 and DBE-224) were incorporated at high amounts (e.g., >1 wt.%, based on total resin solid). Thus, to achieve durable icephobic coatings for leading edge icing protection, new surface-modifying polymers (SMP-1 to SMP-3) were designed and synthesized in this study, which bear low surface tension fluorinated and polydimethylsiloxane (PDMS) branches, and have good compatibility with the polyurethane matrix, to enable high PU-R surface hydrophobicity.

Scheme 1 shows the synthetic scheme of the SMPs, where the multifunctional polyisocyanate Z4470 BA ($f \approx 3.5$) first reacts with the mono hydroxyl compounds (i.e., PFOA and MCR-C18) to produce a reaction mixture, followed by polymerizing with the diol PTMEG-650. The intermediate reaction mixture consists of a distribution of reaction products of Z4470 with the mono hydroxyl compound (e.g., unreacted, mono-, di-, tri- and fully reacted Z4470), depending on the molar ratio of Z4470/(PFOA+MCR-C18). Structure-wise, it is preferred to have a minimum amount of unreacted and fully reacted Z4470 in the intermediate reaction mixture. The former has high functionality and tends to lead to crosslinking when polymerizing with PTMEG-650, while the latter may contribute to incompatibility of SMP with matrix PU-R due to poor inter-chain interactions. At the same time, the di-reacted Z4470 product that has a remaining isocyanate functionality of about 2 should be maximized so as to produce high molecular weight SMPs with branched structures. For the reaction system of this study, it was experimentally found that a suitable molar ratio of Z4470/(PFOA+MCR-R18) was about 1/2.2, where highly branched polymers could be obtained from the subsequent polymerization reaction with PTMEG-650 without crosslinking.



Scheme 1. Synthetic scheme of the surface-modifying polymers.

Table 1 summarizes the syntheses of the SMPs using different combinations of PFOA and MCR-C18 as the mono hydroxyl compounds for the purpose of examining the effects of fluorinated branches and silicone branches of the SMPs on coating properties. The reaction of N4470 with PFOA and MCR-C18 at 60 °C in the presence of DBTDL as a catalyst gave clear solutions, although MCR-C18 was initially immiscible with the reaction mixture. The addition of PTMEG-650 quickly increased the solution viscosity, suggesting the build-up of molecular weight. FTIR investigations showed the disappearance of the characteristic NCO absorption at around 2265 cm⁻¹ in about 2 h of reaction time, indicating the completeness of the reactions. SMP-1 was obtained as a clear rubbery gel, while SMP-2 and SMP-3 were white soft gels. The white color of SMP-2 and MSP-3 may be attributed to the phase separation of PDMS segments within the SMPs. Theoretical calculations based on the stoichiometry ratios gave a residual hydroxyl content in SMPs in the range of 0.029–0.040 mmol/g, which is small and not expected to affect the stoichiometry of PU-R coating formulation.

Table 1. Syntheses of SMPs.

SMPs	Molar Equivalence				PFOA (wt.%)	MCR-C18 (wt.%)	Residual OH (mmol/g)
	Z4470	PFOA	MCR-C18	PTMEG-650			
SMP-1	1	2.2	-	0.7	31.8%	0.0%	0.040
SMP-2	1	2.1	0.1	0.7	25.7%	16.8%	0.034
SMP-3	1	2.0	0.2	0.7	21.1%	29.0%	0.029

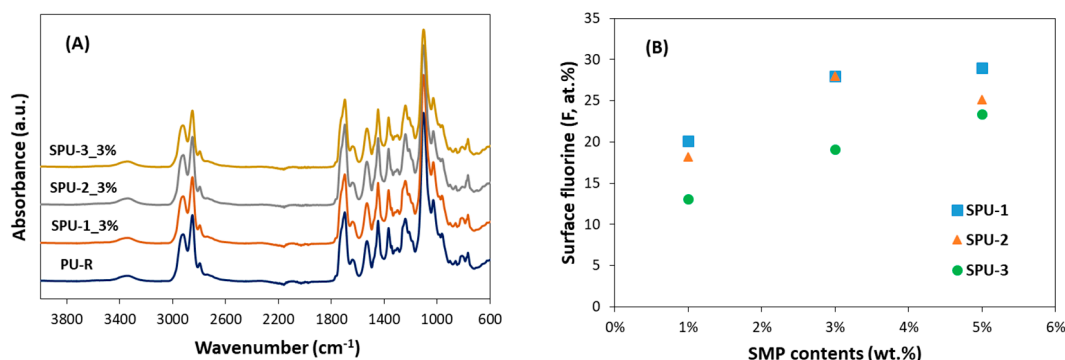
3.2. Coating Formulation and Preparation

To prepare coatings with high surface hydrophobicity and excellent erosion durability, the SMPs were formulated into the 2-part solvent-borne PU-R coatings at loading levels of ca. 1 wt.%, 3 wt.% and 5 wt.%, respectively, based on the total resin solid (Table 2). All the coating solutions (i.e., PU-R, SPU-1 to SPU-3) are clear, homogenous and free of bubbles. They have comparable solid contents of ca. 58 wt.% and complex viscosities of ca. 200–230 cp. Pot life was about 4 h, when the viscosity increased by 50%. The coatings can be easily applied using a low volume medium pressure (LVMP) spray gun or by solution casting. The tack-free times, when the coating surfaces became non-sticking to a touching spatula, were about 4 h. Although the FTIR spectra of the thin film samples indicated that curing was complete after 2 days (Figure 2A), as evidenced by the disappearance of characteristic NCO absorption peak at around 2240 cm⁻¹, all coating and thin film samples were allowed to cure at ambient conditions (e.g., 21 ± 2 °C, 20–80% relative humidity) for 7 days before property testing. Tough and elastomeric SPU dry films with a Shore A hardness of about 70 were obtained after the curing. Both PU-R and SPU coatings showed good adhesion to FR-4. No coating removal could be made without damaging the fiberglass substrate.

For property studies, coating and free-standing thin film samples were prepared by casting the coating solutions onto a fiberglass substrate (FR-4, 2 × 2 × 1/4 in) and into an aluminum mold (4.5 × 4.5 in) pre-treated with X-9032/G401 Nix Stix[®] release agent, respectively, followed by drying and curing at ambient conditions.

Table 2. Preparation and water contact angle measurements of SPU coatings.

Coatings	SMPs	wt.% of SMPs	θ , Water	θ_{adv} , Water	θ_{rec} , Water
PU-R	-	0	69.0	77.4	20.4
SPU-1_1%	SMP-1	1.0%	103.7	108.0	80.2
SPU-1_3%		3.0%	109.7	115.5	82.1
SPU-1_5%		5.0%	109.6	114.0	82.0
SPU-2_1%	SMP-2	1.0%	100.0	101.2	78.3
SPU-2_3%		3.0%	109.0	114.0	80.5
SPU-2_5%		5.0%	109.3	115.9	79.4
SPU-3_1%	SMP-3	1.0%	96.9	100.7	69.4
SPU-3_3%		3.0%	109.5	114.8	78.8
SPU-3_5%		5.0%	112.0	117.5	81.5

**Figure 2.** (A) FTIR spectra of PU-R and SPU coating films after curing at ambient conditions for 2 days, and (B) surface fluorine content (at.%) of SPU coatings from XPS studies.

3.3. Properties of SPU Coatings

Table 2, above, displays the static and dynamic water contact angles of the coatings, measured using a goniometer equipped with an automated dispenser. As expected, the unmodified matrix PU-R is hydrophilic and has a static water contact angle (θ) of 69° , whereas all SPU coatings comprising the SMPs are hydrophobic, with θ being larger than 97° . Water beaded up quickly and slid easily on the coating surfaces. Different SMPs showed no substantial differences in producing hydrophobic surfaces. However, SPU-2 and SPU-3 did give a more slippery feel than SPU-1 when rubbing fingers on the coating, probably due to the presence of PDMS on the surface. No smudge was observed after the finger rubbing, and the surface hydrophobicity could be easily restored for oil-contaminated surfaces by washing with detergent. A dependence of the water contact angle on the SMP content was revealed, as evidenced by the increase in θ when the SMP loading was increased from 1 wt.% to 3 wt.%, based on the total resin solid. Further increasing the SMP loadings to 5 wt.% did not lead to additional increase of θ . The hydrophilicity of PU-R was more clearly seen from its small receding angle (θ_{rec}) of ca. 20° and large contact angle hysteresis (CAH) of ca. 57° . In contrast, all SPU coatings exhibited high θ_{rec} of ca. 80° and small CAH in the range of $22\text{--}36^\circ$. Based on the relationship between water wettability and ice adhesion proposed by Muller et al. [27], as illustrated by Equation (1), where τ_{ice} is the ice adhesion strength, the matrix PU-R is expected to have an IAS of ca. 650 kPa, while the SPU coatings should have reduced IAS of ca. 400 kPa.

$$\tau_{ice} = (340 \pm 40 \text{ kPa})(1 + \cos\theta_{rec}), \quad (1)$$

To understand the surface elemental compositions, XPS was recorded for PU-R and the SPU coatings. As shown in Table 3, all the SMP-containing SPU coatings showed a high

fluorine content in the range of 13–29 at.%, indicating the enrichment of SMPs on coating surfaces. In contrast, the PU-R showed no fluorine on the surface. Figure 2B compares the surface fluorine contents of the SPU coatings. It can be seen that SPU-1 coatings have the highest fluorine contents, compared to SPU-2 and SPU-3, due to the high PFOA content in SMP-1. SPU-3 coatings, which are based on SMP-3, showed the lowest surface fluorine contents. For SPU-1 and SPU-2, the fluorine content seems to reach a plateau at a SMP loading of 3 wt.%, which agrees with the water contact angle measurement, where an increase of static water contact angle occurred from SPU-1_1% and SPU-2_1% to SPU-1_3% and SPU-2_3%, respectively, and leveled off thereafter. The SPU-3 coatings showed a monotonous increase of fluorine content with the SMP-3 loadings. For SPU-2 and SPU-3 coatings, it was expected that the silicone branches would behave similarly to the fluorinated chains in terms of surface enrichment. However, due to unknown reasons, XPS analysis of the Si content did not show a clear trend of increasing Si with the increasing MCR-C18 content of SMP. The detection of Si for PU-R and SPU-1 coatings, where no MCR-C18 was used, may be attributed to the presence of a silicone-containing surface additive, namely BYK-306 (BYK Additives and Instruments), in the PU-R formulation at a loading level of ca. 0.3 wt.%, based on total coating formulation. The decreasing Si content from PU-R to SPU-1 and to SPU-2 may be attributed to the strong tendency of SMP-1 to migrate to the surface during the drying and curing processes, which suppressed the enrichment of BYK-306 at the surface.

Table 3. XPS analysis of PU-R and SPU coatings.

Coatings	Elemental Content (at.%)				
	C 1s	N 1s	O 1s	F 1s	Si 2p
PU-R	69.38	2.79	20.79	0	7.04
SPU-1_1%	59.11	4.31	13.14	20.08	3.37
SPU-1_3%	56.66	4.96	9.56	27.96	0.87
SPU-1_5%	56.16	4.87	9.18	28.95	0.85
SPU-2_1%	58.56	4.00	14.28	18.21	4.95
SPU-2_3%	56.83	4.73	9.41	27.95	1.08
SPU-2_5%	56.31	4.49	11.02	25.16	3.03
SPU-3_1%	58.76	3.39	16.91	13.05	7.89
SPU-3_3%	56.05	3.64	14.05	19.07	7.19
SPU-3_5%	56.00	4.24	11.92	23.36	4.48

All SPU coatings exhibited good thermal stability with no material softening or degradation after heating at 121 °C for 24 h. Figure 3 shows the representative second DSC heating scans of the coatings recorded in nitrogen at a heating rate of 20 °C/min, which revealed no thermal transitions in the temperature range of −80 °C to 200 °C. These coating samples were pre-treated by heating to 200 °C at 20 °C/min, cooling to −50 °C at a rate of 10 °C/min, and stabilized at −80 °C before the second heating. Neither the first heating nor the cooling scans showed discernible glass or melting transitions, indicating thermoset properties for the coatings and high heat resistance.

Table 4 summarizes the tensile properties of the thin film samples, measured according to ASTM Standard D412 at a grip separation rate of 500 mm/min. It can be seen that all coating films exhibited high tensile strength (e.g., 19–27 MPa), high elongation at break (e.g., 640–730%) and low tensile set (e.g., 20–35%). In comparison with the matrix PU-R, the incorporation of SMP-1 did not substantially affect the tensile strength (SPU-1 in Figure 4A), but a slight decrease in modulus, as indicated by stress at 500% strain, was observed (Figure 4B). For SPU-2 and SPU-3, marginally decreased tensile strength and modulus were noticed with the increasing amount of SMP-2 and SMP-3, respectively. Elongation at break increased from 640% for PU-R to 680–730% for SPUs, depending on the SMP content, but no sizable changes in tensile set were observed. The small tensile sets (i.e., 20–35%) recorded within 1 min of sample failure indicate high resilience of the coating films.

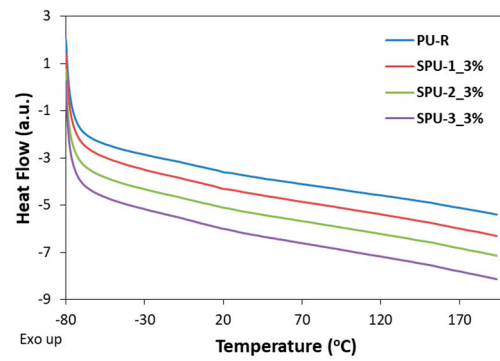


Figure 3. Representative second DSC heating scans of PU-R and SPU coatings in nitrogen at a heating rate of 20 °C/min.

Table 4. Tensile properties of PU-R and SPU coating films.

	Tensile Strength (MPa)	Stress at 300% Strain (MPa)	Stress at 500% Strain (MPa)	Elongation at Break (%)	Tensile Set (%)
PU-R	26.8	5.4	12.2	640%	25%
SPU-1_1%	27.2	5.2	11.2	680%	20%
SPU-1_3%	26.7	5.2	11.0	700%	20%
SPU-1_5%	23.9	4.9	9.9	720%	30%
SPU-2_1%	25.2	5.2	11.3	690%	20%
SPU-2_3%	18.9	4.5	8.9	690%	20%
SPU-2_5%	20.1	4.2	8.5	730%	30%
SPU-3_1%	23.0	5.1	10.7	690%	25%
SPU-3_3%	22.9	5.0	10.6	700%	35%
SPU-3_5%	18.7	4.5	8.8	700%	30%

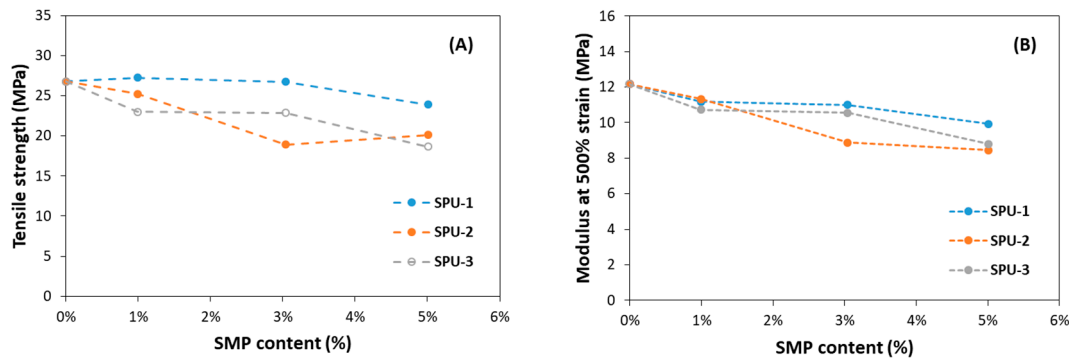


Figure 4. Plots of tensile strength (A) and modulus (B), as indicated by stress at 500% strain of SPU coatings against the SMP contents.

Figure 5A presents the IAS of the SPU coatings measured at $-14\text{ }^{\circ}\text{C}$. All the detachment occurred at the ice-coating interface due to adhesion failure, no breakage of ice block was observed. The matrix PU-R showed an IAS of about 622 kPa and the SPU coatings showed IAS in the range of 220–480 kPa. No substantial differences in IAS were discovered between the SPU coatings, regardless of the different SMPs and varying SMP loadings, except for SPU-3, which exhibited some lower IAS (e.g., ca. 250 kPa) at SMP-3 loadings of ≥ 3 wt.%. However, as expected, all these IAS values are in the range of hydrophobic fluorinated polymers (e.g., 150–350 kPa for PTFE [28]) and silicones (200–400 kPa [20]) and agree well with the predicted values according to Equation (1) by Muller et al. [27]. Figure 5B displays the IAS test results for coating samples that were subjected to repeated icing/ice removal cycles. As it can be seen, the IAS of matrix PU-R fluctuated in the range of 606–715 kPa

while the IAS of SPU-3_3% varied in the range of 220–370 kPa, which are in the error range based on Equation (1). The fact that no substantial increase in IAS was observed for SPU-3_3% indicates a good stability against multiple icing/ice removal cycles.

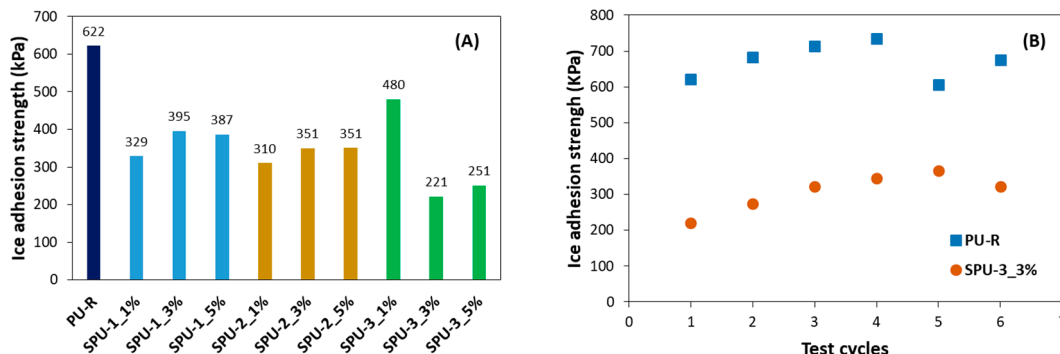


Figure 5. Ice adhesion strength (in kPa) of SPU coatings measured using a static push rig at $-14\text{ }^{\circ}\text{C}$ (A) and ice adhesion strength of PU-R and SPU-3_3% coatings that were subjected to repeated icing/ice removal cycles (B).

Although hydrophobic PTFE and commercial silicones showed reduced ice adhesion strength, they were found to have neither good erosion durability against high-speed particles nor good applicability for aircraft leading edge protection applications. To address these shortcomings, the erosion durability of the SPU coatings against both solid particles and water droplets were evaluated according to ASTM Standards G76 and G73, respectively.

Figure 6 shows the solid particle erosion rates and maximum particle loads of the matrix PU-R and representative SPU coatings (i.e., SPU-1_3% and SPU-2_3%), by blasting the coatings with angular alumina particles of $50\text{ }\mu\text{m}$ at an impinging velocity of 150 m/s and an impinging angle of 30° . Figure 6 compares the erosion rates and maximum particle loads between the coatings. It can be seen that both SPU-1_3% and SPU-2_3% exhibited low erosion rates of about $130\text{--}140\text{ }\mu\text{g/g}$ sand and high particle loads of $66\text{--}73\text{ g/cm}^2$. In comparison with the matrix PU-R, only a slight increase in erosion rate was observed for the SPU coatings due to the incorporation of SMPs; the maximum particle loads remained substantially unchanged. As comparative references, commercial aircraft exterior coatings such as Alumigrip 4200 polyurethane topcoat (Akzo Nobel) and Aeroglaze[®] 1433 polyurethane midcoat (Socomore) were subjected to the same erosion test and failed, with extensive coating removal and substrate exposure at particle loads of $<20\text{ g/cm}^2$.

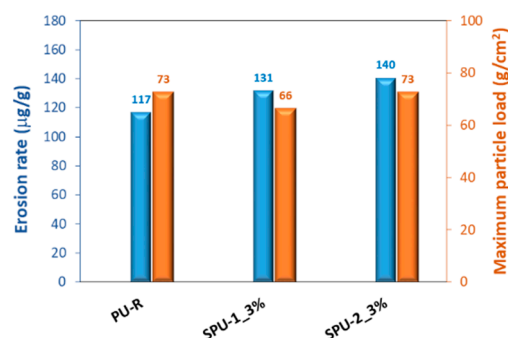


Figure 6. Sand erosion resistance of PU-R and SPU coatings. Test conditions: $50\text{ }\mu\text{m}$ angular alumina particles, impact velocity of 150 m/s , impact angle of 30° .

The water droplet erosion (WDE) resistance of the SPU coatings was evaluated using a water spin rig test facility, at an impact velocity of 175 m/s and an impingement angle of 90° . The coating configuration is Metaflex[®] SP 1050 pretreatment/Aerodur HS 2118 primer (ca. $30\text{ }\mu\text{m}$)/PU-R or SPU (ca. 0.35 mm). Figure 7 presents the pictures of the coatings

after certain periods of WDE testing. In comparison with commercial Alumigrip 4200 polyurethane topcoat, where total material removal was observed at the impact area (a line of ca. 2 mm wide) at 2.5 min of testing, the PU-R and SPU coatings showed only minimal material loss at the edges even after 20 min of testing, indicating excellent water droplet erosion resistance of the coatings. The introduction of SMPs did not substantially affect the water droplet erosion resistance of PU-R.

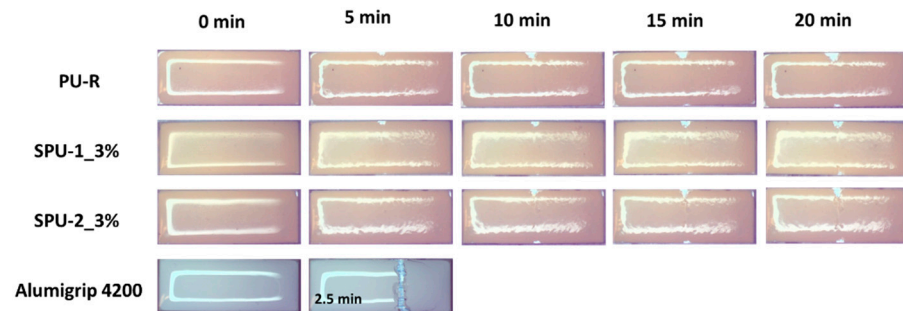


Figure 7. Water droplet erosion resistance of SPU coatings. Test conditions: 463 μm water droplets, impact velocity of 175 m/s, impact angle of 90° , impact frequency of 42,000 droplets per minute.

4. Conclusions

Novel surface-modifying polymers (SMPs) were designed, synthesized and formulated into the erosion resistant polyurethane coating PU-R to produce highly hydrophobic SPU coatings with superior erosion durability. The SPU coatings had high solid contents of ca. 58 wt.% (based on total resin solid) and could be easily applied by spraying or solution casting. Drying and curing of the coatings at ambient conditions produced elastomeric coatings with high water contact angles ($100\text{--}115^\circ$), high mechanical strength (19–27 MPa), high elongation at break (640–730%) and low tensile set (20–35%). Reduced ice adhesion strength in the range of 220–400 kPa was measured for the SPU coatings using a static push rig test at -14°C . Repeated icing/ice removal cycles led to no substantial increase in the ice adhesion strength. The ASTM G76 and G73 standard tests demonstrated excellent erosion resistance against both high-speed solid particles and water droplets for the SPU coatings. Thus, the combination of high erosion durability, high mechanical strength, high surface hydrophobicity and reduced ice adhesion strength makes the SPU coatings attractive for ice protection of leading edge surfaces of fast moving aerodynamic structures, such as aircraft wings and helicopter rotor blades.

Author Contributions: Conceptualization, N.S. and A.B.; methodology, N.S. and A.B.; validation, N.S.; investigation, N.S.; resources, A.B.; writing—original draft preparation, N.S.; writing—review and editing, A.B.; project administration, A.B. All authors have read and agreed to the published version of the manuscript.

Funding: This research was funded by the Integrated Aerial Mobility program and the Aerospace Future Initiative Program of the National Research Council Canada, and the Canadian Department of National Defence—Royal Canadian Navy.

Institutional Review Board Statement: Not applicable.

Informed Consent Statement: Not applicable.

Data Availability Statement: No extra supporting information is provided.

Conflicts of Interest: The authors declare no conflict of interest. The funders had no role in the design of the study; in the collection, analyses, or interpretation of data; in the writing of the manuscript.

References

1. Yamazaki, M.; Jemcov, A.; Sakaue, H. A Review on the Current Status of Icing Physics and Mitigation in Aviation. *Aerospace* **2021**, *8*, 188. [CrossRef]
2. Federal Aviation Administration. *Aircraft Icing Handbook*; U.S. Department of Transportation: Washington, DC, USA, 1991; Volume 1.
3. Federal Aviation Administration. *AC 91-74B Pilot Guide: Fight in Icing Conditions*; U.S. Department of Transportation: Washington, DC, USA, 2015.
4. Federal Aviation Administration. *Aircraft Icing Handbook*; U.S. Department of Transportation: Washington, DC, USA, 1991; Volume 2.
5. Huang, X.; Tepylo, N.; Pommier-Budinger, V.; Budinger, M.; Bonaccorso, E.; Villedieu, P.; Bennani, L. A survey of icephobic coatings and their potential use in a hybrid coating/active ice protection system for aerospace applications. *Prog. Aerosp. Sci.* **2019**, *105*, 74–97. [CrossRef]
6. He, Z.; Zhuao, Y.; Zhang, Z.; He, J. Design of icephobic surfaces by lowering ice adhesion strength: A mini review. *Coatings* **2021**, *11*, 1343. [CrossRef]
7. Bharathidasan, T.; Kumar, S.V.; Bobji, M.S.; Chakradhar, R.P.S.; Basu, B.J. Effect of wettability and surface roughness on ice adhesion strength of hydrophilic, hydrophobic and superhydrophobic surfaces. *Appl. Surf. Sci.* **2014**, *314*, 241–250. [CrossRef]
8. Davis, A.; Yeong, Y.H.; Steele, A.; Bayer, I.S.; Loth, E. Superhydrophobic nanocomposite surface topography and ice adhesion. *ACS Appl. Mater. Interfaces* **2014**, *6*, 9272–9279. [CrossRef] [PubMed]
9. Oberli, L.; Caruso, D.; Hall, C.; Fabretto, M.; Murphy, P.J.; Evans, D. Condensation and freezing of droplets on superhydrophobic surfaces. *Adv. Colloids Interface Sci.* **2014**, *210*, 47–57. [CrossRef]
10. Varanasi, K.K.; Deng, T.; Smith, J.D.; Hsu, M.; Bhate, N. Frost formation and ice adhesion on superhydrophobic surfaces. *Appl. Phys. Lett.* **2010**, *97*, 234102. [CrossRef]
11. Zhang, R.; Hao, P.; Zhang, X.; He, F. Supercooled water droplet impact on superhydrophobic surfaces with various roughness and temperature. *Int. J. Heat Mass Transfer* **2018**, *122*, 395–402. [CrossRef]
12. Kim, P.; Wong, T.S.; Alvarenga, J.; Kreder, M.J.; Adorno-Martinez, W.E.; Aizenberg, J. Liquid-infused nanostructured surfaces with extreme anti-ice and anti-frost performance. *ACS Nano* **2012**, *6*, 6569–6577. [CrossRef]
13. Sun, X.; Damle, V.G.; Liu, S.; Rykaczewski, K. Bioinspired stimuli-responsive and antifreeze-secreting anti-icing coatings. *Adv. Mater. Interfaces* **2015**, *2*, 1400479. [CrossRef]
14. Ma, L.; Zhang, Z.; Gao, L.; Liu, Y.; Hu, H. Bio-Inspired Icephobic Coatings for Aircraft Icing Mitigation: A Critical Review. *Prog. Adhes. Adhes.* **2021**, *6*, 171–201.
15. Rykaczewski, K.; Anand, S.; Subramanyam, S.B.; Varanasi, K.K. Mechanism of frost formation on lubricant-impregnated surfaces. *Langmuir* **2013**, *29*, 5230–5238. [CrossRef] [PubMed]
16. Chen, D.; Gelenter, M.D.; Hong, M.; Cohen, R.E.; McKinley, G.H. Icephobic surfaces induced by interfacial nonfrozen water. *ACS Appl. Mater. Interfaces* **2017**, *9*, 4202–4214. [CrossRef]
17. Chen, J.; Dou, R.; Cui, D.; Zhang, Y.; Xu, F.; Zhou, X.; Wang, J.; Song, Y.; Jiang, L. Robust prototypical anti-icing coatings with a self-lubricating liquid water layer between ice and substrate. *ACS Appl. Mater. Interfaces* **2013**, *5*, 4026–4030. [CrossRef] [PubMed]
18. He, Z.; Wu, C.; Hua, M.; Wu, S.; Wu, D.; Zhu, X.; Wang, J.; He, X. Bioinspired multifunctional anti-icing Hydrogel. *Matter* **2020**, *2*, 723–734. [CrossRef]
19. Chatterjee, R.; Bararnia, H.; Anand, S. A Family of Frost-Resistant and Icephobic Coatings. *Adv. Mater.* **2022**, *34*, 2109930. [CrossRef] [PubMed]
20. Golovin, K.; Kobaku, S.P.R.; Lee, D.H.; DiLoreto, E.T.; Mabry, J.M.; Teteja, A. Designing durable icephobic surfaces. *Sci. Adv.* **2016**, *2*, e1501496. [CrossRef] [PubMed]
21. Irajizad, P.; Al-Bayati, A.; Eslami, B.; Shafquat, T.; Nazari, M.; Jafari, P.; Kashyap, V.; Masoudi, A.; Araya, D.; Ghasemi, H. Stress-localized durable icephobic surfaces. *Mater. Horiz.* **2019**, *6*, 758–766. [CrossRef]
22. Golovin, K.; Dhyani, A.; Thouless, M.D.; Tuteja, A. Low-interfacial toughness materials for effective large-scale deicing. *Science* **2019**, *364*, 371–375. [CrossRef]
23. Schneeberger, G.M.; Kozlowski, R.; Wolfe, D.; Palacios, J.L. Development of a durable ice protective coating for use on rotorcraft. *Cold Reg. Sci. Technol.* **2022**, *193*, 103427. [CrossRef]
24. Soltis, J.; Palacios, J.; Eden, T.; Wolfe, D. Evaluation of ice-adhesion strength on erosion resistant materials. *AIAA J.* **2015**, *53*, 1825–1835. [CrossRef]
25. Song, N. *Erosion Protective Coatings for RCAF Helicopter Rotor Blades*; LTR-SMM-2021-0065; The National Research Council of Canada: Ottawa, ON, Canada, 2021.
26. Kool, N.; Orchard, D.M.; Chevrette, G. Testing of elastomer icephobic coatings. In Proceedings of the AIAA Aviation Forum, Atlanta, GA, USA, 25–29 June 2018.
27. Meuler, A.J.; Smith, J.D.; Varanasi, K.K.; Mabry, J.M.; McKinley, G.H.; Cohen, R.E. Relationships between water wettability and ice adhesion. *ACS Appl. Mater. Interfaces* **2010**, *2*, 3100–3110. [CrossRef] [PubMed]
28. Ghalmi, Z.; Farzaneh, M. Experimental investigation to evaluate the effect of PTFE nanostructured roughness on ice adhesion strength. *Cold Reg. Sci. Technol.* **2015**, *115*, 42–47. [CrossRef]

Article

Numerical Modelling of Droplets and Beads Behavior over Super-Hydrophobic and Hydrophilic Coatings under in-Flight Icing Conditions

Giulio Croce * , Nicola Suzzi, Marco Pretto and Pietro Giannattasio

Dipartimento Politecnico di Ingegneria e Architettura, University of Udine, Via delle Scienze 206, 33100 Udine, Italy; nicola.suzzi@uniud.it (N.S.); marco.pretto@uniud.it (M.P.); pietro.giannattasio@uniud.it (P.G.)

* Correspondence: giulio.croce@uniud.it; Tel.: +39-3204365840

Featured Application: Use of hydrophobic coatings as passive inflight icing safety device.

Abstract: Current technology has produced a wide range of advanced micro-structured surfaces, designed for achieving the best wettability and adhesion performances for each specific application. In the context of in-flight icing simulations, this opens new challenges since the current most popular and successful ice accretion prediction tools neglect the details of the droplet behavior opting for a continuous film model. Here, a phenomenological model, following, in a Lagrangian approach, the evolution of the single droplets from the impinging to the onset of rivulets, is developed to simulate the performances of super-hydrophobic surfaces in icing application. Possible rebound and droplet spread on the impact, coalescence, single ice bead formation and droplet to rivulet transition are taken into account. The first validation shows how the models are able to predict the anti-icing capability of a super-hydrophobic surface coupled with a heating system.

Keywords: droplets; super hydrophobic; phenomenological model; icing; rivulets



Citation: Croce, G.; Suzzi, N.; Pretto, M.; Giannattasio, P. Numerical Modelling of Droplets and Beads Behavior over Super-Hydrophobic and Hydrophilic Coatings under in-Flight Icing Conditions. *Appl. Sci.* **2022**, *12*, 7654. <https://doi.org/10.3390/app12157654>

Academic Editor: Filomena Piscitelli

Received: 27 December 2021

Accepted: 25 July 2022

Published: 29 July 2022

Publisher's Note: MDPI stays neutral with regard to jurisdictional claims in published maps and institutional affiliations.



Copyright: © 2022 by the authors. Licensee MDPI, Basel, Switzerland. This article is an open access article distributed under the terms and conditions of the Creative Commons Attribution (CC BY) license (<https://creativecommons.org/licenses/by/4.0/>).

1. Introduction

Most of the numerical models adopted in in-flight icing simulations are essentially based on the Messinger model [1] and its extension to three-dimensional arbitrary surfaces [2], combined with the prediction of impinging mass flow following either a Lagrangian or Eulerian [3] droplet flow field analysis. The runback water layer is implicitly assumed to behave as a continuous film whose velocity is mainly defined by the shear stress. In the most sophisticated form, this approach allows for full integration into a three-dimensional computational fluid dynamics (CFD) model, and offered efficient and accurate results in a number of highly complex applications, up to the analysis of a whole aircraft. However, it inherently skips most of the micro-scale effects related to the wettability and adhesion properties of the substrate, as well as the details of the transitions between moving droplets, rivulets, and full film flow regimes; actually, the smaller scale of these phenomena would require unpractically refined grids. An exception is given by roughness models developed on the basis of a droplet distribution analysis [4].

On the other hand, the advances in the development of micro- and nano-structured surfaces provide a number of highly specialized surfaces, designed either for hydrophobicity or low ice adhesion properties, that are promising as passive anti-icing tools [5–8]. Although ice phobicity and hydrophobicity are not synonyms, and their correlation is a matter of basic research [9,10], it is clear that some typical features of super-hydrophobic surfaces, such as the higher probability of impinging droplet rebound or the reduction of liquid–solid contact (and heat transfer) areas will help with an anti-icing strategy. Laboratory tests can define such micro-scale properties, usually via the analysis of a single droplet,

but the actual performance under real-world in-flight icing conditions is highly dependent on their interaction with the outer, macroscale flow field.

Thus, a kind of bridge is required to transfer the relevant micro-scale information to the macroscale analysis around a whole airfoil or a whole airplane. In particular, considering a super-hydrophobic surface, we have a few mechanisms that affect the ice accretion process. First, above a threshold impinging velocity (i.e., Weber number) and low wettability, impinging droplets may rebound, effectively reducing the collection efficiency, or (at even higher Weber) may break down into smaller droplets [11], affecting the local ice beads' related roughness and coalescence processes [12,13]. For an extremely water repellent surface, the rebound may occur at relatively low We [14,15], and it is worth noting that the physical phenomena behind the rebound are quite complex and might be strongly affected by the topological details of the surface roughness and its different scales [15,16]. Furthermore, the jumping droplet may stick to the surface after a few rebounds at lower energies.

As a second relevant effect, low hysteresis greatly enhances the runback water drainage, since most droplets are quickly removed, ideally preventing the formation of a continuous film. A population of droplets, either still or moving, will obviously have different active heat transfer surfaces with respect to a continuous film [17–19], as well as different equivalent runback water velocities, thus strongly affecting both the ice accretion and the evaporation process. In particular, solid–liquid and air–liquid heat transfer will occur through the droplet base circle (wet area fraction) and spherical cap surfaces, respectively, while the velocity will be defined by the balance of forces acting on the droplets.

However, if the liquid water content is high enough, the moving droplets may merge, forming individual rivulets; the rivulets, then, may coalesce forming a continuous film [20]. Even these transitions are strongly affected by the wettability properties, which in turn control the stability of the contact lines.

Here, a phenomenological approach is chosen in order to assess the performance of super-hydrophobic coatings under icing conditions. The unsteady evolution of a population of individual droplets is predicted as a function of flow conditions (median volume diameter MVD, liquid water content LWC) and surface wetting properties (contact angles, surface tension) on uniform or non-homogeneous surfaces. The simulations are performed following a Lagrangian approach, where the individual impinging droplets behave according to specified rules driving rebound, break-up, and shear-induced motion. The droplet will grow or reduce due to coalescence, evaporation or freezing.

The main aim of the work is to provide a suitable framework for an efficient evaluation of the cumulative effect of a large ensemble of droplets over a (relatively) large surface characterized by variable wettability properties and local fluid dynamic related parameters (shear stress, pressure gradients), validating the results on a typical icing example. In such cases, the full numerical modeling of all of the smaller scale effects would become prohibitive, while the phenomenological approach preserves the computational efficiency.

2. Phenomenological Model

The process of in-flight ice accretion includes several steps, each involving different physical phenomena, different scales and different regimes. The starting point is a cloud of supercooled droplets. These droplets, driven by the airflow field, impinge on the surface: the first impact location is entirely defined by the macroscopic scale droplet and airflow fields, and may be predicted via straight CFD modeling.

On the other hand, the post-impact evolution of the droplet is defined by the solid–liquid interaction features at the microscale. In particular, following [11], at low velocity, small droplet size, and high surface tension (i.e., low Weber number), the droplets stick on the surface, after a brief unsteady spreading step, assuming a roughly spherical cap shape defined by the liquid–solid contact angle. Above a threshold We number, they will rebound, re-emerging from the surface with a lower kinetic energy. Following the first rebound, the droplet will be driven again by the airflow drag forces, which may either move it far away from the solid surface or push it to a secondary impingement, possibly

ending as a sticking drop further downstream. Furthermore, we have the possibility of rebounding droplets interactions with new incoming ones. As noted in the introduction, the physical mechanisms inducing super-hydrophobicity are quite complex, and at extreme low wettability rebound may occur even at the lowest We : thus, the proposed description and modeling of the process does not pretend to be appropriate for any possible coating design (which would be a task well beyond the scope of the present work), but aims to offer a suitable tool for the analysis of the most common standard super-hydrophobic isotropic surfaces.

The actual quantity of water on the surface, in the form of a collection of spherical cap-shaped droplets, is thus a result of the initial collection efficiency, reduced by the rebounding mass flow, plus the water mass recovered from the secondary rebound and drop–drop collisions.

The droplet’s evolution on the surface is driven by aerodynamic drag, pressure gradient and surface tension, as well as by the growth via coalescence with new impinging drop and mass losses via evaporation or freezing. Thus, they may remain as sticking droplets, evolving into frozen beads, or they may run along the surface as individual droplets or merge into rivulets and possibly a film.

In order to develop a complete phenomenological model, each of the above-mentioned steps and mechanisms must be described and taken into account with reasonable accuracy.

2.1. Droplet Impact Modeling

The evaluation of impinging collection efficiency requires interaction with the macro-scale flow. Here, the amount of water hitting the airfoil is evaluated in a standard way via Lagrangian tracing of droplets within a flow field computed via CFD tools (SU2 open-source code), assuming one-way coupling (droplets do not impact on the airflow field). The impact dynamics are quite complex: a comprehensive analysis and comparison may be found in [15]. Here, we follow the model of Attane et al. [13].

The droplet energy is the sum of kinetic E_K and surface energy E_σ , which in turn is the sum of the contributions from both solid–liquid S_{sl} and liquid–air S_{la} interfaces.

$$E_\sigma = S_{la}\sigma + S_{sl}\sigma(1 - \cos\theta_s) \tag{1}$$

The droplet energy decreases in time due to the sum of internal viscous dissipation E_μ and the capillary rim dissipation E_μ^* [13]:

$$\frac{dE_K}{dt} + \frac{dE_\sigma}{dt} + E_\mu + E_\mu^* = 0 \tag{2}$$

The surface and kinetic energy terms, as well as the internal viscous dissipation E_μ (which include dissipation within the droplets and friction losses at the liquid–solid interface), are integrated approximating the droplet shape during the impact as a shallow cylinder of radius r and height h , while assuming an axisymmetric velocity field in the radial x and normal coordinate y :

$$u_x = \frac{2\dot{r}}{rh}xy \quad u_y = -\frac{2\dot{r}}{rh}y^2 \tag{3}$$

Figure 1 shows a sketch of the approximated geometries. In Equation (3), \dot{r} is the time derivative of the base radius of the droplet, i.e., its spreading (or retracting) velocity. The rim dissipation E_μ^* is evaluated via the following correlation [13]:

$$E_\mu^* = 4.48\pi \cdot \mu \cdot r \left(\frac{Re}{\sqrt{We}} \right)^{\frac{2}{3}} \dot{r}^2 \tag{4}$$

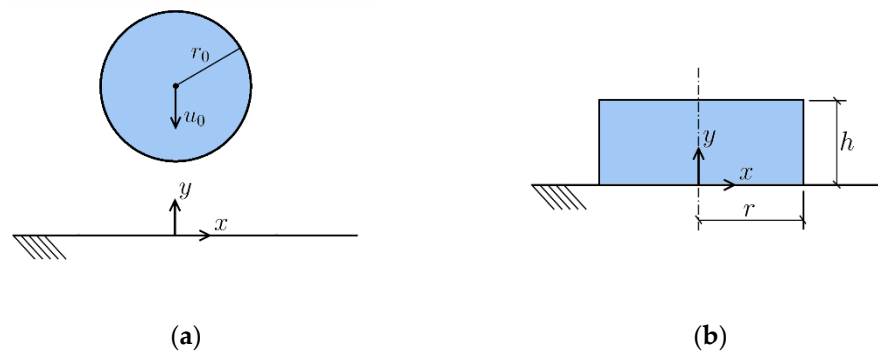


Figure 1. Droplet evolution sketch, following [13], and coordinate system. (a) impinging droplet, (b) shallow cylinder approximating the droplet shape during the spreading and retreat phase.

The local droplet Weber and Reynolds numbers are defined as

$$We = \frac{\rho u_0^2 r_0}{\sigma} \tag{5}$$

$$Re = \frac{\rho u_0 r_0}{\mu} \tag{6}$$

where r_0 and u_0 are the incoming droplet radius and velocity, while σ , μ and ρ represent water surface tension, viscosity and density. Substituting in (1) we obtain an ordinary differential equation that can be solved in time. As initial conditions, we assume that both kinetic and surface energies are still equal to the incoming spherical droplet values: such conditions enable the evaluation of both the initial drop diameter and its advancing velocity. Figure 2 shows the time history of the droplet base radius r (normalized with the incoming droplet radius r_0): agreement with experimental data as in [13] is reasonably good, in particular in terms of maximum spread, while the radius oscillation time scale is over-predicted.

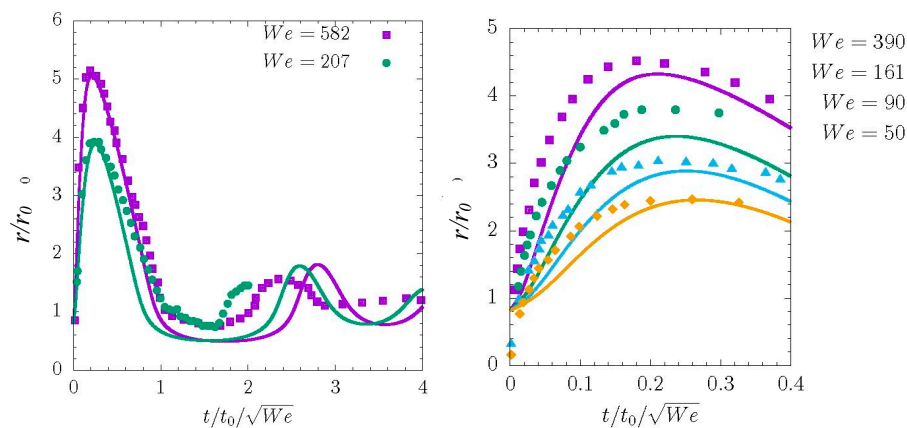


Figure 2. Droplet base radius r evolution in time: symbol: experimental data, lines: computed values. Left, $\theta_s = 87^\circ$, $Re = 588 \cdot We^{0.5}$; right, $\theta_s = 100^\circ$, $Re = 454 \cdot We^{0.5}$.

Time-dependent simulations at increasing We may be used to define a rebounding condition, which occurs when the droplet returns to its initial impact shape with residual kinetic energy. The identification of the transition to splashing is a complex problem. Different regimes (aerodynamic or hydrodynamic dominated) lead to different functional dependencies [15]. Here, for the sake of consistency, we follow the same approach used for the rebound limit: a further increase in We leads to a second threshold, above which the droplet radius oscillations appear overdamped and it no longer retracts down to the initial shape. This second level is assumed as the onset of corona splashing.

A computation campaign at different We and Re was performed, and from post-processing of the result the following correlations are derived for the two limiting values:

$$We_{c,r} = a \frac{(1 - \cos \theta_s)^l}{\log(1 + Re) - b\theta_s^m} \tag{7}$$

$$We_{c,s} = c(1 - \cos \theta)^n Re^2 \tag{8}$$

With $a = 2.85737$, $b = 10.0471$, $l = -2.32544$, $m = -1.01734$, $c = 7.13676 \times 10^{-5}$, $n = 6.81775$. Results are shown in Figure 3, where it is evident that for any Re the range of We allowing for full rebound gets smaller and smaller at low contact angles. Results from Equation (7) can be compared with a regime map obtained from numerical fully 3D, level set approach-based results at $Re = 800$ [21]: at $\theta_s = 100$ and 120 the transition from adhesion and rebound is located at $We \sim 2.0$ and $We \sim 0.6$, respectively, while Equation (7) offers $We = 2.0$ and $We = 0.57$. Note also that Equation (8), for a given contact angle, locates the splashing at constant product of $We_{c,s} \cdot Re^{-2}$, which is consistent with the experimental results in [22].

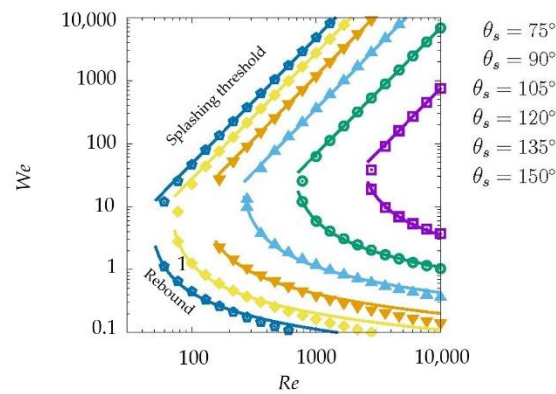


Figure 3. Rebound threshold (lower branch) and splashing threshold (upper branch) as a function of We , Re and wettability. Solid lines: correlations Equations (7) and (8). Symbols: computed values. For any given Re and contact angle rebound occurs if We falls between the two thresholds.

2.2. Collection Efficiency

The actual water mass flowing on the wall surface will be the combined result of the first impact, possible rebound, secondary impingement and, potentially, the interaction between rebounding and incoming droplets. Several CFD tools may be used at this step: here, we combine the SU2 open-source solver with an in-house Lagrangian droplet tracking code. Eulerian modeling is in general more efficient, but it is trickier to take into account the rebound and the secondary impacts on the walls and between droplets.

A population of incoming droplets is generated according to the LWD and airspeed, and their individual behavior is followed. The threshold values from the previous paragraph are used to determine whether the impinging droplet sticks on the surface or rebounds: in the latter case, the residual kinetic energy determines the speed at which the bouncing droplet leaves the surface and, thus, the subsequent droplet trajectory and its maximum height. The droplet re-emerging from the surface may be driven away from the wall, or experience a secondary impact a bit downstream. Since at any impact we have some dissipation, most droplets will then stick at a location a bit downstream of the first one. In such a case, the final position is noted and collection efficiency is evaluated by integrating over a reasonable time interval Δt . If the incoming droplet volume is V_d , and n_i is the number of droplets that came to halt on a wall element of the CFD mesh of surface ΔS , during Δt , the collection efficiency β is computed as:

$$\beta = \frac{u_0 LWC \cdot \Delta t \cdot \Delta S}{n_i \cdot \rho V_d} \tag{9}$$

The correlations defined in Equations (7) and (8) are extended to the case of droplets impinging at a non-zero incidence by using the normal component of the incoming velocity, as suggested in [23].

2.3. Droplet Behavior and Runback Water Modeling

Modeling the runback water flow over a hydrophobic surface requires a simulation of the evolution of the droplet population that takes properly into account the wetting properties of the surface. These phenomena involve small-scale modeling, on the size of the individual droplets, and the information required from the larger-scale flow field is limited essentially to the amount of incoming water (i.e., the collection efficiency) and its geometrical and dynamic characteristics (diameter, velocity components normal and parallel to the wall), as well as the wall shear stress and pressure gradients. A possible choice is to follow the evolution of each individual droplet after impinging via a Lagrangian approach: since the number of involved droplets is very high, a full multiphase CFD computation would quickly become unpractical. However, it is possible to simplify the process with a phenomenological model that describes the main steps of the evolution, namely impinging density, growth or reduction via coalescence and/or phase change and aerodynamic drag-induced motion. These computations will be performed over a small portion of the surface and are meant to provide, via integration, useful information in order to offer corrections to the standard, continuous film models usually assumed for icing simulation on regular surfaces.

We will assume that the droplets have a spherical cap shape, defined by their static contact angle θ_s , while the hysteresis between advancing and receding contact angles will be used in order to define the droplet's force and energy balances. Additional elements that need to be tracked are frozen beads and possibly rivulets. The former appears as spherical segments, covering the base of the droplet and progressively growing until the liquid phase disappears; the latter is modeled as an ensemble of interconnected droplets. The simulation is carried out on a two-dimensional domain, which may be representative of an arbitrarily shaped surface as long as we provide the proper distribution of shear stress, collection efficiency and pressure gradients from the CFD solution of the macro-scale problem.

The main workflow of the procedure may be summarized in the following steps:

1. Generation of N impinging sites at random locations, depending on local collection efficiency.
2. Coalescence check between new impinging droplets and existing ones.
3. Heat transfer balance for any single droplet.
4. Evaluation of freezing or evaporating mass flow.
5. Frozen mass will either contribute to the growth of an existing ice bead or create a new one at the freezing bead location.
6. Droplet stretching limit check, detecting possible rivulet onset.
7. Droplet and rivulet movement check, including coalescences along the moving path.
8. Next time step.

The procedure described above was originally developed for a high-fidelity modeling of icing roughness [4], and it has already been validated and applied to different problems [18,19,24].

A population of incoming droplets is randomly generated at each time step. As an example, on a rectangular domain $L_x \times L_y$ we define a maximum number of impinging sites at any time step as

$$N^0 = \frac{u_0 LWC \cdot \Delta t \cdot L_x \times L_y}{\rho V_d} \quad (10)$$

Then, given three random numbers $\alpha_x, \alpha_y, \alpha_c$; $0 < \alpha < 1$ the possible impinging sites $(x, y)_i$, $i = 1, N^0$ are defined as $(L_x \alpha_x, L_y \alpha_y)_i$, but they get activated only if $(\alpha_c)_i < \beta$, thus statistically complying with the computed collection efficiency.

Once an initial distribution of the impinging droplets is given, we check if any coalescence occurs. Coalescence takes place when the distance between the centers of two droplets is less than the sum of their radii, and it results in a larger drop whose volume is equal to the sum of the volumes of the parent droplets, located at the center of mass of the two parent droplets. In the case of partially frozen beads, coalescence will involve only the residual liquid volume, leaving the existing solid beads unchanged.

For hydrophilic substrates ($\theta_s < 90^\circ$), coalescence will occur if the distance d between the centers on the surface is lower than the sum of the base area radii:

$$d \leq r_1 \sin \theta_s + r_2 \sin \theta_s \tag{11}$$

while under hydrophobic conditions it will occur according to the geometrical consideration in Figure 4, as

$$\sqrt{d^2 + (r_1 - r_2)^2 \cos^2 \theta_s} \leq r_1 + r_2 \tag{12}$$

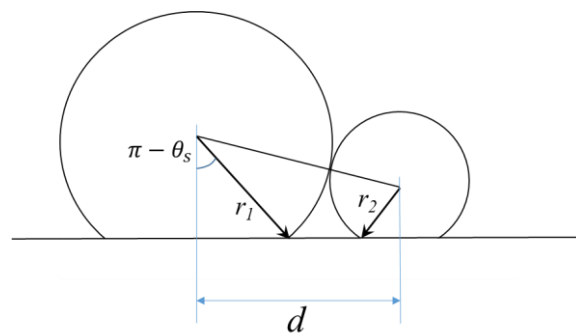


Figure 4. Coalescence condition for the hydrophobic substrate.

Droplets are subjected to external forces, namely gravity, aerodynamic drag and pressure gradient if exposed to a fluid flow. Drag is evaluated via a drag coefficient computed for spherical caps and from the local flow velocity. The local velocity, given the small height of the droplets, is computed from the local shear stress, assuming a linear profile normal distance from the wall. These forces deform the droplet shape, inducing hysteresis due to the difference between the advancing θ_a and receding θ_r contact angles. The actual contact angle will be a function of the azimuthal angle along the contact line, as reported in [25,26]. The balance of drag, gravitational force projected along the surface, and surface tension defines whether the droplet will stay still or will be shed away. Since aerodynamic drag increases with r^2 , gravity contribution with r^3 , and surface tension only with r , we can find a maximum radius allowing for immobile drops.

Then, the next step is the modeling of the moving droplet. A power balance between aerodynamic force work, surface tension work, and viscous dissipation (sum of laminar viscous dissipation within the droplet and wedge dissipation) is performed.

Then, the next step is the modeling of the moving droplet. Following [18,19], a power balance between aerodynamic force work, gravity force work, surface tension work and viscous dissipation (sum of laminar viscous dissipation within the droplet and wedge dissipation) is performed,

$$\Phi_D + \Phi_g - \Phi_\sigma - \Phi_\mu = 0 \tag{13}$$

$$\Phi_D = F_D \cdot \mathbf{u}_d = \frac{1}{2} \rho_a c_D |\mathbf{u}_a - \mathbf{u}_d| (\mathbf{u}_a - \mathbf{u}_d) \cdot \mathbf{u}_d \tag{14}$$

$$\Phi_g = F_g \cdot \mathbf{u}_d = \rho_l V_d \mathbf{g} \cdot \mathbf{u}_d \tag{15}$$

where \mathbf{u}_a is the local airflow velocity and c_D is the drag coefficient, which can be estimated as the one of a flow past a sphere, as done by [27]. The further condition that the droplet moving direction agrees with the one of the resulting force $F_g + F_D$ is required in order to close the problem. The derivation of surface tension work Φ_σ and viscous dissipation Φ_μ

(given by the sum of laminar viscous dissipation within the droplet and wedge dissipation) are given in [18,19]. The procedure is suited for both planar and curved surfaces, provided that the substrate radius of curvature is larger than the droplet one.

2.4. Phase Change

At each time step, the energy balance of each individual droplet is performed in order to define the freezing and evaporating mass flow rates [28]:

$$q_s = q_a + m_{ev}\lambda_{ev} - m_f\lambda_f \quad (16)$$

Here, q_s is the heating flux from the solid wall, if present, and q_a is the convective heat transfer computed using the local heat transfer from the macroscale computation and the actual droplet surface exposed to the air, while evaporating mass flow m_{ev} comes from a heat and mass transfer analogy, m_f is the freezing mass and λ_{ev} , λ_f the evaporation and fusion of latent heat.

2.5. Rivulet Onset

At high wettability, or for high impinging mass flow, and low freezing rate, we can have a runback water mass flow so high that the individual droplet regimes may give way to the onset of rivulets. Here, a rivulet threshold is obtained via a force balance over half of the droplet, as suggested in [20]. Essentially, we cut the droplet with a midspan plane, normal to the drop velocity and to the substrate (Figure 5). If the resultant R of the forces (due to drag, gravity, surface tension along the contact line, viscous force on the wet area) over half of the droplet (assumed symmetric) is larger than the surface tension action F_{σ_i} along the wet perimeter on the plane cut, we can assume that the droplet is starting to stretch and is evolving into a rivulet.

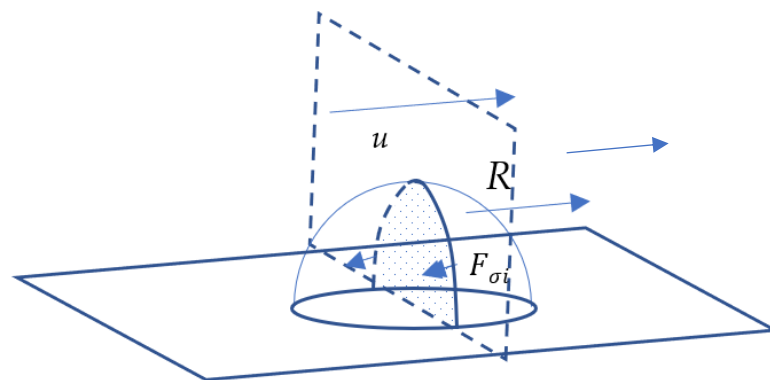


Figure 5. Sketch of the droplet stability balance.

Once the rivulet has started, it will move downstream driven by the sheart stress. At high wettability, or for high impinging mass flow, and low freezing rate, we can have a high runback water mass flow so high that the individual droplet regimes may give way to the onset of the rivulet. Once the rivulet is generated, it is modeled as a series of interconnected circles, in order to easily allow for coalescence check with the existing droplets according to Equations (11) and (12). In Figure 6, the typical evolution is shown: to the left, a large droplet is running from the bottom to the top until the growth due to the coalescence with the other drops along its trajectory triggers the rivulet transition. From this point, the rivulet height is fixed, and the possible increase in mass flow due to coalescences results in its widening. Furthermore, we assume a triangular velocity profile normal to the wall aligned with the shear as in the usual continuum model based on Messinger's approach.

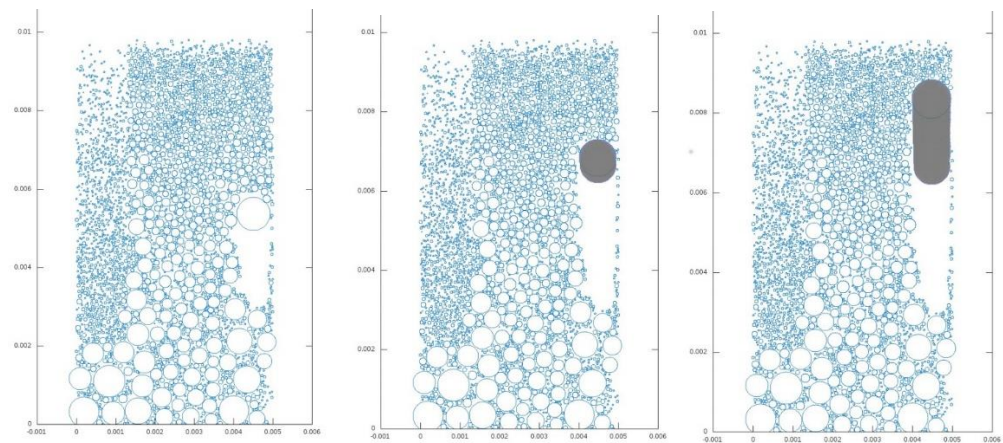


Figure 6. Droplet–rivulet transition, droplet distribution at three different time steps. From left to right: individual droplet running downstream, rivulet onset (grey area), rivulet development.

3. Results

For a first assessment of the capability of the procedure outlined above, the experimental setup of [29] was simulated. A small-scale NACA0012 profile is considered, with a chord of 150 mm, partially heated and coated with combinations of hydrophobic and hydrophilic sections.

In particular, we considered a case with a freestream velocity of 40 m/s, freestream temperature of $-5\text{ }^{\circ}\text{C}$, $\text{LWC} = 1.0\text{ g/m}^3$, and droplet size of $30\text{ }\mu\text{m}$. The airfoil is heated for 5% of the chord length, with a heat flux of 33 W along the 400 mm spanwise length. We compare two cases: in the first, the heated region is hydrophilic ($\theta_s = 65^{\circ}$, $\theta_a = 105^{\circ}$, $\theta_r = 50^{\circ}$) and the remaining area super-hydrophobic ($\theta_s = 157^{\circ}$, $\theta_a = 159^{\circ}$, $\theta_r = 154^{\circ}$), in the second case the whole surface is super-hydrophobic.

Figure 7 shows the collection efficiency, taking into account rebound and secondary impacts for both cases. The effect is quite dramatic, with a nearly clean leading edge region, although it is important to note that the very small thickness of the airfoil maximizes the effect of rebound. The droplets with higher We will rebound around the leading edge, and due to the small thickness of the airfoil, only a small fraction of them stops on the solid wall after a few secondary impacts. However, these droplets landing somewhat downstream with respect to their first impact are responsible for the recovery at $x = 0.01$, where the collection efficiency is even higher than that in the hydrophilic region.

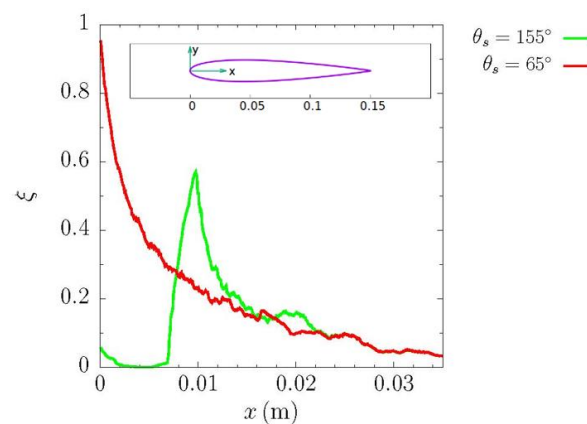


Figure 7. Resulting collection efficiency, taking into account super-hydrophobic surface rebound.

The effect of the reduction in water gathering, combined with the improved drainage of the smaller, low hysteresis droplets on the super-hydrophobic surface, leads to a better performance of the fully hydrophobic airfoil. In particular, the droplet evolution was computed on a small strip near the leading edge, as shown in Figure 8. Two snapshots

of the droplet population are presented: red circles refer to liquid droplets and blue ones to frozen beads. It is clear that we have better drainage in the hydrophobic setup, with smaller and quicker droplets that evaporate or run downstream before any freezing. On the other hand, the hydrophilic leading edge generates larger droplets and slower flow, and thus we still have runback water beyond the heated strips, allowing for ice accretion as observed in the experiment.

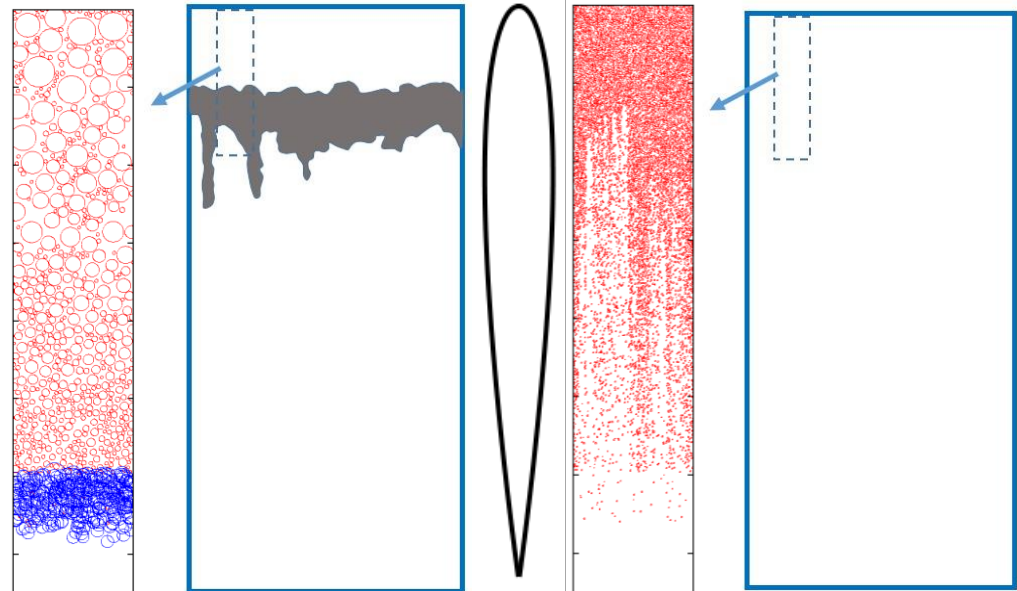


Figure 8. Computed results: red, liquid droplets. Blue, frozen beads. Experimental data, reconstructed from [29]: dark grey: iced area. Left, hydrophilic leading edge on an otherwise hydrophobic coated airfoil. Right, fully hydrophobic coated airfoil.

Interactions between rebounding and incoming droplets are, on the contrary, nearly negligible: Figure 9 shows the computed collision density, i.e., the number of collisions between rebounding and incoming droplets per unit time and volume, around the airfoil profile. The maximum value is attained in the region of the secondary peak in the collection efficiency, at $x \sim 10$ mm, and is a bit less than $140 \text{ s}^{-1} \cdot \text{m}^{-2}$, i.e., it is several orders of magnitude lower than the number of the actual flying droplets at the same location.

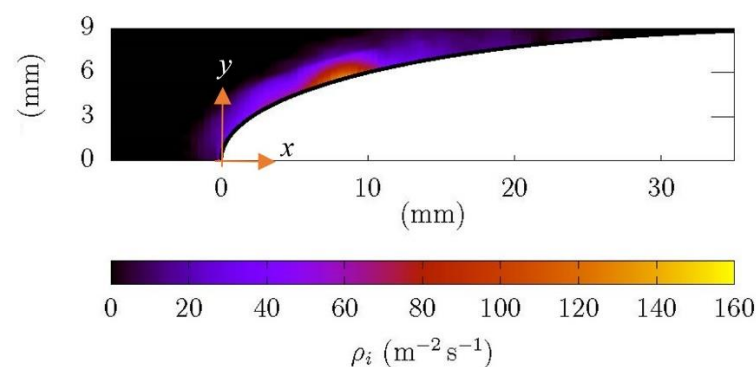


Figure 9. Collision density between rebounding and incoming droplets on NACA 0012 profile, super-hydrophobic surface.

4. Conclusions

A comprehensive workflow, designed to simulate the effects of hydrophobic coatings under icing conditions, was described. The aim was to offer the possibility to estimate the impact of wettability properties in an efficient way, using a phenomenological model that

takes advantage of several models either readily available in the literature or adapted for the specific application.

A number of different effects, however, had to be taken into account, involving different scales: droplet rebound, rivulet formation, and droplet–droplet interactions. The first validation case offers only a threshold-like comparison, which allows verifying that protection from ice formation is predicted. Thus, further detailed analysis and validation of the individual mechanisms are still required: due to the complexity of the physical phenomena and to the variability of the design of super super-hydrophobic coatings, the models and phenomenological rules, in particular those related to the bouncing/splashing, proposed in the present work, do not pretend to cover all of the possible regimes and surfaces topology beyond those used in the validation cases. However, these first results demonstrate that via the proposed computational framework it is actually possible to predict the beneficial effect of properly designed coatings for ice mitigation purposes in a real-world application.

Author Contributions: Writing—original draft, G.C. and N.S.; Writing—review & editing, M.P. and P.G. All authors have read and agreed to the published version of the manuscript.

Funding: The present work was funded by the EU, within IMPACT project, call JTI-CS2-2019-CfP10-LPA-01-80, Clean Sky 2 Joint Undertaking (JU) under grant agreement No. 885052.

Data Availability Statement: Validation data come from quoted open literature.

Conflicts of Interest: The authors declare no conflict of interest.

Nomenclature

h	droplet height
E_σ	surface energy
E_K	kinetic energy
E_μ	viscous dissipation
E_μ^*	rim dissipation
F_D	drag force
F_g	gravity force
F_σ	rigidity force
g	gravity acceleration
\dot{m}_{ev}	evaporating mass flow rate
\dot{m}_f	freezing mass flow rate
N^0	number of impinging sites
q	heat flux
r	droplet radius
Re	droplet Reynolds number, $\rho ur/\mu$
S_{la}	liquid–air interface area
S_{sl}	solid–liquid interface area
t	time
u_a	air velocity
u_d	droplet velocity
V_d	droplet volume
We	droplet Weber number, $\rho u^2 r/\sigma$
x, y	Cartesian coordinates
β	collection efficiency
θ_s	static contact angle
λ_{ev}	evaporation latent heat
λ_f	fusion latent heat
μ	dynamic viscosity
ρ	Density

σ	surface tension
Φ_D	drag force work
Φ_g	gravity force work
Φ_σ	surface tension work
Φ_μ	viscous dissipation

References

- Messinger, B.L. Equilibrium Temperature of an Unheated Icing Surface as a Function of Air Speed. *J. Aeronaut. Sci.* **1953**, *20*, 29–42. [CrossRef]
- Bourgault, Y.; Beaugendre, H.; Habashi, W. Development of a shallow-water icing model in FENSAP-ICE. *J. Aircr.* **2000**, *37*, 640–646. [CrossRef]
- Bourgault, Y.; Boutanios, Z.; Habashi, W.G. Three-dimensional Eulerian approach to droplet impingement simulation using FENSAP-ICE, Part 1: Model, algorithm, and validation. *J. Aircr.* **2000**, *37*, 95–103. [CrossRef]
- Croce, G.; De Candido, E.; Habashi, W.G.; Munzar, J.; Aubé, M.S.; Baruzzi, G.S.; Aliaga, C. FENSAP-ICE: Analytical model for spatial and temporal evolution of in-flight icing roughness. *J. Aircr.* **2010**, *47*, 1283–1289. [CrossRef]
- Villeneuve, E.; Brassard, J.-D.; Volat, C. Effect of various surface coatings on de-icing/anti-icing fluids aerodynamic and endurance time performances. *Aerospace* **2019**, *6*, 114. [CrossRef]
- Rose, J.B.R.; Hamilton, J.A.J.L. Experimental investigation on the alternate coating method for aircraft anti-icing applications. *IMEchE J. Aerosp. Eng.* **2017**, *231*, 407–418. [CrossRef]
- Zheng, S.; Li, C.; Fu, Q.; Hu, W.; Xiang, T.; Wang, Q.; Du, M.; Liu, X.; Chen, Z. Development of stable superhydrophobic coatings on aluminum surface for corrosion-resistant, self-cleaning, and anti-icing applications. *Mater. Des.* **2016**, *93*, 261–270. [CrossRef]
- Tarquini, S.; Antonini, C.; Amirfazli, A.; Marengo, M.; Palacios, J. Investigation of ice shedding properties of superhydrophobic coatings on helicopter blades. *Cold Reg. Sci. Technol.* **2014**, *100*, 50–58. [CrossRef]
- Esmeryan, K.D. From Extremely Water-Repellent Coatings to Passive Icing Protection-Principles, Limitations and Innovative Application Aspects. *Coatings* **2020**, *10*, 66. [CrossRef]
- He, Z.; Zhuo, Y.; Zhang, Z.; He, J. Design of Icephobic Surfaces by Lowering Ice Adhesion Strength: A Mini Review. *Coatings* **2021**, *11*, 1343. [CrossRef]
- Rioboo, R.; Voué, M.; Vaillant, A.; De Coninck, J. Drop Impact on Porous Superhydrophobic Polymer Surfaces. *Langmuir* **2008**, *24*, 14074–14077. [CrossRef] [PubMed]
- Mao, T.; Kuhn, D.C.S.; Tran, H. Spread and Rebound of Liquid Droplets upon Impact on Flat Surfaces. *AIChE J.* **1997**, *43*, 2169–2179. [CrossRef]
- Attané, P.; Girard, F.; Morin, V. An energy balance approach of the dynamics of drop impact on a solid surface. *Phys. Fluids* **2007**, *19*, 012101. [CrossRef]
- Esmeryan, K.D.; Bressler, A.S.; Castano, C.E.; Fergusson, C.P.; Mohammadi, R. Rational strategy for the atmospheric icing prevention based on chemically functionalized carbon soot coatings. *Appl. Surf. Sci.* **2016**, *390*, 452–460. [CrossRef]
- Marengo, M.; Antonini, C.; Roisman, I.V.; Trope, C. Drop collisions with simple and complex surfaces. *Curr. Opin. Colloid Interface Sci.* **2011**, *16*, 292–302. [CrossRef]
- Bird, J.C.; Dhiman, R.; Kwon, H.; Varanasi, K.K. Reducing the contact time of a bouncing drop. *Nature* **2013**, *503*, 385–388. [CrossRef] [PubMed]
- Qi, W.; Weisensee, P.B. Dynamic wetting and heat transfer during droplet impact on bi-phobic wettability patterned surfaces. *Phys. Fluids* **2020**, *32*, 067110. [CrossRef]
- Croce, G.; Suzzi, N.; D'Agaro, P. Numerical prediction of dropwise condensation performances on hybrid hydrophobic-hydrophilic surfaces. *J. Phys. Conf. Ser.* **2020**, *1599*, 012006. [CrossRef]
- De Candido, E.; Croce, G.; D'Agaro, P. Droplet Buildup and Water Retention Prediction in Condensation Processes. *Heat Transf. Eng.* **2012**, *33*, 1130–1137. [CrossRef]
- Wang, F.; Cheng, X. Modeling approach of flowing condensate coverage rate on inclined wall for aerosol wash down. *Nucl. Eng. Des.* **2019**, *355*, 110349. [CrossRef]
- Caviezel, D.; Narayanan, C.; Lakehal, D. Adherence and bouncing of liquid droplets impacting on dry surfaces. *Microfluid. Nanofluidics* **2008**, *5*, 469–478. [CrossRef]
- Burzynski, D.A.; Roisman, I.V.; Bansmer, S.E. On the splashing of high-speed drops impacting a dry surface. *J. Fluid Mech.* **2020**, *892*, A2. [CrossRef]
- Sikalo, S.; Trope, C.; Ganic, E.N. Impact of droplets onto inclined surfaces. *J. Colloid Interface Sci.* **2005**, *286*, 661–669. [CrossRef]
- Croce, G.; D'Agaro, P.; Suzzi, N. *Optimization of Hybrid Hydrophilic-Hydrophobic Surfaces for Dropwise Condensation Enhancement*; ASME Paper ICNMM2019-4291; ASME: New York, NY, USA, 2019.
- El Sherbini, A.I.; Jacobi, A.M. Liquid Drops on Vertical and Inclined Surfaces I. An Experimental Study of Drop Geometry. *J. Colloid Interface Sci.* **2004**, *273*, 556–565. [CrossRef]
- El Sherbini, A.I.; Jacobi, A.M. Liquid Drops on Vertical and Inclined Surfaces II. A Method for Approximating Drop Shapes. *J. Colloid Interface Sci.* **2004**, *273*, 566–575. [CrossRef]

27. Tancon, M.; Parin, R.; Martucci, A.; Bortolin, S.; Del Col, D. Effect of steam velocity during dropwise condensation. *Int. J. Heat Mass Transf.* **2021**, *165*, 120624. [CrossRef]
28. Croce, G.; D'Agaro, P.; Della Mora, F. Numerical simulation of glass fogging and defogging. *Int. J. Comput. Fluid Dyn.* **2007**, *19*, 437–445. [CrossRef]
29. Hu, H.; Hu, H.; Liu, Y. *An Explorative Study to Use Super-Hydrophilic/Super-Hydrophobic Hybrid Surfaces for Aircraft Icing Mitigation*; SAE Technical Paper 2019-01-1995; SAE International: Warrendale, PA, USA, 2019. [CrossRef]

Article

Parameter Study for the Ice Adhesion Centrifuge Test

Nadine Rehfeld *, Björn Speckmann and Volkmar Stenzel 

Department Paint Technology, Fraunhofer Institute for Manufacturing Technology and Advanced Materials IFAM, 28359 Bremen, Germany; bjoern.speckmann@ifam.fraunhofer.de (B.S.); Volkmar.stenzel@ifam.fraunhofer.de (V.S.)

* Correspondence: Nadine.Rehfeld@ifam.fraunhofer.de

Abstract: In this study, we assessed the effects of ice types, test parameters, and surface properties on measurement data of the ice adhesion centrifuge test. This method is often used for the evaluation of low ice adhesion surfaces, although no test standard has been defined yet. The aim of this paper is to improve the understanding of the relevant test parameter and identify crucial criteria to be considered in harmonization and standardization efforts. Results clearly indicate that the ice type (static vs. impact ice) has the greatest impact on the test results, with static ice delivering higher values in a broader data span. This is beneficial for material developers as it eases the evaluation process, but it contradicts the technical efforts to design tests that are as close as possible to realistic technical environments. Additionally, the selected ice type has a significant impact on the relevance of the surface properties (roughness, wettability). Despite the complexity of interactions, a trend was observed that the roughness is the determining surface parameter for high impact velocity ice (95 m/s). In contrast, for tests with static ice, the wettability of the test surface is of higher relevance, leading to the risk of overestimating the icephobic performance of structured surfaces. The results of this paper contribute to the demanding future tasks of defining well-founded test standards and support the development of icephobic surfaces.

Keywords: ice adhesion; centrifuge test; static ice; impact ice; wettability; roughness



Citation: Rehfeld, N.; Speckmann, B.; Stenzel, V. Parameter Study for the Ice Adhesion Centrifuge Test. *Appl. Sci.* **2022**, *12*, 1583. <https://doi.org/10.3390/app12031583>

Academic Editor: Filomena Piscitelli

Received: 14 December 2021

Accepted: 25 January 2022

Published: 1 February 2022

Publisher's Note: MDPI stays neutral with regard to jurisdictional claims in published maps and institutional affiliations.



Copyright: © 2022 by the authors. Licensee MDPI, Basel, Switzerland. This article is an open access article distributed under the terms and conditions of the Creative Commons Attribution (CC BY) license (<https://creativecommons.org/licenses/by/4.0/>).

1. Introduction

The measurement of ice adhesion to surfaces is highly relevant for developers of icephobic materials that aim to reduce ice adhesion to an extent, at which only low energy is required to remove this ice. These so-called low ice adhesion surfaces would benefit many technical applications, such as in the energy and transport sector.

Many different test methods have been developed over the past few decades to assess this functionality, addressing different complexity levels, ice types, and ice removal techniques. An extensive review on these methods is given by Work and Lian, with the aim to compare the different test designs with the needs for aircraft-relevant icing conditions. It included the centrifuge test as one of the most prominent methods for ice adhesion assessments, highlighting the benefit (throughput) but also the drawbacks (e.g., missing strain rate control, edge effects, and vibration) [1]. Despite these drawbacks, the centrifuge tests used for ice adhesion measurements appeared to be robust, easy to handle, and relatively accessible test devices that deliver reproducible results in a reasonable time [2–8]. They are generally used in a comparative manner, using reference or benchmark surfaces (e.g., aluminum, steel, unmodified coatings) to identify improvements (reduced ice adhesion) for the new developed materials. The tests support the iterative formulation work on low ice adhesion surfaces and allow the selection of promising candidates. As a tool for the initial assessments, they do not address the performance prediction in the target technical environment. In this study, the centrifuge test is also used for the assessment of relevant test parameters and influential surface properties.

Work and Lian used available test results from the literature to identify parameter correlations [1]. The first trend they observed is that the ice adhesion strength increases

with decreasing temperatures, regardless of the used test method. The second raised aspect covers the effects of velocity (and resulting ice type). Derived from literature data, they identified a decrease in the maximum observed adhesion values for impact ice (accreted at different velocities) compared to static ice (formed by pouring water into a mold and freezing it) [1]. Unfortunately, the data consistency was rather poor, and the comparability of different test designs was limited. To account for this, in this study, we addressed the effects of the velocity during the ice formation process in the ice adhesion centrifuge test. The gained knowledge will contribute to an improved understanding of the influencing test parameters, paving the way to harmonize test designs based on substantiated test data.

Besides the efforts on the development and definition of test designs for ice adhesion, many research activities are dealing with the understanding of the required surface characteristics to achieve low ice adhesion surfaces. Table 1 summarizes studies on the correlations between surface properties and ice adhesion test results, derived from centrifuge tests. The ice formation type is also indicated as one determining parameter of ice adhesion test results.

Table 1. Summary of studies on the surface properties and their influence on ice adhesion strength, assessed in centrifuge test designs.

Ice Formation Type	Main Conclusions on Surface Property Dependencies	Ref.
Impact ice 10 m/s	Low ice adhesion was measured on superhydrophobic low contact angle hysteresis coatings.	[9]
Impact ice (rotor testing)	Ice adhesion strength increases with increasing roughness.	[7,10]
Impact ice 25 m/s	Low contact angle hysteresis and low surface roughness enable low ice adhesion.	[4]
Static ice	Contact angle hysteresis is a crucial parameter for the determination of icephobicity, whereas hydrophobicity (water contact angle) is not linked to icephobicity	[11]
Impact ice (velocity not indicated)	Increasing coating thickness (0.1 to 2 mm) of elastomeric materials leads to decreasing ice adhesion strength.	[12]
Impact ice 95 m/s	Optimum in surface free energy for the lowest ice adhesion values. A further decrease in the surface free energy is accompanied with increased roughness, leading to increased ice adhesion strength.	[13]
Impact ice 10 m/s	Decreasing receding contact angle data correlate with increasing ice adhesion strength for superhydrophobic surfaces (assessed during the degradation process).	[14]
Impact ice 25 m/s	Hydrophobicity is beneficial for low ice adhesion in many cases but has a better relationship with contact angle hysteresis. Higher roughness can increase ice adhesion but can also be beneficial (for slippery liquid-infused porous surfaces: SLIPS approach).	[15]
Impact ice 95 m/s	Coating-specific correlations of ice adhesion strength vs. surface properties during coating degradation. No general rules for correlating parameters are identifiable.	[16]
Static ice	Ice adhesion strength decreased with surface roughness. For surfaces with similar roughness, low surface free energy favored a reduction in ice adhesion. Materials with different wettability showed a similar ice adhesion strength.	[17]

The papers summarized in Table 1 mainly addressed material properties, such as the surface roughness and wettability, which are also covered in the current study. The surfaces used for the current study had to fulfil two main requirements: first, a high surface robustness (mechanical, chemical) to guarantee high repeatability of the tests without performance degradation; and second, a range of surface properties from rough to smooth

and good to poor water wettability to assess the effects of the surface properties on the ice adhesion test results.

With this study, we aimed to provide data for the effects of ice types on the results of the ice adhesion centrifuge test. We also investigated a relevant range of surface properties to clarify the impact of the roughness and surface wettability on the measured ice adhesion strength. With these topics, we offer an improved understanding of the needs for ice adhesion test procedures that can be used for necessary harmonization and standardization activities.

2. Materials and Methods

Material selection for this study was based on the results of a pre-screening process to identify robust and long-lasting surfaces that deliver reproducible results over the complete duration of tests. The preparation of test samples was performed in a single process with identical material batches to avoid deviations due to changes in the material composition, handling, or environmental conditions. Test samples (EN AW 5083, dimension $220 \times 30 \times 4 \text{ mm}^3$ for IFAM centrifuge tests) were sanded and cleaned with isopropanol prior to material application. For the first coating type, "Primer", an epoxy primer (Aerodur 37045 Barrier Primer White with Hardener S66/22R; Akzo Nobel, Sassenheim, The Netherlands), was used in a mixing ratio of 2:1 by volume. Material preparation and application were performed according to the supplier's specifications using a spray gun (SATA Jet 90, $\text{\O} 1.3 \text{ mm}$; pressure 1.6 Bar; distance 40 cm) under standard conditions (temperature $21 \text{ }^\circ\text{C}$, relative humidity 40%). After the coating application, samples were stored at room temperature in a clean environment for 12 h prior to thermal curing at $60 \text{ }^\circ\text{C}$ for 60 min. The resulting dry film thickness of the primer was $40 \pm 10 \text{ }\mu\text{m}$ (according to DIN EN ISO 2808:2019 with byko-test 8500 P Fe/NFe, Byk Gardner, Geretsried, Germany) [18].

The second coating type, "Stadox", is a clear coat that is used for repair purposes in the automotive industry. It was applied on the primer coating (described above) to ensure sufficient adhesion properties. Standocryl VOC-Premium Clear K9540 with Hardener VOC 10–20 was purchased (Stadox GmbH, Wuppertal, Germany) and material preparation was performed according to the supplier's specifications at a mixing ratio of 3:1 (by volume). The application and curing parameters were identical to those of the primer coating. The same conditions were applied to the third coating type, "PUR C25", which is a non-commercial 2-component formulation based on silanized polyisocyanate-curing acrylic resin, as described in [16]. The material was selected as a potential icephobic material and was applied on the primer coating. The total film thickness (including primer) for the samples Stadox and PUR C25 was $70 \pm 15 \text{ }\mu\text{m}$ [18]. The fourth material in this study was "PTFE-tape" (extruded polytetrafluoroethylene PTFE film tape 5490; 3M Deutschland GmbH, Neuss, Germany), which was applied on primed test samples according to the supplier's specifications. The film thickness of the tape was $90 \text{ }\mu\text{m}$.

All selected materials in the pre-tests showed sufficient mechanical and chemical resistance with no changes in the basic surface properties prior to and after repeated cleaning with isopropanol or during icing/de-icing cycles. Wettability tests were performed with the Drop Shape Analyzer DSA 100S (Krüss GmbH, Hamburg, Germany), according to relevant specifications (DIN EN ISO 19403-2) [19]. Surface free energy (SFE) was determined by measuring the dynamic contact angle of three liquids: water, diiodomethane, and ethylene glycol (droplet application of $0.2 \text{ }\mu\text{L/s}$, total volume of $6.0 \text{ }\mu\text{L}$), and calculated according to the method of Owens, Wendt, Rabel, and Kaelble (OWRK). The water contact angle (WCA) was extracted from this measurement. The water sliding angle (WSA) was determined with a water droplet volume of $20 \text{ }\mu\text{L}$ and tilting speed of $60 \text{ }^\circ/\text{min}$. The sliding angle was defined as the angle at which the advancing and receding angles of the water droplet moved at least 1 mm from the starting point [20]. Contact angle hysteresis (CAH) was determined at this sliding angle or at the maximum tilting angle of 90 ° (in the case where the water droplet did not run off) by calculating the difference between advancing and receding angles. The tilting method was chosen as it delivers consistent results for fresh

and aged coating surfaces. Roughness data R_a (arithmetic average value of the roughness profile) and R_z (maximum height of the profile) were determined using a Perthometer M2 (Mahr GmbH, Göttingen, Germany).

The four selected materials represent a reasonable range of wettability and roughness properties (from smooth to rough and hydrophilic to hydrophobic). Surface parameters are expressed in Table 2 as the means of 6 measurements from 3 test samples.

Table 2. Summary of the surface characterization data for the used materials.

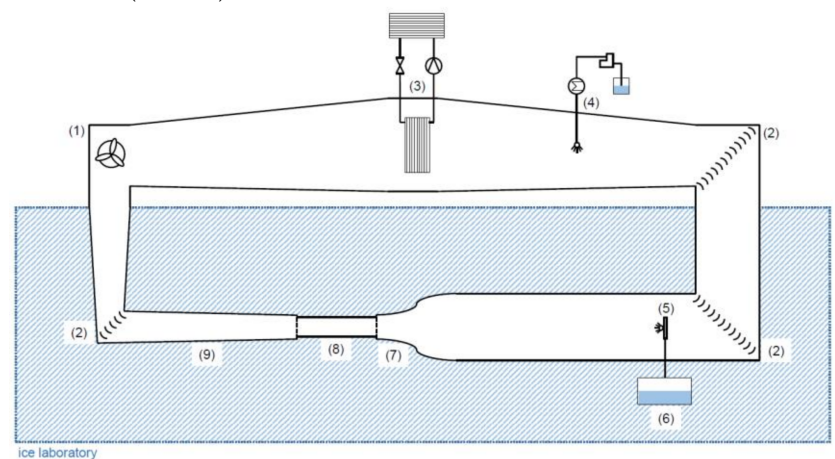
	Primer	Standox	PUR C25	PTFE-Tape
SFE (mN/m)	38.5	36.0	18.0	15.1
WCA (°)	83	86	100	110
WSA (°)	>90	67	41	29
CAH (°)	40	36	26	22
R_a (μm)	1.5	0.07	0.05	0.11
R_z (μm)	8.3	0.38	0.29	0.68

Tests started 21 days after coating application, at the earliest. Prior to each test, samples were cleaned using isopropanol and soft tissue. Between the tests, samples were stored in a dry and dark environment at room temperature.

Ice adhesion centrifuge tests were conducted in the Fraunhofer IFAM ice lab with an integrated ice wind tunnel (Figure 1). The ambient temperature during the ice formation and adhesion tests was kept constant at $-8\text{ }^\circ\text{C}$. This temperature was selected as it is low enough to prevent unstable icing conditions (these may occur close to $0\text{ }^\circ\text{C}$). Additionally, at $-8\text{ }^\circ\text{C}$, different ice types can form in the ice wind tunnel, depending on the air velocity. Prior to the ice formation process, test samples were pre-conditioned to this test temperature. Four different scenarios were defined for the assessment of the ice adhesion depending on the ice types and velocities (Table 3).



(a)



(b)

Figure 1. View inside the Fraunhofer IFAM ice lab (a) and scheme of the closed-loop ice wind tunnel (b) with a fan drive system (1), turning vanes (2), heat exchanger of refrigeration system (3), humiditystat (4), water spray bar (5), water reservoir and pumps (6), test section entrance (7), test section (8), and diffuser (9).

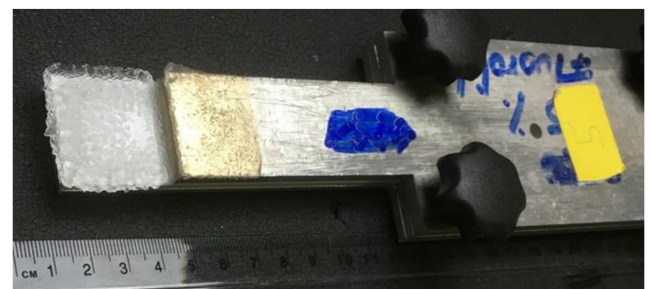
Static ice was produced by inserting each test sample into a silicone mold that allowed defined ice formation in the required area (Figure 2a). Three milliliters of de-ionized water were filled into the mold and allowed to freeze onto the test surface. After 90 min, the silicone mold was removed, and the sample was stored for a minimum of 15 min at the test temperature without any mechanical disturbance prior to the installation into the centrifuge.

Table 3. Conditions for the ice formation processes.

	Static Ice	Impact Ice (Ice Wind Tunnel Velocity)		
		40 m/s	60 m/s	95 m/s
Temperature (°C)	−8 (±0.5)	−8 (±0.1)	−8 (±0.1)	−8 (±0.1)
Icing duration	90 min	55 s	50 s	50 s
Resulting ice mass (g)	3.0	2.0 (±0.1)	2.2 (±0.1)	2.5 (±0.1)
Ice area (cm ²)	9	9	9	9
Liquid water content (g/m ³)	n.a.	1.2	1.0	0.6
Median volume diameter (µm)	n.a.	15	15	15



(a)



(b)

Figure 2. Test sample preparation with: (a) a silicone mold for static ice; (b) specimen holder for ice wind tunnel insertion for impact ice formation.

For impact ice, the pre-conditioned test sample was mounted onto a custom-made sample holder that allowed the positioning of the test surface in the center of the ice wind tunnel test section for a defined time (Figure 2b). After impact ice formation, the sample was removed from the ice wind tunnel and kept in the specimen holder for 10 min at a constant temperature of $-8\text{ }^{\circ}\text{C}$. After disassembly from the specimen holder, the test sample was stored for an additional five minutes prior to the installation in the centrifuge for testing of the ice adhesion.



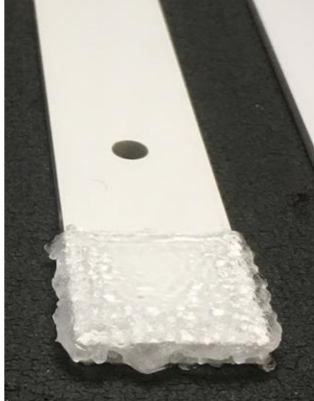

The four icing scenarios resulted in the formation of different ice types and shapes (Table 4). For static ice, compact glaze ice was produced in a well-defined area. Impact ice that was produced at 40 and 60 m/s also appeared as clear glaze ice but with a rough surface. Water droplets in the ice wind tunnel section hit the surface and were frozen at the test surface rather instantly. However, the following water droplets could run over this first icing layer before freezing, resulting in ice formations also at the test sample sides (also covered with the test materials). This phenomenon was not observed for impact ice accreted at a 95 m/s wind tunnel velocity. Short freezing times led to ice growth towards the wind direction instead of ice formations at the sample sides. The ice started to develop a milky appearance and was defined as mixed ice (mixture of glaze and rime ice).

For ice adhesion tests, a custom-made centrifuge with a modified rotor to place and fasten the prepared test samples was used as already described elsewhere [16]. Opposite the ice is a counterweight that can be adjusted, according to the ice mass, to reduce vibrations (see Figure 3). Generally, the centrifuge test uses centripetal forces to apply shear stress to the ice and remove it from the test surface. The prepared sample was fixed in the centrifuge, in which the iced sample was spun at a constantly increasing rate until the ice was sheared off. Separation was detected by a piezoelectric cell (MTN/1185C Series, Monitran Ltd., Penn, UK) when the ice hit the centrifuge wall and was correlated to the rotational speed of the centrifuge rotor. This speed (angular velocity ω in rad/s) was used to calculate the shear strength of ice to the substrate, according to the following equation:

$$\tau = \frac{F}{A} = \frac{m_{ice} \omega^2 r}{A} \quad (1)$$

where m_{ice} is the mass of ice (kg), r is the radius of the rotating beam at the mid-length ice position (m), and A is the surface area of the adherent interface (m^2) [21]. The calculated values in this study express the adhesive strength of the ice.

Table 4. Ice types for ice adhesion tests.

Static Ice	Impact ice: 40 m/s	Impact Ice: 60 m/s	Impact Ice: 95 m/s
			
glaze ice, compact, well-defined, sharp edges	glaze ice, brittle icing over the edges	glaze ice, flat in center, icing over the edges	mixed ice, icing towards wind, no ice on sides

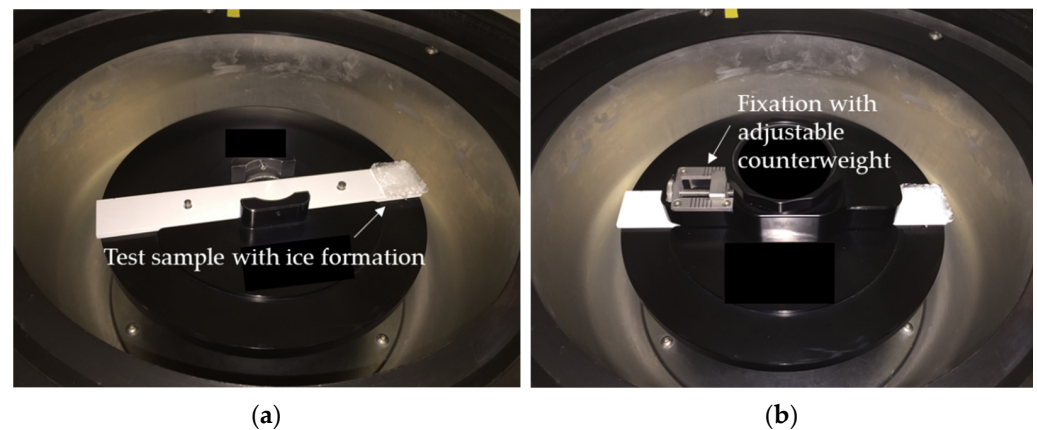


Figure 3. View inside the centrifuge test device with: (a) test sample with ice formation placed in the centrifuge; (b) test sample after fixation.

In addition to the ice types, the centrifuge acceleration speed varied from 100 rpm/s (10.472 rad/s^2) and 200 rpm/s (20.944 rad/s^2) to 300 rpm/s (31.416 rad/s^2) for the static ice test samples. Figure 4a shows the device-specific force evolutions during the test runs with different acceleration speeds up to the maximum centrifuge rotational speed (10,000 rpm) for an ice mass of 3 g. For 300 rpm/s, the maximum speed was reached after 34 s, and for 100 rpm/s, after 100 s. Furthermore, the differences that occurred between the ice masses for impact ice (compared with Table 3) also have an effect on the strength evolution during the centrifuge test. Figure 4b depicts the correlations between the ice masses and adhesion strength for an acceleration speed of 200 rpm/s that was used for impact ice adhesion assessments in this study.

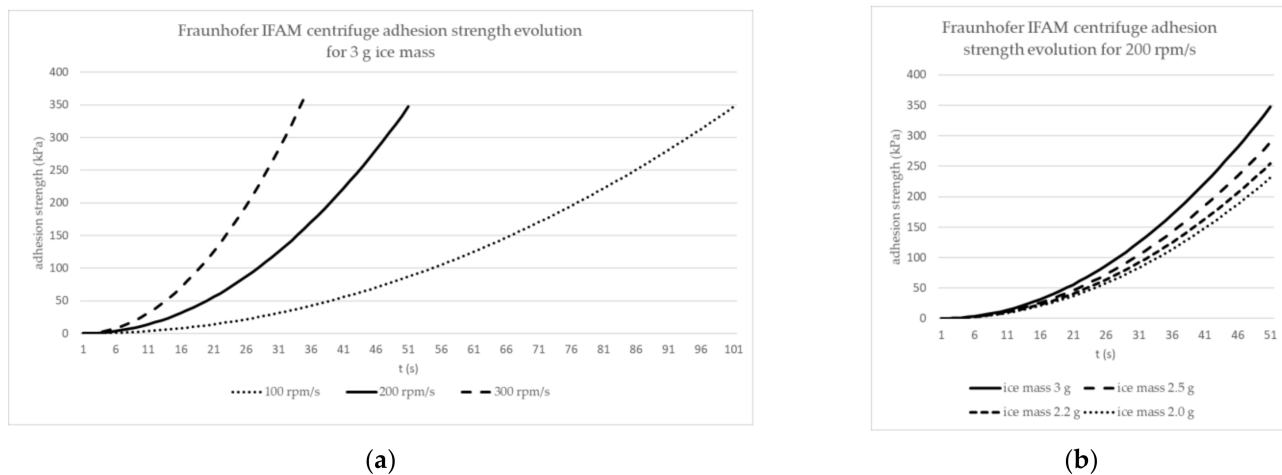


Figure 4. Adhesion strength evolution in the Fraunhofer IFAM centrifuge for: (a) 3 g of ice at various acceleration speeds; (b) 200 rpm/s acceleration speed and various ice masses.

Four to eight test samples per material type were available for the testing period and used randomly over the whole duration of this study with changing ice types and centrifuge acceleration speeds.

3. Results

The results of this study are displayed in the following subsections according to the main questions this study focused on. These include the durability determination of the test surfaces as a pre-requisite for the result interpretation (Section 3.1), detailed assessment of the gained data per scenario and material (Section 3.2), result comparison for different ice types (Section 3.3) and for different ice adhesion test parameter set-ups (Section 3.4), and finally, the interdependencies between the surface properties and ice adhesion test results (Section 3.5).

Quantitative ice adhesion results were derived from tests with 100% adhesive failure of the ice. This was observed for the materials Standox, PUR C25, and PTFE-tape. Partial detachment of the ice or even no ice shedding occurred for the primer coating in all test set-ups. The ice adhesion to the primer surface was higher than the maximum shear strength of the test (at a maximum centrifuge speed of 10,000 rpm: >231 kPa for 2 g of ice and >347 kPa for 3 g ice). This was evaluated as a qualitative result only.

For tests with static ice, one data point per test day and used sample was obtained. A maximum of 10 tests per day were conducted. For impact ice, a maximum of six samples per working day were tested in a twofold measurement. At least three independent test days per parameter set and material were conducted.

3.1. Durability of Test Surfaces

The materials used in this study were selected because of their expected durability to deliver reproducible results over the complete test period. Additionally, due to COVID-19-related restrictions regarding the presence of staff, the duration of this study had to be prolonged (200 days). To guarantee the comparability of the test results over the complete period, test set-ups for static ice (centrifuge acceleration speed: 200 rpm/s) and impact ice (95 m/s; centrifuge acceleration speed: 200 rpm/s) were conducted repeatedly. The results of the ice adhesion strength measurements are summarized in Figure 5a,b (no quantitative results were available for the primer coating due to cohesive ice failure).

For the Standox material, the data points over time were on comparable levels with the resulting means of 39 kPa for impact ice (95 m/s) and 185 kPa for static ice. No trends were identified that indicate material degradation or parameter variances within the test set-ups. The same applied for the PTFE-tape material, with means of 63 kPa for impact ice and 131 kPa for static ice. For the PUR C25 material, the test results remained at a stable

low level over the complete test period for impact ice (mean of 15 kPa) and static ice (mean of 41 kPa).

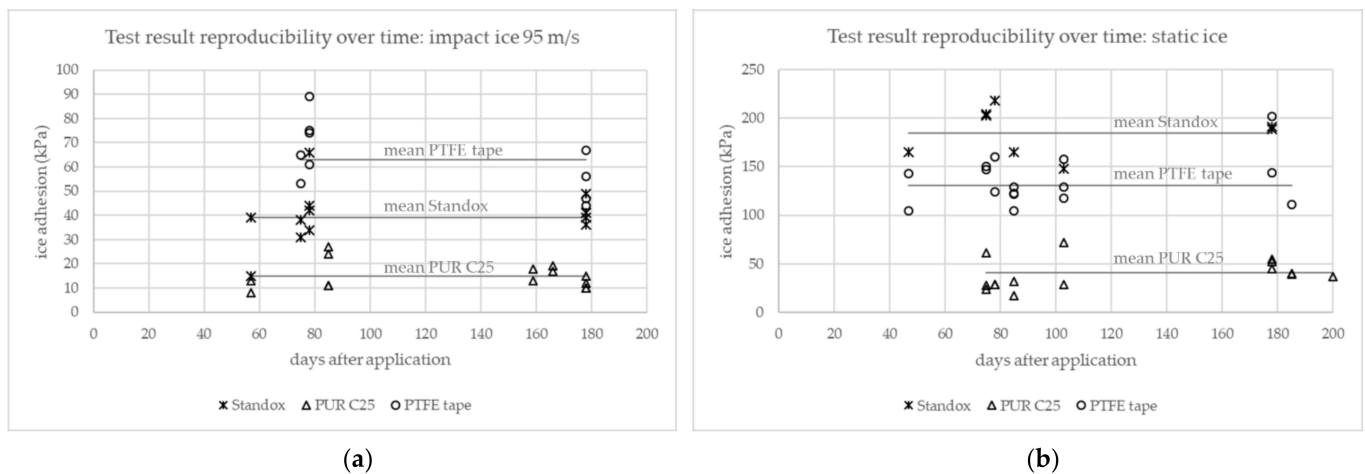


Figure 5. Test result reproducibility for ice adhesion tests over the complete test period: (a) for impact ice 95 m/s (200 rpm/s); (b) for static ice (200 rpm/s) (the given lines indicate the resulting means per material).

No visible defects for the used materials were reported. A comparison of the test results showed no time-dependent changes for the three quantifiable materials Standox, PUR C25, and PTFE-tape. The results already showed differences between surfaces and ice types, which is further assessed in the following sections.

3.2. Data Analysis

Ice adhesion test results are often accompanied by comparably high data scattering, which is caused by the high sensitivity of the ice–substrate interface to fluctuations in temperature, pre-conditioning parameters, and icing durations. Additionally, contaminations in the water and on test substrates may occur, and mechanical disturbances during ice formation and sample handling affect the measurement values. Finally, the test devices and also the staff need to work under harsh lab conditions (in this case, at a temperature of $-8\text{ }^{\circ}\text{C}$), resulting in higher stress levels for man and machine. To account for this, limited overall test times and detailed and robust test protocols are defined. Test repetitions increase the data points and help to identify single measurement errors.

In this study, a minimum of 10 data points per coating material for tests with impact ice and 8 data points for tests with static ice were assessed. For the exploratory data analysis of the ice adhesion test results, box plots were used to achieve a high data quality. To identify extreme values/outlier candidates in the data sets, the $1.5 \times \text{IQR}$ rule was selected (interquartile range IQR multiplied by 1.5 and added to the third quartile or subtracted from the first quartile) as an established statistical tool [22]. Data points outside this calculated range were defined as outliers and subsequently removed prior to the final calculation of the medians, means, and standard deviations per material and parameter set [23].

Tables 5–10 summarize the results of the data analysis, including boxplots that indicate outliers as dots outside the whiskers. The resulting medians, means, and standard deviations for the ice adhesion strength are given prior to and after the removal of identified outliers. The latter are indicated as “cleaned” values.

For impact ice, accreted at a wind speed of 95 m/s in the ice wind tunnel, clear differences between the surfaces were observed (Table 5). For PUR C25, the lowest ice adhesion was observed in this parameter set. The difference between the median and mean value is negligible for the evaluation. No outliers were identified. Standox represents an example where two outliers were observed (dots outside the whiskers). They were removed from the data set, resulting in a reduced standard deviation (“cleaned” data set

used for the following assessments). For PTFE-tape, the highest ice adhesion strength for this parameter set was observed. Here, the data distribution was comparably high, with equal mean and median values.

Table 5. Ice adhesion centrifuge test results for impact ice (95 m/s; acceleration speed 200 rpm/s) with relevant statistical data for result evaluation (given “cleaned” values based on outlier replacements after box plot assessments).

Impact Ice 95 m/s	Standex	PUR C25	PTFE-Tape
box plots			
median in kPa	39, cleaned: 39	13	63
mean (stdev) in kPa	40 (12), cleaned: 39 (5)	15 (6)	63 (14)
no. of data points	12, cleaned: 10	14	10

The results for impact ice, accreted at 60 m/s, are summarized in Table 6. The PUR C25 material again showed the lowest ice adhesion. One identified outlier was removed from the data set, resulting in a slight reduction in the mean and standard deviation. Tests with PTFE-tape showed higher ice adhesion strength data compared to PUR C25. For Standox, data dispersion was high, preventing a clear ranking between PTFE-tape and Standox. However, there was a trend that for tests with the Standox material, higher ice adhesion strength data were observed.

Table 6. Ice adhesion centrifuge test results for impact ice (60 m/s; acceleration speed 200 rpm/s) with relevant statistical data for result evaluation (given “cleaned” values based on outlier replacements after box plot assessments).

Impact Ice 60 m/s	Standex	PUR C25	PTFE-Tape
box plots			
median in kPa	91	26, cleaned: 26	80
mean (stdev) in kPa	103 (27)	28 (8) cleaned: 26 (5)	80 (10)
no. of data points	12	14 cleaned: 12	10

A further general increase in the ice adhesion strength was observed for impact ice, accreted at 40 m/s velocity (Table 7). For the material ranking, PUR C25 again showed the lowest ice adhesion strength. Standox and PTFE-tape were on comparable higher levels.

Ice adhesion tests with static ice were conducted with identical centrifuge acceleration speeds of 200 rpm/s as used for the impact ice tests (Table 8). Again, the PUR C25 material delivered the lowest ice adhesion results. For the PTFE-tape, as the second ranked material in this parameter set, an outlier was identified and removed. Standox material showed the highest ice adhesion strength for this set-up.

Table 7. Ice adhesion centrifuge test results for impact ice (40 m/s; acceleration speed: 200 rpm/s) with relevant statistical data for result evaluation.

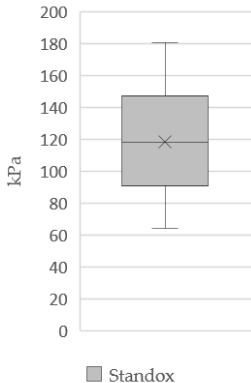
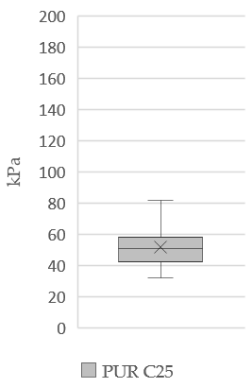
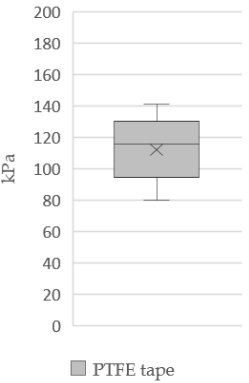
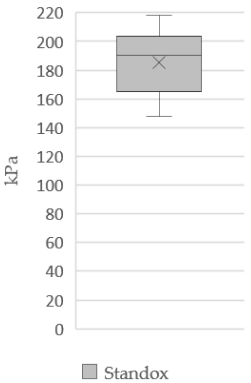
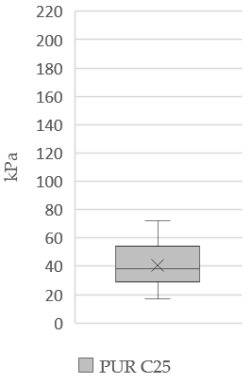
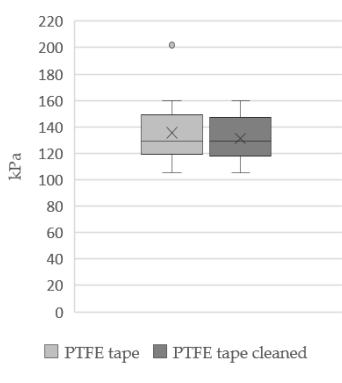
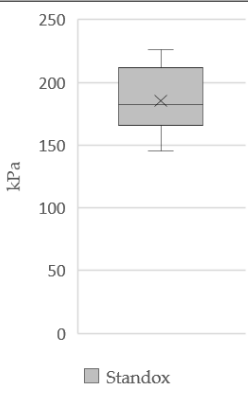
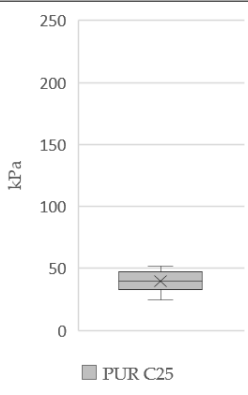
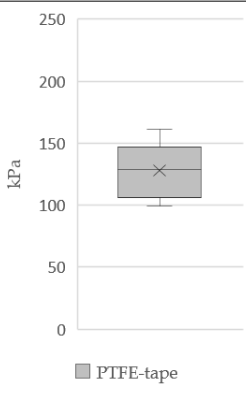
Impact Ice 40 m/s	Standex	PUR C25	PTFE-Tape
box plots			
median in kPa	117	51	116
mean (stdev) in kPa	119 (37)	52 (13)	112 (20)
no. of data points	10	10	12

Table 8. Ice adhesion centrifuge test results for static ice (200 rpm/s) with relevant statistical data for result evaluation (given “cleaned” values base on outlier replacements after box plot assessments).

Static Ice (200 rpm/s)	Standex	PUR C25	PTFE-Tape
box plots			
median in kPa	190	38	129, cleaned: 129
mean (stdev) in kPa	185 (24)	41 (15)	136 (25), cleaned: 131 (18)
no. of data points	8	16	16, cleaned: 15

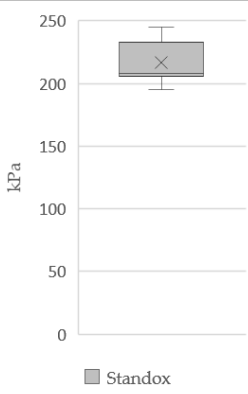
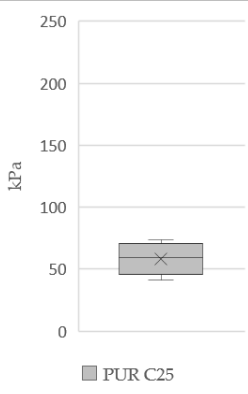
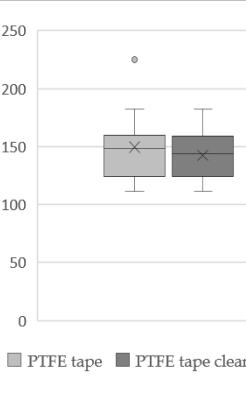
Static ice that was tested at a centrifuge acceleration speed of 100 rpm/s (Table 9) delivered comparable results to those tested with a 200 rpm/s acceleration speed.

Table 9. Ice adhesion centrifuge test results for static ice (100 rpm/s) with relevant statistical data for result evaluation.

Static Ice (100 rpm/s)	Standox	PUR C25	PTFE-Tape
box plots			
median in kPa	182	40	129
mean (stdev) in kPa	185 (27)	40 (9)	128 (22)
no. of data points	8	10	9

For static ice tested with an increased centrifuge acceleration speed of 300 rpm/s, the material ranking was comparable with those of the lower acceleration speeds (Table 10). For PTFE-tape, an outlier was removed, resulting in comparable median and mean values and a reduced standard deviation.

Table 10. Ice adhesion centrifuge test results for static ice (300 rpm/s) with relevant statistical data for result evaluation (given “cleaned” values based on outlier replacements after box plot assessments).

Static Ice (300 rpm/s)	Standox	PUR C25	PTFE-Tape
box plots			
median in kPa	208	59	152, cleaned: 144
mean (stdev) in kPa	217 (17)	58 (13)	149 (31), cleaned: 142 (21)
no. of data points	9	11	12, cleaned: 11

As an overall summary of this evaluation, it can be stated that the obtained data quality is appropriate for further correlation assessments. The identified outliers were removed from the data sets and the resulting means and standard deviations were used for the following correlation assessments.

3.3. Ice Types

The influence of the ice formation process on the ice adhesion strength is one important aspect of this paper. Figure 6 summarizes the centrifuge test results for the materials

Standex, PUR C25, and PTFE-tape. Tests with these materials delivered quantifiable results with complete adhesive failures between the ice and test surface. For the primer coating material, only cohesive ice failures or even no ice shear-off were observed, giving the qualitative result that the ice adhesion strength was significantly higher than the appearing shear forces in the conducted tests. Therefore, the primer is not included in the figure.

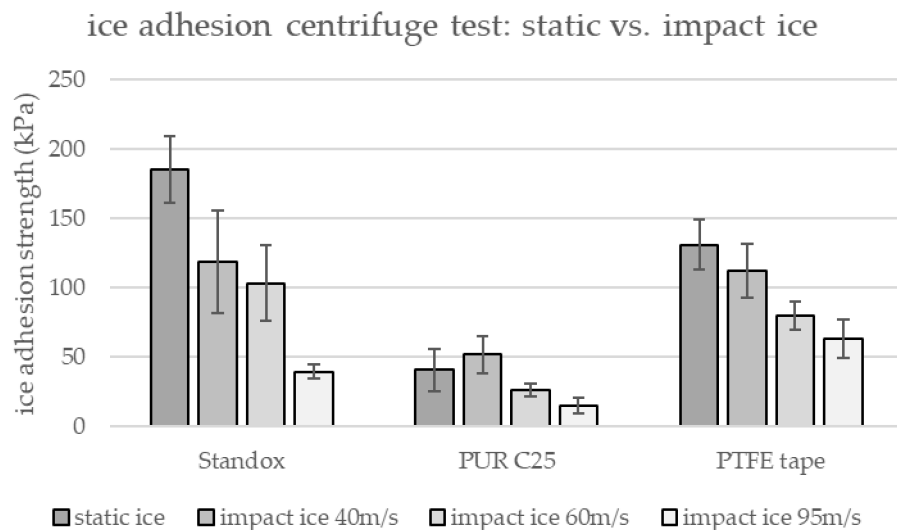


Figure 6. Comparison of the ice adhesion test results for different ice types.

Clear indications show that regardless of the material, the highest impact velocities (95 m/s) of the impinging water droplets led to the lowest ice adhesion strength for the respective materials. A reduction in the impact velocity to 60 and 40 m/s led to an increase in the ice adhesion strength. A further increase was observed for the unmodified polyurethane coating, Standox, for static ice formations. Due to the comparable high standard deviations, no clear difference between static ice and impact ice (40 m/s) was observed for the low ice adhesion material, PUR C25, and PTFE-tape.

By comparing the actual ice formations on the test samples (Table 4), one can argue that increased adhesive strength for ice, accreted at 60 and 40 m/s, may be related to the increased ice area, including the coverage of the (coated) sides of the test specimen to a certain extent. This is caused by water droplets moving over the test sample before freezing. However, this effect seems to have less significance, and for static ice with well-defined ice areas, the trend was continued.

The potential to distinguish between the tested materials is of importance for a lab-based test design. Here, impact ice might be more realistic for technical applications (e.g., aircraft, wind rotor blade) but delivers a narrow range of test results (for 95 m/s, an impact ice minimum of 15 kPa and maximum of 63 kPa). In contrast, static ice delivers a wider result range (minimum of 41 kPa and maximum of 185 kPa), potentially allowing an improved ranking during material development processes. However, surface characteristics (especially roughness) must be considered in the test parameter definition (Section 3.5).

3.4. Centrifuge Acceleration Speed

For tests with static ice formations, the effects of the centrifuge acceleration speed on the ice adhesion strength data were assessed (Figure 7). The results determined at acceleration speeds of 100 and 200 rpm/s, respectively, showed comparable results. A reduced standard deviation was observed for the test results of the low ice adhesion material PUR C25 at 100 rpm/s. This might be linked to an improved test resolution: at 100 rpm/s, the calculated mean of 40 kPa was reached after 34 s, and at 200 rpm/s,

already after 17 s (compare also with Figure 4). For the 300 rpm/s acceleration speed, the adhesive strength slightly increased for all materials but not significantly.

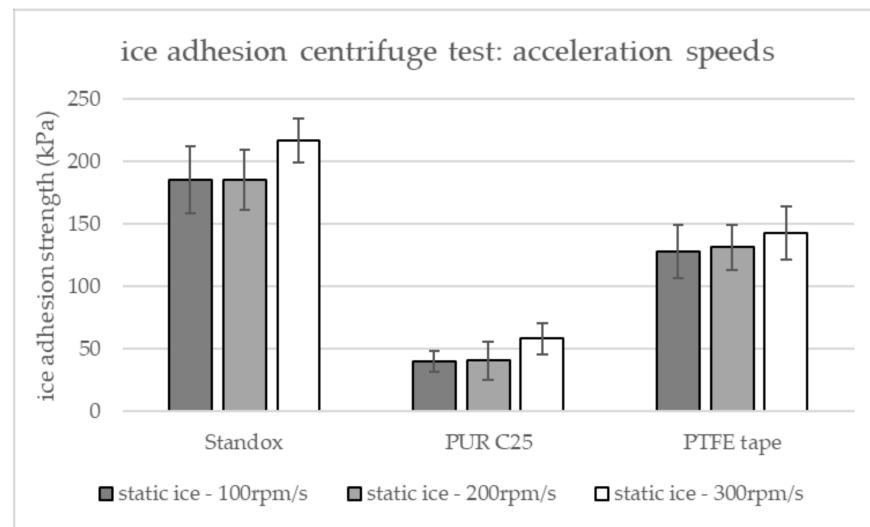


Figure 7. Comparison of the ice adhesion test results at different centrifuge acceleration speeds.

3.5. Interdependencies of the Surface Properties and Ice Adhesion Strength

The effects of the surface properties on results of the ice adhesion centrifuge test are assessed in the following section. Figure 8 shows exemplarily R_a values (arithmetical mean deviation of the assessed surface profile) as an often-used basic parameter for the surface roughness in comparison with the ice adhesion strength per ice formation type.

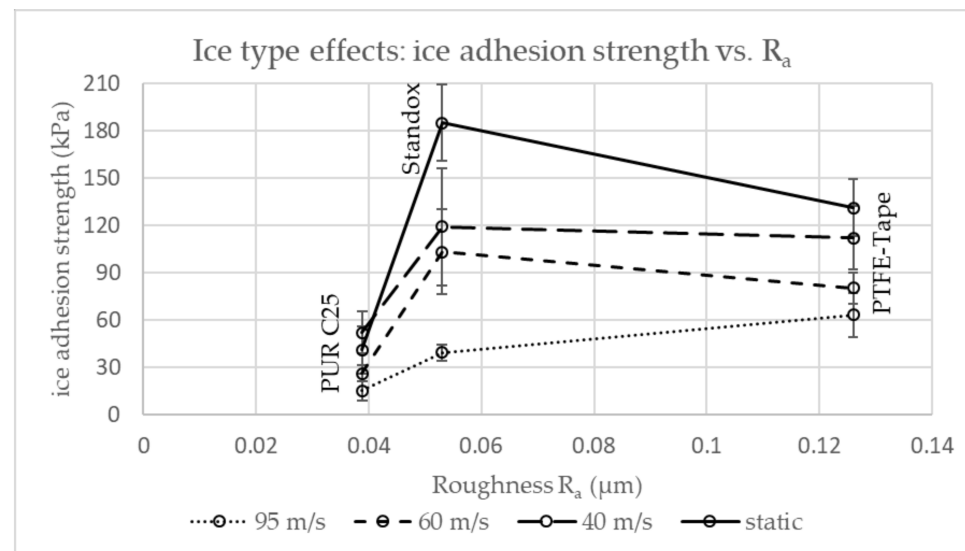


Figure 8. Surface parameter R_a and ice adhesion strength data for different ice formation types.

The PUR C25 material with the lowest material roughness in this study showed the lowest ice adhesion values in all ice formation types. For impact ice, accreted at 95 m/s (dotted line), the increase in the ice adhesion strength correlated with an increase in the roughness for the materials Standox ($R_a = 0.07 \mu\text{m}$) and PTFE-tape ($R_a = 0.11 \mu\text{m}$). This changed for ice accreted at lower velocities and for static ice. The measured ice adhesion strength was comparable (60 and 40 m/s velocity) or higher (static ice) for the smoother Standox material than for the PTFE-tape.

These findings may be explained by the underlying ice formation processes. Impacting water droplets (velocity 95 m/s) may enter the surface structure of PTFE-tape. They can

overcome the low material wettability (SFE = 15.1 mN/m) due to their high energy, resulting in a higher ice adhesion than for water with less or zero impact energy. This is also of specific relevance for superhydrophobic surfaces (high surface roughness, low wettability), which were not included in this test program due to their expected limited durability.

It is further postulated that with a significant increase in the roughness (as for the primer $R_a = 1.5 \mu\text{m}$), the ice adhesion strength increases significantly, regardless of the ice formation type. The surface wettability, as the second main surface property, is displayed in Figure 9 against the ice adhesion test results for different ice types. The surface free energy (SFE) was selected as the parameter for this evaluation.

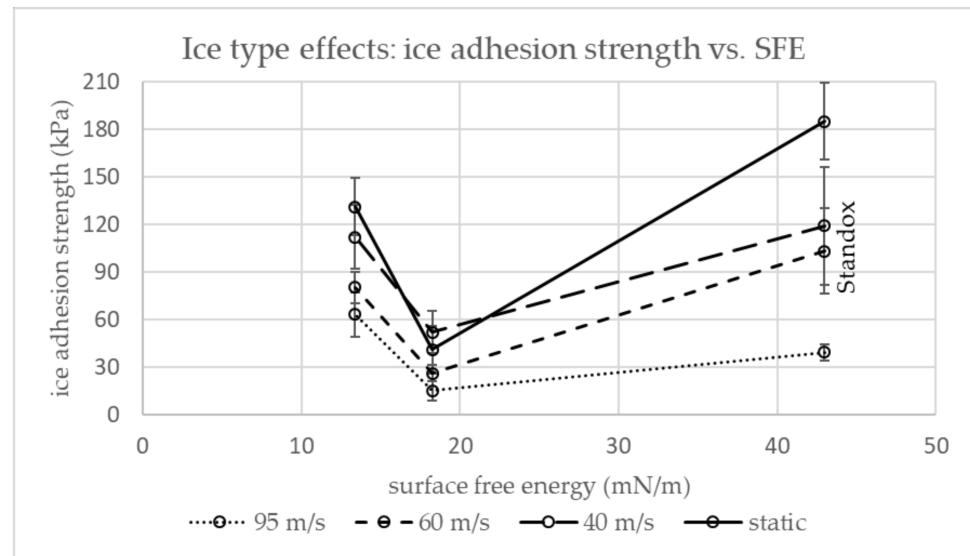


Figure 9. Surface free energy (SFE) and ice adhesion strength data for different ice formation types.

The lowest SFE of the PTFE-tape (SFE = 15.1 mN/m) in this study did not result in the lowest ice adhesion strength (as presented before). PUR C25 (SFE = 18.0 mN/m) showed lower ice adhesion test results for all ice formation types. The effects of the ice formation types and the interdependencies with the surface properties roughness and wettability included the following:

- For high impact velocities (95 m/s), the surface roughness is of higher relevance than the wettability properties, resulting in increased ice adhesion for the rougher but low-wettability PTFE-tape compared to the Standox coating.
- For lower impact velocities (60 and 40 m/s), the roughness and wettability properties cancel each other out, resulting in comparable ice adhesion results for the PTFE-tape and Standox material.
- For zero impact velocities (static ice), the surface wettability is of higher relevance than the roughness, resulting in a higher ice adhesion strength for Standox compared to PTFE-tape.

These findings are of significant importance for the development of icephobic materials and the definition of accompanying test designs. As soon as surface structures (used to reduce the wettability by increasing the roughness) are addressed, impact ice formations need to be considered to minimize the risk of overestimating the reduction in ice adhesion under relevant technical conditions. Therefore, the definition of test parameters should also address the desired technical applications.

4. Discussion

In this study, different test parameter set-ups for the ice adhesion centrifuge test were assessed in combination with durable reference materials, representing different surface properties with regard to the roughness and wettability. With regard to the effects

of ice types, this study showed that the ice adhesion strength is lower for impact ice compared to static ice. This was also reported by Tetteh and Loth in tensile ice adhesion tests [24]. One explanation for this finding is that ice accreted at a high velocity (in our study, 95 m/s) contains more air inclusions due to quasi-instant freezing of the droplets by impacting the surface or ice that has already been built at the test surface. The ice appears opaque, and the trapped air may reduce the contact area with the surface. Reducing the impact energy of the water (in our study, 60 and 40 m/s, static) leads to ice with less air inclusions and more bonding options to the surface, increasing the ice adhesion. Moreover, from a material perspective (at least for polymeric materials), we can postulate that a slower freezing process leads to increased adhesion. At a sub-molecular level, polar groups in the polymer matrix may become oriented to the interface and promote interactions with the water molecules. Work and Lian identified further possible explanations for the finding of higher adhesion strength for static (mold) ice, including stress differences frozen into the ice, larger grains, and, for rough surfaces, weaker stress concentrations at the interface due to a lack of penetration into surface structures [1]. Due to the complexity of ice formation processes, there are certainly overlapping parameters that cancel each other out or intensify the observed effects. This also applies to the effects of drag forces on the different ice shapes (impact vs. static ice) during the centrifuge test. This paper does not further address these aspects but includes a study that was conducted with regard to the effects of ice types on ice adhesion measurements using a centrifuge test. Rønneberg et al. identified for different ice types the following ranking (increasing ice adhesion): precipitation (hard rime) ice 5.6 m/s > impact ice 15 m/s > static ice. They concluded that the ice adhesion strength inversely correlated with the apparent density of the ice type [8]. The same trend was also reported in a related study, but it was less significant [25]. These contrary results emphasize the need to further improve the understanding of ice formation processes to improve test systems and identify crucial parameters for technical applications.

Considering the topic “surface properties” in the overall discussion, the complexity further increases. As summarized in Table 1, different studies have already addressed correlation aspects. The diversity of different correlation findings is now understandable, as the ice type used has a significant impact on the test results and the material ranking with regard to their ability to reduce the ice adhesion. However, roughness is a crucial surface parameter and can increase the ice adhesion strength significantly, as it was observed in this study for the primer coating material ($R_a = 1.5 \mu\text{m}$), only delivering cohesive ice failures or no ice shedding at all. This finding is in agreement with other centrifuge test-related studies for static ice [17], impact ice at 25 m/s [15], and rotor tests [7,14]. Nevertheless, the complexity of the surface roughness is higher than the expressed parameter R_a and R_z , especially for superhydrophobic surfaces. This is to be addressed in future studies.

For the expression of the wettability, this study used the surface free energy (SFE) as the determining parameter. The higher this value, the better the wettability of a liquid (water) at the solid surface due to available bonding options. The roughness and chemical composition of the solid are the determining factors for the SFE and an optimum for the icephobic performance was observed for PUR C25 (18.0 mN/m). A further decrease in PTFE-tape (15.1 mN/m) is related to an increase in the roughness, resulting in a higher ice adhesion strength. This was already published for other polymeric coatings during the degradation process [13]. However, to our knowledge, this has not been reported by other research groups for icephobic properties. Furthermore, the often-highlighted parameter contact angle hysteresis (CAH), as a suitable correlating parameter for the icephobic performance [9,11,15], follows the same trend as the SFE. The identified findings might not be valid for superhydrophobic surfaces (e.g., [26–30]) or materials following or inspired by the slippery liquid-infused porous surfaces (SLIPS) approach (e.g., [24,31–33]), as they can generate “extreme” values, constituting exceptions to the general rule. Moreover, the elastomeric properties of coating materials are discussed as relevant parameters for the ice adhesion strength [12] but should not be dominant in this study due to the low (<100 μm) and comparable material thicknesses.

In general, the data point distribution for ice adhesion tests is comparably high and standard deviations $\geq 20\%$ are often reported (e.g., [8,15,25]). This also applies to the current study, specifically for the low ice adhesion surface PUR C25, with data points below 50 kPa. One reason for this is the limited data resolution in the lower measurement area. Further reasons, such as the limited material durability in repeated tests or disturbing factors (e.g., temperature fluctuation, mechanical disturbance of the ice–test surface interface, contaminations), were excluded in this study as much as possible. All measures to reduce the data scattering need to be considered, and the reduction in the acceleration speed of the centrifuge should be considered in order to increase the test resolution and improve the data quality.

5. Conclusions

In this study, different test parameter set-ups for the ice adhesion centrifuge test were assessed in combination with durable reference materials, representing different surface properties with regard to the roughness and wettability. The following main conclusions can be drawn:

1. The “ice type” plays a significant role in the ice adhesion strength, and static ice formation showed the highest values in this lab-based test.
2. The role of “surface properties” is complex, but clear trends were observed that for high impact ice (95 m/s), the surface roughness is the determining parameter. This is in contrast to static ice formations, in which the wettability parameter gains more relevance. This finding bears the risk of misinterpretations during iterative developments for rough (structured) materials, if tested with static ice.
3. The “acceleration speed” of the centrifuge plays a minor role in the range of 100 to 300 rpm/s but should be considered, especially to improve the data quality for low ice adhesion materials.

The findings in this study and the comparison with related studies from other research groups emphasize the need for future work on the underlying physics of the assessed phenomena to improve the understanding of icing on surfaces.

Author Contributions: Conceptualization, B.S. and N.R.; methodology, B.S. and N.R.; validation, B.S., V.S. and N.R.; formal analysis, N.R.; investigation, N.R.; resources, V.S.; writing—original draft preparation, N.R.; writing—review and editing, B.S. and V.S.; visualization, N.R.; supervision, V.S.; project administration, N.R. All authors have read and agreed to the published version of the manuscript.

Funding: This research received no external funding.

Institutional Review Board Statement: Not applicable.

Informed Consent Statement: Not applicable.

Acknowledgments: The authors would like to thank colleagues at Fraunhofer IFAM working in the field of coating technologies and ice-related topics for their efforts in supporting this study. Special thanks goes to Udo Peltzer for the preparation of test samples and Volker Foeste, Nelson Ehling, and Niklas Pengemann for their active support in improving the test protocols for the centrifuge test and performing the experiments.

Conflicts of Interest: The authors declare no conflict of interest.


References

1. Work, A.; Lian, Y. A Critical Review of the Measurement of Ice Adhesion to Solid Substrates. *Prog. Aerosp. Sci.* **2018**, *98*, 1–26. [CrossRef]
2. Kulinich, S.A.; Farzaneh, M. Ice adhesion on super-hydrophobic surfaces. *Appl. Surf. Sci.* **2009**, *255*, 8153–8157. [CrossRef]
3. Fortin, G.; Beisswenger, A.; Perron, J. Centrifuge Adhesion Test to Evaluate Icephobic Coatings. In Proceedings of the AIAA Atmospheric and Space Environments Conference, Toronto, ON, Canada, 2–5 August 2010. AIAA 2010-7837.
4. Koivuluoto, H.; Stenroos, C.; Ruohomaa, R.; Bolelli, G.; Lusvarghi, L.; Vuoristo, P. Research on icing behavior and ice adhesion testing of icephobic surfaces. In Proceedings of the IWAIS 2015, Uppsala, Sweden, 28 June–3 July 2015.

5. Liu, J.; Janjua, Z.A.; Roe, M.; Xu, F.; Turnbull, B.; Choi, K.-S.; Hou, X. Super-Hydrophobic/Icephobic Coatings Based on Silica Nanoparticles Modified by Self-Assembled Monolayers. *Nanomaterials* **2016**, *6*, 232. [CrossRef]
6. Orchard, D.; Clark, C.; Chevrette, G. Reducing Aviation Icing Risk: Ice Adhesion Measurement in the NRC's Altitude Icing Wind Tunnel. In Proceedings of the SAE AeroTech Conference, FortWorth, TX, USA, 26–28 September 2017.
7. Soltis, J.; Palacios, J.; Eden, T.; Wolfe, D. Evaluation of Ice-Adhesion Strength on Erosion-Resistant Materials. *AIAA J.* **2015**, *53*, 1825–1835. [CrossRef]
8. Rønneberg, S.; Laforte, C.; Volat, C.; He, J.; Zhang, Z. The effect of ice type on ice adhesion. *AIP Adv.* **2019**, *9*, 055304. [CrossRef]
9. Arianpoura, F.; Farzaneha, M.; Kulinich, S.A. Hydrophobic and ice-retarding properties of doped silicone rubber coatings. *Appl. Surf. Sci.* **2013**, *265*, 546–552. [CrossRef]
10. Tarquini, S.; Antonini, C.; Amirfazli, A.; Marengo, M.; Palacios, J. Investigation of ice shedding properties of superhydrophobic coatings on helicopter blades. *Cold Reg. Sci. Technol.* **2014**, *100*, 50–58. [CrossRef]
11. Janjua, Z.A.; Turnbull, B.; Choy, K.-L.; Pandis, C.; Liu, J.; Hou, X.; Choia, K.-S. Performance and Durability Tests of Smart Icephobic Coatings to Reduce Ice Adhesion. *Appl. Surf. Sci.* **2017**, *407*, 555–564. [CrossRef]
12. Kool, N.; Chevrette, G.; Orchard, D.M. Testing of Elastomer Icephobic Coatings. In Proceedings of the Conference Paper for 2018 Atmospheric and Space Environment Conference, Atlanta, Georgia, 25–29 June 2018. [CrossRef]
13. Rehfeld, N.; Speckmann, B.; Grünke, S. Durability of Icephobic Materials. In Proceedings of the IW AIS 2019, Reykjavik, Iceland, 23–27 June 2019.
14. Asadollahi, S.; Farzaneh, M.; Stafford, L. On the Icephobic Performance of Organosilicon-Based Surface Structures Developed through Atmospheric Pressure Plasma Deposition in Nitrogen Plasma. *Coatings* **2019**, *9*, 679. [CrossRef]
15. Koivuluoto, H.; Hartikainen, E.; Niemelä-Anttonen, H. Thermally Sprayed Coatings: Novel Surface Engineering Strategy Towards Icephobic Solutions. *Materials* **2020**, *13*, 1434. [CrossRef] [PubMed]
16. Rehfeld, N.; Speckmann, B.; Schreiner, C.; Stenzel, V. Assessment of Icephobic Coatings—How Can We Monitor Performance Durability? *Coatings* **2021**, *11*, 614. [CrossRef]
17. Memon, H.; Liu, J.; De Focatiis, D.S.; Choi, K.; Hou, X. Intrinsic dependence of ice adhesion strength on surface roughness. *Surf. Coat. Technol.* **2020**, *385*, 125382. [CrossRef]
18. *DIN EN ISO 2808:2019*; Beschichtungsstoffe—Bestimmung der Schichtdicke. Beuth Verlag GmbH: Berlin, Germany, 2019.
19. *DIN EN ISO 19403-2*; Beschichtungsstoffe—Benetzbarkeit—Teil 2: Bestimmung der Freien Oberflächenenergie Fester Oberflächen Durch Messung des Kontaktwinkels. Beuth Verlag GmbH: Berlin, Germany, 2020.
20. *DIN EN ISO 19403-7*; Beschichtungsstoffe—Benetzbarkeit—Teil 7: Messung des Kontaktwinkels bei Neigetischexperimenten (Abrollwinkel). Beuth Verlag GmbH: Berlin, Germany, 2020.
21. Laforte, C.; Beisswenger, A. Icephobic Material Centrifuge Adhesion Test. In Proceedings of the IW AIS 2005, Montréal, QC, Canada, 12–16 June 2005.
22. Fahrmeir, L.; Heumann, C.; Künstler, R.; Pigeot, I.; Tutz, G. *Statistik. Der Weg zur Datenanalyse*, 8th ed.; Springer: Berlin/Heidelberg, Germany, 2016; pp. 59–62.
23. Schendera, C.F.G. *Datenqualität mit SPSS*; Oldenbourg Wissenschaftsverlag GmbH: München, Germany, 2007; pp. 198–200.
24. Tetteh, E.; Loth, E. Reducing Static and Impact Ice Adhesion with a Self-Lubricating Icephobic Coating (SLIC). *Coatings* **2020**, *10*, 262. [CrossRef]
25. Rønneberg, S.; Zhuo, Y.; Laforte, C.; He, J.; Zhang, Z. Interlaboratory Study of Ice Adhesion Using Different Techniques. *Coatings* **2019**, *9*, 678. [CrossRef]
26. Kulinich, S.A.; Farhadi, S.; Nose, K.; Du, X.W. Superhydrophobic Surfaces: Are They Really Ice-Repellent? *Langmuir* **2011**, *27*, 25–29. [CrossRef]
27. Antonini, C.; Innocenti, M.; Horn, T.; Marengo, M.; Amirfazli, A. Understanding the Effect of Superhydrophobic Coatings on Energy Reduction in Anti-Icing Systems. *Cold Reg. Sci. Technol.* **2011**, *67*, 58–67. [CrossRef]
28. De Pauw, D.; Dolatabadi, A. Effect of Superhydrophobic Coating on the Anti-Icing and De-Icing of an Airfoil. *AIAA J. Aircr.* **2017**, *54*, 490–499. [CrossRef]
29. Esmeryan, K.D. From Extremely Water-Repellent Coatings to Passive Icing Protection—Principles, Limitations and Innovative Application Aspects. *Coatings* **2020**, *10*, 66. [CrossRef]
30. Milles, S.; Vercillo, V.; Alamri, S.; Aguilar-Morales, A.I.; Kunze, T.; Bonaccorso, E.; Lasagni, A.F. Icephobic performance of Multi-Scale Laser-Textured Aluminum Surfaces for Aeronautic Applications. *Nanomaterials* **2021**, *11*, 135. [CrossRef]
31. Wong, T.S.; Kang, S.; Tang, S.; Smythe, E.; Hatton, B.D.; Grinthal, A.; Aizenberg, J. Bioinspired self-repairing slippery surfaces with pressure-stable omniphobicity. *Nature* **2011**, *477*, 443–447. [CrossRef]
32. Liu, G.; Yuan, Y.; Liao, R.; Wang, L.; Gao, X. Fabrication of Porous Slippery Icephobic Surface and Effect of Lubricant Viscosity on Anti-icing Properties and Durability. *Coatings* **2020**, *10*, 896. [CrossRef]
33. Donadei, V.; Koivuluoto, H.; Sarlin, E.; Niemelä-Anttonen, H.; Varis, T.; Vuoristo, P. The effect of mechanical and thermal stresses on the performance of lubricated icephobic coatings during cyclic icing/deicing tests. *Prog. Org. Coat.* **2022**, *163*, 106614. [CrossRef]

Article

A Multi-Tool Analysis to Assess the Effectiveness of Passive Ice Protection Materials to Assist Rotorcraft Manual De-Icing

Jean-Denis Brassard ^{1,*}, Dany Posteraro ² , Sarah Sobhani ¹, Marco Ruggi ² and Gelareh Momen ¹

¹ Department of Applied Sciences, Université du Québec à Chicoutimi (UQAC), 555 Boulevard de l'Université, Chicoutimi, QC G7H 2B1, Canada; sarah.sobhani1@uqac.ca (S.S.); gelareh_momen@uqac.ca (G.M.)

² APS Aviation Inc., Groupe RHEA, 6700 Chemin de la Côte-de-Liesse, Suite 102, Montréal, QC H4T 2B5, Canada; dposteraro@apsaviation.ca (D.P.); mruggi@apsaviation.ca (M.R.)

* Correspondence: jean-denis1_brassard@uqac.ca

Featured Application: A comprehensive procedure to evaluate the effectiveness of a polymeric material that aims to reduce ice and snow adhesion.

Abstract: Search and rescue missions using rotorcrafts need to be reliable all year long, even in winter conditions. In some cases of deployment prior to take off, the crew may need to manually remove accumulated contaminant from the critical surfaces using tools at their disposal. However, icy contaminant may be hard to remove since the rotorcrafts critical surfaces could be cooler than the environment, thus promoting adhesion. Currently, there exists several passive ice protection materials that could reduce the ice adhesion strength and assist the manual de-icing. The aim of this paper is to propose a detailed comparative procedure to assess the ability of materials to assist the manual de-icing of rotorcrafts. The proposed procedure consists of the characterization of materials using several laboratory tests in order to determine their characteristics pertaining to wettability, their icephobic behavior, and finally their assessment under a multi-tool analysis to evaluate if they can assist. The multi-tool analysis uses different mechanical tools, which are currently used during normal operation, to execute a gradual de-icing procedure, which begins with the softest to the hardest tool using a constant number of passes or strokes, under different types of simulated precipitation. Five different materials were used to evaluate the proposed procedure: Aluminum (used as a reference), two silicone-based coatings (Nusil and SurfEllent), an epoxy-based coating (Wearlon), and finally a commercial ski wax (Swix). All of the tested materials could assist the manual de-icing, within a certain limit, when compared to the bare aluminum. However, SurfEllent was the material that obtained the best overall results. This procedure could be easily adapted to different fields of application and could be used as a development tool for the optimization and the assessment of new materials aimed to reduce ice adhesion.

Keywords: icephobic; de-icing; anti-icing; multi-tool; rotorcraft; coating; polymers; passive ice protection



Citation: Brassard, J.-D.; Posteraro, D.; Sobhani, S.; Ruggi, M.; Momen, G. A Multi-Tool Analysis to Assess the Effectiveness of Passive Ice Protection Materials to Assist Rotorcraft Manual De-Icing. *Appl. Sci.* **2021**, *11*, 11847. <https://doi.org/10.3390/app112411847>

Academic Editor: Filomena Piscitelli

Received: 5 November 2021

Accepted: 8 December 2021

Published: 13 December 2021

Publisher's Note: MDPI stays neutral with regard to jurisdictional claims in published maps and institutional affiliations.



Copyright: © 2021 by the authors. Licensee MDPI, Basel, Switzerland. This article is an open access article distributed under the terms and conditions of the Creative Commons Attribution (CC BY) license (<https://creativecommons.org/licenses/by/4.0/>).

1. Introduction

Search and rescue missions can be hazardous and dangerous for emergency teams, especially when winter conditions bring about snowy, stormy, or icy precipitation that adheres to emergency vehicles. The situation becomes even more difficult when rescue teams need to use aircrafts such as helicopters. If a life is in danger, the operation becomes a critical mission; therefore, rotorcraft need to be dispatched, takeoff, and land safely in any condition to successfully complete their mission. De-icing at the base is normally easier with appropriate tools, or if the rotorcraft is kept inside a hangar, icing challenges can be minimized [1]. However, the major issues may occur when they are deployed on a mission. Sometimes, ice or wet snow can deposit and adhere quickly on the critical surfaces, and it needs to be removed before an eventual takeoff. This becomes especially limiting when

rotorcrafts are deployed to remote locations where de-icing capabilities are limited, and the crew need to rely on primarily manual methods (such as brushes or brooms) to remove snow and ice.

In a subfreezing environment, ice in the form of rime and glaze may accumulate on the surface of rotorcraft blades [2]. Rotor blades covered with a thin ice layer can have a strong negative impact on aerodynamics. Increases in drag and flow separation, which significantly reduces lift and can often make controlling the aircraft extremely difficult [3–8]. Therefore, designing methodologies that prevent ice accumulation, reduce its adhesion, or even assist during the de-icing are incredibly important in eliminating the latter issues [2]. The following sections will review the main methods presently used for this application.

Innovative de-icing and anti-icing protection systems have been developed and studied by numerous researchers. Several of these methods have also been investigated regarding their effectiveness in a laboratory setting prior to deployment in actual operations. The two main methodologies that have been explored are the following:

- Active methods; and
- Passive methods.

Active methods are those requiring external energy sources to work; they are divided in two main categories. The thermal methods consist of increasing the temperature of a critical surface to which ice may have formed or adhered. This is done to reduce ice adherence, by creating a water layer between the ice and the surface, and consequently allows for its removal under the effect of gravity. Some of these methods can also be used as a form of anti-icing. By increasing the temperature of the critical surface, it can effectively prevent supercooled water droplets from freezing upon impact. Some rotorcrafts are equipped with an electrothermal ice protection system for the main rotor blade, which can prevent grounding even in inclement icing conditions. Unfortunately, due to the significant energy load necessary for heating, the high electrical current in the slip rings, and the extensive cabling needed, approved electro-thermal de-icing systems can currently only equip the primary rotors of large rotorcrafts. However, this de/anti-icing methodology requires a significant amount of energy and adds a considerable amount of weight to the aircraft. In addition, it does not allow for the complete de-icing of the rotorcraft [5,7,8].

The mechanical methods consist of using tools that break the ice adhering to the aircraft structure by shocking or inducing vibrations [7,9–12]. In most cases, mechanical methods can be considered as de-icing methods since they are used to speed the shedding process after snow or ice has accumulated or formed on the structure. Studies show that mechanical methods require approximately 100,000 times less energy than thermal methods to induce ice shedding [13].

The principal mechanical methods are based on two strategies:

- One consists of breaking the ice by means of scraping, rollers, hooks, cutters or rope; and
- The other consists of releasing energy from shock waves or vibrations to break and remove the ice.

Since ice is a very brittle material at high-strain rates, relatively little mechanical energy is required for breaking ice by using mechanical shocks as energy is not readily dissipated [7]. A main advantage of using a mechanical method instead of a thermal method is the relative ease of application. In fact, mechanical methods are the preferred choice for a timely and fast intervention to de-ice short critical sections [7]. Palacios et al. presented a novel pneumatic method to assist rotorcraft de-icing [10]. The pneumatic method consists of using a low-power, non-thermal, ultrasonic de-icing system as a potential replacement to current electro-thermal systems on helicopter rotor blades. Villeneuve et al. also proposed a low-energy de-icing system based on piezo-electric actuators [7]. The developed model allows for the design of a proper actuator to efficiently deice.

Passive methods do not use conventional sources of energy as other methods do. Instead, they use natural forces such as wind, gravity, or solar radiation. Consequently,

they can be applied on any structure, including rotorcraft. The main passive method consists of utilizing coatings that reduce the ice adhesion on structures of interest. These coatings are known as icephobic materials and have been used in several fields [14–16]. The benefit of using icephobic coatings is the decrease in ice adhesion to a structure and/or prevent supercooled water droplets from freezing.

In order to achieve an icephobic surface, three different approaches have been introduced including fabricating a superhydrophobic surface [17], delaying ice nucleation [18], and designing a surface with low ice adhesion strength [19]. Superhydrophobic materials were introduced by Saito [20] and claimed to exhibit promising anti-icing performance. However, Saito showed in another study that by increasing the surface roughness of a superhydrophobic surface, ice adhesion increases [20]. In some cases, icephobic coatings have shown to exhibit good performance for rotor blades. Unfortunately, in most cases, these coatings lose their icephobic properties soon after application and exhibit poor durability [21,22]. Hence, research in the field of icephobic coatings for rotorcraft applications is still ongoing.

Many studies have been performed to both quantify and qualify the performance of coatings. For example, by assessing the icephobicity of superhydrophobic coatings of a helicopter blade in an icing chamber, Tarquini [23] revealed that temperature and surface roughness have a strong impact on ice adhesion. The latter study showed that by decreasing the chamber temperature and increasing the coating roughness, ice adhesion strength increases. In another study, Kimura [24] developed an icephobic coating based on acrylic urethane resin and polytetrafluoroethylene (PTFE) particles for aircraft applications. The coating proved to be superhydrophobic and effective in anti-/de-icing aircrafts.

Karmouch [25], in 2009, impregnated a PTFE nanoparticle coating on a wind turbine blade surface. It was found that the very simple dipping provided a superhydrophobic surface and reduced ice adhesion. Antonini [26] investigated the effectiveness of superhydrophobic coatings on surfaces exposed to icing conditions equipped with an electrical heater. The results showed that superhydrophobic coatings could lead to a remarkable reduction of heating power on surfaces exposed to icing conditions. Recent advances in the development of icephobic coatings were also undertaken using superhydrophobic surfaces [27–29].

In order to evaluate the capability of a system subjected to icing conditions, ice adhesion is the main parameter used in industrial and academic investigations. As a complex physicochemical process, ice adhesion is not easy to quantify or compare since it depends on process parameters. Examples of these include ice density, ice formation conditions and substrate nature, and surface profile [30]. Therefore, ice adhesion comparative tests should be performed using the same conditions throughout the evaluation process.

As discussed, many methods are available to deice rotorcrafts. Unfortunately, none of the strategies proposed is sufficient to completely prevent ice and snow accumulation. However, by combining some of these methods, for example, the thermal and coating methods, the efficiency can be significantly increased. Nevertheless, this may necessitate the deployment of complex apparatuses, which can be costly. One way to overcome this is by associating the icephobic coating with simple manual de-icing tools. This can serve as a more economical solution since it only requires the action of crew members. In fact, icephobic coatings may facilitate or assist the manual de-icing process by reducing ice adhesion. The aim of this paper is, therefore, to present a comprehensive manual de-icing procedure that will aid in assessing the effectiveness of different passive ice protection materials.

2. Materials and Methods

The proposed methodology consists of a multi-criterion assessment of the materials using conventional and newly developed laboratory tests. The idea is to obtain comparative results between tests so that a full assessment can be done on each coating. These tests include contact angle measurements, centrifuge ice adhesion, ice push-off, freezing delay measurements, and finally, one test that simulates operational conditions—the multi-tools analysis test. The next sections describe all tests that were carried out for this analysis.

2.1. Substrates

Testing was conducted using coated and uncoated aerospace-grade 6061-T6 aluminum test plates. Each coated plate contained the specific material to be tested, whereas the uncoated plates represented the baseline or reference. This aluminum alloy was selected as it is widely used in the aerospace industry and used as the standard in previously completed studies. The characterization phase was performed using 2.5 cm per 2.5 cm substrates. The same size substrates were used during the push-off test and the freezing delay measurement. The centrifuge ice adhesion measurements were then carried out using 3.3 cm per 30 cm substrates. Finally, 30 by 50 cm plates were used for the multi-tools analysis.

Throughout testing, all results were compared to the aluminum baseline. Since bare aluminum reacts similarly to painted plates, the same paints as used on rotorcrafts, it was determined that these tests can be used to deduce the coating efficiency in assisted manual de-icing.

2.2. Physical Characterization Using Contact Angle Measurement

The first test undertaken considered the wettability of the surface using the water droplet contact angle (WCA) and contact angle hysteresis (CAH). The measurements were carried out using sessile drop technique by means of Kruss™ DSA100 goniometer at 25 ± 0.5 °C. A 4 μ L water droplet was placed on the surface to evaluate the WCA by Young–Laplace approximation. By displacing the needle tip within the water droplet, the CAH was determined by evaluating the difference between the advancing and receding contact angles.

2.3. Icephobic Behavior Assessment

Three laboratory tests were used to evaluate the icephobic behavior of materials:

- The centrifugal force adhesion test (CAT);
- The push-off test; and
- The freezing delay test.

The CAT apparatus consists of a centrifuge developed at the Anti-Icing Material International Laboratory (AMIL) as seen in Figure 1.



Figure 1. Overview of the centrifuge apparatus. Equipped with an accelerometer, the iced beam is rotated until the ice is detached and captured by the pan.

The ice adhesion strength is the centrifugal shear stress exerted on the ice sample at the time of detachment. A CAT sampling consists of six different coating samples that are compared to six reference blank aluminum sheets. All samples are subjected to icing simultaneously under freezing drizzle conditions set at $-8\text{ }^{\circ}\text{C}$ and tested at $-10.0\text{ }^{\circ}\text{C}$. Afterwards, samples are rotated at an acceleration speed of 300 rpm/s until the ice is detached by centrifugal force. This acceleration creates a strain rate of approximately 10^{-6} s^{-1} . The rotational speed is controlled during the acceleration phase by the AMIL-made software, which records and plots the angular velocity in real time with data from installed sensors. An accelerometer sensor located on the wall of the centrifuge is used to determine the exact time of ice detachment. This time corresponds to a sharp increase in the vibration signal. The centrifugal force is calculated using the following equation:

$$F_c = mr\omega^2 \quad (1)$$

where:

F_c = centrifugal force;

ω = ice detachment velocity;

m = mass of ice; and

r = beam radius at the center of the sample.

The ice adhesion shear stress is then obtained as follows:

$$\tau_{ia} = \frac{F_c}{A} \quad (2)$$

where:

τ_{ia} = ice adhesion shear stress;

F_c = centrifugal force; and

A = iced area in contact with the coating.

The adhesion reduction factor (ARFs) of coating i is calculated as follows:

$$ARF_i = \frac{\tau_{bA}}{\tau_{bi}} \quad (3)$$

where:

ARF_i = adhesion reduction factor of coating i ;

τ_{bA} = bulk shear stress of the aluminum; and

τ_{bi} = bulk shear stress of coating i .

The push-off test is conducted by first placing a thin 1 cm diameter cylindrical plastic mold onto a substrate. The mold is then filled with deionized water and placed together with the substrate into a cold chamber at $-10.0 \pm 0.2\text{ }^{\circ}\text{C}$ for 24 h to form an ice cylinder. The test sample is placed onto the holder and fixed into position by a vacuum (using two specialty screws on the apparatus). In our test, a remote computer-controlled interface controlled the velocity of these specialty screws at a fixed rate of $0.05\text{ mm}\cdot\text{s}^{-1}$ so that the sample holder gradually approached the force gauge. The force gauge was set to measure the shear force every Deci-second (one-tenth of a second) until the ice was detached. The adhesion stress was then calculated based on the maximum force and icing area. As previously stated, the adhesion reduction factors (ARF) of the coatings are obtained by dividing the bulk shear stress value of the uncoated aluminum sheets by the bulk shear stress of the coated sheets. Figure 2 illustrates the push-off apparatus.

The two methods previously described were used to determine ice adhesion. The CAT is a method that uses simulated atmospheric ice, while the push-off test is a better representative of ice removal during actual operations. The use of the centrifugal force, however, allows for a direct comparison of coatings.



Figure 2. Overview of the push-off apparatus. The ice adhering to the coating is pushed off by the force gauge and evaluates the adhesion.

The final method consists of measuring the water freezing delay on the coatings interface, namely the nucleation time. The experimental freezing device used allows for the precise determination of the time required for a water drop to solidify under controlled environmental conditions. The volume of the water droplet was 10 μL and the test was performed at $-10\text{ }^{\circ}\text{C}$. The reported values are the average of seven experimental runs.

These three laboratory tests were used to predict the icephobic behavior. In the case where more materials need to be evaluated, these methods could be used for screening purposes to adequately select the most promising materials prior to performing an extended evaluation.

2.4. Multi-Tools Analysis

The goal of this study was to evaluate coatings under specific environmental conditions that simulate actual operations. For this purpose, a procedure based on utilizing different tools under different icing conditions was developed. The test protocol is based on the Mohs scale. The Mohs scale was invented in 1812 by the German mineralogist Friedrich Mohs to measure the hardness of minerals. It is based on 10 readily available minerals. As it is an ordinal scale, one must proceed by comparison (ability of one to scratch the other) with two other minerals of known hardness. This scale is neither linear nor logarithmic.

For this project, the comparison scale uses the five tools as illustrated in Figure 3. These tools are available for purchase at any local supply store. All tools were classified in order of hardness according to the expertise of the research team.

In Figure 3, tool A represents a typical car brush. The brush is generally the first piece of equipment used to remove snow or other loose contamination. The second tool, shown in Figure 3 (tool B), is the flexible polymer blade. This type of instrument allows for the removal of snow without damaging the surface. For the purpose of this study, only the widest part was used. The third tool utilized, tool C, was a squeegee as depicted in Figure 3. Normally used for window cleaning, the squeegee was slightly stronger than the flexible polymer blade but less than the hard polymer blade (tool D in Figure 3). Lastly, two rigid polymer blades, one smooth and one corrugated (tool D and tool E in Figure 3, respectively), were used for de-icing. Both blades are normally used to remove adhering contaminants from surfaces and require the application of some form of pressure and, most importantly, the passage of several steps for complete removal.

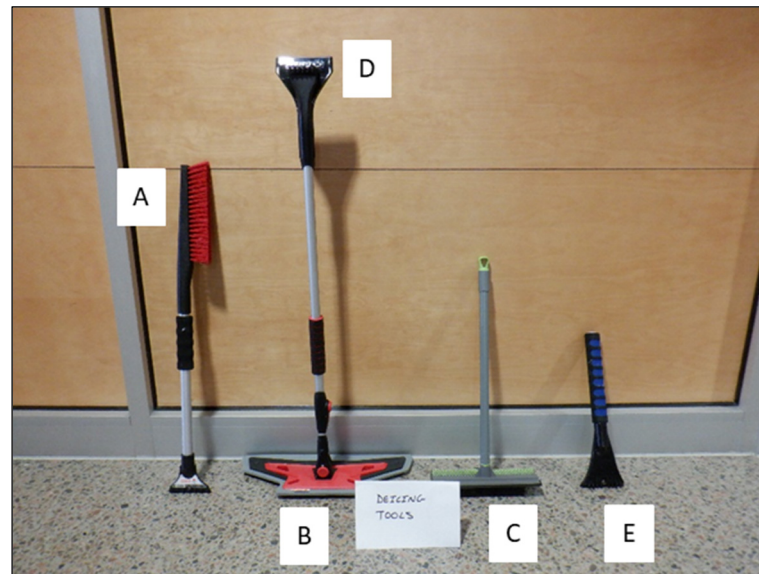


Figure 3. De-icing tools used in the multi-tools analysis, which range from softest to hardest: (A) the brush, (B) the flexible polymer blade, (C) the squeegee, (D) the hard polymer blade, and (E) the corrugated polymer blade.

The protocol was to begin with the brush (least amount of force needed during de-icing) and conduct five passes (sweeps). If contamination was still present, we moved on to the next available tool with respect to increasing force (flexible polymer blade), and repeated until all contamination was removed or until all tools were tested with five passes. The objective was to identify the level of force and number of passes required to remove the ice. These icing and de-icing tests were performed in the AMIL 9M cold room. All de-icing tests were performed by the same technician and in the same timeframe to ensure repeatability. The technician also applied the same pressure on each material during each icing condition. The speed of passing each tool, the positioning of hands on each tool, and the technician's posture and stance, along with plate restraining, were all kept consistent. After each passage, the plates were inspected visually, photographed, and weighed.

2.5. Icing Conditions

The above-mentioned tools were used under four different icing conditions to evaluate how each coating may assist in manual de-icing.

The first icing condition consisted of high-intensity freezing rain (HZR) of short duration at a temperature of $-10\text{ }^{\circ}\text{C}$. For operations, this type of precipitation can occur in a very short period of time and coat cold rotorcraft surfaces with a thin layer of ice. The duration of precipitation was determined to be 5 min. This precipitation was generated using two $1000\text{ }\mu\text{m}$ pneumatic sprinklers with tap water at a temperature of $4\text{ }^{\circ}\text{C}$ positioned at the top of the cold chamber. The total water droplet free fall distance was 7.1 m. The rate of precipitation was calibrated by adjusting the "On" time and "Off" time of the sprinkler. The sprayers were kept centered with the available support. A typical representation of the obtained icing condition is presented in Figure 4. The resulting ice does not cover the entire surface but is interconnected, and the contaminant adheres strongly to the substrates.



Figure 4. High-intensity freezing rain over aluminum reference plate.

The second condition consisted of low-intensity freezing rain (LZR). The lower icing intensity was obtained using the same conditions as the high-intensity freezing rain but with the application of an “Off” time of 25 s for about 2 min. Under these conditions, the performance of the hydrophobic coated surfaces was exploited, to a greater extent, allowing for the formation of ice beads instead of an ice sheet. The amount of ice obtained on the plate was not as uniform as the high-intensity freezing rain and is seen in Figure 5.



Figure 5. Low-intensity freezing rain over aluminum reference plate.

The third condition consisted of dry snow. This was done to simulate an aircraft, which landed prior to a dry snow event and was cold soaked. The snow used during testing was obtained from a snow event that occurred 3 days prior to testing. This snow was collected in a cooler and stored in a freezer at a temperature of $-10\text{ }^{\circ}\text{C}$. Prior to testing, a 200 mm diameter sieve with 1.4 mm openings was used to sift the snow onto the test plate. The average snow accumulation for each test was 3 mm as seen in Figure 6.



Figure 6. Dry snow over aluminum reference plate.

The fourth condition consisted of partially melted and refrozen snow. To simulate a more conservative or worse condition involving snow, the accretion of snow was performed on a warm surface in a cold room. In an operational perspective, this simulates an aircraft, which landed during a dry snow event with some surfaces above the freeze point (warm soaked surface), likely due to engine exhaust, etc. This was achieved by sifting snow as previously described for dry snow, with the aluminum plate tempered to 8 °C and subsequently placed in the cold chamber at −10 °C for the application of snow. As the snow was accumulating on the test plate, the initial snow particles melted and refroze with the cooling of the plate, and snow was added until a 3 mm thickness was achieved. The result was snow and ice adhesion on the test plate with added snow on the surface as shown in Figure 7.



Figure 7. Partially melted and refrozen snow over aluminum reference plate of 30 cm by 50 cm.

2.6. Materials

Five different materials were used to evaluate the proposed procedure and to assess their efficiency in assisting a manual de-icing. The test materials were as follows:

- Aerospace-grade 6061-T6 aluminum

As previously stated, the aluminum test plate served as the benchmark or reference. The surface finish as well as its wettability can thus be used to represent a painted rotorcraft surface.

- Nusil

This material consisted of a commercial silicone elastomer named Nusil. A hydrophobic surface results when applied to different substrates. The silicone polymerizes at room temperature to obtain a smooth surface finish. A primer was added to the surface prior to application to promote silicone adhesion. Since silicone is a viscous material prior to polymerization, it was applied using a simple brush.

- SWIX LF5

This material consisted of a commercial Ski wax named SWIX LF5. This material is fragile when applied to a substrate and is generally used to enhance the performance of skiers in alpine ski. It is a fluoro-carbon-based wax, which is most effective in the temperature range of −8 °C to −14 °C. Fluorinated components have been shown to be efficient against water and ice adhesion. The application process consisted of heating the wax to 150 °C using an electric iron. Once melted, it was applied uniformly on the substrates which were at room temperature.

- SurfEllent

This material consisted of the commercial coating named SurfEllent. It is a commercially advanced anti-icing coating and is used for multiple applications. The material formulation is based on polydimethylsiloxane and acetoxy silane cross-linker. The coating was applied using a spray applicator.

- Wearlon super F1-Ice

This material is the commercial coating named Wearlon super F1-Ice. It is an epoxy/latex-based coating used on communication towers and bridge structures. The coating consists of two-parts applied simultaneously by a spray applicator.

The selection of different materials that are based on differing chemical compositions allows for a comprehensive assessment of the proposed procedure. Each material consisted of a thin and uniform layer that entirely covered the surface.

2.7. Scoring Methodology

The scoring methodology employed consists of ranking each result with a maximum score of 85.

The score of the CAT, push-off test, and freezing delay were based on the value of the reduction factor compared to that of the reference. In order to adequately score the performance of all materials tested, both the ARF and MTA were used. It is important to note that the MTA should have a greater weight on the final score compared to the ARF due to its significance in real-world operations. Therefore, in order to decrease the impact of the ARF values on the final results and increase the impact of the MTA, the ARF values were proportionally down scaled using a maximum value of 5. The surface with the best ARF thus obtains a value of 5, while the others are reduced on the scale. This new score out of 5 was named the icephobic rating.

For the MTA tests, the maximum possible score of 20 represents the most effective de-icing process, which consists of using the softest tool, i.e., the brush, and eliminates all contaminants with a single pass. A score of 0 thus represents the most ineffective de-icing process and resulted in the use of the hardest coarse polymer blade with 5 consecutive passes. The latter score is obtained if contamination is still present after the de-icing process is complete. Thus, the maximum score per condition is 20 with a maximum result of 80.

3. Results and Discussion

The results presented in this paper are as follows: the characterization results, the icephobic behavior, and the MTA results. The characterization results are presented in Table 1.

Table 1. Wettability results.

Material #	1: Reference	2: Nusil	3: Swix	4: SurfEllent	5: Wearlon
Material Type	Aluminum	RTV Silicone	Fluorinated wax	Silicone Coating	Epoxy coating
CA (°)	93 ± 2	114 ± 2	112 ± 1	112 ± 2	110 ± 3
CAH (°)	34 ± 3	6 ± 2	6 ± 2	10 ± 1	35 ± 3

The procedure consisted of two main comparisons. The first was between the experimental materials and the reference aluminum, while the second was between the materials themselves. This allowed us to draw two main conclusions: (i) to determine if the proposed material was better than that of the reference and (ii) to establish which product was best for each condition, which in turn allowed for its classification. The characterization of the material was done using contact angle and contact angle hysteresis, which gave relevant information to understanding their behavior under the precipitation. The reference material, aluminum, had a contact angle of $93 \pm 2^\circ$. The surface was at the limit of being considered hydrophobic. However, the contact angle hysteresis, measured at $34 \pm 3^\circ$, shows that the surface was not at all uniform and that it could have some asperities that could aid in anchoring water. When a layer of material #2, i.e., Nusil, was applied to the same aluminum, the contact angle increased to $114 \pm 2^\circ$, signifying that the surface is clearly hydrophobic. Since the layer of the RTV silicone was sufficient to fill all of the aluminum's asperities, the contact angle hysteresis was then reduced to a value of $6 \pm 2^\circ$. Visually, the Nusil RTV silicone is soft and smooth. In the same way, the Swix Ski Wax, since it is more friable, showed results comparable to that of Nusil, with a contact angle of

$112 \pm 1^\circ$ and a contact angle hysteresis of $6 \pm 2^\circ$. The SurfEllent silicone coating also had a contact angle in the same range with a value of $112 \pm 2^\circ$ but with a slightly higher contact angle hysteresis of $10 \pm 1^\circ$. Finally, material #5, i.e., the epoxy-based coating Wearlon, had a contact angle in the same range with a value of $110 \pm 3^\circ$; however, its contact angle hysteresis was practically the same as that of aluminum with a value of $35 \pm 3^\circ$. From these results, we can see that all of the materials' outer surfaces are in the same range with respect to contact angle and are more hydrophobic than that of the reference material, aluminum.

The same comparisons can be made with the icephobic behavior characteristics as presented in Table 2.

Table 2. Icephobic assessment.

Material #	1: Reference	2: Nusil	3: Swix	4: SurfEllent	5: Wearlon
τ CAT (KPa)	609.5 ± 36.8	72.5 ± 4.1	319.0 ± 70	89.2 ± 1.9	101.5 ± 9.1
ARF CAT	-	8.4	2.2	6.8	6.0
τ PO (KPa)	604.0 ± 8.6	48.5 ± 8.5	56.4 ± 9.7	67.9 ± 4.1	527.0 ± 5.6
ARF PO	-	12.5	10.7	8.9	1.1
Freezing delay (sec)	126	1982	1045	828	336

The two first characteristics are concerned with the ice adhesion measurement using two laboratory tests: the centrifuge adhesion test (CAT) and the push-off test (PO). These two methods are complimentary to each other since the CAT uses simulated atmospheric ice and is widely used and recognized by the industry. While PO, although it uses molded ice, better mimics the passage of a tool, and is therefore more representative of the targeted application presented here. The results presented for both aforementioned methods are illustrated as a function of bulk shear stress (τ) and also in terms of adhesion reduction factors (ARF). The first material, i.e., the reference aluminum, had an ice adhesion value in the same range for both methods with 609.5 ± 36.8 KPa and 604.0 ± 8.6 KPa for CAT and PO, respectively. This value of ice adhesion is in the typical range obtained for bare aluminum. The material showing the best results was Nusil with ARFs of 8.4 and 12.5 for the CAT and PO, respectively. It signifies that the ice adhesion was reduced by 88% to 97% depending on the method. The second-best ranked material was SurfEllent, with ARFs of 6.8 and 8.9 for the CAT and PO, respectively. SurfEllent, similarly to Nusil, is a silicone-based coating. Both showed a contact angle that is clearly hydrophobic and a contact angle hysteresis below 10° , which shows that they are unlikely to interact with water in its liquid state or adhere with water in its solid state. The second element to consider was their uniformity and smoothness. Both offered a complete smooth coating of the surface and did not show visual anchoring points for ice adhesion. The third-best ranked material was the Swix wax with an ARF of 2.2 with the CAT and an ARF of 10.7 with the PO. The results were much better with the PO than the CAT. This can be attributed to the type of ice used during the tests. Since the waxy material is not designed to adhere perfectly to a metal surface, the coating may not be completely uniform. So, when small droplets like freezing drizzle are deposited on the materials surface, some of these droplets will remain on the top of the wax; however, some may penetrate further to the substrates surface and can thus partially anchor themselves with the aluminum. This phenomenon is less pronounced with the PO test because the ice is formed by molding a fixed quantity of water that does not penetrate the wax prior to freezing. The same reasoning can be drawn with the contact angle since the water drop of $5 \mu\text{L}$ remains on the top and does not penetrate. Finally, the last performant material, in terms of low ice adhesion, was the epoxy base Wearlon. Although the result in the CAT provided an ARF of 6.0, the ARF in the PO test was only 1.1. In this particular case, we can correlate it with the value of the contact angle hysteresis, which is practically the same as that of aluminum, and thus the presence of anchoring points promotes ice adhesion. Visual inspection of the Wearlon also confirmed the presence of millimetric anchoring points that may increase ice adhesion. Materials may react differently depending on the icing conditions used. Therefore, ice adhesion

measurements illustrate the importance of using multiple methods prior to establishing a material as icephobic.

To deepen the understanding of icephobic material behavior for aircraft application, it is necessary to thoroughly analyze the mechanism of ice formation (the process of nucleation and growth). The fundamental and crucial step for the formation of ice is known as nucleation. Freezing of a small quantity of water (e.g., a droplet) does not occur immediately after contact with a cold sub-zero surface. Prior to nucleation, the time required for a droplet of water to freeze, once in a supercooled state, is called the induction period. This induction period is often referred to as the “freezing time delay.” In this project, the longer the freezing delay, the better the material. The freezing time delay is defined as the time interval between the impacting of the water droplet on the pre-cooled substrate and the onset of freezing.

Preliminary data on the freezing delay of the water droplet for the reference material surface, aluminum, were determined to be 126 s. Overall, the initial results showed that the maximum freezing delay of 1982 s was achieved with the Nusil surface, which was more than 15 times that of the reference aluminum. In other words, the formation of ice can be effectively delayed by the Nusil surface at a temperature and humidity of $-10\text{ }^{\circ}\text{C}$ and 20%, respectively. The effect was less with Swix with 1045 s and SurfEllent with 828 s, but they were still 6 to 8 times longer than aluminum. Finally, the Wearlon provided the poorest performance when compared to the other materials with a freezing delay of 336 s. The benefit obtained from these experiments is that the freezing delay can be used as a prediction tool to evaluate the effectiveness of the material. The longer the freezing delay, the longer the user has to remove the contamination before it adheres and requires more energy for removal.

3.1. Multi-Tool Analysis

The following section describes the results of the multi-tool analysis (MTA). Refer to Figure 3 for details related to the de-icing tools used, as they are referred to by a range of numbers in the figures of this section. Using the four icing conditions identified in Section 2.5, the plates were subjected to manual MTA de-icing cycles with a gradation in tool hardness. The results are presented in Table 3.

Table 3. MTA results.

	1: Reference	2: Nusil	3: Swix	4: SurfEllent	5: Wearlon
High-intensity freezing rain	Score: 0 Hard, ridged polymer 5 passes Ice remaining	Score: 6 Hard polymer 5 passes	Score: 10 Hard polymer 1 pass	Score: 1 Hard, ridged polymer 5 passes	Score: 0 Hard, ridged polymer 5 passes Ice remaining
Low-intensity freezing rain	Score: 0 Hard polymer 5 passes Ice remaining	Score: 6 Medium polymer 5 passes	Not tested	Score: 9 Medium polymer 2 passes	Score: 9 Medium polymer 2 passes
Dry snow	Score: 20 Brush 1 pass	Score: 14 Soft polymer 2 passes	Score: 20 Brush 1 pass	Score: 20 Brush 1 pass	Score: 15 Soft polymer 1 pass
Adhering snow	Score: 5 Hard polymer 1 pass	Score: 5 Hard polymer 1 pass	Score: 10 Medium polymer 1 pass	Score: 10 Medium polymer 1 pass	Score: 8 Medium polymer 3 passes

The results are presented in terms of the score obtained as per the procedure explained in Section 4. To recap, the scores can range from 20, which is considered the most effective, to 0, which is considered the least effective, as seen in red in Table 3. For simplicity, the

tool name and the number of passes were added. Each type of precipitation is treated individually and is discussed below.

3.1.1. MTA vs. High-Intensity ZR

The first condition to be investigated was high-intensity freezing rain. The resulting ice, regardless of material tested, consisted of an even ice cover. The results are presented in Figure 8 as the weigh percentage of remaining ice contaminant, as a function of tool used, and as the number of passages conducted. When the mass remains constant, it indicates that the tool passed over the ice without removing any. For all coatings except the ski wax, the use of the brush (A) and the soft polymer blade (B) did not result in any ice removal. In the specific case of the ski wax, the first pass of the flexible polymer blade (B) resulted in the removal of approximately 25% of the mass of ice. In all cases, the use of the rigid polymer blade (D) resulted in the removal of the most significant amounts of contaminants. In some cases, the use of the ridged, hard polymer blade was necessary to complete the de-icing cycle. In two cases, namely the aluminum baseline and Wearlon, the selected tools did not completely remove the ice. The obtained results correlate well with the results obtained using the PO. For this condition, the best materials were the Ski Wax, with a score of 10, and Nusil, with a score of 6. However, the SurfEllent, with a score of 1, still assisted de-icing in a more effective manner than the reference surface. Generally, the de-icing process was much easier on soft materials such as Nusil; however, this type of surface finish did slightly hinder the passage of certain blades. Although the Swix provided the best results, the material was broken and torn apart during the de-icing process and acted more like a one-time use sacrificial layer.

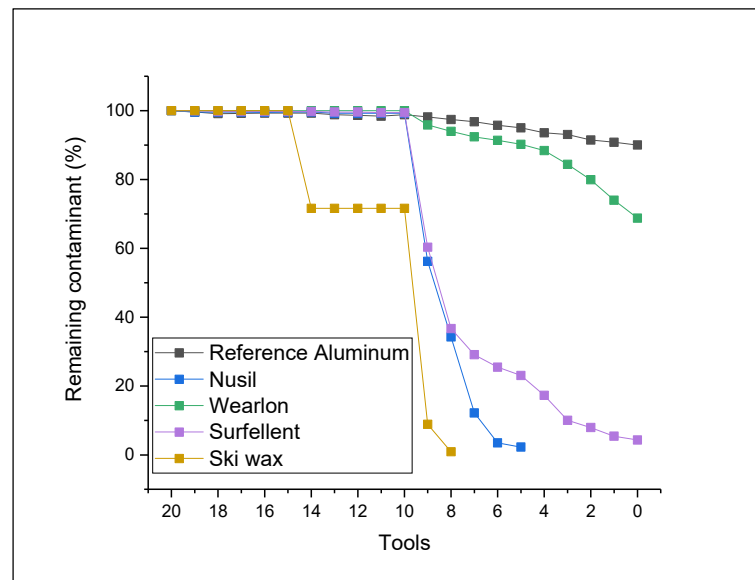


Figure 8. Multi-tool analysis under high-intensity freezing rain. Note: Numbers correspond to the tool used and number of passages during de-icing. Where “20 to 16” represent the broom, “15 to 11” represent the soft polymer blade, “10 to 6” represent the hard polymer blade, “5 to 1” represent the ridged polymer blade, and 0 indicates that ice remained on the surface.

3.1.2. MTA vs. Low-Intensity ZR

The second type of icing simulated was low-intensity freezing rain. The results are presented in Figure 9 as the weigh percentage of remaining ice as a function of tools and the number of passages. The corresponding picture after icing is illustrated in Figure 5. At the lower intensity of freezing rain precipitation, the materials’ hydrophobic properties are more effective and can therefore delay the solidification of water droplets or cause them to solidify in beaded form. In this case, an additional tool was added that was stiffer than the soft polymer blade (B) but less than the solid polymer blade (D), namely the squeegee

(tool C). The aluminum surface was again observed to be the least favorable one, not allowing for the complete de-icing after the passage of all tools. In the case of the SurfEllent coating, however, the soft polymer blade (B) was able to partially remove some of the ice. In almost all cases, the use of tool C (squeegee) removed most of the contaminants from the Wearlon- and SurfEllent-coated surfaces. Nevertheless, the use of the solid blade was necessary to remove some residual contamination present on the Nusil surface. Note that the ski wax was not tested in this condition. However, we can assume that a similar result to the previous condition would be obtained.

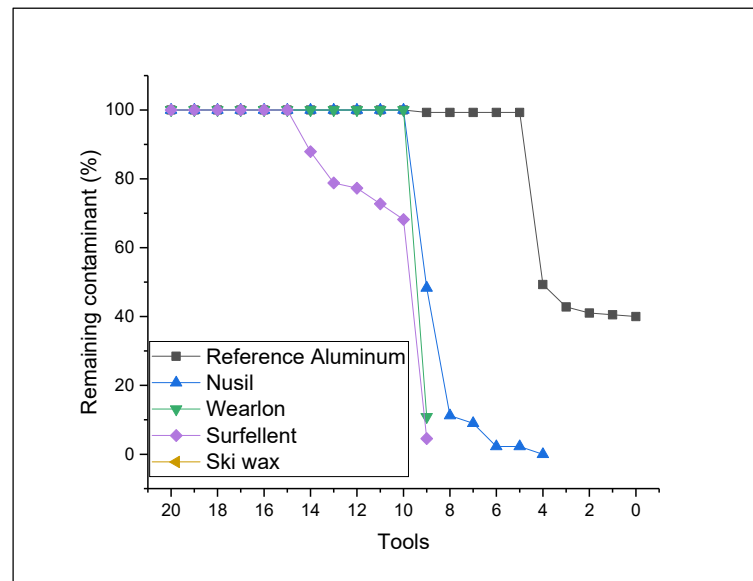


Figure 9. Multi-tool analysis under low-intensity freezing rain. Note: Numbers correspond to the tool used and the number of passages during de-icing. Where “20 to 16” represent the Broom, “15 to 11” represent the soft polymer blade, “10 to 6” represent the squeegee, “5 to 1” represent the hard polymer blade, and 0 indicates that ice remained on the surface.

A simple 2D representation of ice covering two different tested materials is presented in Figure 10 below. The left portion of the figure shows how ice typically accumulates on an aluminum surface. The ice is shown to cover the surface uniformly, exploiting the available roughness and all anchoring points, which in turn increases ice adhesion. In the same manner, when the MTA is applied using soft tools, such as the broom and the polymer, they are not rigid enough to break the adhesive bond with the surface. Instead, the cohesive bonds are first broken within the ice itself followed by the breakage of adhesive bonds. Therefore, a harder tool, such as hard and ridged polymer, is needed to effectively remove the ice. In the case of hydrophobic materials, such as a Nusil coating for example, the film of ice is not uniform, as represented in the right portion of Figure 10. The higher contact angle and the longer freezing delay of the material causes the water to agglomerate in large beads (droplets) prior to freezing. This effect is more noticeable when the precipitation rate is low. However, since the surface is hydrophobic, the ice covering the surface is less uniform, which reduces the adhesion of ice compared to that of aluminum alone. Hence, the passage of a soft tool allows for the gradual removal of small pieces of ice with substantially less effort. In essence, there is no need to break the cohesive bond prior to the adhesive bond since it is weaker when compared to the reference aluminum surface.

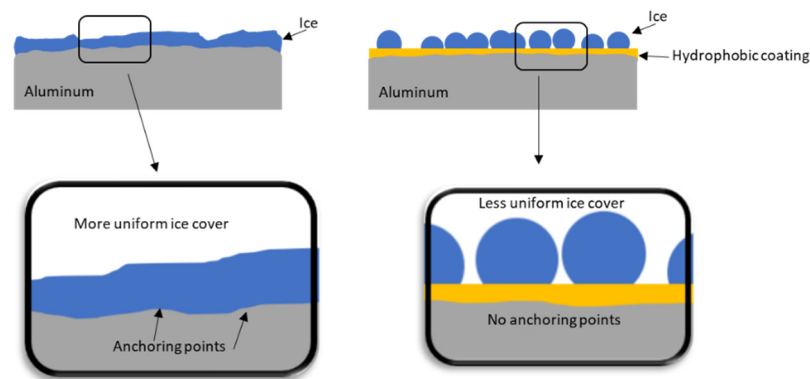


Figure 10. 2D representation of ice accumulation over bare aluminum (left portion) and over hydrophobic coating (right portion).

3.1.3. MTA vs. Dry Snow

The third condition tested was dry snow. This precipitation is non-adherent when falling on a cold-soaked surface, and this type of precipitation occurs very commonly in the winter season. The main results are presented in Figure 11.

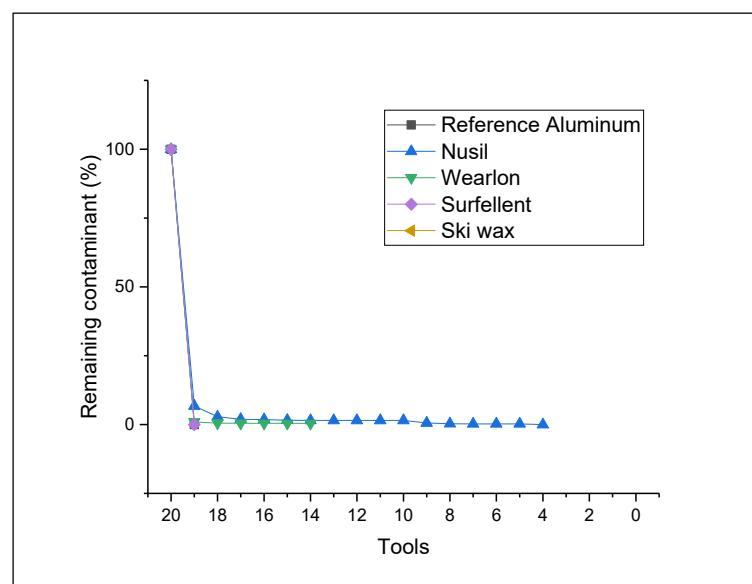


Figure 11. Multi-tool analysis under dry snow. Note: Numbers correspond to the tool used and number of passages during de-icing. Where “20 to 16” represent the broom, “15 to 11” represent the soft polymer blade, “10 to 6” represent the squeegee, and “6 to 1” represent the hard polymer blade.

In almost all cases, including aluminum, the snow was removed on the first pass of the brush (the softest tool). However, two surfaces, Wearlon and Nusil, caused a very thin layer of snow to stick to their surfaces, requiring the use a rigid surface to scrape it off effectively.

It was initially expected that all materials would react the same in the presence of dry snow. However, soft materials such as Nusil allowed for a very small amount of snow to stick to its surface upon passage of the broom. By using the soft polymer, the remaining snow was easily removed. As presented in Figure 11, further passage of the tools was undertaken to ensure that all contamination was removed.

3.1.4. MTA vs. Dry Snow on a Warm Surface

Finally, in the fourth targeted condition, the cold snow was deposited on a warm surface having an approximate temperature of 8 °C. This was done in order to replicate

a scenario where a critical surface was heated by the warm air of an engine. The snow thus partially melted and, under the effect of the cold temperature of the chamber, refroze and adhered to the surface. The results obtained using different surfaces are shown in Figure 12 as the weigh percentage of remaining contaminant as a function of tools used and the number of passages.

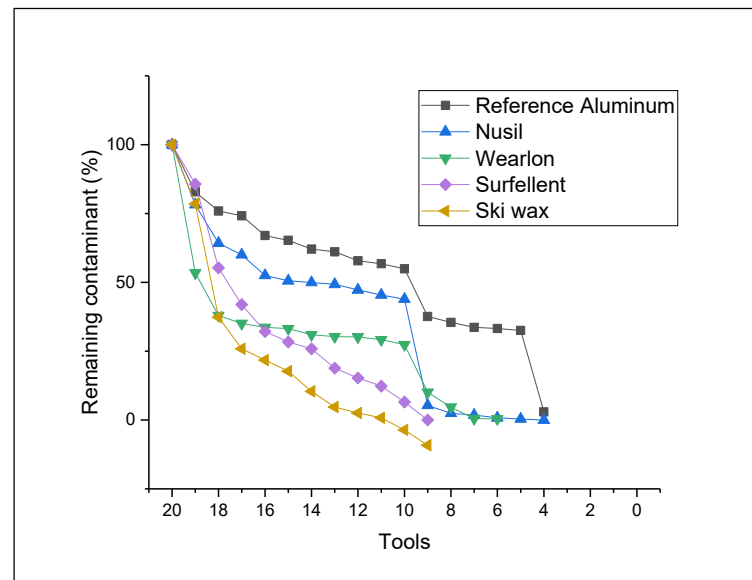


Figure 12. Multi-tool analysis under partially melted and refrozen snow-simulation of dry snow on a warm soaked surface. Note: Numbers correspond to the tool used and number of passages during de-icing. Where “20 to 16” represent the broom, “15 to 11” represent the soft polymer blade, “10 to 6” represent the squeegee, and “5 to 1” represent the hard polymer blade.

In all cases, it was possible to remove the contaminants. In the first instance, the first layer of snow that was not melted and was situated over the resolidified contamination was removed by brushing. The reference surface, aluminum, required the passage of a solid polymer blade to completely remove all surface contamination. The SurfEllent, Swix, and Wearlon were similar in terms of difficulty in removal of surface contamination. Both required tool C, i.e., the Squeegee, to remove most of the contamination followed by the medium polymer to remove the remaining frozen snow. The Nusil coating performed similarly to the aluminum reference as contamination was mostly removed with the hard polymer blade.

Typically, this case where snow is adhering to a critical surface represents the most conservative case, which could be encountered by crew members while inflight. Because some of the snow partially melted upon contact with the warm surface, the resulting melt water can penetrate both the surface and the remaining unmelted snow and thus act as an adhesive.

3.2. Correlating the Laboratory Results of Plates and Rotor Blade Sections

In order to validate the procedure for use on rotorcraft tail blade profiles, it was determined that scaling upward from a plate generated correlated results. This in turn validated the procedure for use on rotorcraft tail blades. It is important to note that the goal was to determine if the military blade, painted in matte, and the commercial blade, painted in gloss (both salvaged from an operational aircraft) presented in Figure 13, would generate similar results to the aluminum baseline test plate surfaces.



Figure 13. (A) Commercial gloss and (B) military matte-painted tail blade profiles.

All tools previously described in Sections 2.4 and 3.1 were used in the same order with the same numbers of passages. When considering the condition of HZR, for all samples tested, ice remained after all tools were used with five passes. The same results were obtained with the matte, gloss profiles, and under the condition of LZR. When tested using snow as the contamination, the snow was removed after only one brush stroke for all trials. It is therefore reasonable to conclude that, under identical icing conditions, the aluminum plates behave the same way as the tail blade profiles. Additional testing was conducted with profiles coated with ski wax and Nusil and then compared with the aluminum reference plates. Under the precipitation conditions studied, the Swix wax obtained comparable results, including de-icing with the same tools and the same number of passes. A considerable difference, however, was noticed with Nusil. The latter coating applied to the profile required the use of a harder tool. It did not facilitate the de-icing process in certain concave areas or on the leading edge.

The majority of the tests conducted demonstrated that testing on flat plates can reproduce the de-icing process done on a rotorcraft tail profile. However, they also demonstrated the importance of testing in actual conditions on a full-sized aircraft before considering use due to the possible complexities associated with geometries.

Although the results obtained with this procedure are repeatable and provides relevant information regarding the behavior of a material under winter decontamination conditions, some improvements could be made. To ensure a more reliable and repeatable process, the tools could be instrumented to measure the shear stress applied as a function of time for the purpose of classification. However, at the present moment, the proposed procedure is highly representative of the operational techniques currently used.

3.3. Overall Classification of the Materials

As the aim of this procedure is to evaluate each material's ability to assist in manual de-icing, their individual results were compiled to obtain an overall ranking. The results used for this ranking are presented in Table 4. As specified in the methodology, the icephobic behaviors were regrouped to produce one rating out of five. The icephobic rating was obtained using the average of their reduction factor as compared to the reference aluminum. The best overall coating regarding the icephobic behavior was Nusil with a rating of 5.0, followed by SurfEllent with 3.0, then Swix with 2.9, and then Wearlon with 1.3. Aluminum was awarded a rating of 0.4 for comparison purposes. The ratings obtained from the MTA using the four targeted conditions were used without any further modification, with an individual maximum score of 20.

Table 4. Ranking of tested materials.

	1: Reference	2: Nusil	3: Swix	4: SurfEllent	5: Wearlon
ARFCAT	1	8.4	2.2	6.8	6
ARFPO	1	12.5	10.7	8.9	1.1
RF Freezing delay	1	15.7	8.3	6.6	2.6
RF Average	1	12.2	7.1	7.4	3.2
Icephobic Rating (/5)	0.4	5.0	2.9	3.0	1.3
MTA HZR	0	6	10	1	0
MTA LZR	0	6	Not tested	9	9
MTA Dry SNW	20	14	20	20	15
MTA Adh SNW	5	5	10	10	8
Total	25.4	36.0	42.9	43.0	33.3
Ranking	5	3	2	1	4

The final results for each material were given a score out of 85. The criterion that stipulates if a material can assist in a manual de-icing is to obtain an overall result higher than that of the aluminum reference. Given this criterion, all tested materials could assist the manual de-icing since each of them received a score higher than that of aluminum, i.e., greater than 25.4. The material with the best performance was found to be SurfEllent with a score of 43.0, followed by Swix with 42.9. The slight difference between the two materials is due to the poor results obtained in the CAT for Swix where the ice had significantly more adherence. The third ranked material was Nusil, even though it demonstrated increased icephobic behavior, it reacted negatively under snow conditions. Finally, the last ranked material was Wearlon, which performed somewhat like aluminum in some conditions, for example, in the MTA high-intensity freezing rain.

From these results, it is important to note that, although a material may show promising results using the CAT or PO, it is not inherent that it will behave the same way when subjected to different icing or snowing precipitation. CAT and PO are good predictors; however, other icing conditions need to be evaluated before claiming a material to be icephobic.

It is important to note that other significant factors could be integrated within the evaluation process throughout this procedure. One important factor that could be added is the evaluation of the coating's mechanical resistance, especially if the targeted application is in aerospace for aircrafts or rotorcrafts. The critical surfaces of these aircrafts are subjected to several inclement conditions such as rain and sand. It is important to recognize that ice can also undermine the integrity of a coating and significantly reduce its efficiency. Erosion that occurs during normal operation, especially to leading edges, is a serious issue that needs to be evaluated prior to large-scale implementation. Standard tests that are documented and well known to the industry could be used and given a certain weighted percentage within the procedure. On the other hand, a pass/fail criterion could be implemented depending on its criticality.

A second factor that could be added to this analysis is a weighted score reflecting the ease of application. Treating already deployed rotorcrafts with a new material like a coating could be easily done if the method does not require multiple layers or pre-treatments.

Finally, this procedure can be modified to better reflect the needs of the end-user by allocating more weight to a characteristic that is deemed significant for the targeted field of application. Using our classification as an example, if the icing condition deemed to be the most relevant is light-intensity freezing rain and snow is no longer considered to be significant, by increasing the weighted score of LZR to 50 and decreasing all others to 10, the final result would indicate that Nusil should be considered as the coating of choice. However, if the opposite is to be assessed, then more weight should be given to adhering snow, which will ultimately result in Nusil as the least-favorable coating.

When a coating is developed for a targeted application, industrials and academics need to assess if their materials are efficient or at the very least have the capability to optimize their properties. The presented procedure could then be used as a development tool by subjecting materials to the proposed controlled conditions. The main objective

is to obtain the most efficient materials with tailored performance properties. However, the use of these tools with the proposed conditions and tests may be adapted to ensure that the materials are accurately evaluated. Finally, the most promising materials could be assessed in a full-scale trial with an actual operational setup, i.e., a rotorcraft, to validate the laboratory results. This testing should focus on identifying the vulnerabilities of the coating's performance in the context of an actual rotorcraft operation. This can be done either outdoors in natural icing conditions, or in an appropriately sized icing laboratory capable of accommodating a full-sized aircraft.

4. Conclusions

The aim of this paper was to propose a detailed comparative procedure to assess the ability of passive ice protection materials in assisting the manual de-icing of a rotorcraft. The proposed procedure consisted of the characterization of materials under several laboratory tests in order to determine their characteristics of wettability and their icephobic behavior. Finally, their assessment under a multi-tool analysis was conducted to evaluate if they can assist in the manual de-icing, which includes conditions resembling operational reality. The multi-tool analysis allowed for the classification of materials depending on which tools were used, the number of passes necessary, and different atmospheric icing conditions. The comparison scale used five tools that are commercially available. The four icing conditions at $-10\text{ }^{\circ}\text{C}$ simulated in the laboratory included the following: high-intensity freezing rain, low-intensity freezing rain, dry snow, and partially melted and refrozen snow. Five different materials were used to evaluate the proposed procedure: aluminum, as a reference; two silicone-based coatings, Nusil and SurfEllent; an epoxy-based coating Wearlon; and finally a commercial ski wax, Swix.

The wettability characteristics, which were determined for all materials tested, provided valuable insight into their icephobic behavior. All materials tested were more hydrophobic than aluminum. The material with the most significant icephobic behavior was the Nusil silicone coating with an average reduction factor of 12.2. This was determined by considering the adhesion reduction factor of the CAT, the PO and the reduction factor in freezing delay. The following coatings, SurfEllent, Swix, and Wearlon, also showed some icephobic behavior, however, to a lesser extent, with average reduction factors of 7.4, 7.1, and 3.2, respectively. By evaluating the materials with the MTA, all materials behaved in a different manner. Although Nusil appeared to be promising under ice adhesion, it performed poorly under snow conditions. On the other hand, SurfEllent and Swix received high scores by clearly assisting the manual de-icing in most conditions. Overall, the SurfEllent coating received the highest score, indicating that it could assist the manual de-icing in these targeted conditions.

The overall results show that it is important to undertake several tests including different ice and snow precipitation before concluding a material to be icephobic. On the other hand, having such a procedure, including predictor tests and real operational techniques, certainly allows for a better characterisation of the material(s).

This procedure could easily be adapted to different fields of application by varying the type of frozen precipitation, the type of tools, and even the weight percentage of the results to adequately assess the efficiency of the materials in question. The improvement of the MTA could be undertaken by further instrumenting or automating the process, ensuring repeatability. Finally, this procedure could also be used as a development tool for the optimization and assessment of new materials.

Author Contributions: Conceptualization, J.-D.B., D.P., S.S., M.R. and G.M.; methodology, J.-D.B., D.P. and M.R.; validation, J.-D.B. and G.M.; formal analysis, J.-D.B.; resources, D.P., S.S. and M.R.; writing—original draft preparation, J.-D.B., D.P. and S.S.; writing—review and editing, M.R. and G.M.; supervision, G.M.; project administration, G.M.; funding acquisition, J.-D.B. and G.M. All authors have read and agreed to the published version of the manuscript.

Funding: The authors would like to thank the Department of National Defense of Canada for funding the research under contract W7714-217494.

Conflicts of Interest: The authors declare no conflict of interest.

References

- Ryerson, C.; Gilligan, T.; Koenig, G. Evaluation of three helicopter preflight deicing techniques. In Proceedings of the 37th Aerospace Sciences Meeting and Exhibit, Reno, NV, USA, 11–14 January 1999; p. 499.
- Gent, R.W.; Dart, N.P.; Cansdale, J.T. Aircraft icing. *Philos. Trans. R. Soc. A* **2000**, *358*, 2873–2911. [CrossRef]
- Brouwers, E.W.; Peterson, A.A.; Palacios, J.L.; Centolanza, L.R. Ice Adhesion Strength Measurement for Rotor Blade Leading Edge Materials. In Proceedings of the 67th Annual Forum, Virginia Beach, VA, USA, 3–5 May 2011.
- Kim, J.; Sankar, L.; Palacios, J.; Kreeger, R.E. Numerical and experimental studies of rotorcraft icing phenomena. In Proceedings of the 41st European Rotorcraft Forum 2015, Munich, Germany, 1–4 September 2015.
- Liu, Y.; Li, L.; Ning, Z.; Tian, W.; Hu, H. Experimental investigation on the dynamic icing process over a rotating propeller model. *J. Propuls. Power* **2018**, *34*, 933–946. [CrossRef]
- Palacios, J.L.; Han, Y.; Brouwers, E.W.; Smith, E.C. Icing environment rotor test stand liquid water content measurement procedures and ice shape correlation. *J. Am. Helicopter Soc.* **2012**, *57*, 29–40. [CrossRef]
- Villeneuve, E.; Volat, C.; Ghinet, S. Numerical and Experimental Investigation of the Design of a Piezoelectric De-Icing System for Small Rotorcraft Part 1/3: Development of a Flat Plate Numerical Model with Experimental Validation. *Aerospace* **2020**, *7*, 62. [CrossRef]
- Wang, Z.; Zhu, C.; Zhao, N. Experimental Study on the Effect of Different Parameters on Rotor Blade Icing in a Cold Chamber. *Appl. Sci.* **2020**, *10*, 5884. [CrossRef]
- Palacios, J.L.; Smith, E.C.; Gao, H.; Joseph, L.R. Ultrasonic Shear Wave Anti-Icing System for Helicopter Rotor Blades. In Proceedings of the Annual Forum Proceeding-AHS International 62nd Annual Forum, Phoenix, AZ, USA, 9–11 May 2006; pp. 1492–1502.
- Palacios, J.; Wolfe, D.; Bailey, M.; Szefi, J. Ice testing of a centrifugally powered pneumatic deicing system for helicopter rotor blades. *J. Am. Helicopter Soc.* **2015**, *60*, 1–12. [CrossRef]
- Drury, M.D.; Szefi, J.T.; Palacios, J.L. Full-scale testing of a centrifugally powered pneumatic de-icing system for helicopter rotor blades. *J. Aircr.* **2017**, *54*, 220–228. [CrossRef]
- Budinger, M.; Pommier-Budinger, V.; Reyssset, A.; Palanque, V. Electromechanical Resonant Ice Protection Systems: Energetic and Power Considerations. *AIAA J.* **2021**, *59*, 1–13. [CrossRef]
- Farzaneh, M.; Jakl, F. *Coatings for Protecting Overhead Power Network Equipment in Winter Conditions: Working Group B2. 44*; Cigré; 2015. Available online: <https://e-cigre.org/publication/631-coatings-for-protecting-overhead-power-network-equipment-in-winter-conditions> (accessed on 1 December 2021).
- Vazirinasab, E.; Maghsoudi, K.; Jafari, R.; Momen, G. A comparative study of the icephobic and self-cleaning properties of Teflon materials having different surface morphologies. *J. Mater. Process. Technol.* **2020**, *276*, 116415. [CrossRef]
- Yancheshme, A.A.; Allahdini, A.; Maghsoudi, K.; Jafari, R.; Momen, G. Potential anti-icing applications of encapsulated phase change material-embedded coatings; a review. *J. Energy Storage* **2020**, *31*, 101638. [CrossRef]
- Yancheshme, A.A.; Momen, G.; Aminabadi, R.J. Mechanisms of ice formation and propagation on superhydrophobic surfaces: A review. *Adv. Colloid Interface Sci.* **2020**, *279*, 102155. [CrossRef] [PubMed]
- Jung, S.; Dorrestijn, M.; Raps, D.; Das, A.; Megaridis, C.M.; Poulikakos, D. Are superhydrophobic surfaces best for icephobicity? *Langmuir* **2011**, *27*, 3059–3066. [CrossRef]
- Zhu, T.; Cheng, Y.; Huang, J.; Xiong, J.; Ge, M.; Mao, J.; Liu, Z.; Dong, X.; Chen, Z.; Lai, Y. A transparent superhydrophobic coating with mechanochemical robustness for anti-icing, photocatalysis and self-cleaning. *Chem. Eng. J.* **2020**, *399*, 125746. [CrossRef]
- Jamil, M.I.; Zhan, X.; Chen, F.; Cheng, D.; Zhang, Q. Durable and scalable candle soot icephobic coating with nucleation and fracture mechanism. *ACS Appl. Mater. Interfaces* **2019**, *11*, 31532–31542. [CrossRef] [PubMed]
- Saito, H.; Takai, K.; Yamauchi, G. Water-and ice-repellent coatings. *Surf. Coat. Int.* **1997**, *80*, 168–171. [CrossRef]
- Brouwers, E.W.; Palacios, J.L.; Smith, E.C. The experimental investigation of a rotor hover icing model with shedding. In Proceedings of the American Helicopter Society 66th Annual Forum, Phoenix, AZ, USA, 11–13 May 2010.
- Laforte, C.; Laforte, J.L. How a Solid Coating Can Reduce the Adherence of Ice on a Structure. In Proceedings of the Aircraft Ground De-Icing, July 2001. Available online: https://www.researchgate.net/publication/228473956_How_a_solid_coating_can_reduce_the_adhesion_of_ice_on_a_structure (accessed on 1 December 2021).
- Tarquini, S.; Antonini, C.; Amirfazli, A.; Marengo, M.; Palacios, J. Investigation of ice shedding properties of superhydrophobic coatings on helicopter blades. *Cold Reg. Sci. Technol.* **2014**, *100*, 50–58. [CrossRef]
- Kimura, S.; Yamagishi, Y.; Sakabe, A.; Adachi, T.; Shimanuki, M. *A New Surface Coating for Prevention of Icing on Airfoils*; SAE Technical Paper; 2007; pp. 148–1791. Available online: <https://www.sae.org/publications/technical-papers/content/2007-01-3315/> (accessed on 1 December 2021).
- Karmouch, R.; Coudé, S.; Abel, G.; Ross, G.G. Icephobic PTFE coatings for wind turbines operating in cold climate conditions. In Proceedings of the 2009 IEEE Electrical Power & Energy Conference (EPEC), Montreal, QC, Canada, 22–23 October 2009; pp. 1–6.

26. Antonini, C.; Innocenti, M.; Horn, T.; Marengo, M.; Amirfazli, A. Understanding the effect of superhydrophobic coatings on energy reduction in anti-icing systems. *Cold Reg. Sci. Technol.* **2011**, *67*, 58–67. [CrossRef]
27. Zhang, S.; Huang, J.; Cheng, Y.; Yang, H.; Chen, Z.; Lai, Y. Bioinspired Surfaces with Superwettability for Anti-Icing and Ice-Phobic Application: Concept, Mechanism, and Design. *Small* **2017**, *13*, 1701867. [CrossRef] [PubMed]
28. Shen, Y.; Wu, X.; Tao, J.; Zhu, C.; Lai, Y.; Chen, Z. Icephobic materials: Fundamentals, performance evaluation, and applications. *Prog. Mater. Sci.* **2019**, *103*, 509–557. [CrossRef]
29. Zheng, W.; Teng, L.; Lai, Y.; Zhu, T.; Li, S.; Wu, X.; Cai, W.; Chen, Z.; Huang, J. Magnetic responsive and flexible composite superhydrophobic photothermal film for passive anti-icing/active deicing. *Chem. Eng. J.* **2022**, *427*, 130922. [CrossRef]
30. Laforte, C.; Blackburn, C.; Perron, J.; Aubert, R. Icephobic Coating Evaluation for Aerospace Application. In Proceedings of the 55th AIAA/ASMe/ASCE/AHS/SC Structures, Structural Dynamics, and Materials Conference, National Harbor, MD, USA, 13–17 January 2014.

MDPI
St. Alban-Anlage 66
4052 Basel
Switzerland
www.mdpi.com

Applied Sciences Editorial Office
E-mail: applsci@mdpi.com
www.mdpi.com/journal/applsci



Disclaimer/Publisher's Note: The statements, opinions and data contained in all publications are solely those of the individual author(s) and contributor(s) and not of MDPI and/or the editor(s). MDPI and/or the editor(s) disclaim responsibility for any injury to people or property resulting from any ideas, methods, instructions or products referred to in the content.



Academic Open
Access Publishing

mdpi.com

ISBN 978-3-7258-0763-5